

# Biomechanics in Musculoskeletal Health

Lead Guest Editor: Wenxin Niu

Guest Editors: Ming Zhang, Jie Yao, Liping Wang, and Ka-Chun Siu





---

# **Biomechanics in Musculoskeletal Health**

Journal of Healthcare Engineering

---

## **Biomechanics in Musculoskeletal Health**

Lead Guest Editor: Wenxin Niu

Guest Editors: Ming Zhang, Jie Yao, Liping Wang,  
and Ka-Chun Siu



---

Copyright © 2017 Hindawi. All rights reserved.

This is a special issue published in “Journal of Healthcare Engineering.” All articles are open access articles distributed under the Creative Commons Attribution License, which permits unrestricted use, distribution, and reproduction in any medium, provided the original work is properly cited.

---

## Editorial Board

Saverio Affatato, Italy  
William Bertucci, France  
Tiago H. Falk, Canada  
Mostafa Fatemi, USA  
Jesus Favela, Mexico  
Joseph Finkelstein, USA  
Antonio Gloria, Italy  
Philippe Gorce, France

Andreas H. Hielscher, USA  
Zhongwei Jiang, Japan  
John S. Katsanis, Greece  
Feng-Huei Lin, Taiwan  
Maria Lindén, Sweden  
Francisco Lopez-Valdes, Spain  
Andreas Maier, Germany  
Rafael Morales, Spain

David Moratal, Spain  
Jose Joaquin Rieta, Spain  
Hélder A. Santos, Finland  
Emiliano Schena, Italy  
Maurizio Schmid, Italy  
Jiann-Shing Shieh, Taiwan  
Vinoy Thomas, USA  
Ioannis G. Tollis, Greece

# Contents

## **Biomechanics in Musculoskeletal Health**

Wenxin Niu, Ming Zhang, Jie Yao, Liping Wang, and Ka-Chun Siu  
Volume 2017, Article ID 8916431, 2 pages

## **Inhibitory Effect of Propolis on Platelet Aggregation In Vitro**

Yun-Xiang Zhang, Ting-Ting Yang, Liu Xia, Wei-Fen Zhang, Jia-Fu Wang, and Ya-Ping Wu  
Volume 2017, Article ID 3050895, 6 pages

## **The Biomechanical Study of Extraforaminal Lumbar Interbody Fusion: A Three-Dimensional Finite-Element Analysis**

Mingjie Yang, Guixin Sun, Song Guo, Cheng Zeng, Meijun Yan, Yingchao Han, Dongdong Xia, Jingjie Zhang, Xinhua Li, Yang Xiang, Jie Pan, Lijun Li, and Jun Tan  
Volume 2017, Article ID 9365068, 8 pages

## **Early Spatiotemporal Patterns and Knee Kinematics during Level Walking in Individuals following Total Knee Arthroplasty**

Xubo Wu, Lixi Chu, Lianbo Xiao, Yong He, Shuyun Jiang, Songbin Yang, and Yijie Liu  
Volume 2017, Article ID 7056469, 5 pages

## **Joint Torque and Mechanical Power of Lower Extremity and Its Relevance to Hamstring Strain during Sprint Running**

Yunjian Zhong, Weijie Fu, Shutao Wei, Qing Li, and Yu Liu  
Volume 2017, Article ID 8927415, 7 pages

## **Effects of Two Fatigue Protocols on Impact Forces and Lower Extremity Kinematics during Drop Landings: Implications for Noncontact Anterior Cruciate Ligament Injury**

Rui Xia, Xini Zhang, Xi Wang, Xiaole Sun, and Weijie Fu  
Volume 2017, Article ID 5690519, 8 pages

## **Study of the Mechanical Environment of Chondrocytes in Articular Cartilage Defects Repaired Area under Cyclic Compressive Loading**

Hai-Ying Liu, Hang-Tian Duan, Chun-Qiu Zhang, and Wei Wang  
Volume 2017, Article ID 1308945, 10 pages

## **Influence of Gait Speeds on Contact Forces of Lower Limbs**

Xin Wang, Yue Ma, Bo Yi Hou, and Wing-Kai Lam  
Volume 2017, Article ID 6375976, 6 pages

## **Effects of Pectus Excavatum on the Spine of Pectus Excavatum Patients with Scoliosis**

WeiHong Zhong, JinDuo Ye, JingJing Feng, LiYang Geng, GuangPu Lu, JiFu Liu, and ChunQiu Zhang  
Volume 2017, Article ID 5048625, 6 pages

## **A Strain Feedback Compensation Method during Cell Tensile Experiments**

Rong Zhou, Yunshu Yang, Wenzhuo Zhang, and Yuanwen Zou  
Volume 2017, Article ID 1587670, 6 pages

## **Biomechanical Property of a Newly Designed Assembly Locking Compression Plate: Three-Dimensional Finite Element Analysis**

Jiang-Jun Zhou, Min Zhao, Da Liu, Hai-Ying Liu, and Cheng-Fei Du  
Volume 2017, Article ID 8590251, 10 pages

**Endogenous Production of n-3 Polyunsaturated Fatty Acids Promotes Fracture Healing in Mice**

Yuhui Chen, He Cao, Dawei Sun, Changxin Lin, Liang Wang, Minjun Huang, Huaji Jiang, Zhongmin Zhang, Dadi Jin, Baiyu Zhang, and Xiaochun Bai

Volume 2017, Article ID 3571267, 6 pages

**The Effect of Lumbar Disc Herniation on Spine Loading Characteristics during Trunk Flexion and Two Types of Picking Up Activities**

Shengzheng Kuai, Weiqiang Liu, Run Ji, and Wenyu Zhou

Volume 2017, Article ID 6294503, 10 pages

**A Numerical Investigation into the Effects of Overweight and Obesity on Total Knee Arthroplasty**

Changjiang Wang, Yuan Guo, Junfen Shi, and Weiyi Chen

Volume 2017, Article ID 1496379, 8 pages

**Numerical Investigation on the Biomechanical Performance of Laparoscopic-Assisted Plate Used for Fixing Pelvic Anterior Ring Fracture**

Yiqian He, Yongtao Lu, Baosheng Yin, and Li Yu

Volume 2017, Article ID 9261037, 7 pages

**How Arch Support Insoles Help Persons with Flatfoot on Uphill and Downhill Walking**

Yu-Ping Huang, Kwantae Kim, Chen-Yi Song, Yat-Hon Chen, and Hsien-Te Peng

Volume 2017, Article ID 9342789, 6 pages

**Effect of Graded Facetectomy on Lumbar Biomechanics**

Zhi-li Zeng, Rui Zhu, Yang-chun Wu, Wei Zuo, Yan Yu, Jian-jie Wang, and Li-ming Cheng

Volume 2017, Article ID 7981513, 6 pages

## Editorial

# Biomechanics in Musculoskeletal Health

**Wenxin Niu,<sup>1,2</sup> Ming Zhang,<sup>3</sup> Jie Yao,<sup>4</sup> Liping Wang,<sup>5</sup> and Ka-Chun Siu<sup>6</sup>**

<sup>1</sup>Shanghai Yangzhi Rehabilitation Hospital, Tongji University School of Medicine, Shanghai 201619, China

<sup>2</sup>Department of Rehabilitation Sciences, Tongji University School of Medicine, Shanghai 200092, China

<sup>3</sup>Interdisciplinary Division of Biomedical Engineering, The Hong Kong Polytechnic University, Hung Hom, Hong Kong

<sup>4</sup>Key Laboratory for Biomechanics and Mechanobiology of Ministry of Education,

School of Biological Science and Medical Engineering, Beihang University, Beijing 100191, China

<sup>5</sup>Sansom Institute for Health Research and School of Pharmacy and Medical Sciences, University of South Australia, Adelaide, SA 5001, Australia

<sup>6</sup>College of Allied Health Professions, University of Nebraska Medical Center, Omaha, NE 68198, USA

Correspondence should be addressed to Wenxin Niu; [niu@tongji.edu.cn](mailto:niu@tongji.edu.cn)

Received 10 August 2017; Accepted 10 August 2017; Published 30 October 2017

Copyright © 2017 Wenxin Niu et al. This is an open access article distributed under the Creative Commons Attribution License, which permits unrestricted use, distribution, and reproduction in any medium, provided the original work is properly cited.

Musculoskeletal problems, such as traumatic injury, osteoporosis, and osteoarthritis, are one of the leading causes of disability worldwide and are therefore a crucial branch of public health. Biomechanics has been proven to play a critical role in musculoskeletal pathology, treatment, and rehabilitation. Biomechanical factors could influence cell's metabolic activity, bone remodeling, and sequelae development. Advancement in biomechanical theory, methodology, and technique could also promote the improvement on the design of protective, surgical, and rehabilitation equipment. Advancement in computational technique even promoted the development of computational biomechanics.

The focus of this special issue is on innovative theory and application of biomechanics to understand musculoskeletal pathology and to improve the techniques for the treatment and rehabilitation. This special issue can serve as a platform for biomechanical researchers, rehabilitation therapists, protective device designers, and orthopedic surgeons.

Finite element (FE) analysis is a powerful tool for biomechanical investigations, especially in orthopedic surgery. Two independent research groups from the School of Medicine, Tongji University, respectively, constructed two separate three-dimensional FE models of lumbar spine (L3-L5). Z. Zeng et al. studied the biomechanical effect of different grades of facetectomy, while M. Yang et al. evaluated the stability of extraforaminal lumbar interbody fusion and

traditional transforaminal lumbar interbody fusion under various internal fixations.

Researchers from Tianjin University of Technology also conducted a study in FE modeling. They developed and validated a refined FE model of middle femoral comminuted fracture to compare the biomechanical stability after two kinds of plate fixations. H.-Y. Liu et al. established a solid-liquid coupling biphasic model of articular cartilage and a microscopic model of chondrocytes to analyze the biomechanical response under cyclic compressive loading. Additionally, they performed a comprehensive analysis about the impact of pectus excavatum on scoliosis and elaborated its biomechanical mechanism in pectus excavatum patients with scoliosis. Y. He et al. studied the biomechanical performance of the laparoscopic-assisted plate.

Mechanism and protection of sports injury are another focus of this special issue. A researcher from Shanghai University of Sports contributed two articles. R. Xia et al. determined the effects of fatigue on the impact forces and sagittal plane kinematics of the lower extremities of recreational athletes in a drop-landing task. They also studied joint torque and mechanical power of lower extremities and its relevance to hamstring strain during sprint running. A group of researchers from Shenyang Sport University determined the contact force loading associated with different walking speeds.

Biomechanics is also very popular in rehabilitation in recent years. X. Wu et al. studied early spatiotemporal patterns and knee kinematics during level walking in individuals following total knee arthroplasty (TKA). An article contributed by authors from Taiyuan University of Technology, University of Sussex, and University of Southampton studied the effects of overweight and obesity on TKA. Y.-P. Huang et al. investigated the effect of arch support insoles on uphill and downhill walking of persons with flatfoot. S. Kuai et al. examined the compensatory response of the muscle activities of seventeen major muscle groups in the spinal region, intradiscal forces of the five lumbar motion segment units.

This special issue also included cell biomechanics and other topics. To achieve the accurate strain control of the membrane during stretching, a strain feedback compensation method based on the digital image correlation is proposed by authors from Sichuan University. Y. Chen et al. investigated the effect of endogenous *n*-3 PUFAs on fracture healing by measuring femur fracture repair in both *fat-1* transgenic mice and WT mice. Y.-X. Zhang et al. investigated the effects of different extracts of propolis and component of flavonoids on platelet aggregation.

Overall, this special issue covers a wide range of biomechanics in musculoskeletal health. More research is needed to investigate further in computational modeling in bones, sport injury prevention, rehabilitation, and cellular level to advance the field of biomechanics.

*Wenxin Niu*  
*Ming Zhang*  
*Jie Yao*  
*Liping Wang*  
*Ka-Chun Siu*

## Research Article

# Inhibitory Effect of Propolis on Platelet Aggregation In Vitro

**Yun-Xiang Zhang,<sup>1</sup> Ting-Ting Yang,<sup>2</sup> Liu Xia,<sup>3</sup> Wei-Fen Zhang,<sup>2</sup> Jia-Fu Wang,<sup>4</sup> and Ya-Ping Wu<sup>5</sup>**

<sup>1</sup>Department of Pathology, Weifang People's Hospital, Weifang, Shandong Province 261041, China

<sup>2</sup>School of Pharmacy, Weifang Medical University, Weifang, Shandong Province 261053, China

<sup>3</sup>Department of Ophthalmology, Weifang Medical University, Weifang, Shandong Province 261053, China

<sup>4</sup>Department of Pathology and Pathophysiology, Taishan Medical University, Taian, Shandong Province 271016, China

<sup>5</sup>Departments of Haematology of University Medical Center, Utrecht University, 3508GA Utrecht, Netherlands

Correspondence should be addressed to Yun-Xiang Zhang; [zhangbing199592@163.com](mailto:zhangbing199592@163.com)

Received 23 February 2017; Accepted 2 May 2017; Published 10 October 2017

Academic Editor: Wenxin Niu

Copyright © 2017 Yun-Xiang Zhang et al. This is an open access article distributed under the Creative Commons Attribution License, which permits unrestricted use, distribution, and reproduction in any medium, provided the original work is properly cited.

Platelet hyperactivity plays an important role in arterial thrombosis and atherosclerosis. The present study was aimed to investigate the effects of different extracts of propolis and components of flavonoids on platelet aggregation. Platelet-rich plasma was prepared and incubated in vitro with different concentrations of the tested extracts and components of flavonoids. Platelets aggregation was induced by different agonists including adenosine diphosphate (ADP, 10  $\mu$ M), thrombin receptor activator peptide (TRAP, 50  $\mu$ M), and collagen (5  $\mu$ g/mL). At 25 mg/L to 300 mg/mL, the water extract propolis (WEP) inhibited three agonists-induced platelet aggregations in a dose-dependent manner. The flavonoids isolated from the propolis also showed markedly inhibited platelet aggregation induced by collagen, ADP, and TRAP, respectively. The components including caffeic acid phenethyl ester (CAPE), galangin, apigenin, quercetin, kaempferol, ferulic acid, rutin, chrysin, pinostrobin, and pinocembrin and their abilities of inhibiting platelet aggregation were studied. It was concluded that propolis had an antiplatelet action in which flavonoids were mainly implicated.

## 1. Introduction

Nowadays, cardiovascular diseases (CVD) are the leading cause of morbidity and mortality worldwide [1–3] and bring a huge burden to the world economic development and people's living standard. It has been widely known that platelets play important roles in both hemostasis and pathogenesis of CVD such as acute coronary syndrome [4]. Platelet inhibition has shown improved short- and long-term clinical outcomes for CVD patients. However, increased bleeding risk and the high rates of recurrent ischemic events could not be ignored [5]. Furthermore, the activation of platelets was also related to circulation and vascular damage in patients with hypertension and diabetes [6]. Antiplatelet drugs used clinically to treat and prevent coronary syndromes and stroke are accompanied by a variety of side effects such as thrombocytopenia, hemorrhage, gastric

ulcers, and therapeutic resistance [7, 8]. More safe and effective antiplatelet drugs would be urgently needed based on the current situation.

In recent, natural products and alternative medicine are now getting significant attention. Propolis, a complex mixture containing various compounds, such as flavonoids, terpenes,  $\beta$ -steroids, aromatic aldehydes, and alcohols, is a plant-derived substance collected from plant materials by honeybees [9, 10]. Propolis is extensively used in food and beverages to improve health because of its unique pharmacological activities including antimicrobial, antioxidant, immunomodulatory, hepatoprotective, antitumor, and cardioprotective effects [11–21]. Recently, Liu and his colleagues put forward that chrysin in propolis performs antiplatelet activity via inhibiting platelet  $\alpha$ IIb $\beta$ 3-mediated signaling pathway [22]. In addition, evidence data showed that propolis coated Co-Cr could significantly reduce adhesion

of platelets [23]. Many studies demonstrated that the propolis components were varied in different geographic and climatic zones [24]. Thus, the aim of the present study was to examine the effects of propolis extracts on human platelet aggregation *in vitro* and to identify the nature of the compounds responsible for the antiplatelet activity.

## 2. Materials and Methods

**2.1. Materials.** Propolis sample was obtained from Taishan fir in the autumn. Adenosine diphosphate (ADP) was purchased from Arkray (Aggregpack, Japan). Collagen was purchased from NYCOMED (Kollagenreagens Horm, Austria). Thrombin receptor activator peptide (TRAP) was purchased from Bachem (Germany). Caffeic acid phenethyl ester (CAPE), galangin, acacetin, and pinostrobin were purchased from Sigma Chemical Co. (USA).

**2.2. Preparation of Water Extract of Propolis (WEP) and Flavonoid.** According to previous research [25], a certain amount of dried propolis sample frozen at  $-20^{\circ}\text{C}$  was dissolved in 30 mL of distilled water at  $60^{\circ}\text{C}$  for 7 h. The crude extract was filtered, then centrifuged at 28000 rpm for 30 min, and the supernatants were concentrated under reduced pressure to produce the WEP. Flavonoid was obtained from another 10.0 g dried propolis dissolved in 300 mL 70% ethanol 7 h at room temperature using the same method [26].

**2.3. Component Analysis of WEP and Flavonoid.** For the components of WEP and flavonoid, a ZQ-4000 HPLC apparatus (Waters, USA) was used. The chromatographic separation was achieved using a Waters Symmetry C18 column (4.6 mm I.D.  $\times$  150 mm, 3.5  $\mu\text{m}$ ), with the column oven temperature maintained at  $25^{\circ}\text{C}$ . The mobile phase consisted of acetonitrile and 2% acetic acid. The mobile phase flow rate was 0.2 mL/min, and UV absorbance was monitored at 280 nm. Diluted standard solutions of galangin, CAPE, apigenin, quercetin, kaempferol, ferulic acid, rutin, chrysin, pinostrobin, and pinocembrin were analyzed in the same HPLC conditions, and furthermore, the calibration of the detector response was done. Quantification of the main bioactive compounds from WEP and flavonoid was based on the calibration curves. The results were confirmed by the Department of Agriculture Bee Products Quality Supervision and Inspection Center (Beijing).

**2.4. The Platelet Aggregation Tests.** Human platelet suspensions were prepared as previously described [27]. In this study, human volunteers had been given informed consent. In brief, blood was collected from healthy human volunteers who had taken no medicine during the preceding 2 weeks and was mixed with 3.4% Na-citrate (9: 1, vol/vol). The blood was centrifuged at 1100 rpm for 15 min at  $20^{\circ}\text{C}$ . Then, platelet-rich plasma (PRP) was collected with pipette and stored at room temperature. The tubes containing PRP were centrifuged at 3000 rpm for 10 min at  $20^{\circ}\text{C}$  to obtain the platelet-pool plasma (PPP). After a platelet count (Sysmex SE-9000, Kobe, Japan), a standard concentration of  $200 \times 10^9/\text{L}$  was obtained by diluting PRP with PPP.

TABLE 1: The components of WEP and flavonoids.

Compounds of propolis	Concentration in WEP (mg/L)	Concentration in flavonoids (mg/g)
Galangin	4477.09	37.24
CAPE	6329.74	5.55
Apigenin	305.76	0.34
Quercetin	2681.01	0.17
Kaempferol	897.80	1.79
Ferulic acid	3593.05	0.06
Rutin	—	3.56
Chrysin	—	13.94
Pinostrobin	—	95.52
Pinocembrin	—	0.84

The turbidimetric method was applied to measure platelet aggregation stimulated by the various kinds of agonists using an aggregometer [28]. Previous study mentioned different flavonoid components present in propolis (CAPE, galangin, acacetin, and pinostrobin) were able to inhibit platelet aggregation, so CAPE, galangin, acacetin, and pinostrobin were tested in our study [29]. All aggregation tests were performed within 2 h after isolation and carried out in triplicate. Each person had his/her own 0% PRP and 100% PPP aggregation calibration. Before aggregation was started, standard platelet concentration was incubated in solutions of different concentrations, including WEP (300 mg/L, 100 mg/L, 25 mg/L), flavonoids (400 mg/L, 100 mg/L, 25 mg/L), CAPE (352  $\mu\text{M}$ , 88  $\mu\text{M}$ , 6  $\mu\text{M}$ ), galangin (370  $\mu\text{M}$ , 185  $\mu\text{M}$ , 46  $\mu\text{M}$ ), acacetin (352  $\mu\text{M}$ , 176  $\mu\text{M}$ , 44  $\mu\text{M}$ ), and pinostrobin (370  $\mu\text{M}$ , 92  $\mu\text{M}$ , 23  $\mu\text{M}$ ) for 30 min at the room temperature, then prewarmed at  $37^{\circ}\text{C}$  for two minutes. The aggregation was induced by ADP, collagen, or TRAP, respectively. The extent of aggregation was expressed in light transmission units.

**2.5. Statistical Analysis.** The results were shown as mean  $\pm$  standard deviations, and each experiment was performed in triplicate. Statistical analysis was carried out using SPSS19.0, and differences were considered to be significant at a level of  $P < 0.05$ .

## 3. Results and Discussion

**3.1. Chemical Components of Propolis.** Flavonoids are the major constituents of propolis and contribute greatly to the pharmacological activities of propolis. Usually, the quality of propolis was based on flavonoids quality [30]. The contents of flavonoids depend on the harvest region because the characteristics of propolis are influenced by the local plant varieties and weather [31]. Report of component analysis of WEP and flavonoids was shown in Table 1. The contents of CAPE were the highest in the WEP, followed by galangin, ferulic acid, quercetin, kaempferol, and apigenin. Pinostrobin was the most abundant chemical compound in flavonoids, followed by galangin, chrysin, CAPE, rutin, kaempferol, pinocembrin, apigenin, quercetin, and ferulic acid.

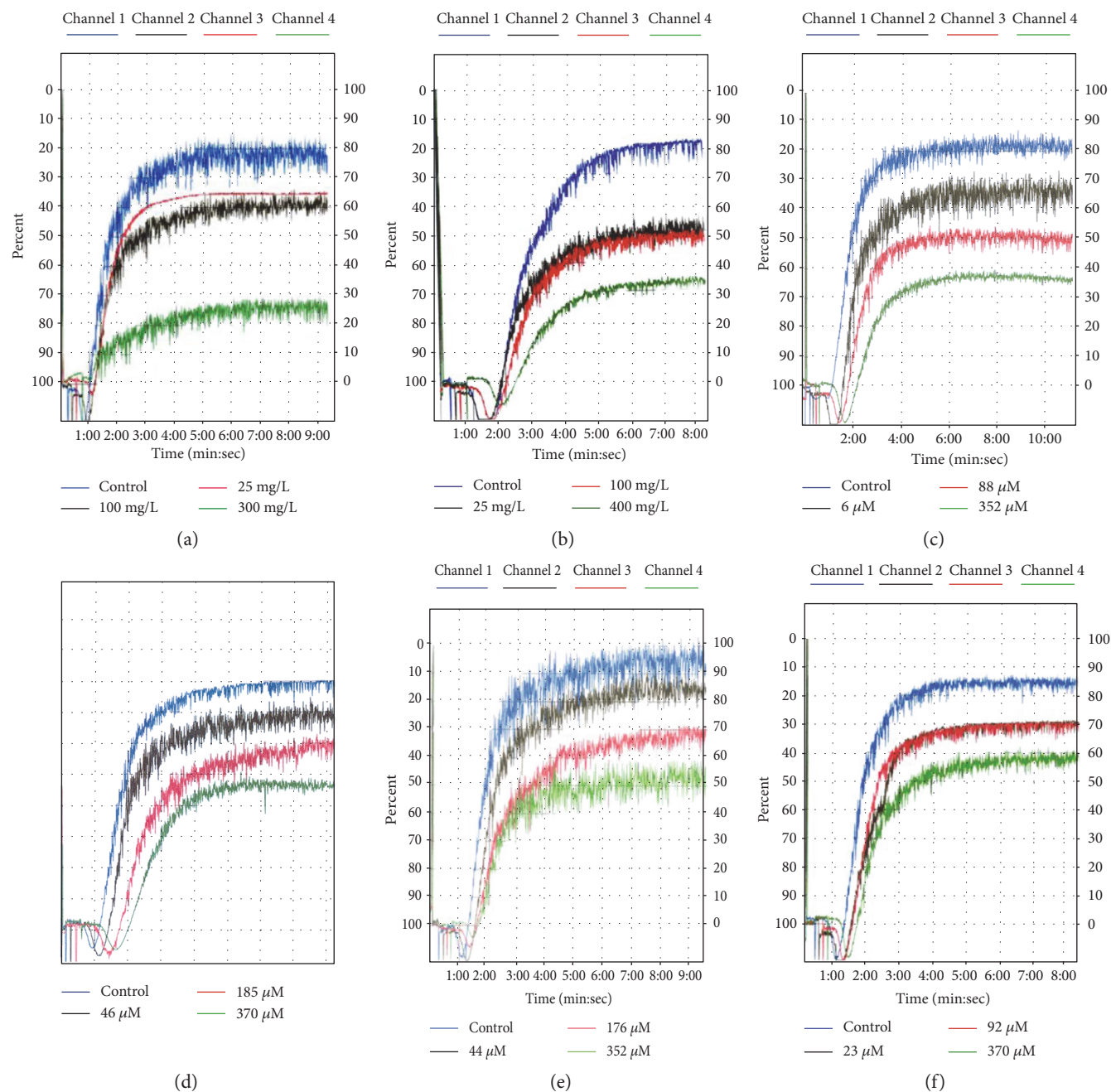


FIGURE 1: Original tracings showing the dose-dependent inhibitory effect of different extracts including WEP (a) and flavonoids (b) and pure components including CAPE (c), galangin (d), acacetin (e), and pinostrobin (f) on collagen-induced platelet aggregations in vitro.

3.2. *The Inhibition Effect of Different Components on Platelet Aggregation Induced by Different Agonists.* Results of the platelet aggregation tests were shown in Figures 1 and 2. The results showed that the crude WEP inhibited platelet aggregation in a dose-dependent manner, which might be stimulated with different agonists including ADP, collagen, and TRAP. For instance, 300 mg/L WEP significantly decreased platelet aggregation induced by ADP, collagen, and TRAP to  $35.00 \pm 5.34\%$ ,  $35.00 \pm 6.61\%$ , and  $42.33 \pm 13.24\%$  ( $n = 3$ ;  $P < 0.01$ ), respectively, indicating that propolis contains compounds having antiplatelet aggregation

activity. This effect might be attributed to polar compounds such as flavonoids and polyphenols.

Flavonoids inhibited the three agonist-induced platelet aggregations in a dose-dependent manner, and the percent of inhibition were  $53.11 \pm 1.90\%$ ,  $51.12 \pm 9.30\%$ , and  $51.98 \pm 22.20\%$  at concentrations of 400 mg/L, respectively. This finding was consistent with previous studies showing the antiplatelet aggregation activity of flavonoids in vitro [32] and in vivo [33]. We also test four purified components, including CAPE, galangin, acacetin, and pinocembrin. All test dose CAPE added to the PRP platelet aggregation

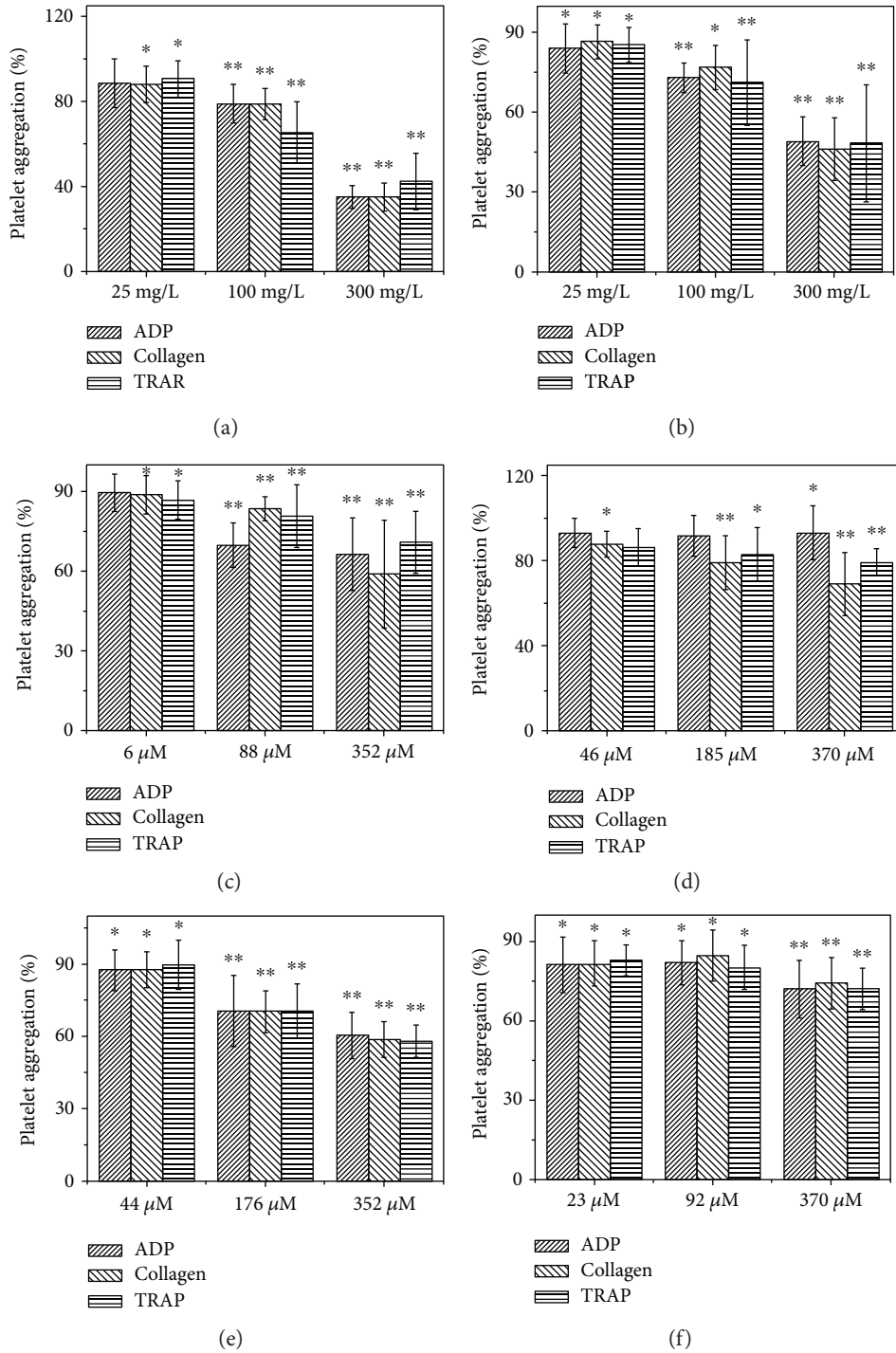


FIGURE 2: Inhibitory effect of different extracts including WEP (a) and flavonoids (b) and pure components including CAPE (c), galangin (d), acacetin (e), and pinostrobin (f) on platelet aggregation induced by different agonists including ADP, collagen, and TRAP, respectively. \*Compared with the control ( $P < 0.05$ ) was observed. \*\*Compared with the control ( $P < 0.01$ ) was observed. Data are represented as the mean  $\pm$  SD ( $n = 3$ ).

induced by collagen and TRAP significantly decreased ( $P < 0.05$ ), and the most antiplatelet aggregation effect occurred in the collagen-included platelet aggregation test group with an inhibition of  $58.82 \pm 4.51\%$  at  $176 \mu\text{M}$ . Significant inhibition was not detected in the ADP-included platelet aggregation test group when adding  $6 \mu\text{M}$  CAPE.

When  $46 \mu\text{M}$  or more galangin was added to PRP, significant inhibition was detected in the collagen-included platelet aggregation test group in a dose-dependent manner. Galangin was not able to inhibit ADP-induced platelet aggregation until  $370 \mu\text{M}$  galangin had been added. Acacetin could significantly inhibit platelet aggregation induced by

ADP, collagen, and TRAP at concentrations of 44, 176, and 352  $\mu\text{M}$  in the concentration-dependent manner ( $P < 0.05$ ). The antiplatelet aggregation activity of pinostrobin isolated from propolis (23  $\mu\text{M}$ , 92  $\mu\text{M}$ , and 370  $\mu\text{M}$ ) was evaluated upon ADP-, collagen-, and TRAP-induced aggregation. As shown in Figures 1(f) and 2(f), the platelet aggregation could be suppressed by pinostrobin at concentrations of 23–370  $\mu\text{M}$  ( $P < 0.005$ ). CAPE appeared to be more effective inhibitors than galangin and acacetin. This difference in potency could be explained by their chemical structures [34].

The isolated flavonoids markedly inhibited platelet aggregation induced by ADP, TRAP, and collagen. The inhibition might be introduced by holding back fibrinogen binding to its platelet membrane receptor (glycoprotein (GP) IIb-IIIa), which is a final and common pathway of platelet aggregation. It was reported that the flavonoid phloretin diminished ADP and TRAP-stimulated expression of the activated form of the GPIIb/IIIa complex and reduced platelet aggregation stimulated by ADP [30]. Several other studies had shown that flavonoids inhibited platelet function through a multitude of mechanisms including decreasing phospholipase C activity [31], scavenging of reactive oxygen species such as superoxide anion, and inhibiting cyclic nucleotide phosphodiesterase and thromboxane A2 synthesis [32].

#### 4. Conclusion

The main components of propolis were galangin, CAPE, apigenin, quercetin, kaempferol, ferulic acid, rutin, chrysin, pinostrobin, and pinocembrin. The WEP and flavonoids extracted from propolis exhibited dose-dependent inhibitory effects on platelet aggregation induced by different agonists including ADP, collagen, and TRAP, respectively. CAPE, galangin, and pinostrobin might be mainly implicated. Further studies are necessary to clarify the mechanism of platelet inhibition.

#### Conflicts of Interest

The authors indicated no potential competing interests.

#### Acknowledgments

The authors are grateful for the generous financial support from the National Natural Science Foundation of China (no. 81573717), the National Key Technology R&D Program of the Ministry of Science and Technology (no. 2013GA740103), the Scientific and Technological Development Project of Shandong Province (2015GSF118168) and the Department of Science and Technology of Weifang City (20100220).

#### References

- [1] D. Massai, G. Cerino, D. Gallo et al., “Bioreactors as engineering support to treat cardiac muscle and vascular disease,” *Journal of Healthcare Engineering*, vol. 4, no. 3, p. 329, 2013.
- [2] X. Zhuang, “Challenges and methodologies of fully automatic whole heart segmentation: a review,” *Journal of Healthcare Engineering*, vol. 4, no. 3, p. 371, 2013.
- [3] E. Zahedi, V. Sohani, M. A. Ali, K. Chellappan, and G. K. Beng, “Experimental feasibility study of estimation of the normalized central blood pressure waveform from radial photoplethysmogram,” *Journal of Healthcare Engineering*, vol. 6, no. 1, pp. 121–144, 2015.
- [4] A. Papapanagiotou, G. Daskalakis, G. Siasos, A. Gargalionis, and A. G. Papavassiliou, “The role of platelets in cardiovascular disease: molecular mechanisms,” *Current Pharmaceutical Design*, vol. 22, pp. 4493–4505, 2016.
- [5] M. Ueno, M. Kodali, A. Tello-Montoliu, and D. J. Angiolillo, “Role of platelets and antiplatelet therapy in cardiovascular disease,” *Journal of Atherosclerosis and Thrombosis*, vol. 18, pp. 431–442, 2011.
- [6] R. Hernandez Hernandez, A. R. Carvajal, J. Guerrero Pajuelo et al., “The effect of doxazosin on platelet aggregation in normotensive subjects and patients with hypertension: an in vitro study,” *American Heart Journal*, vol. 121, pp. 389–394, 1991.
- [7] V. Fuster, L. Badimon, J. J. Badimon, and J. H. Chesebro, “The pathogenesis of coronary artery disease and the acute coronary syndromes (1),” *The New England Journal of Medicine*, vol. 326, pp. 242–250, 1992.
- [8] N. E. Barrett, L. Holbrook, S. Jones et al., “Future innovations in anti-platelet therapies,” *British Journal of Pharmacology*, vol. 154, pp. 918–939, 2008.
- [9] E. Szliszka, A. Sokół-Łętowska, A. Z. Kucharska, D. Jaworska, Z. P. Czuba, and W. Król, “Ethanolic extract of Polish propolis: chemical composition and TRAIL-R2 death receptor targeting apoptotic activity against prostate cancer cells,” *Evidence-Based Complementary and Alternative Medicine*, vol. 2013, Article ID 757628, 12 pages, 2013.
- [10] C. C. Gonçalves, L. Hernandez, C. A. Bersani-Amado, S. L. Franco, J. F. Silva, and M. R. Natali, “Use of propolis hydroalcoholic extract to treat colitis experimentally induced in rats by 2, 4, 6-trinitrobenzenesulfonic acid,” *Evidence-Based Complementary and Alternative Medicine*, vol. 2013, Article ID 853976, 11 pages, 2013.
- [11] R. S. Veiga, S. Mendonça, P. B. Mendes et al., “Artepillin C and phenolic compounds responsible for antimicrobial and antioxidant activity of green propolis and *Baccharis dracunculifolia* DC,” *Journal of Applied Microbiology*, vol. 122, no. 4, pp. 911–920, 2017.
- [12] K. M. Kasiotis, P. Anastasiadou, A. Papadopoulos, and K. Machera, “Revisiting Greek propolis: chromatographic analysis and antioxidant activity study,” *PLoS One*, vol. 12, no. 1, article e0170077, 2017.
- [13] M. C. Búfalo, A. P. Bordon-Graciani, B. J. Conti, G. M. de Assis, and J. M. Sforcin, “The immunomodulatory effect of propolis on receptors expression, cytokine production and fungicidal activity of human monocytes,” *Journal of Pharmacy and Pharmacology*, vol. 66, no. 10, pp. 1497–1504, 2014.
- [14] R. V. Ambardekar, K. R. Mahadik, A. R. Paradkar, and A. M. Harsulkar, “Enhancement of hepatoprotective efficacy of propolis by fabrication of liposomes, as a platform nanoformulation for multi-component natural medicine,” *Current Drug Delivery*, vol. 9, no. 5, pp. 477–486, 2012.
- [15] J. Wu, C. Omene, J. Karkoszka et al., “Caffeic acid phenethyl ester (CAPE), derived from a honeybee product propolis, exhibits a diversity of anti-tumor effects in pre-clinical models of human breast cancer,” *Cancer Letters*, vol. 308, no. 1, pp. 43–53, 2011.

- [16] M. F. Tolba, S. S. Azab, A. E. Khalifa, S. Z. Abdel-Rahman, and A. B. Abdel-Naim, "Caffeic acid phenethyl ester, a promising component of propolis with a plethora of biological activities: a review on its anti-inflammatory, neuroprotective, hepatoprotective, and cardioprotective effects," *IUBMB Life*, vol. 65, no. 8, p. 699, 2013.
- [17] S. De Marco, M. Piccioni, R. Pagiotti, and D. Pietrella, "Antibiofilm and antioxidant activity of propolis and bud poplar resins versus *Pseudomonas aeruginosa*," *Evidence-Based Complementary and Alternative Medicine*, vol. 2017, Article ID 5163575, 11 pages, 2017.
- [18] T. Bonamigo, J. F. Campos, T. M. Alfredo et al., "Antioxidant, cytotoxic, and toxic activities of propolis from two native bees in Brazil: *Scaptotrigona depilis* and *Melipona quadrifasciata anthidioides*," *Oxidative Medicine and Cellular Longevity*, vol. 2017, Article ID 1038153, 12 pages, 2017.
- [19] A. P. Dos Santos Thomazelli, F. Tomiotto-Pellissier, S. S. da Silva et al., "Brazilian propolis promotes immunomodulation on human cells from American Tegumentar Leishmaniasis patients and healthy donors infected with *L. braziliensis*," *Cellular Immunology*, vol. 311, pp. 22–27, 2017.
- [20] I. R. Babatunde, A. Abdulbasit, M. I. Oladayo, O. I. Olasile, F. R. Olamide, and B. W. Gbolahan, "Hepatoprotective and pancreatoprotective properties of the ethanolic extract of Nigerian propolis," *Journal of Intercultural Ethnopharmacology*, vol. 4, no. 2, pp. 102–108, 2015.
- [21] K. Ren, W. Zhang, G. Wu et al., "Synergistic anti-cancer effects of galangin and berberine through apoptosis induction and proliferation inhibition in oesophageal carcinoma cells," *Biomedicine & Pharmacotherapy*, vol. 84, pp. 1748–1759, 2016.
- [22] G. Liu, W. Xie, A. D. He et al., "Antiplatelet activity of chrysin via inhibiting platelet  $\alpha\text{IIb}\beta\text{3}$ -mediated signaling pathway," *Molecular Nutrition & Food Research*, vol. 60, no. 9, pp. 1984–1993, 2016.
- [23] E. Lih, J. W. Jung, Y. K. Joung, D. J. Ahn, and D. K. Han, "Synergistic effect of anti-platelet and anti-inflammation of drug-coated Co-Cr substrates for prevention of initial in-stent restenosis," *Colloids and Surfaces B: Biointerfaces*, vol. 140, pp. 353–360, 2016.
- [24] A. Russo, R. Longo, and A. Vanella, "Antioxidant activity of propolis: role of caffeic acid phenethyl ester and galangin," *Fitoterapia*, vol. 73, Supplement 1, pp. S21–S29, 2002.
- [25] X. Guo, B. Chen, L. Luo, X. Zhang, X. Dai, and S. Gong, "Chemical compositions and antioxidant activities of water extracts of Chinese propolis," *Journal of Agricultural and Food Chemistry*, vol. 59, no. 23, pp. 12610–12616, 2011.
- [26] Y. X. Zhang, Z. X. Yang, W. An, and J. F. Wang, "Effects of different solvents on the extraction rate of propolis flavonoids (in Chinese)," *Lishizhen Medicine and Material Medical Research*, vol. 17, no. 1, pp. 9–10, 2006.
- [27] J. R. Sheu, C. R. Lee, C. C. Lin et al., "The antiplatelet activity of PMC, a potent  $\alpha$ -tocopherol analogue, is mediated through inhibition of cyclo-oxygenase," *British Journal of Pharmacology*, vol. 127, no. 5, pp. 1206–1212, 1999.
- [28] M. Roest, J. J. Sixma, Y. P. Wu et al., "Platelet adhesion to collagen in healthy volunteers is influenced by variation of both alpha (2) beta (1) density and von Willebrand factor," *Blood*, vol. 96, no. 4, pp. 1433–1437, 2000.
- [29] Y. P. Wu, A. Huisman, C. Weeterings et al., "Caffeic acid phenyl ester, a component of the Chinese herb propolis, inhibits platelet aggregation via competition with fibrinogen for binding to  $\alpha\text{IIb}\beta\text{3}$ ," *Blood*, vol. 112, pp. 53–67, 2008.
- [30] Z. Cui-ping, H. Shuai, W. Wen-ting et al., "Development of high-performance liquid chromatographic for quality and authenticity control of Chinese propolis," *Journal of Food Science*, vol. 79, pp. C1315–C1322, 2014.
- [31] C. B. S. M. Beatriz, C. C. P. José, and D. H. Miriam, "Concentration of flavonoids and phenolic compounds in aqueous and ethanolic propolis extracts through nanofiltration," *Journal of Food Engineering*, vol. 96, no. 4, pp. 533–539, 2010.
- [32] S. H. Tzeng, W. Ko, C. Ko FN, and C. M. Teng, "Inhibition of platelet aggregation by some flavonoids," *Thrombosis Research*, vol. 64, no. 1, pp. 91–100, 1991.
- [33] J. G. Keevil, H. E. Osman, J. D. Reed, and J. D. Folts, "Grape juice, but not orange juice or grapefruit juice, inhibits human platelet aggregation," *Journal of Nutrition*, vol. 130, no. 1, pp. 53–56, 2000.
- [34] E. Middleton Jr and G. Drzewiecki, "Flavonoid inhibition of human basophil histamine release stimulated by various agents," *Biochemical Pharmacology*, vol. 33, no. 21, p. 3333, 1984.

## Research Article

# The Biomechanical Study of Extraforaminal Lumbar Interbody Fusion: A Three-Dimensional Finite-Element Analysis

Mingjie Yang,<sup>1</sup> Guixin Sun,<sup>2</sup> Song Guo,<sup>1</sup> Cheng Zeng,<sup>1</sup> Meijun Yan,<sup>1</sup> Yingchao Han,<sup>1</sup>  
Dongdong Xia,<sup>1</sup> Jingjie Zhang,<sup>1</sup> Xinhua Li,<sup>1</sup> Yang Xiang,<sup>1</sup> Jie Pan,<sup>1</sup> Lijun Li,<sup>1</sup> and Jun Tan<sup>1</sup>

<sup>1</sup>Department of Spine, Shanghai East Hospital, Tongji University School of Medicine, No. 150 Jimo Road, Shanghai 200120, China

<sup>2</sup>Department of Traumatology, Shanghai East Hospital, Tongji University School of Medicine, No. 150 Jimo Road, Shanghai 200120, China

Correspondence should be addressed to Lijun Li; [liliju@163.com](mailto:liliju@163.com) and Jun Tan; [tanjuntj2012@163.com](mailto:tanjuntj2012@163.com)

Received 19 February 2017; Revised 12 June 2017; Accepted 25 July 2017; Published 26 September 2017

Academic Editor: Jie Yao

Copyright © 2017 Mingjie Yang et al. This is an open access article distributed under the Creative Commons Attribution License, which permits unrestricted use, distribution, and reproduction in any medium, provided the original work is properly cited.

**Objective.** Finite-element method was used to evaluate biomechanics stability of extraforaminal lumbar interbody fusion (ELIF) under different internal fixation. **Methods.** The L3–L5 level finite-element model was established to simulate decompression and internal fixation at L4–L5 segment. The intact finite model was treated in accordance with the different internal fixation. The treatment groups were exerted 400 N load and 6 N·m additional force from motion to calculate the angular displacement of L4–L5. **Results.** The ROMs were smaller in all internal fixation groups than those in the intact model. Furthermore, the ROMs were smaller in ELIF + UPS group than in TLIF + UPS group under all operating conditions, especially left lateral flexion and right rotation. The ROMs were higher in ELIF + UPS group than in TLIF + BPS group. The ROMs of ELIF + UPS + TLFS group were much smaller than those in ELIF + UPS group, and as compared with TLIF + BPS group, there was no significant difference in the range of experimental loading. **Discussion.** The biomechanical stability of ELIF with unilateral pedicle screw fixation is superior to that of TLIF with unilateral pedicle screw fixation but lower than that of TLIF with bilateral pedicle screws fixation. The stability of ELIF with unilateral fixation can be further improved by supplementing a translaminar facet screw.

## 1. Introduction

Lumbar degenerative disease has been the main cause of lower back pain and leg pain in adults [1–3]. There are a large number of treatment options available including both conservative and operative approaches. A systematic review by Phillips et al. [4] indicates that lumbar spinal fusion can be an effective treatment strategy for patients who are refractory to conservative treatment. The clinical consensus of lumbar interbody fusion is that as far as possible, the posterior tensile structures should be retained and unnecessary trauma should be reduced to ensure postoperative short-term stability and long-term fusion rate [5, 6]. Therefore, transforaminal lumbar interbody fusion (TLIF) with bilateral pedicle screw (BPS) fixation has been considered as the classical surgical approach in the recent years. However, TLIF still needs to

resect the inferior facet joint firstly to provide access for the resection of the superior facet joint to decompress the nerve root. We wonder if it is feasible to release the compressed nerve root by the direct resection of the superior facet joint with retaining the inferior facet joint. Hence, we deeply study the anatomical structure of the intervertebral foramen. Intervertebral foramen is a circular area formed by the semicircular notches between the two pedicles of vertically adjacent vertebral bodies. The anterior wall of the foramen is the intervertebral disc, the superior and inferior walls are the superior and inferior pedicle notches, respectively, and the posterior wall is the facet joint and joint capsule formed by the superior and inferior facet joints of adjacent vertebral bodies. The upper edge and ventral side of the superior facet joint are in close contact with the nerve root, which is an important anatomic factor leading to nerve root compression. Additionally,

this superior facet joint also participates in the construction of the lateral spinal canal, and thus it is also the main reason for lateral spinal stenosis [7, 8]. In the clinic, it has also been suggested that the lateral spinal stenosis and nerve root compression was rarely caused by the osteophytes of the inferior facet joint. Therefore, the inferior facet joint is not regarded as the decompression target and gains a great possibility to release the compressed nerve root without the resection of inferior facet joints. Our preliminary paper has proved the feasibility of that surgery and developed a new lumbar fusion technique called ELIF [9–11].

In the extraforaminal lumbar interbody fusion (ELIF) technique, only the superior facet joint is resected and the inferior facet joint and soft tissues attached behind it are retained. Compared with conventional transforaminal lumbar interbody fusion (TLIF), ELIF technique retains the posterior structures more completely and could potentially improve the immediate stability. Therefore, we analyzed the lumbar biomechanical stability of ELIF surgery by using 12 cadaveric spine specimens [12]. To make this analysis of the biomechanical stability more accurate, the 3D finite-element method was employed. In this study, L3–L5 ELIF and TLIF 3D finite-element models with different internal fixation and fusion methods were established. The model stability and stress of the pedicle screws, connecting rods and interbody fusion cages were tested under different operating conditions, namely, anterior flexion, posterior extension, left and right lateral flexion, and left and right rotation.

## 2. Data and Methods

*2.1. Ethics Statement.* This study has been reviewed and approved by the ethics committee of Shanghai East Hospital, Tongji University School of Medicine.

*2.2. Establishment of 3D Finite-Element Model.* In September 15, 2015, a 26-year-old man (height, 172 cm; weight, 67 kg; body mass index, 22.6 kg/m<sup>2</sup>) diagnosed with L4-L5 lumbar disc herniation was recruited for a preoperative lumbar computed tomography scan from T12 level to pelvic inlet using a dual source scanner (SOMATOM Definition Flash; Siemens Medical Solutions Inc., Forchheim, Germany). This participant provided the written informed consent to participate in this study. The scanning parameters were as follows: tube current = 250 mA, tube voltage = 120 kV, scanning slice thickness = 1.0 mm, and reconstruction slice thickness = 1.0 mm. The data in the commonly used DICOM 3.0 format were read using the medical finite-element modeling software Simpleware 2.0 (Simpleware Ltd., Exeter, UK), and an L3–L5 3D geometric model was established. We utilized the finite-element preprocessing software HyperMesh (Altair Engineering, Troy, USA) and select the appropriate element types and materials for mesh generation. The mesh model includes 124,528 elements and the mesh size is 2 mm. The materials for the various parts of the input model and their characteristics including elastic modulus and Poisson ratio are listed in Table 1 [13–17]. An intact L3–L5 segment finite-element model was shown in Figure 1.

TABLE 1: Material property of spinal components and implants.

Component	Young's modulus (MPa)	Poisson's ratio	Cross section (mm <sup>2</sup> )
Cortical bone	12000.0	0.30	
Endplate	1200.0	0.29	
Cancellous bone	100.0	0.30	
Annulus ground substance	4.2	0.45	
Nucleus pulposus	1.0	0.49	
Annulus fiber	450.0	0.45	
Anterior longitudinal ligaments	20.0	0.30	63.7
Posterior longitudinal ligaments	20.0	0.30	20.0
Intertransverse ligament	58.7	0.30	3.6
Ligamentum flavum	19.5	0.30	40.0
Interspinous ligament	11.6	0.30	40.0
Supraspinous ligament	15.0	0.30	30.0
Capsular ligament	32.9	0.30	60.0
Pedicle screws and rod	110000.0	0.28	20.0
PEEK cage	3600.0	0.25	

*2.3. Establishment of Models with Different Fusion and Internal Fixation Methods.* Images of the pedicle screw system and intervertebral fusion cage (DePuy Spine, Johnson & Johnson, New Jersey, USA) in the IGES format were imported into HyperMesh, and the finite-element model was constructed for ELIF and TLIF based on the requirements listed below. The elastic modulus for screws in ELIF and TLIF groups was 110,000 MPa and the Poisson ratio was 0.3. The intervertebral fusion cage was a bullet-type cage with dimensions of 9 mm × 11 mm × 27 mm, and the elastic modulus and Poisson ratio were 3700 MPa and 0.25, respectively. The screw diameter was 6.0 mm, and length was 45 mm. The implanting angle of fusion cage was 80° at the spine sagittal plane in the ELIF group and 45° in the TLIF group. In both groups, the fusion cage was placed into the intervertebral space obliquely from the right side. The experimental groups were divided into as follows: ELIF with unilateral pedicle screw (ELIF+UPS), TLIF with unilateral pedicle screw (TLIF+UPS), TLIF with bilateral pedicle screws (TLIF+BPS), and ELIF with unilateral pedicle screw + translaminar facet screw (ELIF+UPS+TLFS). The designs of the experimental models were exactly based on the clinical surgical approaches. In the ELIF+UPS group, the superior facet joint of the L5 vertebra was removed along with the entire nucleus pulposus in the L4-L5 disc and the right posterior two-thirds of the fibrous ring. The posterior supraspinous ligament, interspinous ligament, spinous process, and the left side structures were retained. The pedicle screws were placed in the L4 and L5 pedicles on the right side (the entry point of each screw was the transition point of the superior facet joint and transverse process, and the screw was inserted at a 45° angle with the sagittal plane; Figure 2). In the TLIF+UPS group, the inferior facet joint of the L4 vertebra and the superior facet joint of the L5 vertebra were removed.

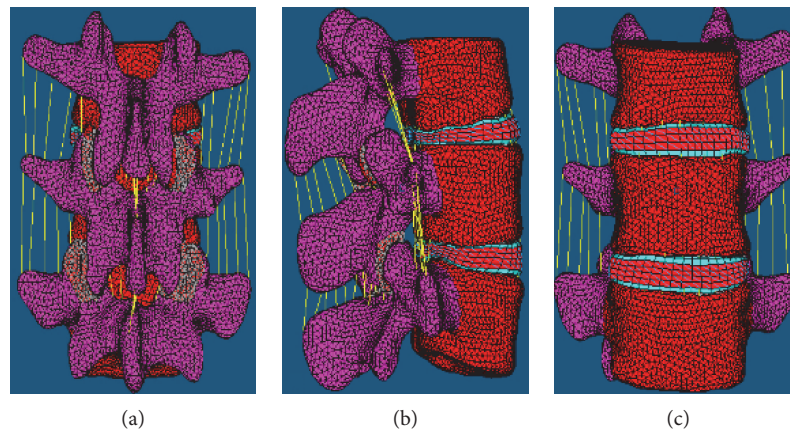


FIGURE 1: The intact model. (a) Posterior view. (b) Lateral view. (c) Anterior view.

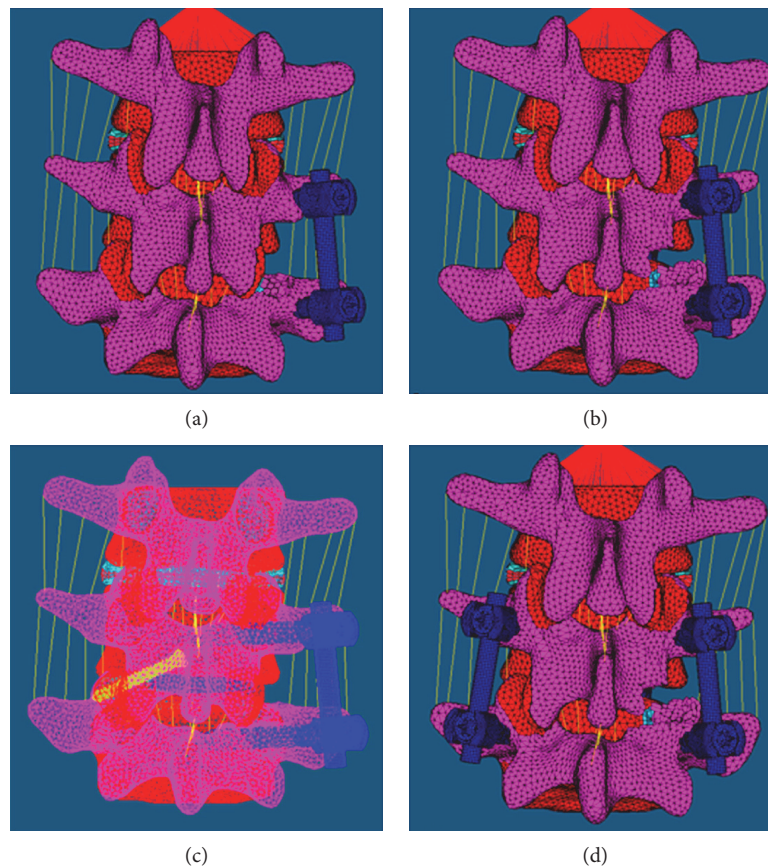


FIGURE 2: Finite-element model of ELIF and TLIF under different internal fixation modes. (a) ELIF + UPS. (b) TLIF + UPS. (c) ELIF + UPS + TLFS. (d) TLIF + BPS. ELIF: extraforaminal lumbar interbody fusion; TLIF: transforaminal lumbar interbody fusion; UPS: unilateral pedicle screw fixation; BPS: bilateral pedicle screw fixation; TLFS: translaminal facet screw.

The entire nucleus pulposus in the L4-L5 disc and the right posterior two-thirds of the fibrous ring were resected. The posterior supraspinous ligament, interspinous ligament, spinous process, and left structures were retained. The pedicle screws were placed in the right pedicles of the L4 and L5 vertebrae (the entry point of each screw was the traditional entry point, and the screws were inserted at a 15° angle with the sagittal plane; Figure 2). In the TLIF + BPS group, the

decompression range was the same as that in the TLIF + UPS group. The pedicle screws need to be further implanted at the left side pedicles compared to the TLIF + UPS group. The decompression range in the ELIF + UPS + TLFS group was the same as that in the ELIF + UPS group. Once pedicle screws were placed in the right L4 and L5 pedicles, a screw was implanted in the contralateral facet joint through the lamina (Figure 2).

**2.4. Loading and Recording Methods.** The inferior surface of the L5 vertebral body was totally fixed. Surface loading was applied on the superior surface of the L3 vertebral body, vertically in the downward direction and with uniform distribution on the entire superior endplate of the L3 vertebral body. The load applied on the model was 400 N and the additional force from motion was 6 N·m [18]. The data were input in Abaqus 6.10 (Dassault Systemes Simulia Corp., Providence, RI, USA), and calculations were performed under six operating conditions: lumbar spine anterior flexion, posterior extension, left and right lateral flexion, and left and right rotation. The main parameters observed were as follows: (1) L4-L5 range of motion (ROM), represented by the segmental angular displacement. The spatial coordinates of 4 points (the most forward point, most backward point, most leftward point, and most rightward point) on the superior surfaces of the L4 and L5 vertebrae were measured and connected with lines. The angles between the lines represented the angles between the superior surfaces of two neighboring vertebral bodies. The absolute value of the difference in these angles before and after loading was the angular displacement of the L4-L5 segments. (2) Stress diagrams were used to represent the stress on the pedicle screws, connecting rods and intervertebral fusion cages, under six operating conditions.

**2.5. Validation Process of Finite-Element Model.** This intact L3-L5 finite-element model was validated by comparing the intact finite-element model reported by the literature [17–19].

### 3. Results

**3.1. Verification of the Effectiveness of the Models.** The whole L3–L5 3D nonlinear finite-element model consists of the cortical bone shell, endplate, cancellous bone core, intervertebral disc (ground substance, collagen fibers, and nucleus pulposus), and 7 types of ligaments, yielding a total of 13 types of materials (Table 1). The model contained 124,528 units and 49,235 nodes. After defining the constraints and loading conditions for this model, the angular displacements of the L4-L5 segments in intact model were calculated under six operating conditions (lumbar spine anterior flexion, posterior extension, left and right lateral flexion, and left and right rotation). The results were basically consistent with those of the finite-element study by Chen et al. (Figure 3). Thus, we concluded that this 3D finite model was effective under certain conditions and could be applied for clinical and experimental studies [17–19].

**3.2. L4-L5 ROM.** The ROMs were smaller in all internal fixation groups than those in the intact group (Table 2, Figure 4). Furthermore, the ROMs were smaller in the ELIF + UPS group than those in the TLIF + UPS group under all operating conditions, especially left lateral flexion and right rotation. During left lateral flexion and right rotation, the ROMs of ELIF+UPS were reduced by 56.32% and 53.33%, respectively. The ROMs were smaller in the TLIF + BPS group than those in the ELIF+UPS group, and the percentages of decrease were as follows: anterior flexion

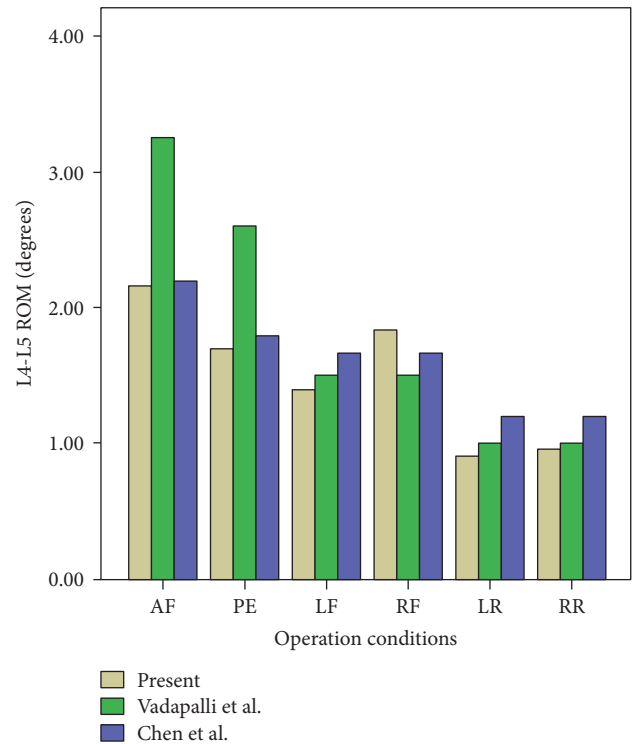


FIGURE 3: Comparison between the current intact model and previous studies for the validation. Comparison with Vadapalli et al. and Chen et al. AF: anterior flexion; PE: posterior extension; LF: lateral flexion; RF: right flexion; LR: left rotation; RR: right rotation.

11.27%, posterior extension 80.49%, left lateral flexion 42.11%, right lateral flexion 45.45%, left rotation 61.54%, and right rotation 50.00% (Table 2 and Figure 4). Similarly, in the ELIF + UPS + TLFS group, the ROMs were much smaller than those in the ELIF + UPS group. The percentages of decrease were as follows: anterior flexion 9.86%, posterior extension 75.61%, left lateral flexion 36.84%, right lateral flexion 9.09%, left rotation 34.62%, and right rotation 42.86% (Table 2, Figure 4). When compared to those in the TLIF + BPS group, the ROMs in the ELIF + UPS + TLFS group show no significant difference in the range of experimental loading.

**3.3. Stress Analysis of the Pedicles, Connecting Rods, and Intervertebral Fusion Cages in the ELIF and TLIF Finite-Element Models.** The maximum stress concentration point on the connecting rod was the junction between the screw and its head in the ELIF and TLIF models. The stress on the proximal end was greater than that on the distal end. The stresses on the connecting rod under all operating conditions were greater in the case of unilateral pedicle screw fixation than those in the case of bilateral pedicle screw fixation. Furthermore, the stresses on the connecting rods were smaller in the ELIF+UPS group than those in the TLIF+UPS group, especially under right lateral flexion (Figure 5). With additional contralateral translamina facet screw fixation, the stresses on the connecting rods were decreased as compared to only unilateral pedicle screw

TABLE 2: The L4-L5 range of motion (ROM) in different groups under six operating conditions.

ROM ( $n = 12$ )	AF (°)	PE (°)	LF (°)	RF (°)	LR (°)	RR (°)
Control	2.16	1.70	1.40	1.84	0.90	0.96
ELIF + UPS	0.71	0.41	0.38	0.11	0.26	0.28
TLIF + UPS	0.88	0.48	0.87	0.12	0.28	0.60
TLIF + BPS	0.63	0.08	0.22	0.06	0.10	0.14
ELIF + UPS + TLFS	0.64	0.10	0.24	0.10	0.17	0.16
Percentage decrease from control to ELIF + UPS	67.13%	75.88%	72.86%	94.02%	68.89%	70.83%
Percentage decrease from control to TLIF + UPS	59.26%	71.76%	37.86%	93.48%	52.45%	37.50%
Percentage decrease from TLIF + UPS to ELIF + UPS	19.32%	14.58%	56.32%	8.33%	7.14%	53.33%
Percentage decrease from ELIF + UPS to TLIF + BPS	11.27%	80.49%	42.11%	45.45%	61.54%	50.00%
Percentage decrease from ELIF + UPS to ELIF + UPS + TLFS	9.86%	75.61%	36.84%	9.09%	34.62%	42.86%
Percentage decrease from ELIF + UPS + TLFS to TLIF + BPS	1.56%	20.00%	8.33%	40.00%	41.18%	12.50%

ELIF: extraforaminal lumbar interbody fusion; UPS: unilateral pedicle screw; TLIF: transforaminal lumbar interbody fusion; BPS: bilateral pedicle screw; TLFS: translamina facet screw; AF: anterior flexion; PE: posterior extension; LF: lateral flexion; RF: right flexion; LR: left rotation; RR: right rotation.

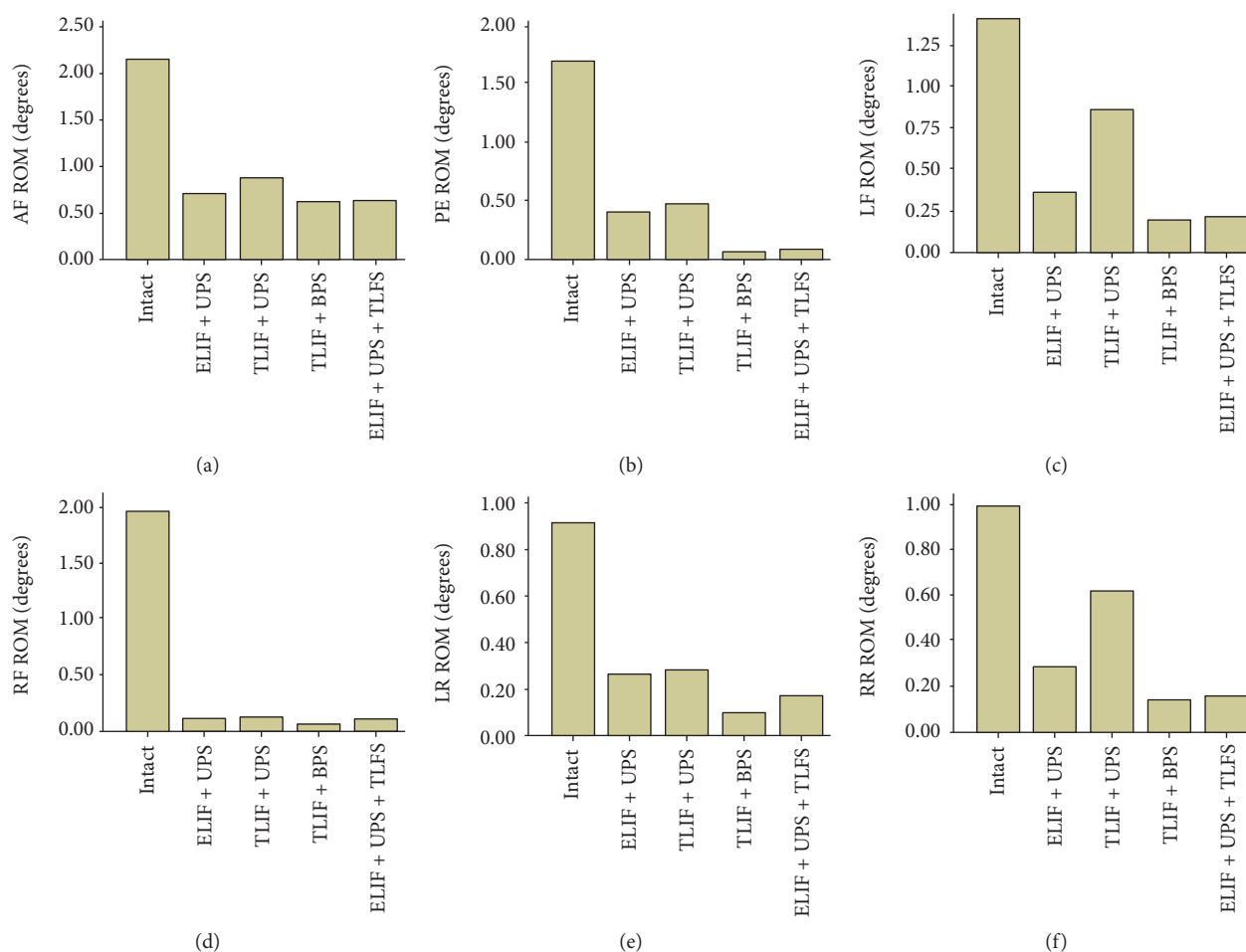


FIGURE 4: Range of motion at L4-L5 in intact and fixation models under six operation conditions. The ROM was smaller in all internal fixation groups than in the intact group. Furthermore, the ROM was smaller in the ELIF + UPS group than in the TLIF + UPS group, under all operating conditions, especially left lateral flexion and right rotation. The ROM was smaller in the TLIF + BPS group than in the ELIF + UPS group. Similarly, in the ELIF + UPS + TLFS group, the ROMs were much smaller than those in the ELIF + UPS group. When compared with the TLIF + BPS group, the ROM in the ELIF + UPS + TLFS group shows no obvious difference in the range of experimental loading. AF: anterior flexion; PE: posterior extension; LF: left lateral flexion; RF: right lateral flexion; LR: left rotation; RR: right rotation.

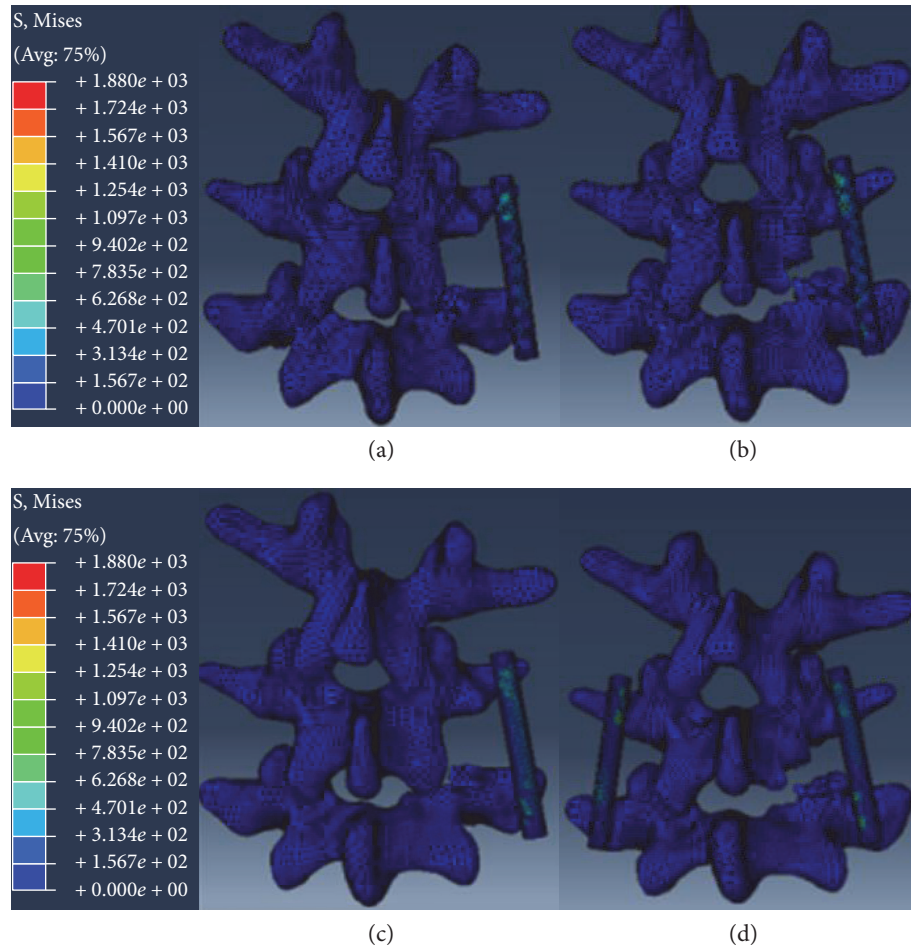


FIGURE 5: Stress analysis of the connecting rods in the ELIF and TLIF finite-element models under right lateral flexion. (a) ELIF + UPS. (b) TLIF + UPS. (c) ELIF + UPS + TLFS. (d) TLIF + BPS. The maximum stress concentration point on the connecting rod was the junction between the screw and its head in the ELIF and TLIF models. The stress on the proximal end was greater than that on the distal end. The stresses on the connecting rod under all operating conditions were greater in the case of unilateral pedicle screw fixation than in the case of bilateral pedicle screw fixation. Furthermore, the stress on the connecting rod was smaller in the ELIF + UPS group than in the TLIF + UPS group, especially under right lateral flexion. With additional contralateral translaminar facet screw fixation, the stress on the connecting rod was decreased as compared with simple unilateral pedicle screw fixation.

fixation. The stresses on the fusion cages did not significantly differ between the ELIF and TLIF groups under six operating conditions (Figure 5).

#### 4. Discussion

TLIF has gained increasing popularity in the treatment of degenerative lumbar disease due to its advantages including direct decompression on the nerve root and less risk of complications and good fusion result [20–22]. However, TLIF as the classical posterior lumbar interbody fusion technique can also lead to lumbar muscle injury and reduce the postoperation lumbar spine stability [23, 24]. To improve the postoperation lumbar spine stability, a large number of new fusion techniques such as ALIF, DLIF, and OLIF have been designed and applied [25–28]. Although the stability has been enhanced with these techniques, the outcome of decompression on nerve root cannot be ensured because direct decompression on nerve root cannot be accessed

through these surgical approaches. Therefore, we designed and tested the biomechanical stability of the new fusion technique (ELIF) based on the direct decompression and less trauma principles. In this study, the finite-element analysis of this fusion technique under different internal fixation conditions was performed to further evaluate the lumbar spine stability of this fusion surgery.

Finite-element models are widely applied in understanding of biomechanical function of the spine due to the effective stimulation, high repeatability, and less cost [29]. Before a new surgery technique is used in the clinic, the corresponding 3D model can be designed to test the reliability and safety of this new technique. The analyses indicated that lumbar stability was better in the case of ELIF with unilateral pedicle screw fixation than in the case of TLIF with unilateral pedicle screw fixation, under six operating conditions, especially, left lateral flexion and right rotation. The reason for the above finding is that ELIF with unilateral pedicle screw fixation can retain part of the superior facet joint to associate with

the inferior facet joint to limit left lateral flexion and right rotation of the lumbar spine. Additionally, the retention of posterior capsular ligaments in this joint can also be the beneficial factor to restrict lumbar movement. Last but not least, pedicle screws in ELIF with unilateral fixation group had greater extraversion, which was also beneficial to improve stability. Therefore, ELIF with unilateral fixation gained a better lumbar stability. However, the stability of the above ELIF was significantly weaker than that of TLIF with bilateral pedicle screw fixation. It means that although ELIF with unilateral pedicle screw fixation improved stability compared by TLIF with unilateral pedicle screw fixation, it still could not reach the stability achieved by TLIF with bilateral pedicle screw fixation. Moreover, the stability of ELIF with unilateral pedicle screw fixation could be improved by additional contralateral translaminar facet screw fixation. Thus, ELIF with unilateral pedicle screw fixation supplemented with translaminar facet screw fixation could meet the stability requirements for lumbar fusion surgeries [30, 31]. Stress analysis of the pedicle screws, connecting rods, and intervertebral fusion cages have also been compared between the ELIF and TLIF finite-element models. The stress on the connecting rod was smaller in the ELIF+UPS group than that in the TLIF+UPS group. It is because that part of L5 superior facet joint in the ELIF+UPS group was retained so that it can be associated with L4 inferior facet joint. Further, this joint can partly share the stress on the connecting rod. Additionally, the retention of posterior capsular ligaments in this joint can also provide the beneficial factor to share the stress on the connecting rod. Therefore, the possibility of rod breakage would theoretically be lower in the ELIF+UPS group than in TLIF+UPS group. As the stress on fusion cages is concerned, there was no significant difference between ELIF groups and TLIF groups. It is because the function of fusion cage was to support the anterior pillar, and thus the retention of the posterior pillar structures had little impact on the stress exerted on the fusion cage. Additionally, ELIF can achieve the direct decompression on nerve root and decrease internal fixation cost which consists of the majority of the whole cost in china. Therefore, this new ELIF surgery can potentially be a stable fusion technique which use a more invasive and economic internal fixation than classical TLIF with bilateral pedicle screw fixation.

Although this study has achieved primary success, more work needs to be done. Firstly, material properties in these 3D models were simplified and idealized. Although these simplifications were reasonable, it influenced the exact ROM value. Thus, the results obtained in these analyses reflect the difference of ROMs among groups instead of the exact ROM value. Secondly, the soft tissue environment was different between these models and human lumbar spines because the whole spinal model including lumbar spine muscle failed to be established.

## Disclosure

Mingjie Yang, Guixin Sun, and Song Guo are co-first authors.

## Conflicts of Interest

There was not any personal and organizational conflict of financial interests in this study.

## Authors' Contributions

Mingjie Yang, Guixin Sun, and Song Guo contributed equally to this work.

## Acknowledgments

Mingjie Yang and Lijun Li were supported by projects of Shanghai Municipal Commission of Health and Family Planning (201440049, 2013025); Jun Tan and Lijun Li were supported by Programs for Academic Leaders in Shanghai Pudong New Area (PWRd-2011-02, PWRL2012-03).

## References

- [1] C. Weiler, M. Lopez-Ramos, H. M. Mayer et al., "Histological analysis of surgical lumbar intervertebral disc tissue provides evidence for an association between disc degeneration and increased body mass index," *BMC Research Notes*, vol. 4, p. 497, 2011.
- [2] Y. S. Choi, "Pathophysiology of degenerative disc disease," *Asian Spine Journal*, vol. 3, pp. 39–44, 2009.
- [3] U. Quint and H. J. Wilke, "Grading of degenerative disk disease and functional impairment: imaging versus patho-anatomical findings," *European Spine Journal*, vol. 17, pp. 1705–1713, 2009.
- [4] F. M. Phillips, P. J. Slosar, J. A. Youssef, G. Andersson, and F. Papatheofanis, "Lumbar spine fusion for chronic low back pain due to degenerative disc disease: a systematic review," *Spine*, vol. 38, pp. E409–E422, 2013.
- [5] A. Sethi, A. M. Muzumdar, A. Ingalthalika, and R. Vaidya, "Biomechanical analysis of a novel posterior construct in a transforaminal lumbar interbody fusion model an in vitro study," *The Spine Journal*, vol. 11, pp. 863–869, 2011.
- [6] C. L. Tai, P. H. Hsieh, W. P. Chen, L. H. Chen, W. J. Chen, and P. L. Lai, "Biomechanical comparison of lumbar spine instability between laminectomy and bilateral laminotomy for spinal stenosis syndrome—an experimental study in porcine model," *BMC Musculoskeletal Disorders*, vol. 9, p. 84, 2008.
- [7] P. P. Mura, M. Costaglioli, M. Piredda, S. Caboni, and S. Casula, "TLIF for symptomatic disc degeneration: a retrospective study of 100 patients," *European Spine Journal*, vol. 20, Supplement 1, pp. 57–60, 2011.
- [8] D. Lau, J. G. Lee, S. J. Han, D. C. Lu, and D. Chou, "Complications and perioperative factors associated with learning the technique of minimally invasive transforaminal lumbar interbody fusion (TLIF)," *Journal of Clinical Neuroscience*, vol. 18, pp. 624–627, 2011.
- [9] M. J. Yang, C. Zeng, S. Guo, J. Pan, Y. C. Han, and Z. Q. Li, "Digitalized design of extraforaminal lumbar interbody fusion: a computer-based simulation and cadaveric study," *PLoS One*, vol. 9, 2014.
- [10] L. J. Li, Y. C. Han, and M. J. Yang, "A digital anatomic study of minimally invasive extreme lateral transforaminal lumbar interbody fusion," *Chinese Journal of Orthopaedic Trauma*, vol. 15, pp. 50–54, 2013.

- [11] M. J. Yang, H. R. Yan, and L. J. Li, "Bio-mechanical evaluation of extreme lateral transforaminal lumbar interbody fusion," *Chinese Journal of Surgery*, vol. 50, pp. 62–65, 2012.
- [12] S. Guo, C. Zeng, M. Yan et al., "A biomechanical stability study of extraforaminal lumbar interbody fusion on the cadaveric lumbar spine specimens," *PLoS One*, vol. 11, no. 12, article e0168498, 2016.
- [13] Y. M. Lu, W. C. Hutton, and V. M. Gharpuray, "Do bending, twisting, and diurnal fluid changes in the disc affect the propensity to prolapse? A viscoelastic finite element model [J]," *Spine (Phila Pa 1976)*, vol. 21, no. 22, pp. 2570–2579, 1996.
- [14] A. Polikeit, S. J. Ferguson, L. P. Nolte, and T. E. Orr, "Factors influencing stresses in the lumbar spine after the insertion of intervertebral cages: finite element analysis [J]," *European Spine Journal*, vol. 12, no. 4, pp. 413–420, 2003.
- [15] V. K. Goel, B. T. Monroe, L. G. Gilbertson, and P. Brinckmann, "Interlaminar shear stresses and laminae separation in a disc. Finite element analysis of the L3-L4 motion segment subjected to axial compressive loads," *Spine (Phila Pa 1976)*, vol. 20, no. 6, pp. 689–698, 1995.
- [16] A. Rohlmann, T. Zander, and G. Bergmann, "Effects of fusion-bone stiffness on the mechanical behavior of the lumbar spine after vertebral body replacement," *Clinical Biomechanics (Bristol, Avon)*, vol. 21, no. 3, pp. 221–227, 2006.
- [17] H. Schmidt, F. Heuer, J. Drumm, Z. Klezl, L. Claes, and H. J. Wilke, "Application of a calibration method provides more realistic results for a finite element model of a lumbar spinal segment," *Clinical Biomechanics (Bristol, Avon)*, vol. 22, no. 4, pp. 377–384, 2007.
- [18] S. Vadapalli, K. Sairyo, V. K. Goel et al., "Biomechanical rationale for using polyetheretherketone (PEEK) spacers for lumbar Interbody fusion—a finite element study," *Spine*, vol. 31, pp. 992–998, 2006.
- [19] Z. M. Chen, H. Ma, and J. Zhao, "Three-dimensional finite element analyses of unilateral pedicle screws fixation in lumbar spine," *Chinese Journal of Spine and Spinal Cord*, vol. 20, pp. 684–688, 2010.
- [20] J. G. Harms and D. Jeszenszky, "The unilateral transforaminal approach for posterior lumbar interbody fusion," *Orthopaedics and Traumatology*, vol. 6, pp. 88–99, 1998.
- [21] J. G. Harms and H. Rollinger, "A one-stage procedure in operative treatment of spondylolisthesis: dorsal traction–reposition and anterior fusion," *Zeitschrift Orthopadie Und Ihre Grenzgebiete*, vol. 120, pp. 343–437, 1982.
- [22] C. L. Branch, "The case for posterior lumbar interbody fusion," *Clinical Neurosurgery*, vol. 47, pp. 252–267, 2000.
- [23] Y. Kawaguchi, H. Matsui, and H. Tsuji, "Back muscle injury after posterior lumbar spine surgery. A histologic and enzymatic analysis," *Spine*, vol. 21, pp. 941–944, 1996.
- [24] Y. Kawaguchi, H. Matsui, and H. Tsuji, "Back muscle injury after posterior lumbar spine surgery. Part I: histologic and histochemical analyses in rats," *Spine*, vol. 19, pp. 2590–2597, 1994.
- [25] P. J. Rao, A. Loganathan, V. Yeung, and R. J. Mobbs, "Outcomes of anterior lumbar interbody fusion surgery based on indication: a prospective study," *Neurosurgery*, vol. 76, pp. 7–23, 2015.
- [26] S. Tang, W. Xu, and B. J. Rebolz, "Anterior lumbar interbody fusion combined with percutaneous pedicle screw fixation for degenerative lumbar instability: minimum four-year follow-up," *Turkish Neurosurgery*, vol. 22, pp. 156–160, 2012.
- [27] Y. S. Lee, W. P. Seung, and B. K. Young, "Direct lateral lumbar interbody fusion: clinical and radiological outcomes," *Journal of Korean Neurosurgical Society*, vol. 55, pp. 248–254, 2014.
- [28] S. Fujibayashi, R. A. Hynes, B. Otsuki, H. Kimura, M. Takemoto, and S. Matsuda, "Effect of indirect neural decompression through oblique lateral interbody fusion for degenerative lumbar disease," *Spine*, vol. 40, pp. E175–E182, 2015.
- [29] T. A. Jahng, E. K. Young, and Y. M. Kyung, "Comparison of the biomechanical effect of pedicle-based dynamic stabilization: a study using finite element analysis," *Spine journal*, vol. 13, pp. 85–94, 2013.
- [30] K. R. Chin, M. T. Reis, P. M. Reyes et al., "Stability of transforaminal lumbar interbody fusion in the setting of retained facets and posterior fixation using transfacet or standard pedicle screws," *The Spine Journal*, vol. 15, pp. 1077–1082, 2013.
- [31] M. M. Panjabi, "Biomechanical evaluation of spinal fixation devices: a conceptual frame work," *Spine*, vol. 13, pp. 1129–1134, 1988.

## Research Article

# Early Spatiotemporal Patterns and Knee Kinematics during Level Walking in Individuals following Total Knee Arthroplasty

Xubo Wu,<sup>1</sup> Lixi Chu,<sup>1</sup> Lianbo Xiao,<sup>2</sup> Yong He,<sup>2</sup> Shuyun Jiang,<sup>3</sup> Songbin Yang,<sup>1</sup> and Yijie Liu<sup>1</sup>

<sup>1</sup>School of Rehabilitation Science, Shanghai University of Traditional Chinese Medicine, Shanghai, China

<sup>2</sup>Department of Orthopaedic Surgery, Guanghua Integrative Medicine Hospital, Shanghai, China

<sup>3</sup>Gait Analysis Laboratory, Yueyang Hospital of Integrated Chinese and Western Medicine, Shanghai, China

Correspondence should be addressed to Lixi Chu; [chulixi2@126.com](mailto:chulixi2@126.com)

Received 12 February 2017; Revised 5 May 2017; Accepted 23 May 2017; Published 31 July 2017

Academic Editor: Liping Wang

Copyright © 2017 Xubo Wu et al. This is an open access article distributed under the Creative Commons Attribution License, which permits unrestricted use, distribution, and reproduction in any medium, provided the original work is properly cited.

**Purpose.** With the aim of investigating the spatiotemporal features of early gait pattern and knee kinematics after total knee arthroplasty and analyzing the association between outcomes of gait analyses and knee kinematic parameters, the relationship between walking and dynamic knee deformity at the early period after total knee arthroplasty was assessed in this study. **Methods.** Eighteen patients including 14 women and 4 men who underwent total knee arthroplasty were analyzed using three-dimensional gait analysis system to observe gait parameters and values of maximum knee flexion angle (MKFA) during swing phase and knee flexion angle (KFA) and knee valgus angle (KVA) at midstance phase. **Results.** 3D gait analysis showed that operated side exhibited significantly less total support time and single support time as well as significantly longer swing phase compared with the other side. During walking, the operated side had significantly smaller MKFA and greater KFA and KVA than the nonoperated side. There was moderate to significant correlation between gait pattern and the dynamic knee kinematics. **Conclusion.** The gait abnormality of patients after TKA was associated with inadequate flexion of knees at swing phase and insufficient extension at stance phase as well as increased range of valgus.

## 1. Introduction

Total knee arthroplasty (TKA) is performed to restore knee functions and relieve pain in some patients with severe osteoarthritis (OA). With the development of prosthesis design and surgical techniques, TKA has become a well-established treatment for managing end-stage symptomatic knee OA. However, not all patients following the operation obtain satisfactory outcomes. Studies indicated that only 70–89% of patients were satisfied with the surgery [1–3], while some patients suffered from pain, functional limitation, and even revision and indolent infection [4].

The satisfaction of patients is closely related to knee function after surgery and affected by a variety of postoperative complications. The way of improving the gait pattern and efficacy of patients after surgery is an important issue that

challenges clinical professionals. More and more studies recommended early follow-up and monitoring of functional recovery [4, 5]. The way of identifying early specific indicators of some disorders in the future still remains as a problem for surgeons and other healthcare givers.

Kinematic alignment in TKA pursues better anatomical alignment of knee prosthesis with the aim of promoting more physiological motion and concerns with implant survivorship and patellofemoral tracking [6, 7]. However, a recent study showed that small deviations from the static mechanical axis alignment in TKA did not appear to impact overall survivorship or complication rates at short-term follow-up [8]. Moreover, some studies demonstrated that knee kinematics during gait in TKA group still differed from those of healthy control group despite of improved clinical outcomes and spatiotemporal parameters [9, 10].

TABLE 1: General information of the patients.

	Minimum	Maximum	Mean	Standard deviation
Age (years)	48	79	64.50	9.45
Weight (kg)	46	89	68.22	11.13
Height (cm)	150	174	161.61	7.38
BMI (kg/m <sup>2</sup> )	18.66	29.76	25.99	2.85
HSS	42	77	64.06	8.93

This study used three-dimensional (3D) gait analysis technology to investigate the kinematic features of knee undergoing operation and explore the association between parameters of knee kinematics and spatiotemporal patterns during walking in the early recovery period after TKA and search for typical indicators specific to walking function, hence providing theoretical basis for early knee rehabilitation intervention after TKA surgery.

## 2. Materials and Methods

**2.1. Subjects.** The detailed data of eighteen patients with TKA, including 14 women and 4 men is provided in Table 1. There were 10 cases with left affected knee and 8 cases with right affected knee. All 18 patients were confirmed with primary osteoarthritis according to the diagnostic standard of osteoarthritis defined by the American College of Rheumatology. Additional exclusion criteria for patients were previous surgery or pain in the back or lower extremity, neurologic diseases, rheumatism, leg length discrepancy > 1 cm, a body mass index above 33 kg/m<sup>2</sup>, a history of major trauma or injury to the knee, and/or knee surgery within 6 months.

The patients were subjected to continuous epidural anesthesia. The median incision was made on the anterior area of knee with the selection of medial approach beside patella. All patients received surface replacement with prosthesis (Depuy PFC Sigma) fixed by bone cement. None of the patients received surface replacement of patella. After surgery, patients were given antibiotics to prevent infection. Meanwhile, low molecular heparin was subcutaneously injected into abdominal wall to prevent deep venous thrombosis in lower limbs.

All patients had their surgeries in the same surgery department of a hospital, showed good outcome scores, and were satisfied with the procedure. The patients with passive knee flexion in the operated knee of  $\geq 90^\circ$  and a HSS (the Hospital for Special Surgery, USA) score > 40 were included.

**2.2. Gait Analysis.** Gait analysis was conducted for each patient on the 14th day after surgery. The subjects walked on flat ground at self-selected comfortable pace. As shown in Figure 1, the motions were captured using Motion Analysis System (Motion Analysis, USA), which had 12 infrared lenses at high speed including 9 Eagle-4 lenses and 3 Raptor-4 lenses. The ground reaction force of feet was tested by force platform (model OR6-7, AMTI, USA). The Cortex and OrthoTrack software (Motion Analysis, USA) were used for data analysis.



FIGURE 1: 3D gait analysis technology.

To get familiar with the environment, the patients entered the laboratory room of gait analysis 20 minutes prior to test. They were asked to wear swimwear or waistcoat and shorts to fully expose the locations of markers which were placed in accordance with the Helen Hayes gait model.

Before testing, the patients could practice a while to adapt to the environment and know the testing procedures. They were advised to walk back and forth at the most comfortable pace for one-way distance of about 5 meters between two walkers.

**2.3. Data Extraction.** The kinematic parameters of knee joint at sagittal plane and coronary plane were observed using 3D gait analysis technology. For the sagittal plane, the maximum knee flexion angle (MKFA) during swing phase and the knee flexion angle (KFA) at midstance phase were observed. For the coronary plane, the knee valgus angle (KVA) at midstance phase was observed.

A typical gait cycle was selected in this study. The MKFA was selected when the operated lower limb was at swing phase. As regards the stance phase of the operated lower limb, the angles of knee flexion and extension, valgus, and varus were recorded during the midstance phase which was associated with the period of single support.

**2.4. Statistical Analysis.** The statistical analysis was performed using SPSS 22.0 statistical software. The measurement data was expressed as mean  $\pm$  standard deviation ( $x \pm s$ ). The analysis of normal distribution was conducted using K-S test. The analysis of corresponding parameters between two lower limbs during a typical gait cycle was conducted using paired *t*-test. The relationship between different parameters and gaits was analyzed using the Pearson correlation analysis. The test level was set at  $\alpha = 0.05$ .

## 3. Results

**3.1. Spatiotemporal Parameters.** Three-dimensional gait analysis showed that operated side had significantly less total support time ( $P = 0.017$ ) and longer swing phase ( $P = 0.017$ ) as well as lower single support time ( $P = 0.017$ ) compared with the other side. These results are provided in Table 2.

TABLE 2: Comparisons of 3D gait parameters between two sides ( $n = 18$ ).

	Operated side	Nonoperated side	Difference 95% CI	$P$
Step length avg (cm)	41.19 ± 12.42	39.67 ± 13.97	-1.570~4.834	0.297
Stride length avg (cm)	81.27 ± 25.20	81.00 ± 25.95	-0.726~1.710	0.406
Forward velocity avg (cm/s)	63.55 ± 25.21	63.62 ± 25.91	-0.847~1.127	0.768
Cadence avg (steps/min)	90.96 ± 16.27	91.31 ± 15.98	-0.951~0.580	0.616
Total support time (%)*	65.07 ± 4.05	69.16 ± 8.48	-7.694~-0.874	0.017
Swing phase (%)*	34.93 ± 4.05	30.84 ± 8.478	0.874~7.693	0.017
Initial double support time (%)	16.83 ± 6.25	17.74 ± 7.11	-4.882~2.481	0.501
Single support time (%)*	30.84 ± 8.48	34.93 ± 4.05	-7.694~-0.874	0.017

\*Significant difference between two sides,  $P < 0.05$ .

TABLE 3: Knee kinematic parameters (degree) ( $n = 18$ ).

	Operated side	Nonoperated side	Difference 95% CI	$P$
MKFA	39.43 ± 12.11	52.94 ± 11.05	-20.06~-6.97	0.000
Midstance KFA	14.71 ± 4.12	5.71 ± 5.51	5.62~12.37	0.000
Midstance KVA	5.55 ± 3.84	0.08 ± 3.58	3.26~7.68	0.000

MKFA: maximum knee flexion angle; midstance KFA: knee flexion angle at midstance; midstance KVA: knee valgus angle at midstance.

**3.2. Measurements of Knee Kinematic Parameters.** During walking, the operated side had significantly smaller MKFA yet greater KFA and KVA at midstance phase than the nonoperated side. These results are provided in Table 3 and Figure 2.

**3.3. Correlation between Kinematic Parameters of Knee and Parameters of Gait Analysis.** MKFA of the operated knee during swing phase was positively correlated with ipsilateral average cadence ( $r = 0.636$ ,  $P = 0.021$ ). KFA of the operated knee at midstance phase was associated with the single support time of the same lower limb ( $r = -0.671$ ,  $P = 0.038$ ) negatively and the total support time of the other lower limb ( $r = 0.671$ ,  $P = 0.038$ ) positively. KVA of the operated knee at midstance phase was negatively associated with step frequencies of the other lower limb ( $r = -0.486$ ,  $P = 0.041$ ) and the painful lower limb ( $r = -0.597$ ,  $P = 0.036$ ). The results are shown in Table 4.

## 4. Discussion

The gait analysis was conducted in 18 patients on the 14th day after TKA. The results indicated that when patients walked at a comfortable speed, the operated lower limb exhibited significantly less single support time and total support time than nonoperated side. In addition to gait analysis parameters, this study also observed the kinematic parameters of the knee during walking, including MKFA at swing phase and KFA and KVA at midstance phase.

Although TKA surgery improved the static force lines of knee joint, only 20% of patients after a TKA exhibited a normal biphasic flexion-extension moment of the knee during level walking [3]. The limitation of knee flexion and extension after surgery is an important factor that impacts gait. Our study observed that inadequate extension of operated knee at midstance phase was about 14°, which caused shorter

stance phase of operated limb than nonoperated limb (Table 2) and inadequate forward propulsion of body weight and further resulted in lower walking efficiency. Recent studies demonstrated that flexion of operated knee at stance phase was a core indicator that impacted the quality of gait [1, 11, 12], and knee flexion range in stance was the most important variable in discriminating between patients with TKA and controls [11]. The study of Li et al. [13] noted that this was mostly due to inadequate muscle strength of quadriceps femoris and motor control disorder as well as lower moment of force during knee extension.

Table 4 shows that inadequate extension of operated lower limb at midstance phase led to prolonged stance phase of double support, featured by shorter single support time of the affected lower limb ( $r = -0.671$ ) and longer total support time of the other lower limb ( $r = 0.671$ ). The shorter stance phase of single support also caused shorter swing phase of the other side. Subsequently, inadequate swing phase caused reduced step length of the other side [14].

In addition to inadequate knee extension, increased valgus degree of operated knee at midstance phase was also observed in the study. There were significant statistical differences between the valgus of knees at stance phase of both legs ( $P < 0.01$ ). The higher knee valgus of the operated knee during level walking was probably a compensatory mechanism, to avoid pain and provide energy for forward propulsion, and it might be associated with muscle control [15]. Some researchers noted that it might be associated with the type of implants. Renaud et al. compared both TKA designs and showed that Nexgen(TM) implant had significantly more flexion at the end of swing phase than Triathlon(TM) implant while at the midstance phase, Nexgen(TM) TKA exerted significantly more adduction [16]. Some authors actually found increased knee adduction moment during stance phase in TKA patients which stand in contrast to the present study [16, 17].

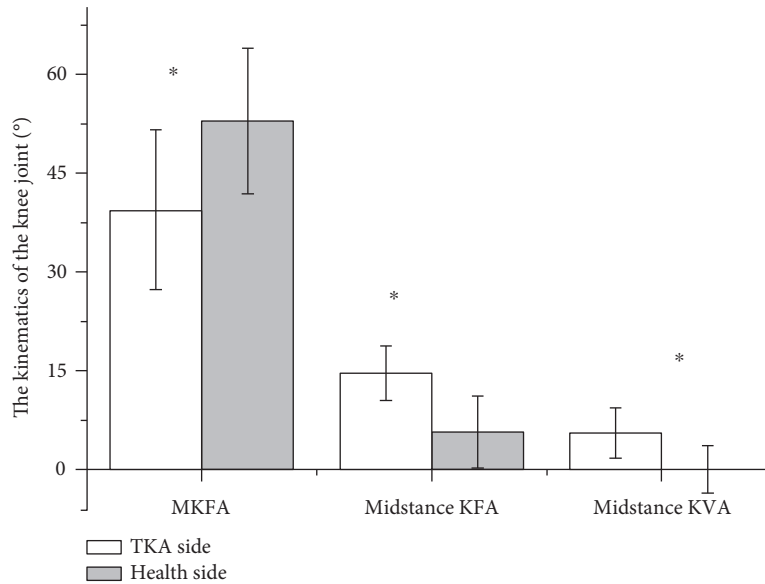


FIGURE 2: Comparison of joint angles between the operated and nonoperated knees (\*significance level refers to paired *t*-test comparing operated and nonoperated knee joint angles with  $P < 0.05$ . MKFA: maximum knee flexion angle; midstance KFA: knee flexion angle at midstance; midstance KVA: knee valgus angle at midstance).

TABLE 4: Correlation between kinematic parameters of knee and parameters of gait analysis ( $n = 18$ ).

	MKFA		Midstance KFA		Midstance KVA	
	<i>r</i>	<i>P</i>	<i>r</i>	<i>P</i>	<i>r</i>	<i>P</i>
Operated side cadence avg	0.636	0.021	-0.277	0.266	-0.486	0.041
Operated side single support time	0.412	0.089	-0.671	0.038	0.350	0.154
Nonoperated side cadence avg	0.418	0.084	-0.254	0.310	-0.597	0.036
Nonoperated side total support time	-0.412	0.089	0.671	0.038	-0.350	0.154

At the stance phase of the operated leg, there was an extension lag associated with the valgus of the knee, which caused changes in mechanical relationships between implant and polyethylene. The abnormal distribution of stress within implants was directly associated with wear of polyethylene pad, which might result in abnormal alignment of joint, implant loosening, pain in soft tissue surrounding the joint, and even shortening of implant survivorship.

The limitations of the study lay in the fact that during postoperative 2 weeks, the pain and swelling that affected the walking of the patients could be eased. Walking involved flexibility of joint and surrounding soft tissues, as well as accurate neuromuscular control and precise feedback by central nervous system [15, 18, 19]. For early patients with TKA, factors such as swelling of joint, pain, and lack of proprioception could impact the motion control on the knee joint, which influenced the motor performance of affected extremities [20–22].

## 5. Conclusion

There are significant abnormalities in early gait of patients after TKA. The gait abnormality is associated with inadequate flexion of knee at swing phase and insufficient

extension at stance phase as well as increased range of valgus. However, TKA with early dynamic deviations in alignment interfered with gait poorly. Further prospective studies with longer term are needed to determine the precise indicators and mechanism of these kinematic parameters resulting in polyethylene wear, aseptic loosening, pain, and other complications.

## Conflicts of Interest

The authors declare that there is no conflict of interest regarding the publication of this paper.

## References

- [1] M. J. Dunbar, O. Robertsson, L. Ryd, and L. Lidgren, "Appropriate questionnaires for knee arthroplasty. Results of a survey of 3600 patients from The Swedish Knee Arthroplasty Registry," *Journal of Bone and Joint Surgery British Volume (London)*, vol. 83, no. 3, pp. 339–344, 2001.
- [2] V. Wylde, I. Learmonth, A. Potter, K. Bettinson, and E. Lingard, "Patient-reported outcomes after fixed- versus mobile-bearing total knee replacement: a multi-centre randomised controlled trial using the Kinemax total knee

- replacement,” *Journal of Bone and Joint Surgery British Volume (London)*, vol. 90, no. 9, pp. 1172–1179, 2008.
- [3] R. B. Bourne, B. M. Chesworth, A. M. Davis, N. N. Mahomed, and K. D. Charron, “Patient satisfaction after total knee arthroplasty: who is satisfied and who is not?,” *Clinical Orthopaedics and Related Research*, vol. 468, no. 1, pp. 57–63, 2010.
  - [4] C. D. Hightower, L. S. Hightower, P. J. Tatman, P. M. Morgan, T. Gioe, and J. A. Singh, “How often is the office visit needed? Predicting total knee arthroplasty revision risk using pain/function scores,” *BMC Health Services Research*, vol. 16, no. 1, p. 429, 2016.
  - [5] J. C. van Egmond, H. Verburg, S. B. Vehmeijer, and N. M. Mathijssen, “Early follow-up after primary total knee and total hip arthroplasty with rapid recovery: focus groups,” *Acta Orthopaedica Belgica*, vol. 81, no. 3, pp. 447–453, 2015.
  - [6] D. M. Fang, M. A. Ritter, and K. E. Davis, “Coronal alignment in total knee arthroplasty: just how important is it?,” *The Journal of Arthroplasty*, vol. 24, 6 Supplement, pp. 39–43, 2009.
  - [7] M. A. Ritter, K. E. Davis, J. B. Meding, J. L. Pierson, M. E. Berend, and R. A. Malinzak, “The effect of alignment and BMI on failure of total knee replacement,” *The Journal of Bone and Joint Surgery American Volume*, vol. 93, no. 17, pp. 1588–1596, 2011.
  - [8] P. M. Courtney and G. C. Lee, “Early outcomes of kinematic alignment in primary total knee arthroplasty: a meta-analysis of the literature,” *The Journal of Arthroplasty*, vol. 32, no. 6, pp. 2028.e1–2032.e1, 2017.
  - [9] D. Bytyqi, B. Shabani, L. Cheze, P. Neyret, and S. Lustig, “Does a third condyle TKA restore normal gait kinematics in varus knees? In vivo knee kinematic analysis,” *Archives of Orthopaedic and Trauma Surgery*, vol. 137, no. 3, pp. 409–416, 2017.
  - [10] V. U. Fenner, H. Behrend, and M. S. Kuster, “Joint mechanics after total knee arthroplasty while descending stairs,” *The Journal of Arthroplasty*, vol. 32, no. 2, pp. 575–580, 2017.
  - [11] J. Rahman, Q. Tang, M. Monda, J. Miles, and I. McCarthy, “Gait assessment as a functional outcome measure in total knee arthroplasty: a cross-sectional study,” *BMC Musculoskeletal Disorders*, vol. 16, p. 66, 2015.
  - [12] M. M. Ardestani and M. Moazen, “How human gait responds to muscle impairment in total knee arthroplasty patients: muscular compensations and articular perturbations,” *Journal of Biomechanics*, vol. 49, no. 9, pp. 1620–1633, 2016.
  - [13] K. Li, D. C. Ackland, J. A. McClelland et al., “Trunk muscle action compensates for reduced quadriceps force during walking after total knee arthroplasty,” *Gait & Posture*, vol. 38, no. 1, pp. 79–85, 2013.
  - [14] A. Lee, J. Park, and S. Lee, “Gait analysis of elderly women after total knee arthroplasty,” *Journal of Physical Therapy Science*, vol. 27, no. 3, pp. 591–595, 2015.
  - [15] G. M. Freisinger, E. E. Hutter, J. Lewis et al., “Relationships between varus-valgus laxity of the severely osteoarthritic knee and gait, instability, clinical performance, and function,” *Journal of Orthopaedic Research*, 2016.
  - [16] A. Renaud, A. Fuentes, N. Hagemester, M. Lavigne, and P. A. Vendittoli, “Clinical and biomechanical evaluations of staged bilateral total knee arthroplasty patients with two different implant designs,” *The Open Orthopaedics Journal*, vol. 10, pp. 155–165, 2016.
  - [17] G. L. Hatfield, W. D. Stanish, and C. L. Hubley-Kozey, “Three-dimensional biomechanical gait characteristics at baseline are associated with progression to total knee arthroplasty,” *Arthritis Care & Research (Hoboken)*, vol. 67, no. 7, pp. 1004–1014, 2015.
  - [18] R. R. Neptune and C. P. McGowan, “Muscle contributions to frontal plane angular momentum during walking,” *Journal of Biomechanics*, vol. 49, no. 13, pp. 2975–2981, 2016.
  - [19] G. Dubois, P. Rouch, D. Bonneau, J. L. Gennisson, and W. Skalli, “Muscle parameters estimation based on biplanar radiography,” *Computer Methods in Biomechanics and Biomedical Engineering*, vol. 19, no. 15, pp. 1592–1598, 2016.
  - [20] J. E. Naili, M. D. Iversen, A. C. Esbjörnsson et al., “Deficits in functional performance and gait one year after total knee arthroplasty despite improved self-reported function,” *Knee Surgery, Sports Traumatology, Arthroscopy*, 2016.
  - [21] K. T. Kang, Y. G. Koh, J. Son et al., “Measuring the effect of femoral malrotation on knee joint biomechanics for total knee arthroplasty using computational simulation,” *Bone Joint Research*, vol. 5, no. 11, pp. 552–559, 2016.
  - [22] A. Bonnefoy-Mazure, S. Armand, Y. Sagawa, D. Suvà, H. Miozzari, and K. Turcot, “Knee kinematic and clinical outcomes evolution before, 3 months, and 1 year after total knee arthroplasty,” *The Journal of Arthroplasty*, vol. 32, no. 3, pp. 793–800, 2017.

## Research Article

# Joint Torque and Mechanical Power of Lower Extremity and Its Relevance to Hamstring Strain during Sprint Running

Yunjian Zhong,<sup>1,2</sup> Weijie Fu,<sup>2,3</sup> Shutao Wei,<sup>2</sup> Qing Li,<sup>4</sup> and Yu Liu<sup>2,3</sup>

<sup>1</sup>College of Physical Education, Nanchang University, Nanchang 330031, China

<sup>2</sup>School of Kinesiology, Shanghai University of Sport, Shanghai 200438, China

<sup>3</sup>Key Laboratory of Exercise and Health Sciences of Ministry of Education, Shanghai University of Sport, Shanghai 200438, China

<sup>4</sup>Teaching and Research Division of Physical Culture, Tsinghua University, Beijing 100083, China

Correspondence should be addressed to Weijie Fu; [fuweijie@sus.edu.cn](mailto:fuweijie@sus.edu.cn) and Yu Liu; [yuliu@sus.edu.cn](mailto:yuliu@sus.edu.cn)

Received 22 February 2017; Revised 11 May 2017; Accepted 29 May 2017; Published 12 July 2017

Academic Editor: Jie Yao

Copyright © 2017 Yunjian Zhong et al. This is an open access article distributed under the Creative Commons Attribution License, which permits unrestricted use, distribution, and reproduction in any medium, provided the original work is properly cited.

The aim of this study was to quantify the contributions of lower extremity joint torques and the mechanical power of lower extremity muscle groups to further elucidate the loadings on hamstring and the mechanics of its injury. Eight national-level male sprinters performed maximum-velocity sprint running on a synthetic track. The 3D kinematic data and ground reaction force (GRF) were collected synchronously. Intersegmental dynamics approach was used to analyze the lower extremity joint torques and power changes in the lower extremity joint muscle groups. During sprinting, the GRF during the stance phase and the motion-dependent torques (MDT) during the swing phase had a major effect on the lower extremity movements and muscle groups. Specifically, during the stance phase, torque produced and work performed by the hip and knee muscles were generally used to counteract the GRF. During the swing phase, the role of the muscle torque changed to mainly counteract the effect of MDT to control the movement direction of the lower extremity. Meanwhile, during the initial stance and late swing phases, the passive torques, namely, the ground reaction torques and MDT produced by the GRF and the inertial movement of the segments of the lower extremity, applied greater stress to the hamstring muscles.

## 1. Introduction

Sprint running is a cyclical movement of alternate support and flight motions and combination of foot-strike and swing. The human body gains forward momentum by the strong push-off of the lower extremity during the stance phase [1, 2]. In terms of motion of each body segment, lower extremity motion is the key part of the entire sprint technique. The ability of the lower extremity muscle groups to perform specific work directly affects running speed and in turn interacts with the loading conditions of the muscle itself. This process may lead to muscle overload (e.g., hamstrings strain) [3, 4].

Several studies have used the inverse dynamics approach to quantify lower extremity joint torques during sprinting [5–8]. These findings are beneficial in examining the function of the lower extremity muscle groups during maximum-

velocity sprint running and further determining muscle loading conditions. Specifically, during the stance phase, the large ground reaction force (GRF) generates contact torques simultaneously on lower extremity joints. Meanwhile, greater motion-dependent torques (MDT; e.g., inertia, Coriolis, and centrifugal forces) will be generated and acted upon each segment when lower extremity joints rapidly alternate between flexion and extension during the swing phase [9]. Torques generated by these external forces play a vital role in affecting the function of the lower extremity muscle groups during sprinting.

Currently, most studies on the different phases in sprinting and different levels of sprinters have focused on the GRF and lower extremity dynamics [10–14]. Analysis of the changes in joint muscle torques (MUS) covers several phases, including the stance phase of the second step after push-off [15], acceleration phase [6, 16], maximum-velocity

phase [1, 8], and swing phase of the maximum-velocity [3]. The sprint technique varies greatly in the different phases and levels of sprinter subjects, resulting in much discrepancy on the characteristics of lower extremity joint MUS in these findings. Additionally, muscle power is an important biomechanical parameter in human gait analysis [17–19]. This analysis explains the formation of and control over human body segmental movements from energy and work generation perspectives. The results can be used to indirectly confirm the type of motion (concentric contraction or eccentric contraction) of the muscle groups (extensors or flexors) around joints. However, among these studies, only a few examined the muscle power of lower limbs [5, 16, 19], and the lower extremity joint torques and muscle power of a gait during maximum-velocity sprint running have not been analyzed yet.

On the other hand, hamstring strain injury is one of the most common injuries during sprinting [20, 21]. However, the underlying mechanisms of these injuries are still ambiguous, because most studies are based on the clinical muscle strain assumption [22]. Limited attempts have been made to measure ground reactions during overground sprinting, and few studies have used such data to estimate hamstring kinetics during stance and swing phases [23]. Therefore, understanding the coordination of muscular torque and the loading conditions of the hamstring during sprinting is beneficial to further quantify the torque component one by one during probing joint torques [24]. These parameters could be determined through an advanced inverse dynamics perspective, and the hamstring strain risk can be explored based on the insight mechanical mechanism. In this study, we adopted the intersegmental dynamics approach to break down the net joint torque (NET) of a gait during maximum-velocity sprint running into the MUS, MDT generated by movement, contact torques (EXF) generated by ground reaction force (GRF), and gravitational torques (GRA) [7, 25, 26].

Based on the above consideration, the purpose of this study was to quantify the contributions of lower extremity joint torques and the mechanical power of lower extremity muscle groups to further elucidate the loadings on hamstring and the mechanics of its injury. We hypothesized that the EXF and MDT could play an important role in the contributions of lower extremity joint torques during stance and swing phases, respectively. The effects of active and passive joint torque components on the risk of hamstring injury were also determined.

## 2. Methods

**2.1. Subjects.** Eight male national level sprinters (age:  $21.1 \pm 1.9$  years, mass:  $74.7 \pm 4.1$  kg, height:  $181.5 \pm 3.9$  cm) were recruited to participate in this study. The best personal performance of the sprinters for 100 m ranged from 10.27 s to 10.80 s. These participants had no history of lower extremity injuries in the six months prior to the study. The study was approved by the local ethical committee. Each subject signed informed consent forms after all questions were answered satisfactorily.

**2.2. Data Collection.** The athletes performed maximal-effort sprints on a synthetic track, and three-dimensional (3D) kinematics data were obtained at a sampling rate of 300 Hz from eight Vicon high-resolution cameras (Vicon Motion Capture, Vicon, England). A total of 57 retro-reflective markers (14.0 mm diameter) comprising the plug-in gait marker set used in our previous study [27] were attached to the lower limb to define hip, knee, and ankle joints. The calibration volume for the kinematics data collection was  $10.0 \times 2.5 \times 2.0$  m<sup>3</sup> and centered 40 m from the sprint start line. A recessed Kistler force plate ( $60 \times 90$  cm<sup>2</sup>) (Kistler 9287B, Kistler Corporation, Switzerland) located at 40 m from the sprint start line was used to measure the GRF. The force signals were amplified and recorded in the Vicon system at a sampling rate of 1200 Hz. After a 5–10 min warm-up, each sprinter wearing track spikes performed three valid trials with sufficient rest intervals. The trial in which no markers dropped and either foot of the subject successfully hit the force plate was analyzed.

**2.3. Data Analysis.** Visual 3D (Version 3.390.23, C-Motion Corporation, USA) was used to calculate the kinematics and dynamics data. The tracks of the markers were filtered by Butterworth low-pass digital filter at a cutoff frequency of 17 Hz [28]. The GRF data were low-pass filtered with a cutoff frequency of 55 Hz.

The joint angles and angular velocity of lower extremity were also computed based on the visual 3D requirement for a skeletal framework. Meanwhile, the intersegmental dynamics model was used, in which the algorithm applied in our previous studies and other former studies was modified [23, 27]. Briefly, the analysis was conducted by a customized program based on intersegmental dynamics model and by inputting limb kinematics, anthropometric data, and GRF [27]. The lower extremity, that is, hip, knee, and ankle, was considered as a generalized linked-segment model. Based on free body diagrams of the segments, the dynamic formula of motion was derived by using the Newton-Euler equations applied to each segment. Torques at each joint can be separated into five categories, namely, NET, GRA, MDT, EXF (termed as ground reaction torques in this study), and MUS, with the first category being the sum of the rest:

$$\text{NET} = \text{MUS} + \text{GRA} + \text{EXF} + \text{MDT}. \quad (1)$$

NET is the sum of all the torque components acting at a joint. MUS is mainly generated by muscle contractions. GRA results from gravitational forces acting at the center of mass of each segment. EXF is generated at joints by the GRF acting on the foot. MDT arises from the mechanical interactions occurring between limb segments and is the sum of all interaction torques produced by segment movements, such as angular velocity and angular acceleration of segments.

The muscle power of the lower extremity joint ( $P_j$ ) was calculated as follows [16]:

$$P_j = M_j \times \omega_j, \quad (2)$$

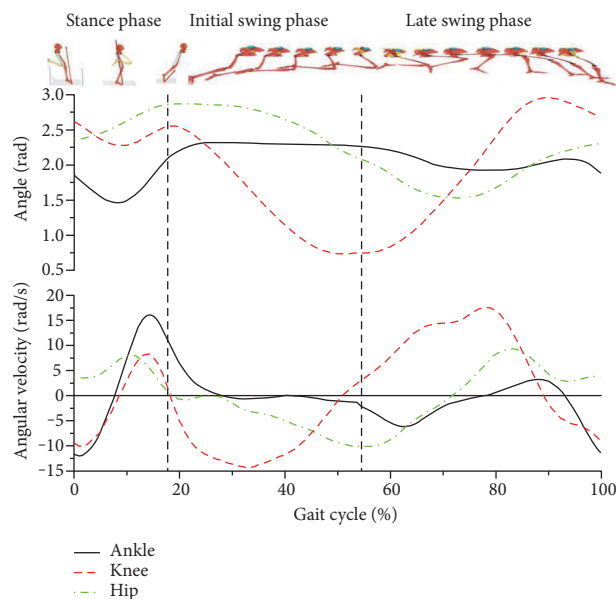


FIGURE 1: Changes in the lower extremity joint angles and angular velocity (rad/s) in a gait cycle. Values on the x-axis represent percentages of total gait time.

where  $M_j$  is the MUS generated by agonist muscles and antagonist muscles during joint movement and  $\omega_j$  is the angular velocity of the joint.

If the values of a joint torque and angular velocity were positive, the function of such torque was classified as extension joints (plantar flexion for ankle). By contrast, the function of torque was categorized as flexion joints (dorsiflexion for ankle). Positive muscle power indicated that the muscle torque and joint angular velocity were moving toward the same direction, and the muscle was doing concentric contraction. By contrast, negative muscle power indicated eccentric contraction of the muscle.

**2.4. Statistics.** Data were expressed as mean  $\pm$  SD. One-way ANOVA and paired  $t$ -tests were used to determine the differences between joints and extensors/flexors in all joint kinematics and kinetic variables, respectively (10.0, SPSS Inc., Chicago, IL, USA). The significance level for all statistical tests was set at  $\alpha = 0.05$ .

### 3. Results

The mean sprinting speed during data collection for the eight subjects was  $9.7 \pm 0.3$  m/s. A stride cycle in this study comprised two phases, namely, stance and swing phases. The stance phase was defined as the phase in which the left foot of an athlete was in contact with the ground (the critical point was standardized instant of  $17.7\% \pm 1.2\%$ ) (Figure 1). The following swing motion of the left leg was defined as the swing phase. This phase was divided into two periods, namely, initial and late swing phases, based on the different timing. The demarcation timing was when the thigh reached an upright posture on the vertical line of the center of mass (standardized instant of  $55.1\% \pm 2.3\%$ ).

Figure 1 and Table 1 show that the peak extension-flexion angular velocity in the ankle joint was significantly greater than that in the hip and knee joints. During the stance phase, the order of occurrence time of the peak values of joint extension was hip, knee, and ankle joints.

Figure 2 illustrates the torque components acting on the subjects' lower extremity segments. In terms of the intersegmental torque curves of hip, knee, and ankle joints during the maximum-velocity sprint running, during stance phase, the torques affecting the three lower extremity joints were mainly MUS and EXF (Figure 2, MUS, EXF, 0%–17%), while in the swing phase, the torques were primarily MUS and MDT (Figure 2, MUS, MDT, 17%–100%).

Figure 3 demonstrates that the GRF passed through the front of three joints which generated the hip flexor, knee extensor, and dorsiflexion torques.

Figure 4 illustrates that, in a gait of sprinting, the hip, knee, and ankle joint muscles all performed negative work with different extents. When these force-generated muscles performed negative work, the contraction type was eccentric and showed passive contraction. During the stance phase, the positive power of the ankle showed greater value compared with the power of the knee and hip joints.

Table 2 shows that the peak powers of the hip extensors, knee flexors, and ankle plantarflexors were all significantly greater than those of the hip flexors, knee extensors, and ankle dorsiflexors. Moreover, the peak power of the hip extensors was significantly greater during their performance of positive work than negative work. By contrast, the peak powers of the ankle plantarflexors and knee flexors were significantly greater during their performance of negative work than positive work.

### 4. Discussion

**4.1. Stance Phase.** Analysis of all lower extremity joint torques during the stance phase showed that the EXF, which was the ground reaction torque, acting on the hip joint was primarily manifested as hip flexor torque. The hip joint muscle torque was mainly manifested as hip extensor torque. Similarly, the torque generated by the EXF acting on the knee and ankle joints was the knee extensor and dorsiflexion torques. The MUS were mainly manifested as the knee flexor and plantar flexion torques. Thus, the hamstring muscles were under considerable demand, because they served both for knee flexors and hip extensors. Apparently, these muscles were vulnerable to strain during the stance phase of sprinting.

The hip joint continued to perform extension during the entire stance phase (Figure 1, hip). The GRF passed through in the front of the hip joint (Figure 3) during the initial ground contact and generated the EXF that caused the hip flexion (Figure 2, hip, EXF). Meanwhile, the hip extensors performed positive work and generated hip extensor torque (Figure 2, hip, MUS) with peak power as high as  $1106 \pm 231$  W (Figure 4, hip). During this earlier stage, the peak hamstring force across the hip joint can be reasonably estimated based on the MUS values at the hip. Additionally,

TABLE 1: Comparison of peak joint extension-flexion angular velocity ( $v_{pA}$ ) between three joints during a gait circle.

$v_{pA}$ (rad/s)	Hip joint		Knee joint		Ankle joint	
	Extension	Flexion	Extension	Flexion	Plantarflexion	Dorsiflexion
	$9.32 \pm 1.15^*$	$9.95 \pm 1.02^\dagger$	$11.64 \pm 1.11^*$	$9.57 \pm 0.95^\dagger$	$16.20 \pm 1.97$	$11.51 \pm 0.96$

\* $\dagger$ Significantly different from ankle plantarflexion and dorsiflexion, respectively.

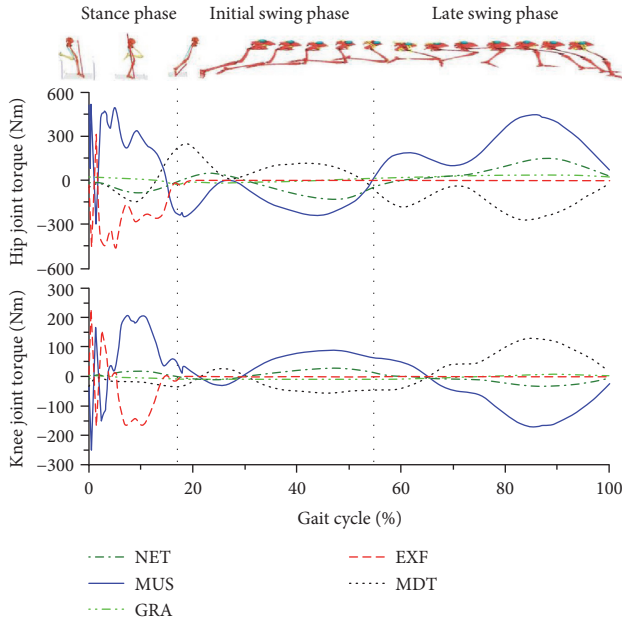


FIGURE 2: Torques of hip and knee joints in a gait cycle. Values on the x-axis represent percentages of total gait time. NET: NET joint torque; MUS: muscle torque; GRA: gravitational torque; EXF: contact torque; MDT: motion-dependent torque.

the hip extensor torque was more than the torque generated by the hip extensor group during the late swing and initial stance phases, but was also a torque buffering the EXF to make the hip joint continue to extend while preventing it from hyperflexion.

Along with the GRF passing through the back of hip joint, the hip extensor torque was produced when the hip flexors performed negative work and a peak muscle power appeared briefly. From this instant until the mid-stance phase, the hip extensors performed positive work, and muscle power was maintained at a greater level with peak power as high as  $2658 \pm 937$  W during the mid-stance phase. The knee extensor torque performed positive work (Figure 4, knee) during the mid- and late stance phases (Figure 2, knee, MUS) to resist the knee flexor torque generated by the GRF to rapidly extend the knee joint with peak power of  $981 \pm 172$  W.

A complex phenomenon occurred during the knee flexion period during the initial stance phase when the knee extensor twice reached its peak values that would have been observed while negative work was performed. This phenomenon would induce great loads to act on the hamstrings along with the loads generated by hip extensors as mentioned above. Meanwhile, the hamstrings also encountered the knee

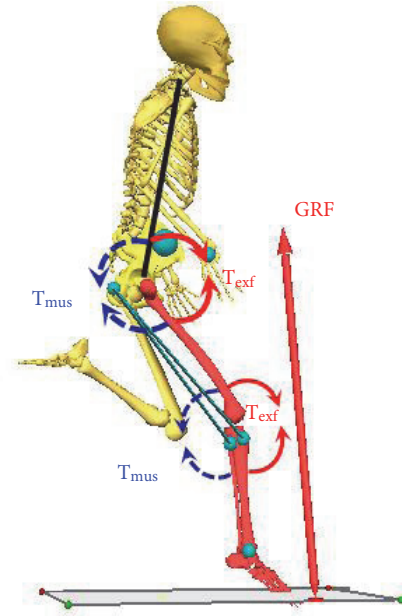


FIGURE 3: Force diagram of human body's initial contact with the ground during maximum-velocity sprint running.  $T_{exf}$ : the torque generated at joints by the GRF acting on the foot;  $T_{mus}$ : the torque generated by muscle contractions.

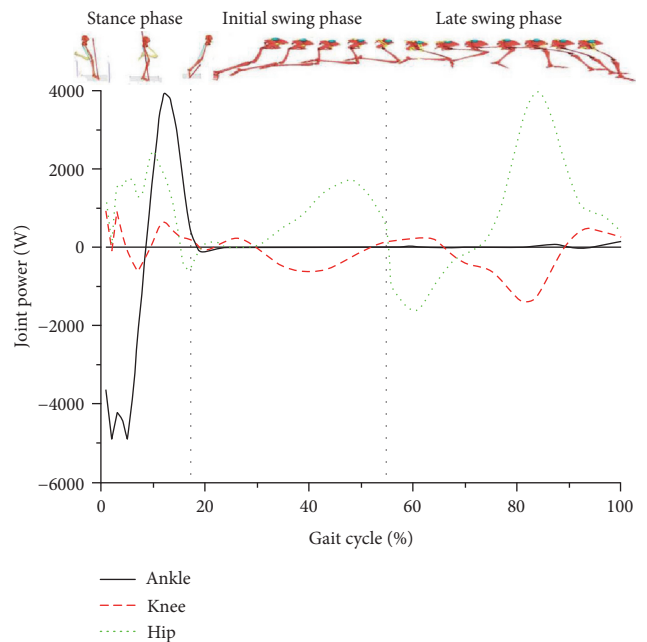


FIGURE 4: Muscle powers of the hip, knee, and ankle joints in a gait cycle.

TABLE 2: Comparison of peak muscle power in the lower extremity muscle groups during a gait circle.

	Hip joint muscle		Knee joint muscle		Ankle joint muscle	
	Extensors	Flexors	Extensors	Flexors	Plantarflexors	Dorsiflexors
Peak positive power (W)	3996 ± 1120* <sup>†</sup>	1735 ± 339	627 ± 113*	1010 ± 208 <sup>†</sup>	3954 ± 673* <sup>†</sup>	135 ± 49
Peak negative power (W)	-1606 ± 781*	-630 ± 108	-655 ± 126*	-1402 ± 372	-4930 ± 933*	-96 ± 25

\*Significantly different from the flexors of identical joint; <sup>†</sup>significantly different from the peak negative power of identical joint muscle (the absolute value).

extensors to generate a large flexor torque (Figure 2, hip and knee, MUS), which further indicates a high strain injury risk exists with loadings induced by both active hip extension and knee flexion during the initial stance phase (Figure 3).

During the push-off, the MUS (knee extensor torque) and power values decreased rapidly and were maintained at low level (Figure 2, knee, MUS). The muscle power of the knee joint was also lower than that of the other joints, because of its lower angular velocity during the stance phase. The angular velocity of the knee joint was lower than that of the other joints as shown by the curves of joint angular velocity and muscle power during the entire stance phase. Therefore, the power value of knee joint muscle groups was lower during the entire stance phase and considerably lower than that of the hip and ankle joint muscle groups. This result coincides with the findings of Bezodis et al. [5]. We believed that the major function of knee joint was to maintain the height of the human body's center of mass and to deliver energy from the hip joint to the ankle joint. Although Johnson also drew a similar conclusion [16], the findings were relatively different. Johnson showed that the muscle power of the knee joint was quite low during the initial stance phase and reached greater power in the mid-stance phase with a peak of 1544 ± 512 W. However, muscle power continued to decline until the foot was off the ground. The discrepancies in the findings might be due to the distinct focus and the acceleration phase of the sprint in Johnson's study.

For the ankle joint torque, the major torque acting on ankle joint was the EXF and MUS, which existed primarily during the stance phase (Figure 2, ankle). As the GRF passed in front of the ankle joint throughout, the contact torque was dorsiflexion torque all along (Figure 2, ankle, EXF). Moreover, the ankle joint muscle group appeared merely as plantar flexion torque during the stance phase to resist the contact torque that made the ankle dorsiflexion. During the initial stance phase, the plantar flexors performed negative work to absorb the GRF and generated the energy for the plantar flexion of ankle with peak power of 4930 ± 933 W. When entering the mid-stance phase, the plantar flexors were transformed from eccentric contraction (doing negative work) into concentric contraction (doing positive work) and pushed the body into the swing phase. During this process, the ankle plantar flexors were experiencing the stretch-shortening cycle and stored great amount of elastic energy prior to shortening, which was advantageous in the driving force supply and power output during the strike-stretch phase [29].

During the stance phase, the major torques acting on lower extremity joint torques were the MUS and EXF. The function of the lower extremity muscle groups was mainly

to resist the contact torques generated by the GRF around the joints and to output positive work for power supply to maintain the velocity during the maximum-velocity phase [29]. However, the loads on the hamstring muscles were considerable, because they served both roles of the knee flexors and the hip extensors to counteract this effect of GRF. Furthermore, the anatomical structure of skeletal muscle linking the single joint to double-jointed joints of the lower limbs was advantageous in transmitting muscle power from the big joints to small joints (from proximal ends to distal ends). When viewing the peak angular velocity and peak muscle power of each joint during the stance phase sprinting, the peak angular velocity and peak extensor positive power appeared in turn from the proximal to distal joints. Meanwhile, during the stance phase, the peak angular velocity and peak muscle power of the ankle were significantly greater than those of the other joints. This result demonstrates that the elite athletes well delivered the hip joint muscle energy to the ankle joint to increase the capability of the ankle joint acting to the ground and better maintain velocity.

**4.2. Swing Phase.** During the swing phase, the primary hip joint MUS were in sequence as the hip flexor and hip extensor torques, while the dominant knee joint MUS manifested in sequence as the knee extensor and flexor torques. In terms of the sprint swing skills with the hip joint center served as an axis, the key of the swing velocity was the rapid flexion of the knee after toe-off as well as the COM acceleration and angular acceleration of the swing leg. Previous studies demonstrated that the muscle groups affecting the folding angle of the thigh and shank (the knee flexion) were the joint muscles, such as the biceps femoris long head, semitendinosus muscle, and semimembranosus, which were responsible for the dual duties of hip extension and knee flexion. When folding started in the initial swing phase, the hip joint was still at an extended status such that these joint muscles were kept at a greater level of activation, resulting in an active insufficiency of knee flexion [1]. Through quantifying the MUS and MDT, the knee flexor torque (Figure 2, knee, MDT) was found to be the major MDT acting on the knee joint during the initial swing phase. The MDTs, not the knee flexors (hamstrings), mainly contributed energy to make the shank fold. The primary MUS was the muscle extensor torque that performed negative work (Figure 4, knee) to control the movements and decelerate the knee flexion motion.

The MUS was manifested as the hip extensor torque which tensed the hamstring almost throughout the entire late swing phase to resist the MDT of the hip flexion (Figure 2, Hip, MDT), decelerate the hip joint flexion, and enter the next step of rapid pressing (hip extension) of the

swing leg (Figure 2, hip, MUS). The hip extensors are shown in Figure 4 (hip) as a sequence of the antagonist (eccentric contraction) and agonist (concentric contraction) that performed negative and positive works, respectively, for the hip movements. The hip extensors, mainly for hamstring muscles, during the late swing phase showed peak positive and negative powers at  $3996 \pm 1120$  and  $-1606 \pm 781$  W, respectively. Meanwhile, the knee flexors, including hamstring muscles, mainly manifested as muscle flexor torques in resisting the MDT by knee extension, and these muscles were performing negative work at this moment to decelerate the knee extension movement and transit to the stance phase. At this point, the knee joint muscle groups reached their peak power at  $-2104 \pm 572$  W. Therefore, the late swing phase of a sprint gait appeared to be the risk period when a hamstring strain would easily occur. These findings were in accordance with the previous studies of Thelen et al. [25], Chumanov et al. [30], and Yu et al. [31].

The major joint torques acting on the lower extremity joints during the swing phase were mainly the MUS and MDT. The inertial torque was the key factor in affecting the MUS, which was a major driving force for the movements of the thigh and shank. Under many circumstances, the MUS performed negative work to control movements. The effects of the ankle joint torques and muscle power on the lower extremity movements are quite limited because they are remarkably low during the swing phase.

## 5. Conclusion

The external and motion-dependent forces (e.g., inertial forces, Coriolis force, and concentric force) that acted on each segment of the human body had vital effects on the function of joint muscle groups during sprinting. During the stance phase, torque produced and work performed by the hip and knee muscles were generally used to counteract GRF. During the swing phase, the role of MUS changed to mainly counteract the effect of MDT to control the movement direction of the lower extremity. Meanwhile, during the initial stance and late swing phases, the passive torques, that is, EXF and MDT produced by GRF and the inertial movement of the segments of the lower extremity, applied greater stress to the hamstring muscles, which put these muscles at a higher risk of strains.

## Conflicts of Interest

The authors declare no conflict of interest in this manuscript.

## Acknowledgments

This study was supported by the National Natural Science Foundation of China (81572213, 11302131). The authors thank Dr. Ying Fang (Worcester Polytechnic Institute, US) for her helpful comments and suggestions.

## References

- [1] R. V. Mann, "A kinetic analysis of sprinting," *Medicine and Science in Sports and Exercise*, vol. 13, no. 5, pp. 325–328, 1981.
- [2] J. B. Morin, J. Slawinski, S. Dorel et al., "Acceleration capability in elite sprinters and ground impulse: push more, brake less?" *Journal of Biomechanics*, vol. 48, no. 12, pp. 3149–3154, 2015.
- [3] V. Vardaxis and T. B. Hoshizaki, "Power patterns of the leg during the recovery phase of the sprinting stride for advanced and intermediate sprinters," *International Journal of Sport Biomechanics*, vol. 5, no. 3, pp. 332–349, 1989.
- [4] J. Mendiguchia, P. Samozino, E. Martinez-Ruiz et al., "Progression of mechanical properties during on-field sprint running after returning to sports from a hamstring muscle injury in soccer players," *International Journal of Sports Medicine*, vol. 35, no. 8, pp. 690–695, 2014.
- [5] I. N. Bezodis, D. G. Kerwin, and A. I. T. Salo, "Lower-limb mechanics during the support phase of maximum-velocity sprint running," *Medicine and Science in Sports and Exercise*, vol. 40, no. 4, pp. 707–715, 2008.
- [6] J. P. Hunter, R. N. Marshall, and P. McNair, "Reliability of biomechanical variables of sprint running," *Medicine and Science in Sports and Exercise*, vol. 36, no. 5, pp. 850–861, 2004.
- [7] J. P. Hunter, R. N. Marshall, and P. J. McNair, "Segment-interaction analysis of the stance limb in sprint running," *Journal of Biomechanics*, vol. 37, no. 9, pp. 1439–1446, 2004.
- [8] R. Mann and P. Sprague, "A kinetic analysis of the ground leg during sprint running," *Research Quarterly for Exercise and Sport*, vol. 51, no. 2, pp. 334–348, 1980.
- [9] M. G. Hoy and R. F. Zernicke, "Modulation of limb dynamics in the swing phase of locomotion," *Journal of Biomechanics*, vol. 18, no. 1, pp. 49–60, 1985.
- [10] L. Charalambous, G. Irwin, I. N. Bezodis, and D. Kerwin, "Lower limb joint kinetics and ankle joint stiffness in the sprint start push-off," *Journal of Sports Sciences*, vol. 30, no. 1, pp. 1–9, 2012.
- [11] J. Slawinski, A. Bonnefoy, J.-M. Levêque et al., "Kinematic and kinetic comparisons of elite and well-trained sprinters during sprint start," *Journal of Strength and Conditioning Research*, vol. 24, no. 4, pp. 896–905, 2010.
- [12] J. Slawinski, A. Bonnefoy, G. Ontanon et al., "Segment-interaction in sprint start: analysis of 3D angular velocity and kinetic energy in elite sprinters," *Journal of Biomechanics*, vol. 43, no. 8, pp. 1494–1502, 2010.
- [13] M. Otsuka, J. K. Shim, T. Kurihara, S. Yoshioka, M. Nokata, and T. Isaka, "Effect of expertise on 3D force application during the starting block phase and subsequent steps in sprint running," *Journal of Applied Biomechanics*, vol. 30, no. 3, pp. 390–400, 2014.
- [14] G. Rabita, S. Dorel, J. Slawinski et al., "Sprint mechanics in world-class athletes: a new insight into the limits of human locomotion," *Scandinavian Journal of Medicine and Science in Sports*, vol. 25, no. 5, pp. 583–594, 2015.
- [15] R. Jacobs and G. J. van Ingen Schenau, "Intermuscular coordination in a sprint push-off," *Journal of Biomechanics*, vol. 25, no. 9, pp. 953–965, 1992.
- [16] M. D. Johnson and J. G. Buckley, "Muscle power patterns in the mid-acceleration phase of sprinting," *Journal of Sports Sciences*, vol. 19, no. 4, pp. 263–272, 2001.
- [17] R. G. Lockie, A. J. Murphy, A. B. Schultz, T. J. Knight, and X. A. K. Janse de Jonge, "The effects of different speed

- training protocols on sprint acceleration kinematics and muscle strength and power in field sport athletes,” *Journal of Strength and Conditioning Research*, vol. 26, no. 6, pp. 1539–1550, 2012.
- [18] A. Mero, S. Kuitunen, M. Harland, H. Kyröläinen, and P. V. Komi, “Effects of muscle-tendon length on joint moment and power during sprint starts,” *Journal of Sports Sciences*, vol. 24, no. 2, pp. 165–173, 2006.
- [19] A. G. Schache, N. A. Brown, and M. G. Pandy, “Modulation of work and power by the human lower-limb joints with increasing steady-state locomotion speed,” *Journal of Experimental Biology*, vol. 218, Part 15, pp. 2472–2481, 2015.
- [20] H. Liu, W. E. Garrett, C. T. Moorman, and B. Yu, “Injury rate, mechanism, and risk factors of hamstring strain injuries in sports: a review of the literature,” *Journal of Sport and Health Science*, vol. 1, no. 2, pp. 92–101, 2012.
- [21] T. Ono, A. Higashihara, J. Shinohara, N. Hirose, and T. Fukubayashi, “Estimation of tensile force in the hamstring muscles during overground sprinting,” *International Journal of Sports Medicine*, vol. 36, no. 2, pp. 163–168, 2015.
- [22] Y. Sun, S. Wei, Y. Zhong, W. Fu, L. Li, and Y. Liu, “How joint torques affect hamstring injury risk in sprinting swing-stance transition,” *Medicine and Science in Sports and Exercise*, vol. 47, no. 2, pp. 373–380, 2015.
- [23] A. G. Schache, T. V. Wrigley, R. Baker, and M. G. Pandy, “Biomechanical response to hamstring muscle strain injury,” *Gait & Posture*, vol. 29, no. 2, pp. 332–338, 2009.
- [24] J. B. Morin, P. Gimenez, P. Edouard et al., “Sprint acceleration mechanics: the major role of hamstrings in horizontal force production,” *Frontiers in Physiology*, vol. 6, p. 404, 2015.
- [25] D. G. Thelen, E. S. Chumanov, D. M. Hoerth et al., “Hamstring muscle kinematics during treadmill sprinting,” *Medicine and Science in Sports and Exercise*, vol. 37, no. 1, pp. 108–114, 2005.
- [26] R. F. Zernicke and K. Schneider, “Biomechanics and developmental neuromotor control,” *Child Development*, vol. 64, no. 4, pp. 982–1004, 1993.
- [27] L. Huang, Y. Liu, S. Wei et al., “Segment-interaction and its relevance to the control of movement during sprinting,” *Journal of Biomechanics*, vol. 46, no. 12, pp. 2018–2023, 2013.
- [28] B. Yu, D. Gabriel, L. Noble, and K.-N. An, “Estimate of the optimum cutoff frequency for the butterworth low-pass digital filter,” *Journal of Applied Biomechanics*, vol. 15, no. 3, pp. 318–329, 1999.
- [29] R. Jacobs, M. F. Bobbert, and G. J. van Ingen Schenau, “Mechanical output from individual muscles during explosive leg extensions: the role of biarticular muscles,” *Journal of Biomechanics*, vol. 29, no. 4, pp. 513–523, 1996.
- [30] E. S. Chumanov, B. C. Heiderscheit, and D. G. Thelen, “The effect of speed and influence of individual muscles on hamstring mechanics during the swing phase of sprinting,” *Journal of Biomechanics*, vol. 40, no. 16, pp. 3555–3562, 2007.
- [31] B. Yu, R. M. Queen, A. N. Abbey, Y. Liu, C. T. Moorman, and W. E. Garrett, “Hamstring muscle kinematics and activation during overground sprinting,” *Journal of Biomechanics*, vol. 41, no. 15, pp. 3121–3126, 2008.

## Research Article

# Effects of Two Fatigue Protocols on Impact Forces and Lower Extremity Kinematics during Drop Landings: Implications for Noncontact Anterior Cruciate Ligament Injury

Rui Xia,<sup>1</sup> Xini Zhang,<sup>1</sup> Xi Wang,<sup>1</sup> Xiaole Sun,<sup>1</sup> and Weijie Fu<sup>1,2</sup>

<sup>1</sup>School of Kinesiology, Shanghai University of Sport, Shanghai 200438, China

<sup>2</sup>Key Laboratory of Exercise and Health Sciences of Ministry of Education, Shanghai University of Sport, Shanghai 200438, China

Correspondence should be addressed to Weijie Fu; fuweijie@sus.edu.cn

Received 23 February 2017; Revised 24 April 2017; Accepted 30 April 2017; Published 12 July 2017

Academic Editor: Wenxin Niu

Copyright © 2017 Rui Xia et al. This is an open access article distributed under the Creative Commons Attribution License, which permits unrestricted use, distribution, and reproduction in any medium, provided the original work is properly cited.

The purpose of the study was to determine the effects of fatigue on the impact forces and sagittal plane kinematics of the lower extremities in a drop landing task. 15 male collegiate athletes were recruited. Five successful trials of a drop landing task were obtained during pre-fatigue and post-fatigue in two fatigue protocols (constant speed running fatigue protocol [R-FP] and shuttle running + vertical jumping fatigue protocol [SV-FP]). Duration time, maximal heart rate, and RPE of each protocol were measured separately. Kinematic measures of the hip, knee, and ankle joints at different times coupled with peak impact force and loading rate were acquired. Our results showed a more flexed landing posture due to an increase in hip and knee flexion angles in the post-fatigue condition. However, no differences in peak impact force and loading rate were found between pre- and post-fatigue conditions. The changes were similar between protocols, but the SV-FP showed a significantly shorter exercise duration time than the R-FP. Fatigued athletes in this study demonstrated altered motor control strategies during a drop landing task, which may be an intentional or unintentional protective strategy for preventing themselves from potential ACL injury.

## 1. Introduction

Exercise is vital for maintaining health and wellness [1–3]. Nevertheless, physical activity may also cause sport-related injuries, which may be responsible for reduced athletic performance and even lead to sport cessation for long periods [4]. About 200 thousands of anterior cruciate ligament (ACL) injuries occur in the US every year [5]. Meanwhile, the lower extremities pose greater potential risk than the upper extremities [4].

Landing is a common maneuver in sports activities, especially for sport events based on running and jumping, which can reflect the control ability of the neuromuscular system [6]. The human body needs to reduce the possible adverse effects of impact during landing, which can reach up to 10 times the body weight, by adjusting landing posture [7]. One can adjust his/her landing posture to reduce the impact force upon ground contact [8]. An average of 5.2°, 5.8°, and 3.3° greater joint flexion has been found in the hip, knee,

and ankle, respectively, at the touchdown phase of drop landing (DL) [9]. However, with prolonged exercise, the human body will produce a temporary reduction in the ability of exercise called sport fatigue, which is an extrinsic factor affecting the neuromusculoskeletal system [10]. These changes are believed to increase the incidence of sport injuries represented by ACL injury [11].

Previous studies have suggested that the excitability of the central nervous system gradually decreases with the development of fatigue, resulting in loss of proprioception [12], delay of the musculoskeletal response [11], change in biomechanical characteristics, and negative effects on motor control [13]. Borowski et al. and Podraza and White found that landing in a fatigued condition results in high impact forces (stiff landing), as well as force transmission, which are the main causes of sports injuries [14, 15]. However, previous studies on the effects of fatigue during landing activities have demonstrated different responses in ground reaction force (GRF) characteristics [16–19]. Smith et al. and Kellis

and Kouveliod found a decrease in peak GRF under fatigued conditions during DL [16, 17], but no differences were observed in peak GRF between nonfatigued and fatigued conditions during the same landing task [18, 19]. The causes of these different responses are multifactorial. One explanation is the difference in fatigue protocols applied in the studies. Current research has mainly focused on either short- or long-term fatigue protocols [20]. The former includes continuous vertical jumps and/or followed by short-distance sprints [10], ~50% 1 RM pedal exercise of the lower limbs [21], and single-leg squats [22], whereas the latter mainly induces fatigue through long-term treadmill running or cycling [20, 22]. Although former studies have shown that the fatigue-induced protocol can affect the landing strategy of the lower extremities, a unified conclusion on the biomechanical alterations caused by the inconsistency of fatigue protocols is rare [20–22].

Collectively, the abovementioned studies investigated the effects of fatigue on the landing strategy of the lower extremity, including kinematics, GRFs, and other biomechanical variables. However, a large inconsistency in the results of kinematics and impact characteristics under a fatigued condition makes it difficult to extract how fatigue contributes to these biomechanical characteristics. Therefore, more studies should be implemented to further explore the biomechanical differences between different fatigue protocols and seek a better fatigue protocol for specific use.

Based on the above consideration, the purpose of this paper is to determine the effects of fatigue on the impact forces and sagittal plane kinematics of the lower extremities of recreational athletes in a DL task. In addition, the biomechanical differences between two fatigue protocols (constant speed running fatigue protocol [R-FP] and shuttle running + vertical jumping fatigue protocol [SV-FP]) were determined by measuring various kinematic and GRF variables to further provide a preliminary reference for the selection of fatigue protocols in laboratory tests. We hypothesized that fatigue would negatively affect the landing biomechanics of the lower extremities. Specifically, participants would have smaller joint flexion angles and range of motion (RoM) in the hip, knee, and ankle joints and a greater peak impact force/loading rate (LR) under a nonfatigued condition compared with a fatigued condition during landing. Furthermore, the abovementioned changes would differ between the two fatigue protocols.

## 2. Methods

**2.1. Participants.** Fifteen trained male volunteers with an average of 4.2 years of experience in jumping events (age:  $20.9 \pm 0.8$  years; height:  $175.5 \pm 4.2$  cm; mass:  $68.9 \pm 5.5$  kg) were recruited in this study. All participants had no known musculoskeletal injuries of the lower extremities in the previous 6 months and did not engage in strenuous exercises within 24 h prior to the study. The sample size of 15 was determined through a G-power statistical calculation with a power level of 80% and an  $\alpha$  level of 0.05 [20]. All participants signed an informed consent form, and the study followed the guidelines of the Declaration of Helsinki and

was approved by the Institutional Review Board of Shanghai University of Sport.

**2.2. Experiment Procedure.** Participants wore a spandex outfit and traditional shoes without a cushioning insole (WD-2A, Warrior, Shanghai, China). For warm-up, 5 min of jogging on the treadmill at 2.5 m/s followed by 3 min of static stretching exercise was required for each participant. After the bipedal DL task was demonstrated and explained, the participants were given practice time to become familiar with the DL task before the formal experiment. During each trial, the participants were asked to perform a bilateral DL from a 60 cm platform [23, 24] as naturally as possible with a toe-heel touchdown and then recover to an upright position (Figure 1). A successful trial was recognized when the participants' landing was completely on both force plates with each foot separately without losing their balance. A 1 min resting interval was allowed between trials to minimize fatigue during pre-fatigue assessment. After completing five successful DL trials, the participants were required to conduct either of the two fatigue protocols. The order of the protocols was randomized using a random number allocation table. Two fatigue protocols were counterbalanced with a 1-week break, which was applied to ensure that fatigue was eliminated and each protocol's effect would not affect each other.

### 2.3. Fatigue Protocol

**2.3.1. Constant Speed Running Fatigue Protocol (R-FP).** The participants were required to run on the treadmill at 4 m/s until they reached a state of volitional fatigue and could not continue running [20, 25]. The treadmill was then slowed down to walking speed for 1 min before the postfatigue DL task was implemented. The participants were considered to have reached a fatigued state [20] and the intervention was terminated when the following two criteria were met: (1) the heart rate (HR) of the participant reached 90% of his age-calculated maximum at least and (2) the participant could not continue running.

**2.3.2. Shuttle Running + Vertical Jumping Fatigue Protocol (SV-FP).** The maximal vertical jump height of each participant was measured before conducting the SV-FP. The SV-FP involved combinations of five consecutive vertical jumps within a height above 70% of their maximal vertical jump height followed by a set of shuttle sprints ( $6 \times 10$  m) with their maximal effort [26]. The participants were required to repeat the above procedure until the maximal height within five consecutive vertical jumps was below 70% of their maximal vertical jump height.

**2.4. Data Collection.** Sagittal kinematic data of the dominant leg (defined as preferred kicking leg) [27] were collected at a sampling rate of 240 Hz using a 16-camera infrared three-dimensional (3D) motion capture system (Vicon T40, Oxford Metrics, UK). A total of 36 retroreflective markers (14.0 mm diameter) comprising the plug-in gait marker set were attached to the lower limb to define the hip, knee, and ankle joints (Figure 1). GRF data were captured at a sampling rate of 1200 Hz using two  $90 \times 60$  cm force plates (9287B,

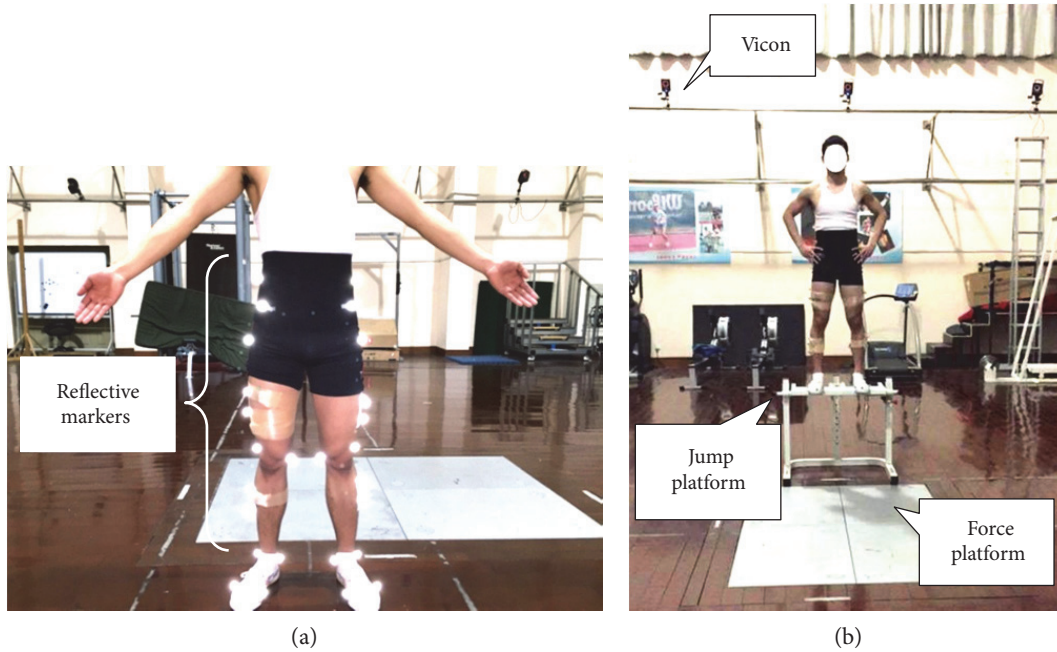


FIGURE 1: Set of reflective markers used in the study (a) and the experimental setup: a landing from a 60 cm platform (b).

Kistler Corporation, Switzerland) flushed with the surrounding floor. The force and 3D kinematic data were collected and synchronized using the Vicon system. The maximum vertical jump height of each participant was acquired via the Quattro Jump force plate (9290BD, Kistler Corporation, Switzerland). It was also employed to monitor the vertical jump height when the SV-FP was implemented. HR was monitored by a HR transmitter belt monitor (SS020674000, Suunto Oy, Finland) attached to the participants' chest during the entire procedure of inducing fatigue, and the maximal HR was recorded. The Borg 15-category rating of perceived exertion (RPE) scale, which served as an auxiliary indicator, was used to evaluate the exertion degree immediately after each fatigue protocol was completed.

## 2.5. Data Reduction

**2.5.1. Impact Forces.** A representative vertical GRF (vGRF)—time curve during the landing phase of DL from a 60 cm height—is presented in Figure 2. The impact phase in this study was defined as the time interval from initial foot contact to the maximum of the vGRF. The main variables of interest during the impact phase included (1) the peak vGRF normalized to body mass ( $F_{Zmax}$ ), (2) the time from contact to  $F_{Zmax}$  ( $t_F$ ), (3) the peak LR normalized to body mass ( $G_{Zmax}$ ; determined by the maximum slope of adjacent points of vGRF, which was calculated using the following equation:  $G = \lim_{\Delta t \rightarrow 0} \Delta F / \Delta t$ ), and (4) the time from contact to  $G_{Zmax}$  ( $t_G$ ).

**2.5.2. Sagittal Plane Kinematics.** The 3D coordinates of the reflective markers of the dominant leg were filtered through a Butterworth fourth-order, zero-lag, low-pass filter at a cut-off frequency of 7 Hz via Visual 3D software (4.00.20,

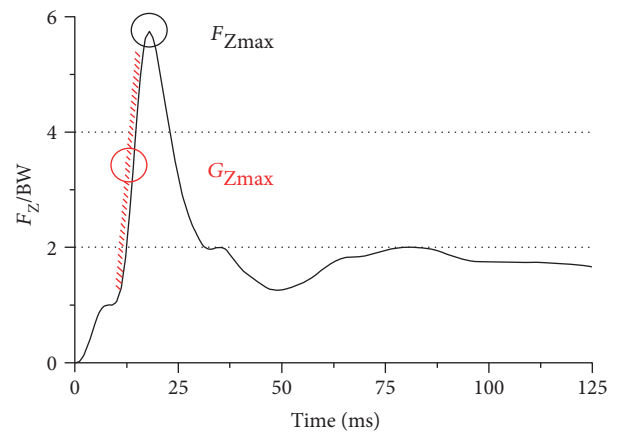


FIGURE 2: Schematic diagram of peak vGRF normalized to body mass ( $F_{Zmax}$ ) and peak loading rate normalized to body mass ( $G_{max}$ ) during landing.

C-Motion Inc., USA) [28]. The dominant leg was defined as the preferred leg when kicking a soccer ball [20]. The landing phase in this study was defined as the time interval from initial foot contact to maximum knee flexion. The main sagittal kinematic variables of the hip, knee, and ankle joints during the landing phase included (1) the initial contact angle ( $\theta_0$ ), (2) the minimal joint angle ( $\theta_{min}$ ) and the occurrence time of  $\theta_{min}$  ( $t_{\theta_{min}}$ ), (3) the maximal joint angular velocity ( $\omega_{max}$ ), and (4) joint RoM. The definition of the sagittal plane angle of the hip ( $\theta_h$ ), knee ( $\theta_k$ ), and ankle ( $\theta_a$ ) joints is presented in Figure 3. The RoM of the hip ( $\Delta\theta_h$ ), knee ( $\Delta\theta_k$ ), and ankle joints ( $\Delta\theta_a$ ) were determined by calculating the difference between the maximum and minimum angles of these three joints separately during the landing

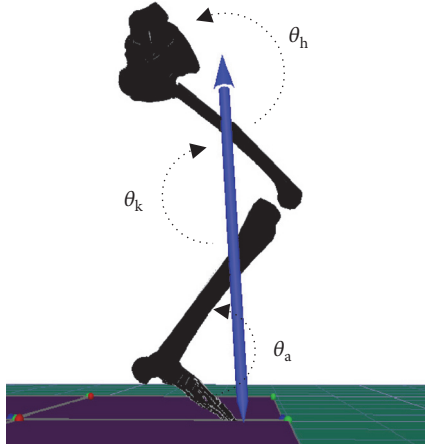


FIGURE 3: Schematic for the definition of hip, knee, and ankle joint angles in the sagittal plane during landing of the subject.

TABLE 1: Comparison of intervention effects for constant speed running fatigue protocol (R-FP) and shuttle running + vertical jumping fatigue protocol (SV-FP).

Variables	R-FP	SV-FP
Duration time/s	1126.5 ± 344.6	257.8 ± 59.3*
Maximal HR/min	189.4 ± 6.9	184.7 ± 6.3
RPE	16.3 ± 1.3	16.7 ± 1.4

\*Significantly different from R-FP with  $p < 0.05$ .

phase. The data of 5 successful trials were averaged to minimize errors.

**2.6. Statistics.** A  $2 \times 2$  (fatigue  $\times$  protocol) repeated measures ANOVA was performed to examine the effect of fatigue and fatigue-induced protocols on impact forces and sagittal plane kinematics. Tukey post hoc tests were performed when a significant interaction effect was observed. Paired  $t$ -tests were used to compare paired changes in the intervention time, maximal HR, and RPE of using two different fatigue protocols (21.0, SPSS Inc., Chicago, IL, USA). The significance level was set at  $\alpha = 0.05$ .

### 3. Results

**3.1. Fatigue-Induced Intervention Effects.** For the intervention effects, no significant differences were observed in maximal HR and RPE between R-FP and SV-FP conditions. However, the SV-FP showed a significantly shorter exercise duration time than the R-FP (Table 1).

**3.2. Impact Forces.** No significant interaction was observed for both  $F_{Zmax}$  and  $t_F$  and  $G_{Zmax}$  and  $t_G$  between fatigue conditions and fatigue protocols. The ANOVA results showed no main effects of a fatigue condition or fatigue protocols for all impact variables during the landing phase (Table 2).

**3.3. Sagittal Plane Kinematics.** No significant interaction was found in sagittal plane kinematics except the RoM of the knee joint ( $p = 0.048$ ). However, a significant effect was associated

with fatigue for the hip and knee joints in both R-FP and SV-FP. Specifically, for the joint angle, the  $\theta_{min}$  values for both the hip ( $p = 0.001$ ) and knee joints ( $p = 0.001$ ) generally decreased, whereas  $t_{\theta_{min}}$  of these two joints ( $p = 0.003$  for hip and  $p = 0.002$  for knee, resp.) increased under a fatigued condition for both R-FP and SV-FP during the landing phase (Table 3 and Figure 4).

In addition, the RoM of the hip ( $p < 0.001$ ) and knee ( $p < 0.001$ ) joints within a fatigued condition increased compared with that in a nonfatigued condition for both fatigue protocols. For the joint angular velocity,  $\omega_{max}$  for the hip joint within a fatigued condition for the two fatigue protocols showed a significant increase ( $p = 0.010$ , Figure 5). Besides, no significant differences in ankle joint kinematics were found for both the fatigue conditions and protocols.

## 4. Discussion

We evaluated the effects of fatigue on lower extremity biomechanics during a DL task in male recreational athletes. We hypothesized that fatigue would negatively affect the landing biomechanics of the lower extremities (e.g., alterations in the hip, knee, and ankle sagittal kinematics) and induce a greater impact force and LR. One of the main results showed a decrease in  $\theta_{min}$  of the hip and knee joints with an increase in the RoM of these joints under a fatigue condition induced by the two protocols. In other words, hip and knee flexion increased under a fatigue condition. Meanwhile, the occurrence time of  $\theta_{min}$  of both the hip and knee joints also significantly increased. However, no significant differences were found in impact forces (i.e., peak vertical GRF and peak LR) during landings between nonfatigued and fatigued conditions, which did not support our hypothesis. Furthermore, we evaluated the effects of two fatigue protocols (R-FP and SV-FP) on the biomechanics of the lower extremities. We hypothesized that the aforementioned changes between the two fatigue protocols under a fatigued condition would differ. Although no differences were found between the R-FP and SV-FP for the effect of fatigue on these biomechanical characteristics during landing, we found that the time duration of the SV-FP was significantly less than that of the R-FP, and the maximal HR/min and RPE for these two protocols were similar. Collectively, the participants showed a more flexed landing posture but not GRF after fatigue, and no differences were presented between the protocols other than time duration of the intervention.

The GRF and LR are commonly used parameters of the external load applied to the musculoskeletal system in biomechanical studies [29]. The LR, acting as a derivative of GRF, can evaluate how fast the GRF rises to its impact peak [30]. From a biomechanical perspective, prolonged exercise can lead to muscle fatigue, which will reduce the ability of posture control to affect collisions at the touchdown phase with the ground [11]. ACL injury during the landing process is usually caused by the lack of proper management of a collision because of neuromuscular fatigue [8]. However, our results showed no significant differences in both the peak GRF and peak LR between the pre- and postfatigue conditions during DL. These results support the findings of James

TABLE 2: Comparison of the peak vGRF ( $F_{Z_{max}}$ ), the peak loading rate ( $G_{max}$ ), and the occurrence times of  $F_{Z_{max}}$  and  $G_{max}$  during landings between pre- and postfatigue test within different fatigue-induced protocols (R-FP and SV-FP).

Variables	R-FP		SV-FP	
	Prefatigue	Postfatigue	Prefatigue	Postfatigue
$F_{Z_{max}}/BW$	$5.8 \pm 0.9$	$5.8 \pm 1.0$	$6.0 \pm 0.8$	$5.9 \pm 0.9$
$t_F/ms$	$29.0 \pm 9.4$	$26.3 \pm 11.0$	$24.4 \pm 11.5$	$25.5 \pm 10.2$
$G_{max}/(BW/s)$	$1037.6 \pm 225.7$	$1053.7 \pm 209.0$	$1086.4 \pm 253.4$	$1076.7 \pm 200.1$
$t_G/ms$	$25.8 \pm 9.6$	$23.2 \pm 11.0$	$21.4 \pm 11.7$	$22.6 \pm 10.4$

TABLE 3: Comparison of the joint angle and angular velocity of lower extremities in the sagittal plane during landings between pre- and postfatigue conditions within different fatigue-induced protocols (R-FP and SV-FP; \* $p < 0.05$ ).

Joints	Variables	R-FP		SV-FP	
		Prefatigue	Postfatigue	Prefatigue	Postfatigue
Hip	$\theta_{min}/(^{\circ})$	$93.9 \pm 26.0$	$85.0 \pm 28.0^*$	$87.8 \pm 20.5$	$80.4 \pm 21.5^*$
	$t_{\theta_{min}}/ms$	$221.1 \pm 75.2$	$246.0 \pm 73.4^*$	$228.1 \pm 57.6$	$251.3 \pm 58.6^*$
	$\theta_0/(^{\circ})$	$142.4 \pm 10.2$	$138.7 \pm 11.9$	$139.2 \pm 10.7$	$139.0 \pm 10.0$
	$\Delta\theta/(^{\circ})$	$48.5 \pm 17.9$	$53.7 \pm 17.5^*$	$50.4 \pm 14.2$	$58.6 \pm 15.8^*$
	$\omega_{max}/(^{\circ}/s)$	$449.2 \pm 95.1$	$469.6 \pm 74.1^*$	$468.7 \pm 79.4$	$490.0 \pm 77.1^*$
Knee	$\theta_{min}/(^{\circ})$	$85.6 \pm 19.8$	$80.4 \pm 22.0^*$	$83.3 \pm 16.9$	$75.5 \pm 17.6^*$
	$t_{\theta_{min}}/ms$	$226.4 \pm 74.0$	$253.9 \pm 67.7^*$	$231.6 \pm 60.6$	$253.8 \pm 58.4^*$
	$\theta_0/(^{\circ})$	$159.4 \pm 7.7$	$158.1 \pm 8.0$	$156.8 \pm 6.6$	$159.2 \pm 6.8$
	$\Delta\theta/(^{\circ})$	$73.8 \pm 14.9$	$78.9 \pm 15.9^*$	$73.6 \pm 13.4$	$83.7 \pm 13.5^*$
	$\omega_{max}/(^{\circ}/s)$	$769.4 \pm 72.6$	$750.2 \pm 75.1$	$767.1 \pm 63.7$	$809.1 \pm 56.5$
Ankle	$\theta_{min}/(^{\circ})$	$79.1 \pm 4.4$	$80.6 \pm 4.5$	$82.1 \pm 4.6$	$81.1 \pm 5.5$
	$t_{\theta_{min}}/ms$	$212.8 \pm 72.1$	$242.2 \pm 62.0$	$218.9 \pm 51.1$	$226.9 \pm 52.5$
	$\theta_0/(^{\circ})$	$123.3 \pm 10.2$	$120.8 \pm 10.2$	$119.9 \pm 10.8$	$121.5 \pm 9.6$
	$\Delta\theta/(^{\circ})$	$44.2 \pm 9.0$	$40.2 \pm 9.5$	$37.9 \pm 9.8$	$40.4 \pm 9.6$
	$\omega_{max}/(^{\circ}/s)$	$596.9 \pm 165.7$	$515.8 \pm 197.0$	$503.9 \pm 205.8$	$530.1 \pm 181.1$

et al. who reported no significant changes in the peak vertical GRF and average LR to the peak force after fatigue during a step-off landing task using an isometric squatting fatigue protocol with maximal effort; thus, no significant changes were observed in the GRF variables with fatigue [19]. One of the plausible explanations from the above study is the body's changing ability in managing the collision with ground with the development of muscle fatigue but not in an exhausted condition. To be consistent with the landing mode under a pre-fatigue condition, appropriate control of the landing posture is required as a protective behavior in terms of maintaining the impact force and LR [30]. However, James et al. also found a greater peak GRF/LR during a DL task using the fatigue protocol of stretch shortening cycle exercise [18]. Therefore, whether the characteristics of the GRF/LR would change with the development of fatigue still needs further investigation.

The characteristics of the GRF/LR may be related to variations between the fatigue protocols. In Kellis and Kouveliod's study, the changes in the peak impact force were different between the two fatigue protocols under a postfatigue condition, suggesting that landing performance is related to fatigue from a specific muscle group (agonist versus antagonist) [17]. However, in other studies [19, 31], no differences

were found in a peak LR between the two protocols under a postfatigue condition during the DL task, and this observation was similar to the results of the current study. In general, for an anticipated movement, such as DL, a pre-designed neuromuscular regulation strategy may be provided with the central nervous system of the body to cope with the landing shock by adjusting muscle activities. To what extent the vertical GRF/LR changes are influenced by the applied fatigue protocols remains unclear.

Fatigue has been shown to alter hip and knee kinematics of the sagittal plane [9, 10, 32, 33]. However, there is no consensus on the flexion angle of the knee joint after fatigue. Specifically, Chappell et al. found both male and female subjects significantly decreased knee flexion angles during landings when fatigued [10]. Conversely, an increase in the knee flexion angle was found by Kernozek et al. [32] and Coventry [9] in the same landing task. In Coventry et al.'s study, hip and knee flexion increased at touchdown under a postfatigue condition. This change was thought to be a compensatory response that might better suit to absorb the mechanical energy of the impact and thus play a positive role in reducing ACL injury to a certain extent [9]. Kernozek et al. also found that male subjects effectively reduced the magnitude of the anterior knee shear force by the means of a greater peak knee

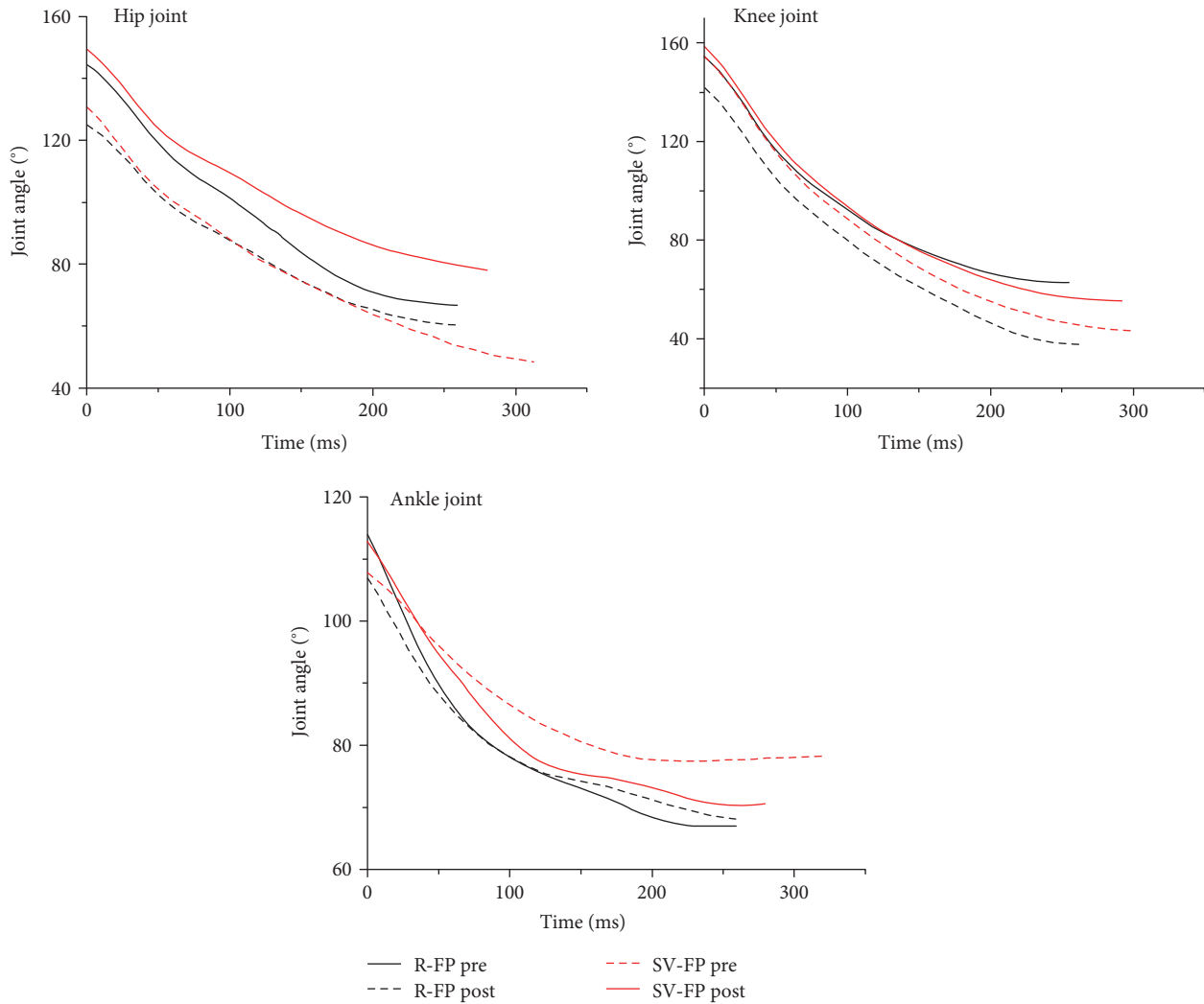


FIGURE 4: Comparison of the joint angles of lower extremities in the sagittal plane between pre- and postfatigue test in different fatigue protocols during landing.

flexion angles postfatigue during a DL task, which partially supports our findings [32]. Apart from the above two results, the participants had approximately the same hip and knee flexion angle at initial contact during a single-leg DL task following a hip abductor fatigue protocol in Patrek et al.'s study [33], which indicated that the role of hip abductor activation in protecting the knee during landing needed to be further justified. In addition, fatigue level was divided into five grades, namely, prefatigue, 25% fatigue, 50% fatigue, 75% fatigue, and 100% fatigue, in Mclean and Samorezov's study [22]. Although they found a decrease in the knee flexion angle at the initial contact phase as fatigue levels progressed from prefatigue to 100% fatigue in a single-leg landing task, no significant differences were observed among 50%, 75%, and 100% fatigue levels [22]. The above results indicated that participants may use a protective strategy under a fatigued condition by adjusting kinematic characteristics in a favorable pattern, which can better absorb the impact force during DL.

Our results suggested that changes in the sagittal plane kinematics of the lower extremities between prefatigue and postfatigue during the DL task were observed regardless of the fatigue protocol used. One possible reason for the similarities between the R-FP and SV-FP may relate to a participant's athletic ability and conditioning level [20]. The participants in our study were trained recreational athletes who were accustomed to various conditioning trainings, including short-term multidirectional movements and long-duration single-directional movements such as running or cycling. Moreover, maximal HR and RPE were used as indicators of reflecting exercise intensity in R-FP and SV-FP during the entire experimental procedure. Notably, the differences between the two protocols were only found in the time duration but not in the intensity of both interventions, indicating that fatigue-related kinematic modifications may occur in a few minutes.

Previous studies suggested that ACL loading decreased when knee flexion angles increased [34, 35]. In the current

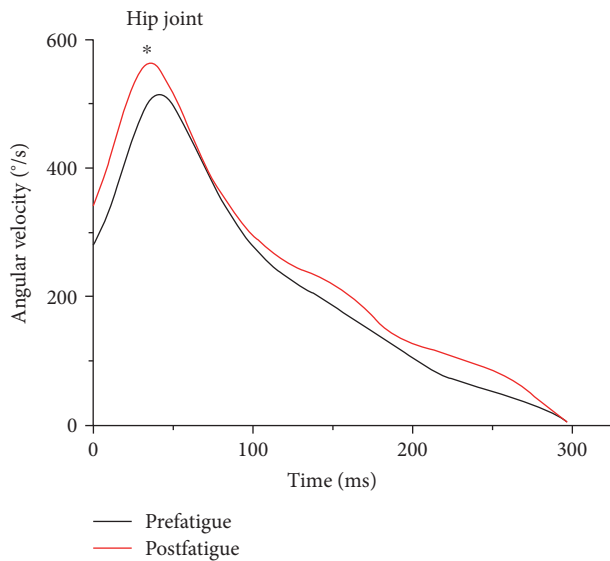


FIGURE 5: Comparison on angular velocity of the hip joint in the sagittal plane between pre- and postfatigue test during landing ( $*p < 0.05$ ).

study, an increased hip/knee flexion angle in the postfatigue condition was found, which obviously opposed to the stiff landing (a small knee flexion angle) with potentially induced ACL injury [36]. This partially suggested that human beings may use a protective motor control strategy of the lower extremities when performing the DL task under a fatigued condition. We thus assumed that these neuromuscular changes dominated by the central/peripheral nervous system may be helpful in decreasing the risk for ACL injuries through altering kinematics consciously or even unconsciously. However, more evidence is needed to confirm this.

## 5. Conclusion

Fatigue induced an increase in hip and knee flexion, resulting in a more flexed landing posture during a drop landing task using two different fatigue protocols. However, no differences in peak impact force and loading rate were found between pre- and postfatigue conditions. Although the intervention effect on these two fatigue protocols was similar in DL performance, the SV-FP presented a shorter intervention time than the R-FP. Nevertheless, either of the two fatigue protocols can be used as a reference for the selection of fatigue protocols in laboratory tests. Furthermore, landing in a more extended position was thought to increase ACL injury risk. To a certain extent, the altered biomechanical characteristics or landing strategies of the lower extremities may prevent detrimental effects under a fatigued condition. However, whether it is an intentional or unintentional means of protection from potential ACL injury still needs further consideration. Further studies are necessary to establish the relationship between motor control strategies of the lower extremities and the risk for ACL injuries.

## Conflicts of Interest

The authors declare no conflict of interest in this manuscript.

## Authors' Contributions

Rui Xia and Xini Zhang contributed equally.

## Acknowledgments

This study was supported by the National Natural Science Foundation of China (11302131), the Innovation Program of Shanghai Municipal Education Commission (14YZ125), and the Postgraduate Students Overseas Visiting Projects of Shanghai University of Sport (stfx20150209).

## References

- [1] L. B. Andersen, C. Riddoch, S. Kriemler, A. P. Hills, and A. Hills, "Physical activity and cardiovascular risk factors in children," *British Journal of Sports Medicine*, vol. 45, no. 11, pp. 871–876, 2011.
- [2] S. J. H. Biddle, T. Gorely, and D. J. Stensel, "Health-enhancing physical activity and sedentary behaviour in children and adolescents," *Journal of Sports Sciences*, vol. 22, no. 8, pp. 679–701, 2004.
- [3] I. Janssen and A. G. Leblanc, "Systematic review of the health benefits of physical activity and fitness in school-aged children and youth," *International Journal of Behavioral Nutrition and Physical Activity*, vol. 7, no. 1, pp. 1–16, 2010.
- [4] C. Chéron, C. L. Scannell, and C. Leboeuf-Yde, "Association between sports type and overuse injuries of extremities in children and adolescents: a systematic review," *Chiropractic & Manual Therapies*, vol. 24, no. 1, pp. 41–50, 2016.
- [5] B. Y. Dai, D. Herman, L. Hui, W. E. Garrett, and B. Yu, "Prevention of ACL injury, part I: injury characteristics, risk factors, and loading mechanism," *Research in Sports Medicine an International Journal*, vol. 20, no. 3-4, pp. 180–197, 2012.
- [6] W. Fu, Y. Liu, and S. Zhang, "Effects of footwear on impact forces and soft tissue vibrations during drop jumps and unanticipated drop landings," *International Journal of Sports Medicine*, vol. 34, no. 06, pp. 477–483, 2012.
- [7] J. L. McNitt-Gray, "Kinematics and impulse characteristics of drop landings from three heights," *International Journal of Sport Biomechanics*, vol. 7, no. 2, pp. 201–224, 1991.
- [8] A. A. Zadpoor and A. A. Nikooyan, "The relationship between lower-extremity stress fractures and the ground reaction force: a systematic review," *Clinical Biomechanics*, vol. 26, no. 1, pp. 23–28, 2011.
- [9] E. Coventry, K. M. O'Connor, B. A. Hart, J. E. Earl, and K. T. Ebersole, "The effect of lower extremity fatigue on shock attenuation during single-leg landing," *Clinical Biomechanics*, vol. 21, no. 10, pp. 1090–1097, 2006.
- [10] J. D. Chappell, D. C. Herman, B. S. Knight, D. T. Kirkendall, W. E. Garrett, and B. Yu, "Effect of fatigue on knee kinetics and kinematics in stop-jump tasks," *American Journal of Sports Medicine*, vol. 33, no. 7, pp. 1022–1029, 2005.
- [11] R. M. Enoka, "Muscle fatigue – from motor units to clinical symptoms," *Journal of Biomechanics*, vol. 45, no. 3, pp. 427–433, 2012.

- [12] N. G. Moreau, L. Li, J. P. Geaghan, and D. L. Damiano, "Fatigue resistance during a voluntary performance task is associated with lower levels of mobility in cerebral palsy," *Archives of Physical Medicine & Rehabilitation*, vol. 89, no. 10, pp. 2011–2016, 2008.
- [13] W. Fu, Y. Liu, S. Zhang, X. Xiong, and S. Wei, "Effects of local elastic compression on muscle strength, electromyographic, and mechanomyographic responses in the lower extremity," *Journal of Electromyography & Kinesiology Official Journal of the International Society of Electrophysiological Kinesiology*, vol. 22, no. 1, pp. 44–50, 2012.
- [14] L. A. Borowski, E. E. Yard, S. K. Fields, and R. D. Comstock, "The epidemiology of US high school basketball injuries, 2005–2007," *American Journal of Sports Medicine*, vol. 36, no. 36, pp. 2328–2335, 2008.
- [15] J. T. Podraza and S. C. White, "Effect of knee flexion angle on ground reaction forces, knee moments and muscle co-contraction during an impact-like deceleration landing: implications for the non-contact mechanism of ACL injury," *The Knee*, vol. 17, no. 4, pp. 291–295, 2010.
- [16] M. P. Smith, P. S. Sizer, and C. R. James, "Effects of fatigue on frontal plane knee motion, muscle activity, and ground reaction forces in men and women during landing," *Journal of Sports Science & Medicine*, vol. 8, no. 3, pp. 419–427, 2009.
- [17] E. Kellis and V. Kouveliod, "Agonist versus antagonist muscle fatigue effects on thigh muscle activity and vertical ground reaction during drop landing," *Journal of Electromyography & Kinesiology: Official Journal of the International Society of Electrophysiological Kinesiology*, vol. 19, no. 1, pp. 55–64, 2009.
- [18] C. R. James, J. S. Dufek, and B. T. Bates, "Effects of stretch shortening cycle exercise fatigue on stress fracture injury risk during landing," *Research Quarterly for Exercise and Sport*, vol. 77, no. 1, pp. 1–13, 2006.
- [19] C. R. James, B. W. Scheuermann, and M. P. Smith, "Effects of two neuromuscular fatigue protocols on landing performance," *Journal of Electromyography & Kinesiology*, vol. 20, no. 4, pp. 667–675, 2010.
- [20] D. Quammen, N. Cortes, B. L. Van Lunen, S. Lucci, S. I. Ringleb, and J. Onate, "Two different fatigue protocols and lower extremity motion patterns during a stop-jump task," *Journal of Athletic Training*, vol. 47, no. 1, pp. 32–41, 2011.
- [21] D. Gehring, M. Melnyk, and A. Gollhofer, "Gender and fatigue have influence on knee joint control strategies during landing," *Clinical Biomechanics*, vol. 24, no. 1, pp. 82–87, 2009.
- [22] S. G. Mclean and J. E. Samorezov, "Fatigue-induced ACL injury risk stems from a degradation in central control," *Medicine & Science in Sports & Exercise*, vol. 41, no. 8, pp. 1661–1672, 2009.
- [23] V. Mrdakovic, D. B. Ilic, N. Jankovic, Z. Rajkovic, and D. Stefanovic, "Pre-activity modulation of lower extremity muscles within different types and heights of deep jump," *Journal of Sports Science and Medicine*, vol. 7, no. 2, pp. 269–278, 2008.
- [24] M. Ruan and L. Li, "Approach run increases preactivation and eccentric phases muscle activity during drop jumps from different drop heights," *Journal of Electromyography & Kinesiology: Official Journal of the International Society of Electrophysiological Kinesiology*, vol. 20, no. 5, pp. 932–938, 2010.
- [25] B. Friesenbichler, L. M. Stirling, P. Federolf, and B. M. Nigg, "Tissue vibration in prolonged running," *Journal of Biomechanics*, vol. 44, no. 1, pp. 116–120, 2011.
- [26] L. C. Tsai, S. M. Sigward, C. D. Pollard, M. J. Fletcher, and C. M. Powers, "Effects of fatigue and recovery on knee mechanics during side-step cutting," *Medicine & Science in Sports & Exercise*, vol. 41, no. 10, pp. 1952–1957, 2009.
- [27] W. Niu, Y. Wang, Y. He, Y. Fan, and Q. Zhao, "Kinematics, kinetics, and electromyogram of ankle during drop landing: a comparison between dominant and non-dominant limb," *Human Movement Science*, vol. 30, no. 3, pp. 614–623, 2011.
- [28] T. Horita, P. Komi, C. Nicol, and H. Kyröläinen, "Interaction between pre-landing activities and stiffness regulation of the knee joint musculoskeletal system in the drop jump: implications to performance," *European Journal of Applied Physiology*, vol. 88, no. 1, pp. 76–84, 2002.
- [29] W. Niu, T. Feng, C. Jiang, and M. Zhang, "Peak vertical ground reaction force during two-leg landing: a systematic review and mathematical modeling," *BioMed Research International*, vol. 2014, Article ID 126860, 2014.
- [30] A. A. Zadpoor and A. A. Nikooyan, "The effects of lower extremity muscle fatigue on the vertical ground reaction force: a meta-analysis," *Proceedings of the Institution of Mechanical Engineers Part H, Journal of Engineering in Medicine*, vol. 226, no. 8, pp. 579–588, 2012.
- [31] E. A. Wikstrom, M. E. Powers, and M. D. Tillman, "Dynamic stabilization time after isokinetic and functional fatigue," *Journal of Athletic Training*, vol. 39, no. 3, pp. 247–253, 2004.
- [32] T. W. Kernozek, M. R. Torry, and M. Iwasaki, "Gender differences in lower extremity landing mechanics caused by neuromuscular fatigue," *American Journal of Sports Medicine*, vol. 36, no. 3, pp. 554–565, 2008.
- [33] M. F. Patrek, T. W. Kernozek, J. D. Willson, G. A. Wright, and S. T. Doberstein, "Hip-abductor fatigue and single-leg landing mechanics in women athletes," *Journal of Athletic Training*, vol. 46, no. 1, pp. 31–42, 2011.
- [34] K. L. Markolf, D. M. Burchfield, M. M. Shapiro, M. F. Shepard, G. A. M. Finerman, and J. L. Slauterbeck, "Combined knee loading states that generate high anterior cruciate ligament forces," *Journal of Orthopaedic Research*, vol. 13, no. 6, pp. 930–935, 1995.
- [35] S. S. Jordan, L. E. Defrate, K. W. Nha, R. Papannagari, T. J. Gill, and G. Li, "The in vivo kinematics of the anteromedial and posterolateral bundles of the anterior cruciate ligament during weightbearing knee flexion," *The American Journal of Sports Medicine*, vol. 35, no. 4, pp. 547–554, 2007.
- [36] B. Dai, D. Mao, W. E. Garrett, and B. Yu, "Anterior cruciate ligament injuries in soccer: loading mechanisms, risk factors, and prevention programs," *Journal of Sport & Health Science*, vol. 3, no. 4, pp. 299–306, 2014.

## Research Article

# Study of the Mechanical Environment of Chondrocytes in Articular Cartilage Defects Repaired Area under Cyclic Compressive Loading

Hai-Ying Liu,<sup>1</sup> Hang-Tian Duan,<sup>1</sup> Chun-Qiu Zhang,<sup>1</sup> and Wei Wang<sup>2</sup>

<sup>1</sup>Tianjin Key Laboratory of the Design and Intelligent Control of the Advanced Mechatronical System, Tianjin University of Technology, Tianjin 300384, China

<sup>2</sup>Department of Mechanics, School of Mechanical Engineering, Tianjin University, Tianjin 300354, China

Correspondence should be addressed to Hai-Ying Liu; liuhaiying22@163.com

Received 24 February 2017; Revised 22 May 2017; Accepted 30 May 2017; Published 9 July 2017

Academic Editor: Liping Wang

Copyright © 2017 Hai-Ying Liu et al. This is an open access article distributed under the Creative Commons Attribution License, which permits unrestricted use, distribution, and reproduction in any medium, provided the original work is properly cited.

COMSOL finite element software was used to establish a solid-liquid coupling biphasic model of articular cartilage and a microscopic model of chondrocytes, using modeling to take into account the shape and number of chondrocytes in cartilage lacuna in each layer. The effects of cyclic loading at different frequencies on the micromechanical environment of chondrocytes in different regions of the cartilage were studied. The results showed that low frequency loading can cause stress concentration of superficial chondrocytes. Moreover, along with increased frequency, the maximum value of stress response curve of chondrocytes decreased, while the minimum value increased. When the frequency was greater than 0.2 Hz, the extreme value stress of response curve tended to be constant. Cyclic loading had a large influence on the distribution of liquid pressure in chondrocytes in the middle and deep layers. The concentration of fluid pressure changed alternately from intracellular to peripheral in the middle layer. Both the range of liquid pressure in the upper chondrocytes and the maximum value of liquid pressure in the lower chondrocytes in the same lacunae varied greatly in the deep layer. At the same loading frequency, the elastic modulus of artificial cartilage had little effect on the mechanical environment of chondrocytes.

## 1. Introduction

Articular cartilage is a layer of load-bearing hydrated soft tissue with low friction, covering the joint surfaces of both ends of long bones. Its mechanical properties and morphology are maintained by the metabolism of chondrocytes [1, 2]. Normal articular cartilage can bear many millions of cycles of high force loading [3], but with exercise of increasing energy and force, the problem of aging becomes increasingly serious. Approximately 65% of the total population had suffered injury to their articular cartilage [4]. Because of the lack of blood vessels, nerves, and lymphatic tissue, cartilage cannot easily repair itself after injury. In recent years, tissue engineering techniques to repair articular cartilage defects have attracted much attention [4, 5]. This technology is expected to be the most effective method to

cure the cartilage defect. Until now, using tissue engineering techniques for repairing cartilage defects result in a clinical therapeutic success rate of approximately 50%, having a good short-term effect but uncertain long-term results due to the occurrence of the graft degeneration, degeneration, joint cracking, hardening, or even the induction of the degeneration of the host cartilage [2, 6, 7]. The main reason is that the mechanical properties of tissue-engineered cartilage are not comparable to those of natural cartilage, and implants will alter the mechanical environment of the solid matrix and chondrocytes within the zone of the repair. Chondrocytes respond to stress stimuli by changing shape. Deviations from physiological load affect the gene expression, metabolism, and also the possible induction of apoptosis of chondrocytes [2, 8]. Experimental results of single chondrocytes in vitro indicate that cyclic loading affects chondrocyte

biosynthesis more significantly than that of static loading [9]. Studies have shown that the specific frequency of cyclic loading can increase the aggrecan synthesis in cartilage explants [10]. Thus, following clinical tissue-engineered cartilage repair, patients are advised to gradually exercise during hospitalization and after discharge [2]. Appropriate rehabilitation exercises may alleviate pain and improve the metabolism of articular chondrocytes.

At present, the principal method used to study the mechanical properties of chondrocytes is to perform in vitro experiments or finite element numerical simulation [11–14] and to directly measure parameters such as cell deformation, elastic modulus, or surface potential. However, the results do not really reflect the micromechanical environment of chondrocytes in vivo. Until now, it has been difficult to monitor the cell volume, stress, and strain or changes in the pressure of intracellular fluid in chondrocytes during cyclic loading [15]. A multiscale study of the biomechanical environment of chondrocytes by finite element analysis could satisfy the requirements for evaluating these measurements. Zhou et al. used multiscale methods to study the distribution of stress and the flow field of fluid in cartilage under static loading and the role of pericellular matrix (PCM) in protecting chondrocytes from high stress damage [16]. Tauska et al. also used multiscale methods to study the mechanical behavior of articular chondrocytes during normal and medial meniscectomy [17]. Guilak and Haider established a multiscale linear biphasic cell-matrix interaction model of articular cartilage, with which the complex correlation between the dynamic environment of chondrocytes and their macroscopic load characteristics under confined compression cyclic load was studied [8]. Erdemir et al. used multiscale methods to establish a high-throughput model of joints, with information transfer being established between different scales generating a simulation study of changes in the mechanical environment in cell scale under macro loading [18].

The mechanical response of chondrocytes to cyclic compression depends on the amplitude and frequency of the load [8, 15, 19]. In this paper, COMSOL finite element software was used to establish an unconfined model of articular cartilage with full-thickness defects and a transscale chondrocyte model. The influence of frequency in cyclic compressive loading and the elastic modulus of artificial cartilage on the micromechanical environment of the chondrocytes in a repaired defect was studied by numerical simulation.

## 2. Materials and Methods

COMSOL Multiphysics (3.5a; Royal Institute of Technology, Stockholm, Sweden), a finite element software, was selected to simulate the mechanical environment of chondrocytes in three steps. The first step established the finite element model of cartilage and chondrocytes. The second step calculated the displacement and stress fields of articular cartilage, so as to provide accurate boundary conditions for the chondrocyte model. The third step mapped the results of the corresponding region of the cartilage model onto the

chondrocyte model using consistent boundary conditions, to accomplish data conversion.

**2.1. Articular Cartilage Model.** In the 1980s, Mow et al. established a solid-liquid coupling biphasic porous medium cartilage model [20]. The model accurately reflects the macroscopic mechanical properties of cartilage because the characteristics of fiber reinforced were considered.

**2.1.1. Material Parameters.** The material parameters of cartilage anisotropy, Poisson's ratio  $\nu$  and the elastic modulus  $E$ , are related in a depth-dependent manner as follows [21–23]:

$$\nu = 0.08 + 0.1 \left( \frac{h-y}{h} \right), \quad (1)$$

$$E(y) = \frac{3.66}{46.2e^{-6.53y} + 2.84}, \quad (2)$$

where  $h$  and  $y$  are thickness and depth of cartilage, respectively.

Cartilage permeability  $k$  is a nonlinear function related to depth and deformation [23, 24]:

$$k = k_0 \psi(y, h) \exp(M \varepsilon_v), \quad (3)$$

where  $k_0 = 2 \times 10^{-15} \text{m}^4/(\text{N}\cdot\text{s})$  is the initial permeability,  $M = 23$  is an arbitrary material parameter,  $\varepsilon_v$  is volumetric strain, and  $\psi(y, h)$  is a function dependent on depth.

$$\psi(y, h) = 1 + 4.3 \left( \frac{y}{h} \right) - 7.8 \left( \frac{y}{h} \right)^2 + 3.1 \left( \frac{y}{h} \right)^3. \quad (4)$$

**2.1.2. Boundary Condition of Articular Cartilage Model.** The contact face between the distal end of the femur and the proximal tibia is curved, so contact stress was calculated using Hertz contact theory [25]. Applying hertz pressure to simulate physiological load results in the following expression:

$$F(x) = \frac{2W}{\pi b} \sqrt{1 - \frac{x^2}{b^2}} \quad (-b < x < b), \quad (5)$$

where  $b = \sqrt{8FR/(\pi E)}$  is half of the contact width,  $R = 0.1 \text{m}$  is the equivalent femoral condylar radius,  $F$  is cyclic loading, and  $E = 10 \text{MPa}$  is equivalent to the elastic modulus. Subchondral bone permeability is very small and approximates to 0, setting the displacement boundary condition:

$$u = v = 0, \quad \frac{\partial p}{\partial y} = 0. \quad (6)$$

The left and right boundaries are symmetrical, the displacement is unconstrained, the pressure is 0, and liquid can flow freely:

$$p = 0. \quad (7)$$

A symmetrical geometric model of cartilage with a length of 2 cm and thickness of 2 mm was established, with the middle area being a defect repair area with a width of 2 mm (Figure 1). The lower boundary was fixed, and the bilateral boundary and the upper surface were allowed to flow freely.

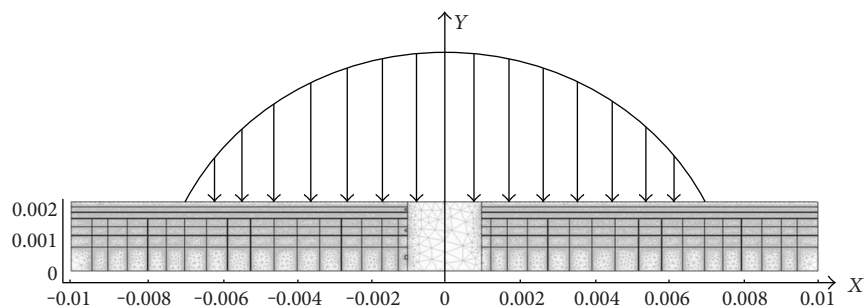


FIGURE 1: Cartilage defect model and boundary load distribution.

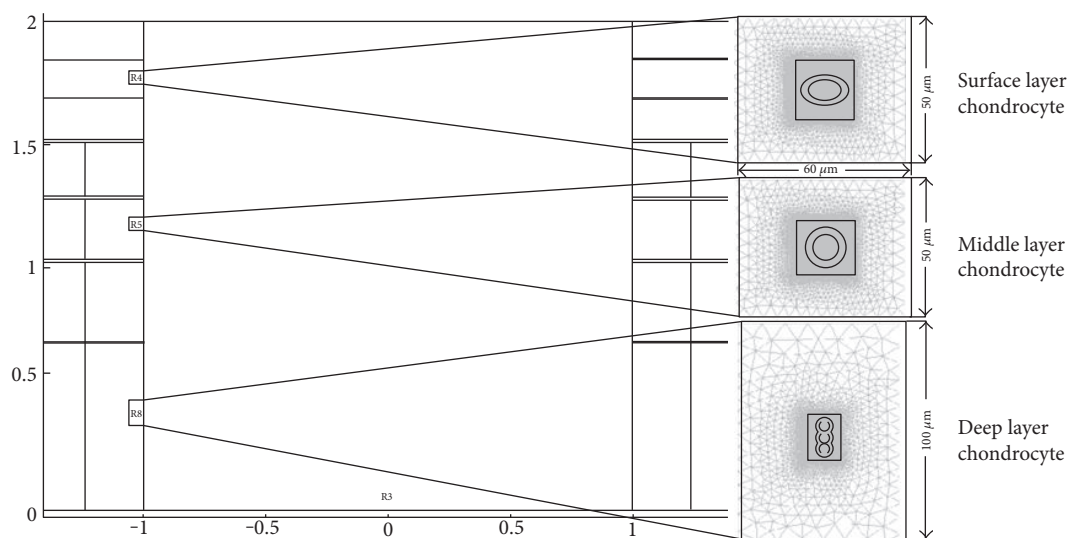


FIGURE 2: Schematic diagram of chondrocytes in each layer.

TABLE 1: Mechanical parameters of chondrocytes.

Position	$E_{ECM}$ (MPa)	$E_{PCM}$ (KPa)	$E_{CELL}$ (KPa)	$k_{CEM}/10^{14}$ (Ns·m <sup>-4</sup> )	$K_{PEM}/10^{15}$ (Ns·m <sup>-4</sup> )	$K_{CELL}/10^{15}$ (Ns·m <sup>-4</sup> )
Superficial layer	0.4	40	4	2	1	2
Middle layer	0.3	30	3	2	1	2
Deep layer	0.2	20	2	2	1	2

A downward cyclic loading was exerted on the upper surface;  $W = F_0 \sin \omega t$ , where  $\omega = 2\pi f$  is the angular frequency,  $f$  is frequency, and  $F_0$  is the load amplitude. Fibers were horizontal in the superficial layer, transverse and vertical fibers crossing oblique fibers in the middle layer, and with deep layer fibers perpendicular to the cartilage surface.

**2.2. Finite Element Model of Chondrocytes.** The mechanical environment of chondrocytes depends on the macroscopic deformation of cartilage and the location of chondrocytes in cartilage. The chondrocyte model was established according to the cell morphology observed in the staining experiments. The chondrocytes in the superficial and middle

layers were oblate and round, with three chondrocytes in a cartilage lacuna forming a cluster (Figure 2). A  $100 \mu\text{m}^2$  region around each chondrocyte was defined as a coherence buffer area. The marginal region was extracellular matrix (ECM); the inward transition region was pericellular matrix (PCM) with the chondrocytes in the central area.

**2.2.1. Chondrocytes Structural Parameters.** The material parameters of the chondrocyte model were taken from the literature [26, 27]:  $\nu_{ECM,1,2,3} = \nu_{PCM,1,2,3} = 0.2$ ,  $\nu_{CELL} = 0.4$ . The remaining parameters are shown in Table 1. In meshing process, the dense of the chondrocyte meshes and the sparse peripheral region of the chondrocyte meshes, the

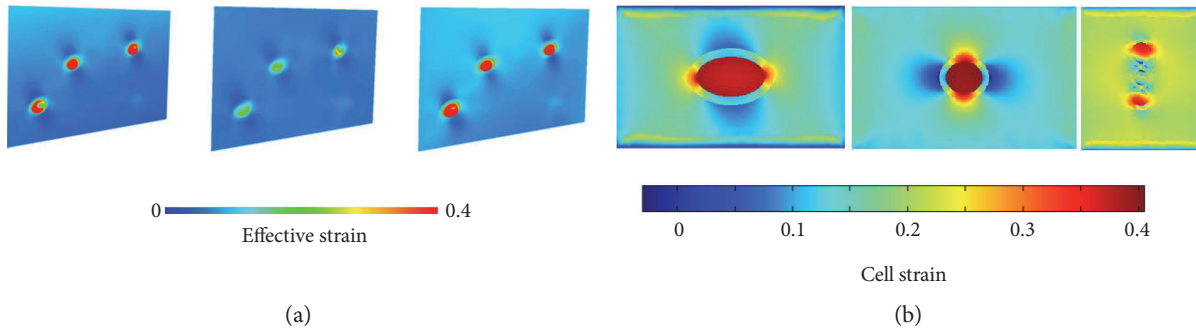


FIGURE 3: Comparison of simulation results of finite element model of chondrocytes with the literature [18]: (a) results from the literature [18]; (b) results from this paper.

method improves the efficiency of calculation, while ensuring its accuracy.

**2.2.2. Validation of Chondrocyte Model.** Previous results of the strain analysis of chondrocytes [18] were compared with the simulation results in this paper (Figures 3(a) and 3(b)). It can be seen that strain gradually increased from the ECM to PCM and into the chondrocytes interior, with PCM having the function of strain conduction amplification. The maximum effective strain was 0.4 (Figure 3(a)), strain extremum 0.41 (Figure 3(b)), and the variance ratio of the two values being 2.5%. The strain nephograms were also similar, demonstrating the accuracy of the chondrocyte model.

### 3. Results

**3.1. Study of the Mechanical Environment of Chondrocytes in the Superficial Layer.** In this paper, the artificial cartilage with elastic modulus of 0.1 MPa was used to repair the cartilage defect. Cyclic compressive loading at different frequencies was used to simulate physiological loads, to study the mechanical environment of the chondrocytes, and to explore the mechanical properties of chondrocytes for the repair of cartilage defects.

**3.1.1. Variation of Stress-Time Curve at Different Points in the Intracellular Center and PCM.** A uniform stimulation of aggrecan synthesis was observed at frequency of 0.01 Hz, while, at a higher frequency of 0.1 Hz, stimulation was only seen at peripheral radial positions of cylindrical explants [10]. So, this study selected the center of a chondrocyte, labelled position 1, and the PCM directly above position 1, labelled position 2, that were subjected to loading frequencies of 0.01 Hz, 0.02 Hz, 0.05 Hz, and 0.1 Hz. Variations in the stress-time curves at positions 1 (a heavy line) and 2 (a fine line) were obtained within the superficial layer (Figure 4). Maximum stress was observed to be approximately 500 Pa~680 Pa at point 1 and a value 5~6 times greater at position 2 (2800 Pa~3600 Pa) at different frequencies, decreasing gradually over time, indicating that PCM plays a protective and transitional role [16]. At a compressive load frequency of 0.1 Hz, the stress at point 2 was reduced by nearly 1000 Pa compared to the stress at 0.01 Hz. At a low frequency, the response to load at

positions 1 and 2 was almost synchronous, but when the frequency was increased to 0.05 Hz, the minimum stress values at positions 1 and 2 were clearly separated. The difference of minimum stress at 0.05 Hz was about 400 Pa and approximately 600 Pa at 0.1 Hz.

The maximum stress decreased at both position 1 and position 2 with increasing frequency, the stress reducing by nearly 170 Pa and 930 Pa at 0.1 Hz compared to that at 0.01 Hz, respectively. However, the minimum stress increased at position 1 and position 2 with increasing frequency, the stress increasing by nearly 160 Pa and 700 Pa at 0.1 Hz compared to that at 0.01 Hz, respectively. At low frequency, positions 1 and 2 respond almost simultaneously to loading. At a frequency of 0.05 Hz, the lowest stress values were separated between positions 1 and 2. The results above indicate that the PCM is sensitive to changes in frequency.

The normal walking gait frequency of human is about 0.5~0.7 Hz. Through the analysis of the maximum and minimum values of the stress response curves at position 1 and position 2, which is higher than the frequency of 0.1 Hz, the variation curves of the extreme value stress at different frequencies were obtained (Figure 5). It can be seen that, with the increase of the load frequency, the minimum value of stress at positions 1 and 2 increased, while the maximum value of stress decreased. When the cyclic loading frequency is higher than 0.2 Hz, the extreme value of stress basically keep constant.

**3.1.2. The Contours of Stress Distribution of Chondrocytes and PCM.** Following loading for 100s, the contours of stress distribution in chondrocytes and PCM under cyclic loading were measured at different frequencies (Figure 6). The numerical simulation shows that the stress of cells with different elastic moduli is not obviously different under the same frequency load. Only when the loading frequency is 0.05 Hz, at greater elastic moduli, the stress on chondrocytes is reduced. When artificial cartilage with an elastic modulus of 0.9 MPa was used to repair the cartilage, the maximum stress value in chondrocytes and PCM was approximately 75% than that of the low modulus (0.1 MPa) repair. When applying low frequency (0.01 Hz) loads, the cumulative effect of the load can be fully reflected due to the viscoelastic properties of cartilage. The maximum value of intracellular stress at low frequency loads (0.01 Hz)

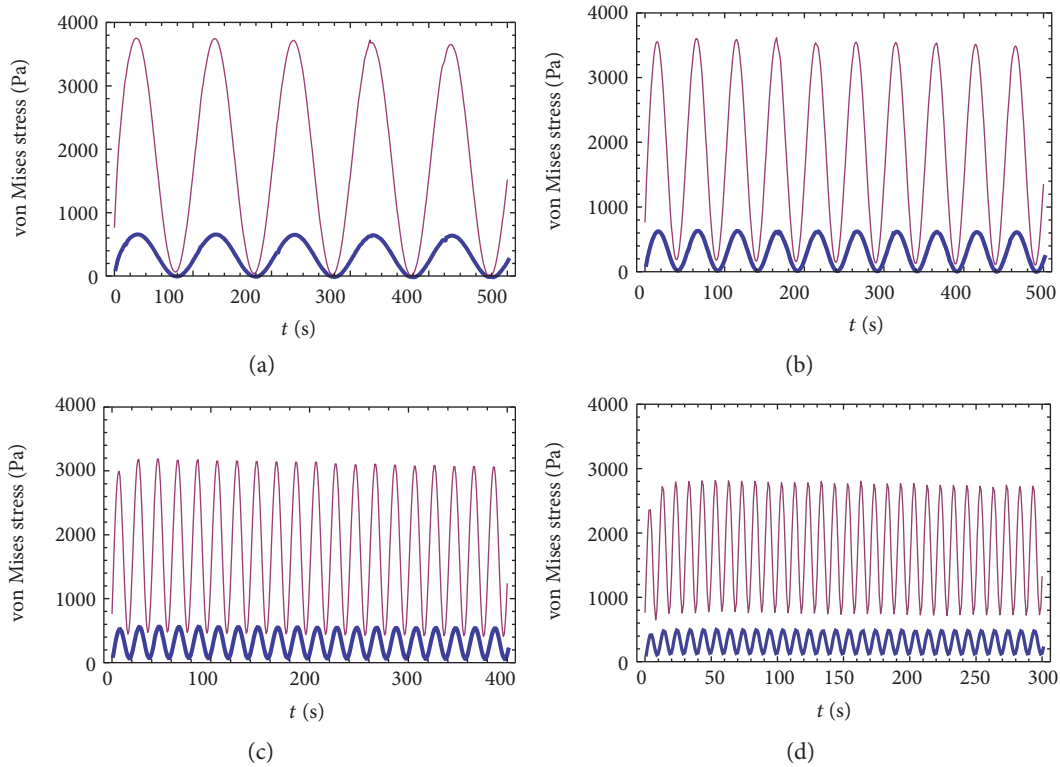


FIGURE 4: Stress curves at position 1 (a heavy line) and position 2 (a fine line) under cyclic loading at different frequencies: (a) 0.01 Hz; (b) 0.02 Hz; (c) 0.05 Hz; (d) 0.1 Hz.

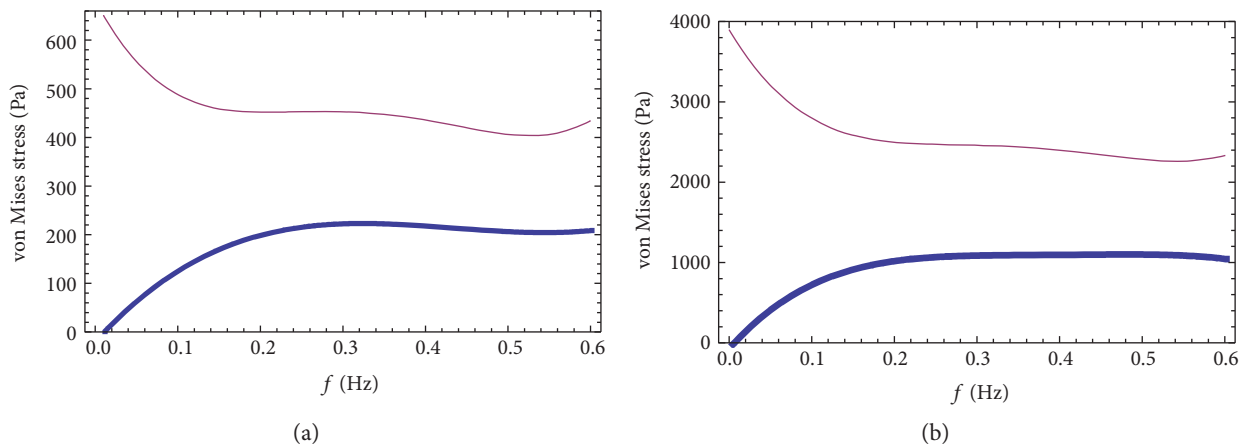


FIGURE 5: The variation curves of minimum value (a heavy line) and maximum value (a fine line) of stress at different cyclic loading frequencies: (a) position 1; (b) position 2.

was higher than that of the high frequency loading (0.05 Hz), the former being 2.53 times the latter. The cumulative effect caused chondrocytes stress to increase with time, but it did not increase indefinitely, and so was beneficial for the protection of chondrocytes from high stress damage and changes in gene expression. Under low frequency loads, using artificial cartilage with larger elastic moduli (0.6 or 0.9 MPa), the stress decreased gradually with increasing load cycle.

**3.1.3. Change in Fluid Velocity in Chondrocytes.** Variation in intracellular liquid velocity was most significant in the superficial layer when the loading frequency was 0.1 Hz, as indicated by the distribution maps of intracellular fluid velocity at different loading times (4 s, 9 s, 14 s, and 19 s) (Figure 7). The results show that there were significant differences in the distribution of liquid velocity. In general, the flow velocity in the peripheral area of the chondrocyte was significantly greater than that in the core region. In

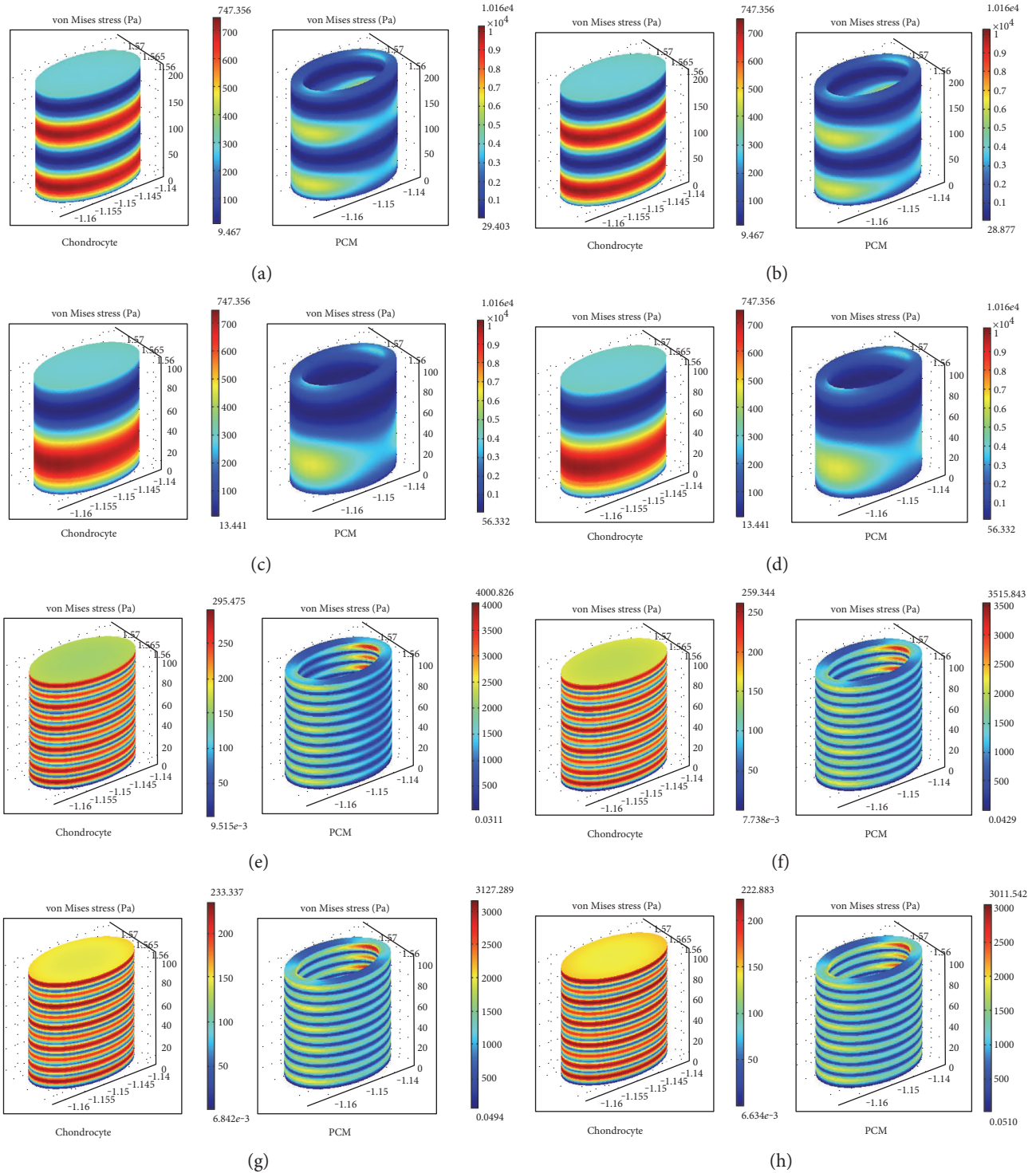


FIGURE 6: Change in stress in chondrocytes and PCM at different loading frequencies (a)–(d) elastic modulus of artificial cartilage repair: 0.1 MPa, 0.3 MPa, 0.6 MPa, and 0.9 MPa, respectively, at a 0.01 Hz loading frequency; (e)–(h) elastic modulus of artificial cartilage repair: 0.1 MPa, 0.3 MPa, 0.6 MPa, and 0.9 MPa, respectively, at a 0.05 Hz loading frequency.

addition, the simulation also showed that when the cyclic load frequency was lower than 0.05 Hz, the distribution of fluid pressure and velocity in the chondrocytes remained the same but the marginal area was large and the central area was small.

**3.2. Intracellular Fluid Pressure Distribution at Each Layer.** The distribution of fluid pressure in the superficial, middle, and deep layers under cyclic compression loads at a frequency of 0.02 Hz is shown in Figures 8, 9, and 10, respectively.

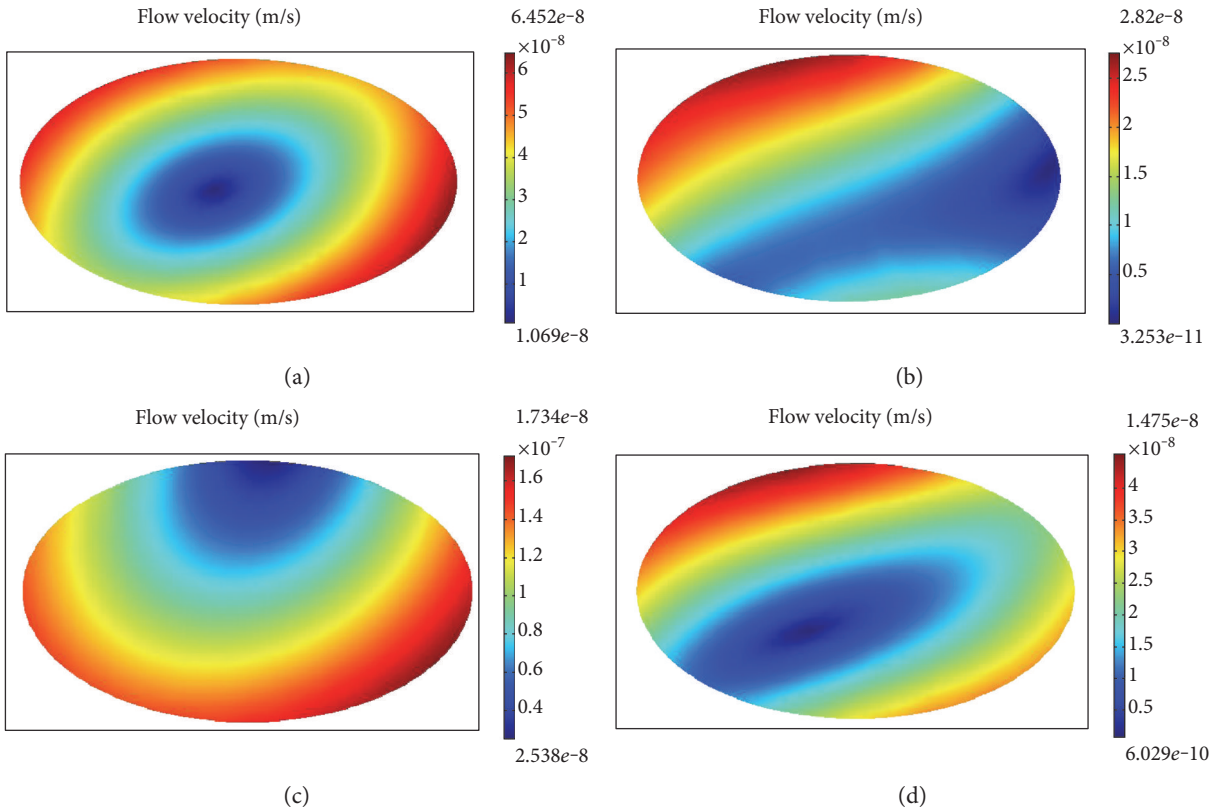


FIGURE 7: Change in flow velocity at different times under cyclic loading (a) at 4 s, (b) at 9 s, (c) at 14 s, and (d) at 19 s.

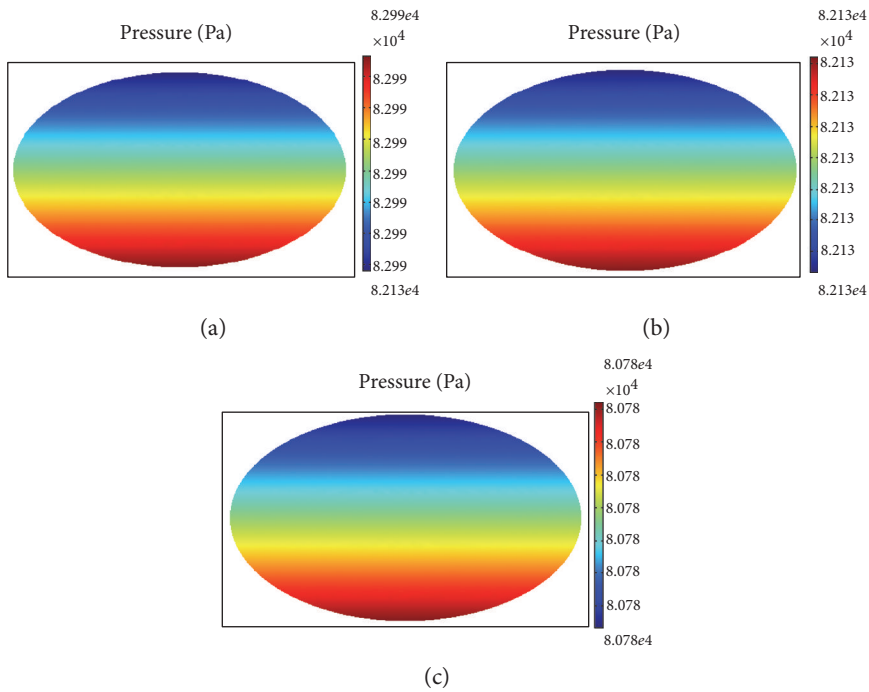


FIGURE 8: Intracellular fluid pressure distribution at different times in the superficial layer (a) at 15 s, (b) at 16 s, and (c) at 17 s.

Intracellular liquid pressure distribution polarization in the superficial layer resulted in smaller values within the top half and gradually increased in the lower part of the

chondrocyte, although the change was not clear (Figure 8). Comparatively speaking, pressure distribution variations were very large in the middle layer. During the process of

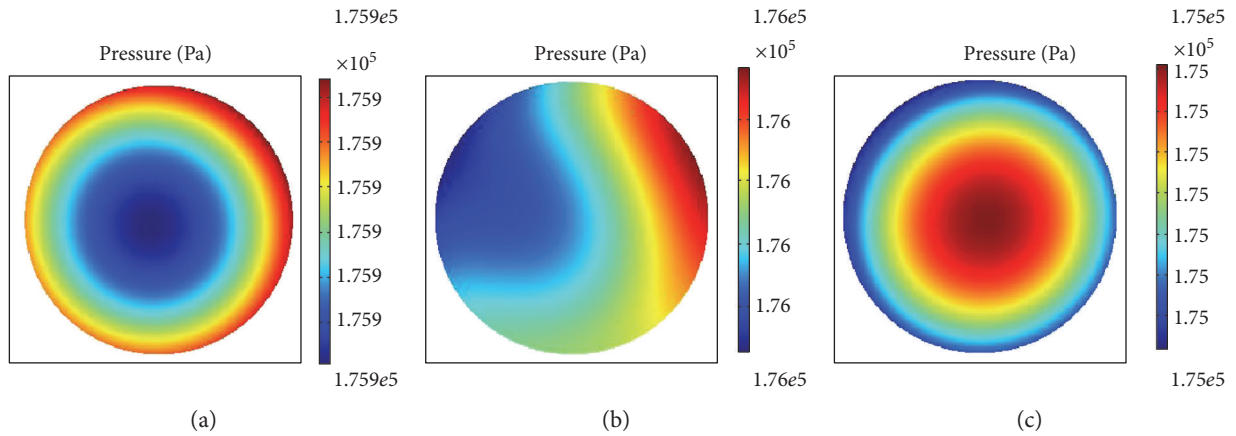


FIGURE 9: Intracellular fluid pressure distribution at different times in the middle layer (a) at 15 s, (b) at 16 s, and (c) at 17 s.

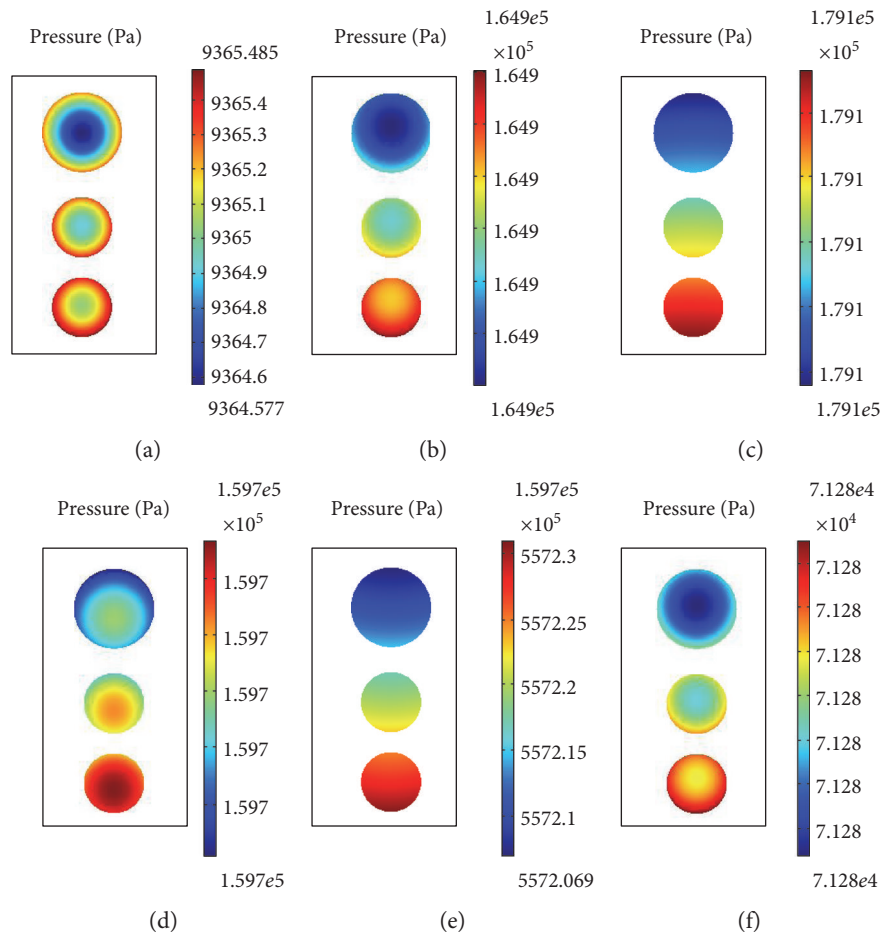


FIGURE 10: Intracellular fluid pressure distribution at different times in the deep layer (a) at 0 s, (b) at 20 s, (c) at 30 s, (d) at 50 s, (e) at 80 s, and (f) at 100 s.

stress loading over a period of 15–17 s, the compressive stress was concentrated in the periphery of the cell at 15 s, stress concentration transitioning to the cell interior at 17 s with a transition period of liquid pressure distribution at 16 s (Figure 9). The abnormal distribution of

cellular fluid pressure may result in gene expression and metabolic abnormalities.

In the deep layer, the pressure within the chondrocytes within the same cartilage lacuna was different (Figure 10). Generally speaking, the largest pressure change was observed

in the uppermost chondrocytes and greatest absolute pressure in the lowermost chondrocytes. In the initial stage of loading, intracellular pressure was smaller than the peripheral pressure, but that pressure increased as loading time increased, meanwhile peripheral pressure decreased gradually. The pressure of the liquid changed periodically with loading time, being subject to a certain degree of hysteresis. Conversely, the distribution of pressure varied from internal to the periphery in the lowermost chondrocytes, basically corresponding to the load frequency. Therefore, chondrocytes at different positions within the same cartilage lacuna exhibited different responses to loading.

#### 4. Discussion

As it is not possible to receive the results of clinical use of the experimental technology of cartilage repair over a short time, it is very important to ascertain the mechanical environment of chondrocytes and their surroundings in vivo using multiscale finite element numerical simulation analysis [16]. In this paper, the micromechanical environment of the chondrocytes in a defect repair zone under cyclic compressive loading was studied for the first time. The simulation results can help explore the causes of tissue-engineered cartilage failure and guide clinical rehabilitation.

Using a multiscale method, the biomechanical properties of chondrocytes in intact articular cartilage and tissue from medial meniscectomy were studied under joint load [16–18]. The focus of study in this paper was on the response of chondrocytes to compressive loading (static or cyclic). In addition, the difference in shape and distribution of chondrocytes in cartilage lacunae in different layers was considered using modeling. According to our simulation, the mechanical environment of chondrocytes is depth-dependent under cyclic loading and the properties of the defect repair significantly alter the mechanical environment of the repair zone, factors not previously considered in former studies.

The mechanical response of chondrocytes depends on the applied load characteristics. According to our findings, the effect of cyclic loading on the micromechanical environment of chondrocytes was different in the different layers in the defect repair zone. The current simulations may be used as a guideline to predict the effect of cyclic variation on the micromechanical environment of chondrocytes as a function of position.

The results of studies of the biomechanical environment of chondrocytes have not been reported during previous repairs of defects using tissue engineering. Thus, the contours of strain distribution were compared with those obtained from high-throughput multiscale 3D models of chondrocytes, with at most differences of 2.5% [18], to ensure validity of the results of subsequent analysis.

In this paper, there are still some deficiencies, ignoring the fine structure of the cell and regarding chondrocytes as a continuum. In fact, the cell structure can be regarded as a type of tension integration model comprising an inner liquid core and organelles [14]. The liquid phase accounts for 95% of the cell, the solid phase 5%. A chondrocyte stent is composed of a fibrous structure of protein filaments and

microtubules, similar to an umbrella frame supporting the umbrella surface. Our assumption was that the artificial cartilage was fully bonded with the host cartilage, whereas cracking and incomplete adhesion may characterize the actual situation. The selected load frequency range is smaller than that experienced in vivo. Subsequent studies need also to consider the effects of different shapes and depth of repair on the biomechanical environment of chondrocytes.

#### 5. Conclusions

In this paper, the changes in stress and fluid pressure in chondrocytes within different regions of a repaired area of cartilage were analyzed. The mechanical environment of each layer of chondrocytes in the host cartilage was inevitably affected. The two-phase solid and liquid structure of articular cartilage provides it with viscoelastic properties. Due to the cumulative effect of the cartilage structure, the lowest frequency (0.01 Hz) of the cyclic load caused increased notable stress concentration in chondrocytes in the superficial layer, while the amplitude of cyclic stress response curve of chondrocytes reduced with increasing frequency. There was no significant effect of cyclic loading on the distribution of intracellular fluid pressure in the superficial layer, but the influence of cyclic loading on the distribution of liquid pressure in the middle and deep layers was significant. However, the change in the mechanical environment of chondrocytes in each layer is likely to result in damage to the chondrocytes or to result in abnormal gene expression.

In general, the elastic modulus of artificial cartilage had little effect on the mechanical environment under the same cyclic loading frequency. Clinically, following the repair using tissue-engineered cartilage, the appropriate loading frequency can be used to produce a reasonable mechanical environment for the chondrocytes, which can help patients to take appropriate exercise for rehabilitation.

#### Conflicts of Interest

The authors indicated no potential conflicts of interest.

#### Acknowledgments

Financial support for this work has been provided by the National Natural Science Foundation of China (NSFC, nos. 11402172 and 11432016).

#### References

- [1] L. Q. Wan and V. C. Mow, "Cellular and molecular biomechanics: the articular cartilage paradigm—a review," *Journal of Mechanical Biomechanics*, vol. 23, no. 1, pp. 1–18, 2008.
- [2] M. Wong and D. R. Carter, "Articular cartilage functional histomorphology and mechanobiology: a research perspective," *Bone*, vol. 33, no. 1, pp. 1–13, 2003.
- [3] L. G. Alexopoulos, L. A. Setton, and F. Guilak, "The biomechanical role of the chondrocyte pericellular matrix in articular cartilage," *Acta Biomaterialia*, vol. 1, no. 3, pp. 317–325, 2005.
- [4] A. Vahdati and D. R. Wagner, "Implant size and mechanical properties influence the failure of the adhesive bond

- between cartilage implants and native tissue in a finite element analysis," *Journal of Biomechanics*, vol. 46, no. 9, pp. 1554–1560, 2013.
- [5] S. Arumugam, B. B. Karthik, R. Chinnuswami et al., "Transplantation of autologous chondrocytes ex-vivo expanded using thermoreversible gelation polymer in a rabbit model of articular cartilage defect," *Journal of Orthopaedics*, vol. 14, no. 2, pp. 223–225, 2017.
- [6] R. Y. Zhang, X. T. Lin, P. Z. Liu, Y. H. Luo, and X. Y. Zheng, "Nursing care of articular cartilage defects treated with autologous chondrocytes and collagen type I scaffold," *Journal of Practical Orthopaedics*, vol. 22, no. 12, pp. 1150–1152, 2016.
- [7] M. S. Venäläinen, M. E. Mononen, J. Salo et al., "Quantitative evaluation of the mechanical risks caused by focal cartilage defects in the knee," *Scientific Reports*, vol. 6, article 37538, 2016.
- [8] K. F. Guilak and M. A. Haider, "The dynamical environment of the chondrocyte: a biphasic finite element model cell-matrix interactions under cyclic compressive loading," *Journal of Biomechanical Engineering*, vol. 130, no. 6, article 061009, 2008.
- [9] B. Kurz, M. Jin, P. Patwari, D. M. Cheng, M. W. Lark, and A. J. Grodzinsky, "Biosynthetic response and mechanical properties of articular cartilage after injurious compression," *Journal of Orthopaedic Research*, vol. 19, no. 6, pp. 1140–1146, 2001.
- [10] M. D. Buschmann, Y. J. Kim, M. Wong, E. Frank, E. B. Hunziker, and A. J. Grodzinsky, "Stimulation of aggrecan synthesis in cartilage explants by cyclic loading is localized to regions of high interstitial fluid flow," *Archives of Biochemistry & Biophysics*, vol. 366, no. 1, pp. 1–7, 1999.
- [11] P. P. Weafer, N. H. Reynolds, S. P. Jarvis, and J. P. McGarry, "Single cell active force generation under dynamic loading – part I: AFM experiments," *Acta Biomaterialia*, vol. 27, pp. 236–250, 2015.
- [12] N. H. Reynolds and J. P. McGarry, "Single cell active force generation under dynamic loading – part II: active modelling insights," *Acta Biomaterialia*, vol. 27, pp. 251–263, 2015.
- [13] A. B. Lennon, "Effect of membrane stiffness and cytoskeletal element density on mechanical stimuli within cells: an analysis of the consequences of ageing in cells," *Computer Methods in Biomechanics and Biomedical Engineering*, vol. 18, no. 5, pp. 468–476, 2015.
- [14] D. E. Ingber, "Cell structure and hierarchical systems biology," *Journal of Cell Science*, vol. 116, no. 7, pp. 1157–1173, 2003.
- [15] J. Z. Wu and W. Herzog, "Analysis of the mechanical behavior of chondrocyte in unconfined compression tests for cyclic loading," *Journal of Biomechanics*, vol. 39, no. 4, pp. 603–616, 2006.
- [16] H. Y. Zhou, Y. C. Li, and C. T. Wang, "Multiscale computation on mechanical environment of chondrocytes," *Journal of Medical Biomechanics*, vol. 27, no. 4, pp. 392–397, 2012.
- [17] P. Tauska, E. M. Mika, and R. K. Krhonen, "A multi-scale finite element model for investigation of chondrocyte mechanics in normal and medial meniscectomy human knee joint during walking," *Journal of Biomechanics*, vol. 48, no. 8, pp. 1397–1406, 2015.
- [18] A. Erdemir, C. Bennetts, S. Davis, A. Reddy, and S. Sibole, "Multi-scale cartilage biomechanics: technical challenges in realizing a high-throughput modeling and simulation workflow," *Interface Focus A Theme Supplement of Journal of the Royal Society Interface*, vol. 5, no. 2, article 20140081, 2015.
- [19] C. Bandejas and A. Completo, "A mathematical model of tissue-engineered cartilage development under cyclic compressive loading," *Biomechanics and Modeling in Mechanobiology*, vol. 16, no. 2, pp. 651–666, 2017.
- [20] V. C. Mow, S. C. Kuei, W. M. Lai, and C. G. Armstrong, "Biphasic creep and stress relaxation of articular cartilage in compression: theory and experiments," *Journal of Biomechanical Engineering*, vol. 102, no. 1, pp. 73–84, 1980.
- [21] R. M. Schinagl, D. Gurskis, A. C. Chen, and R. L. Sah, "Depth-dependent confined compression modulus of full-thickness bovine articular cartilage," *Journal of Orthopaedic Research Official Publication of the Orthopaedic Research Society*, vol. 15, no. 4, pp. 499–506, 1997.
- [22] L. P. Li, M. D. Buschmann, and A. Shiraziadl, "A fibril reinforced nonhomogeneous poroelastic model for articular cartilage: inhomogeneous response in unconfined compression," *Journal of Biomechanics*, vol. 33, no. 12, pp. 1533–1541, 2000.
- [23] D. L. Zignego, A. A. Jutila, M. K. Gelbke, D. M. Gannon, and R. K. June, "The mechanical microenvironment of high concentration agarose for applying deformation to primary chondrocytes," *Journal of Biomechanics*, vol. 47, no. 9, pp. 2143–2148, 2014.
- [24] N. Hosoda, N. Sakai, Y. Sawae, and T. Murakami, "Finite element analysis of articular cartilage model considering the configuration and biphasic property of the tissue," *IFMBE Proceedings*, vol. 23, pp. 1883–1887, 2009.
- [25] H. Y. Zhou, *Biotribological Mechanism of Articular Cartilage*, Shanghai Jiao Tong University, Shanghai, China, 2013.
- [26] S. Q. Zhang, C. Q. Zhang, L. L. Gao, L. Li, M. L. Sun, and J. Li, "Mechanical state research on articular cartilage defects by tissue engineering," *Journal of Clinical Rehabilitative Tissue Engineering Research*, vol. 15, no. 20, pp. 3629–3632, 2011.
- [27] H. Muhammad, Y. Rais, N. Miosge, and E. M. Ornan, "The primary cilium as a dual sensor of mechanochemical signals in chondrocytes," *Cellular and Molecular Life Sciences*, vol. 69, no. 13, pp. 2101–2107, 2012.

## Research Article

# Influence of Gait Speeds on Contact Forces of Lower Limbs

Xin Wang,<sup>1</sup> Yue Ma,<sup>2</sup> Bo Yi Hou,<sup>3</sup> and Wing-Kai Lam<sup>4</sup>

<sup>1</sup>Department of Kinesiology, Shenyang Sport University, Shenyang 110102, China

<sup>2</sup>Key Laboratory of Impression Evidence Examination and Identification Technology, Criminal Investigation Police University of China, Shenyang 110854, China

<sup>3</sup>Ningwu Country Senior High School, Ningwu 036700, China

<sup>4</sup>Li Ning Sports Science Research Centre, Beijing 101111, China

Correspondence should be addressed to Xin Wang; [shin\\_wangwx@126.com](mailto:shin_wangwx@126.com)

Received 23 February 2017; Revised 27 April 2017; Accepted 30 April 2017; Published 9 July 2017

Academic Editor: Wenxin Niu

Copyright © 2017 Xin Wang et al. This is an open access article distributed under the Creative Commons Attribution License, which permits unrestricted use, distribution, and reproduction in any medium, provided the original work is properly cited.

While walking with fast speed aims to promote health and fitness of individuals, the potential risk on lower limb joint loading across walking speed is still unknown. In order to determine the joint contact force loading associated with different walking speeds, fifteen young male and fifteen female participants performed barefoot walking across different speeds (regular = 1.1 m/s, medium = 1.4 m/s, and fast = 1.7 m/s). The synchronized motion and ground reaction force (GRF) data were captured by Codamotion capture system and AMTI force platform. All kinematics and GRF information were input to the AnyBody musculoskeletal model to determine 3-dimensional knee contact forces. The results showed that increased walking speed was associated with a greater proximal-distal and anterior-posterior GRF during early impact phase, implying that the joint stability is more demanding at higher walking speed conditions ( $P < 0.05$ ). In addition, higher proximal-distal and anterior-posterior knee contact forces were found when participants were walking at higher speeds ( $P < 0.05$ ). Therefore, the risk of knee cartilage and ligament damage associated with the increased knee contact forces should require further attention.

## 1. Introduction

Power walking or speed walking, which is defined as the walking with an individual's fastest speed, is a popular fitness exercises among cities in China. The aim of speed walking is to promote heart rate fitness and endurance of participants. However, most participants only concern about the walking speed, but pay little attention on the impact load on lower limbs, which may result in higher injury risks especially in the ankle or knee joint [1–3]. Landing movements during walking [4], running [5], gymnastics [6], volleyball [7], soccer [8], and Australian football [9] have been studied using with kinetic, kinematic, and electromyography parameters for the evaluation of injury risk or performance. In these studies, ground reaction forces (GRF) and the ankle and knee joint forces provide key and fundamental information to understand loading [10, 11]. Furthermore, these force parameters are often compared among different subject groups to identify biomechanical differences [12–14].

Regarding the research on walking biomechanics, the researchers [15, 16] have found that when walking at higher gait speeds, the walking kinematics and kinetics would be changed. Higher gait speeds were associated with larger step length, knee flexion angle, and peak plantar pressure, but with smaller ankle range of motion and shorter total contact times. In addition, other kinetic studies have shown that increased gait speed is related to greater peak plantar pressure and GRF [17–19]. Particularly, Sneyers et al. [20] found that the walking speed had significant impact on the foot pressure at the forefoot and rearfoot regions. Bertseh et al. [21] pointed out that distributing foot plantar pressure evenly can effectively reduce foot injuries. In the similar vein, too soft or hard, the interface material used may cause damage on the foot and affect performance.

In order to determine how GRF influences the risk of injury during landing or performance during push off in different movements, various methods have been used to show high correlations among GRF, lower limb kinematics, and

TABLE 1: Participant information.

	Male ( $n = 15$ )	Female ( $n = 15$ )
Age (years)	$24.6 \pm 1.19$	$24.8 \pm 1.13$
Height (m)	$1.76 \pm 0.02$	$1.64 \pm 0.02$
Weight (kg)	$68.3 \pm 1.72$	$54.0 \pm 1.92$
BMI ( $\text{kg}/\text{m}^2$ )	$21.8 \pm 0.34$	$20.0 \pm 0.41$
Shoe size (UK)	$42.0 \pm 0.00$	$37.0 \pm 0.00$

related muscle activities, suggesting that the GRF has to be overcome or absorbed by musculature supporting of the ankle, knee, and hip joints [22, 23]. However, all of these kinetic and kinematic parameters should be integrated to evaluate the risk of injury and performance in a certain movement task. In addition, the GRF and knee contact forces are the common indicators for interpreting and explaining by the athletic trainers, scientists, and physicians. Furthermore, Haight et al. [15] compared peak tibiofemoral joint contact force (TF) when obese and non-obese participants walking at different speeds and on different slopes. Their results showed that at fast gait speeds, participants would effectively reduce the maximum TF at uphill walking compared with that at level walking. The TF was reduced by 23% (from 2352 N to 1811 N) and 35% (from 1994 N to 1303 N) for obese and nonobese participants, respectively. Nevertheless, TF is the resultant knee force (KF) exerted on the knee, and it is believed that 3D KF information can provide additional information for better estimation of knee joint loadings during walking at different speeds. Hence, the purpose of this study was to investigate joint kinematics, GRF, and KF in each of proximal-distal, anterior-posterior, and medial-lateral components when participants are walking at regular, medium, and fast paces.

## 2. Experimental Work

Fifteen young healthy male participants and fifteen female participants were recruited to perform five successful barefoot walking trials at different speeds (regular 1.1 m/s, medium 1.4 m/s, and fast 1.7 m/s) [4, 16]. The information of participants is listed in Table 1.

GRF were recorded at 1000 Hz using force plate (AMTI, Watertown, MA, USA) and synchronized motion data were captured at 250 Hz using Codamotion infrared capturing system. In order to minimize the body mass effect, all kinematics data were normalized with body mass. All the GRF and lower limb kinematics information were input to determine 3D knee joint forces using the AnyBody musculoskeletal model (AnyBody Modeling System v.6.0.3, Anybody Technology A/S, Aalborg, Denmark) in all walking speed conditions. The model consisted of the pelvis, legs, and feet and 35 leg muscles was built according to the previous studies [11–14]. All statistical analyses were performed with SPSS 19.0 (SPSS, Chicago, IL, USA). 2 (gender)  $\times$  3 (speed) mixed ANOVA were performed on gait parameters to determine if there was any interaction, gender, and speed effects. All data

were presented as mean  $\pm$  standard deviation. Significant level was set at  $P = 0.05$ . Since no gender effect was evident for force parameters, we pooled all subject data and performed one-way repeated measures ANOVA to assess the speed effect on each of the KF components.

## 3. Results

**3.1. Kinematics Data.** In Table 2, longer step length, faster stride frequency, and shorter stance time were observed at a faster walking speed, compared with those at regular and medium speed conditions ( $P < 0.05$ ). Shorter stance, heel contact, forefoot, and toe-off times were found at fast speed compared with those at regular speed condition ( $P < 0.05$ ). Regarding gender effect, male participants had longer step length ( $P < 0.01$ ) and higher stride frequency compared with female participants ( $P < 0.01$ ).

In Table 3, as walking speeds increased, larger dorsiflexion and smaller knee flexion were found at all contact phases ( $P < 0.05$ ). At forefoot contact, knee flexion was decreased by  $10^\circ$  in fast speed compared with that in the other two speed conditions ( $P < 0.05$ ). At toe-off, larger ankle and knee joint angles are at fast speed compared with those at regular speed ( $P < 0.01$ ).

**3.2. GRF Data.** Since no gender effect was evident for each GRF variable, we pooled all participant data to further assess the GRF components associated with walking speeds [7, 8]. In general, there are two peak curves shown for vertical GRF. Figure 1 shows that first peak occurred at heel contact which was about 23 to 26% of stance. The second peak occurred at forefoot contact which was about 73 to 77% of the stance or maximum knee extension during take-off.

In Table 4, a greater first peak of vertical GRF was observed in fast speed condition compared with that in regular speed condition ( $P < 0.05$ ), but no significant speed difference was found for the second peak of vertical GRF. In addition, higher walking speed resulted in higher anterior-posterior and medial-lateral GRF ( $P < 0.01$ ).

**3.3. 3D Knee Joint Contact Forces.** Table 5 shows that participants walking at fast speed experienced higher both proximal-distal and anterior-posterior KFs during heel contact phase compared to those at regular and medium speed conditions ( $P < 0.01$ ). However, medial-lateral KF was not different among speed conditions ( $P > 0.05$ ). The proximal-distal KF was increased by 20.75% and 64.62% when compared to that of medium and fast speeds, respectively. However, there was no main effect of speed in 3D KF at toe-off phase ( $P > 0.05$ ). Regarding the proximal-distal KF, we further calculated the proximal-distal KF the relationship between proximal-distal KF and walking speed using polynomial fitting ( $R^2 = 0.89$ ). The regression model (Figure 2) shows that when walking speed was below 1.2 m/s, only gentle change of the KF would be observed; when the speed exceeded 1.4 m/s, the KF would increase rapidly.

$$Y = 1983.3X^2 - 4228.3X + 3480.3. \quad (1)$$

TABLE 2: Temporal-distance parameters change of stride across different speed conditions.

	Gender	Regular (1.1 m/s)	Medium (1.4 m/s)	Fast (1.7 m/s)
Step length (m)	Male	1.20 ± 0.09	1.30 ± 0.13 <sup>△</sup>	1.50 ± 0.11 <sup>**</sup>
	Female	1.14 ± 0.10	1.21 ± 0.14	1.30 ± 0.17 <sup>^</sup>
Stride frequency	Male	98.21 ± 9.37	114.45 ± 8.21 <sup>△△</sup>	131.12 ± 10.22 <sup>**^^</sup>
	Female	104.12 ± 10.48	125.42 ± 14.26 <sup>△△^</sup>	141.14 ± 9.12 <sup>**^^</sup>
Stance time (%)	Male	59.86 ± 3.13	57.31 ± 4.75 <sup>△</sup>	54.34 ± 4.06 <sup>**</sup>
	Female	60.21 ± 2.99	56.82 ± 2.79 <sup>△</sup>	54.99 ± 3.53 <sup>**</sup>
Heel contact time (%)	Male	15.49 ± 5.31	17.56 ± 5.13	19.32 ± 5.76 <sup>*</sup>
	Female	15.29 ± 6.22	18.90 ± 3.53	20.13 ± 4.21 <sup>*</sup>
Forefoot contact time (%)	Male	17.29 ± 4.99	15.30 ± 4.72	14.86 ± 4.32
	Female	18.22 ± 3.15	16.14 ± 4.68	15.86 ± 4.15
Toe-off time (%)	Male	33.32 ± 4.21	35.74 ± 4.32	37.35 ± 6.76 <sup>*</sup>
	Female	31.68 ± 7.88	34.15 ± 6.07	35.99 ± 4.13 <sup>*</sup>

\* means the significant difference between regular and fast speeds. △ means the significant difference between medium and fast speeds. ^ means the significant difference between genders. \*\* means the significant difference between regular and fast speeds and  $p < 0.01$ . △△ means the significant difference between medium and fast speeds and  $p < 0.01$ . ^^ means the significant difference between genders and  $p < 0.01$ .

TABLE 3: Ankle and knee joint angle positions at different contact phases across different speed conditions.

	Gender	Regular (1.1 m/s)		Medium (1.4 m/s)		Fast (1.7 m/s)	
		Ankle	Knee	Ankle	Knee	Ankle	Knee
At heel contact	Male	104.01 ± 6.21	171.36 ± 7.23	102.31 ± 6.23	169.49 ± 7.43	99.68 ± 5.57 <sup>*</sup>	168.80 ± 7.28
	Female	103.45 ± 7.31	172.64 ± 8.23	100.35 ± 5.14	168.15 ± 4.77	98.18 ± 8.65 <sup>*</sup>	168.24 ± 70.42
At forefoot contact	Male	99.50 ± 5.23	164.98 ± 6.74	99.52 ± 6.21	160.56 ± 5.45 <sup>△</sup>	97.66 ± 4.32	155.70 ± 6.12 <sup>**</sup>
	Female	98.12 ± 6.22	163.67 ± 3.11	97.32 ± 2.71	158.45 ± 6.89 <sup>△</sup>	96.33 ± 3.19	156.33 ± 4.12 <sup>**</sup>
At heel off	Male	93.67 ± 4.25	171.55 ± 6.54	94.32 ± 3.25	170.37 ± 6.47	97.05 ± 5.12 <sup>*</sup>	169.72 ± 6.54
	Female	91.22 ± 5.12	172.01 ± 4.62	92.22 ± 4.12	169.99 ± 4.89	95.48 ± 5.14 <sup>*</sup>	169.34 ± 5.31
At toe-off	Male	108.60 ± 8.21	153.78 ± 6.54	111.65 ± 7.23	155.36 ± 7.56 <sup>△</sup>	116.58 ± 9.12 <sup>*</sup>	159.43 ± 6.32 <sup>**</sup>
	Female	107.2 ± 7.35	154.43 ± 7.45	109.31 ± 4.77	156.33 ± 8.45 <sup>△</sup>	115.22 ± 7.23 <sup>*</sup>	160.47 ± 6.77 <sup>**</sup>

\* means the significant difference between regular and fast speeds. △ means the significant difference between medium and fast speeds. \*\* means the significant difference between regular and fast speeds and  $p < 0.01$ .

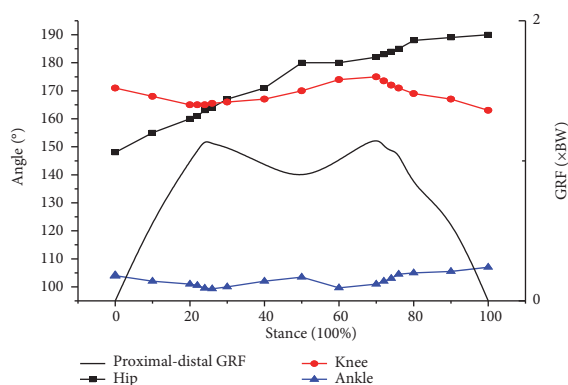


FIGURE 1: Typical joint angles and vertical GRF in regular speed.

### 4. Discussion

This study investigated kinematics, GRF, and KF when participants were walking at regular, medium, and fast paces. Our results showed that increasing of speed was associated with higher strike frequency, shorter stance time, and increased the vertical and anterior-posterior GRF during

impacts. To attenuate the impact forces, one body would elicit larger knee and ankle joint flexion at high walking speed condition compared with those at regular speed condition. In addition, increased knee extension angle during toe-off was found in high speed compared with that in regular speed condition. The extended knee angle and short stance time are thought to be beneficial to generate more muscle power to push body forward in a fast walking pace. Previous studies [19, 27] compared the EMG activation pattern (onset time and magnitude) of hamstring and semimembranosus during different walking conditions. They suggested that at early stance, the greater semimembranosus EMG was found in uphill walking compared with that in level walking and that the estimated muscle forces were increased across the walking speeds.

Regarding GRF in walking, the current results indicated that the vertical GRF was greater than anterior-posterior or medial-lateral GRF, which is in line with most research on walking. Typically, there are two peaks in vertical GRF curve [1]. The first peak force ( $F_1$ ) is produced by the impact of the heel and is always of lower magnitude than that of the second peak force ( $F_3$ ), which occurs at forefoot contact phase [3].

TABLE 4: Vertical GRF across different walking speeds.

		Regular (1.1 m/s)	Medium (1.4 m/s)	Fast (1.7 m/s)
Vertical GRF (BW)	First peak ( $F_1$ )	$1.17 \pm 0.44^\#$	$1.37 \pm 0.42$	$1.52 \pm 0.53^*$
	Minimum ( $F_2$ )	$0.86 \pm 0.22$	$0.76 \pm 0.23$	$0.62 \pm 0.26^*$
	Second peak ( $F_3$ )	$1.10 \pm 0.23$	$1.08 \pm 0.18$	$1.09 \pm 0.16$
Anterior-posterior GRF (BW)	First minimum ( $F_4$ )	$-0.08 \pm 0.03$	$-0.10 \pm 0.06^\Delta$	$-0.13 \pm 0.05^{**}$
	Peak ( $F_5$ )	$0.17 \pm 0.04$	$0.19 \pm 0.05^\Delta$	$0.22 \pm 0.05^{**}$
	Second minimum ( $F_6$ )	$-0.23 \pm 0.06$	$-0.25 \pm 0.05$	$-0.27 \pm 0.07^*$
Medial-lateral GRF (BW)	First peak ( $F_7$ )	$0.06 \pm 0.03$	$0.06 \pm 0.04^\Delta$	$0.08 \pm 0.03^*$
	Second peak ( $F_8$ )	$0.04 \pm 0.03$	$0.05 \pm 0.03^\Delta$	$0.07 \pm 0.04^{**}$

\* means the significant difference between regular and fast speeds.  $\Delta$  means the significant difference between medium and fast speeds. \*\* refers to the significant difference between regular and fast speeds and  $p < 0.01$ . # refers to the significant difference between regular and medium speeds and  $p < 0.05$ .

TABLE 5: Peak knee contact forces (KF) across different walking speeds.

		Regular (1.1 m/s)	Medium (1.4 m/s)	Fast (1.7 m/s)
Heel contact	Proximal-distal KF (BW)	$2.12 \pm 0.51$	$2.56 \pm 0.48^{\Delta\Delta}$	$3.49 \pm 0.53^{**}$
	Anterior-posterior KF (BW)	$0.70 \pm 0.15$	$0.81 \pm 0.17^{\Delta\Delta}$	$1.23 \pm 0.26^{**}$
	Medial-lateral KF (BW)	$0.43 \pm 0.09$	$0.45 \pm 0.12$	$0.45 \pm 0.10$
Toe-off	Proximal-distal KF (BW)	$3.39 \pm 0.57$	$3.39 \pm 0.49$	$3.41 \pm 0.54$
	Anterior-posterior KF (BW)	$1.06 \pm 0.13$	$1.08 \pm 0.17$	$1.11 \pm 0.26$
	Medial-lateral KF (BW)	$0.72 \pm 0.13$	$0.73 \pm 0.12$	$0.75 \pm 0.16$

\*\* means the significant difference between regular and fast speeds and  $p < 0.01$ .  $\Delta\Delta$  means the significant difference between medium and fast speeds and  $p < 0.01$ .

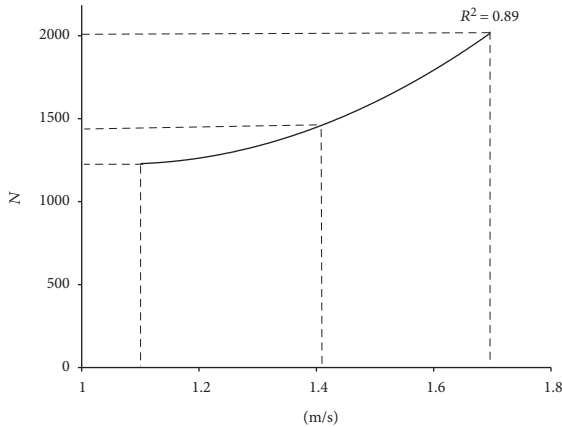


FIGURE 2: Relationship between proximal-distal KF across walking speed.

However it remains debating how GRF peaks would influence the risk of impact injury on lower limbs. It is likely that increased first impact GRF peak is related to plantar load on the heel. For regular walking speed, about  $3.3 \text{ kg/cm}^2$  of the plantar load can be absorbed by heel pad [28]. Plantar loads increase with walking speed. When one person walks with a long period of time, fat at heel pad is gradually shrinking and the heel and foot may be susceptible to damage. During the toe-off phase, knee and ankle extension have to be increased for better transfer of muscular power [29]. The current results indicated that increased walking speed has little

influence on vertical GRF ( $F_3$ ), but has impact anterior-posterior GRF that facilitate faster forward movement.

In addition, the present findings showed the maximum knee contact force had two obvious peaks, which supported the findings measured using embedded sensors [24, 25]. In the present study, at fast walking speed, the proximal-distal and anterior-posterior KF were above three and one times body weight, respectively. These results are in line with a previous study [3, 25], which had obese and nonobese participants walking at fast speed (1.75 m/s) and at slow speed uphill (0.75 m/s,  $6^\circ$  inclined surface) and showed the peak TF was about 3.12 BW. In addition, the maximum knee contact force (2645 N or 3.0 BW) was occurred in 40% of the contact phase [30, 31]. Furthermore, KF become larger across walking speeds regardless of the obese or nonobese participants [15]. Considering the skeletal muscle system may not be fast enough to react and attenuate impact forces effectively, the participants may be exposed to higher risk of knee joint injury.

When interpreting our results, it is important to consider several limitations in our study. First, only young participants were recruited and hence our kinematics findings may not be applicable to the older adults. Second, the surface EMG data were not matched with actual activation of specific lower extremity muscles. A needle EMG or other techniques should be used to explain the change of activity of the leg muscles in different walking speed conditions. Future study should generalize the relationship among 3D knee contact forces, muscle cocontraction, and joint kinematics during walking in different age populations.

## 5. Conclusions

Fast walking is characterized as longer step length, faster step frequency, and shorter stance time. Participants walking at higher speed exhibited greater vertical and anterior-posterior GRF during stance phase, which may challenge walking stability and therefore elicited higher knee joint contact forces. Although fast walking is encouraged to build up fitness, the potential risk of knee cartilage and ligament injuries associated with increased knee contact forces should need further attention.

## Conflicts of Interest

The authors declare that there is no conflict of interest regarding the publication of this paper. None of the authors declare competing financial interests.

## Authors' Contributions

The study was designed by Xin Wang and Yue Ma. Participant recruitment was supervised by Xin Wang and Wing-Kai Lam. Data were collected and analyzed by Bo Yi Hou, Xin Wang, and Yue Ma. Data interpretation and manuscript preparation were undertaken by Wing-Kai Lam, Xin Wang, Bo Yi Hou, and Yue Ma. All authors have read and approved the final version of the manuscript and agree with the order of the authorship.

## Acknowledgments

This work was supported by Key Laboratory of Impression Evidence Examination and Identification Technology, Criminal Investigation Police University of China, Education Department of Liaoning (UPRP20140845), and Shenyang Sport University (XKFX1503).

## References

- [1] W. Niu and Y. Fan, "Terrain stiffness and ankle biomechanics during simulated half-squat parachute landing," *Aviation, Space and Environmental Medicine*, vol. 84, no. 12, pp. 1262–1267, 2013.
- [2] G. A. Mothersole, J. B. Cronin, and N. K. Harris, "Key prerequisite factors influencing landing forces in netball," *Strength and Conditioning Journal*, vol. 35, no. 2, pp. 47–54, 2013.
- [3] Z. F. Lerner, D. J. Haight, M. S. DeMers, W. J. Board, and R. C. Browning, "The effects of walking speed on knee joint loading estimated via musculoskeletal modeling," *Journal of Applied Biomechanics*, vol. 30, no. 2, pp. 197–205, 2014.
- [4] J. H. Hollman, R. H. Brey, T. J. Bang, and K. R. Kaufman, "Does walking in a virtual environment induce unstable gait an examination of vertical ground reaction forces," *Gait Posture*, vol. 26, no. 2, pp. 289–294, 2007.
- [5] Y. Jung, M. Jung, J. Ryu, S. Yoon, S. K. Park, and S. Koo, "Dynamically adjustable foot-ground contact model to estimate ground reaction force during walking and running," *Gait & Posture*, vol. 3, no. 45, pp. 62–68, 2016.
- [6] J. G. Seegmiller and S. T. McCaw, "Ground reaction forces among gymnasts and recreational athletes in drop landings," *Journal of Athletic Training*, vol. 38, no. 4, pp. 311–314, 2003.
- [7] R. W. Bisseling, A. L. Hof, S. W. Bredeweg, J. Zwerver, and T. Mulder, "Relationship between landing strategy and patellar tend in opathy in volleyball," *British Journal of Sports Medicine*, vol. 41, no. 7, article e8, 2007.
- [8] N. Cortes, S. Morrison, B. L. Van Lunen, and J. A. Onate, "Landing technique affects knee loading and position during athletic tasks," *Journal of Science and Medicine in Sport*, vol. 15, no. 2, pp. 175–181, 2012.
- [9] E. Scase, J. Cook, M. Makkissi, B. Gabbe, and L. Shuck, "Teaching landing skills in elite junior Australian football: evaluation of an injury prevention strategy," *British Journal of Sports Medicine*, vol. 40, no. 10, pp. 834–838, 2006.
- [10] W. Niu, Y. Wang, Y. He, and Y. Fan, "Biomechanical gender differences of the ankle joint during simulated half-squat parachute landing," *Aviation, Space, and Environmental Medicine*, vol. 81, no. 8, pp. 761–767, 2010.
- [11] P. J. McNair, H. Prapavessis, and K. Callendar, "Decreasing landing forces: effect of instruction," *British Journal of Sports Medicine*, vol. 34, no. 4, pp. 293–296, 2000.
- [12] W. Niu, T. Feng, C. Jiang, L. Wang, and M. Zhang, "Effects of prophylactic ankle supports on vertical ground reaction force during landing: a meta-analysis," *Journal of Sports Science and Medicine*, vol. 15, no. 2, pp. 1–10, 2016.
- [13] S. N. Zhang, B. T. Bates, and J. S. Dufek, "Contributions of lower extremity joints to energy dissipation during landings," *Medicine & Science in Sports & Exercise*, vol. 32, no. 4, pp. 812–819, 2000.
- [14] W. Niu, M. Zhang, Y. Fan, and Q. Zhao, "Dynamic postural stability for double-leg drop landing," *Journal of Sports Sciences*, vol. 31, no. 10, pp. 1074–1081, 2013.
- [15] D. J. Haight, Z. F. Lerner, W. J. Board, and R. C. Browning, "A comparison of slow, uphill and fast, level walking on lower extremity biomechanics and tibia femoral joint loading in obese and non-obese adults," *Journal of Orthopaedic Research*, vol. 8, pp. 324–356, 2014.
- [16] J. M. Burnfield, C. D. Few, O. S. Mohamed, and J. Perry, "The influence of walking speed and foot wear on plantar pressures in older adults," *Clinical Biomechanics*, vol. 19, pp. 78–84, 2004.
- [17] L. W. Keijser, "The effect of various subject characteristics on plantar pressure pattern," *Foot and Ankle Biomechanics*, vol. 13, pp. 65–72, 2014.
- [18] A. Taylor, H. B. Menz, and A. M. Keenan, "The influence of walking speed on plantar pressure measurements using the two-step gait initiation protocol," *The Foot*, vol. 14, pp. 49–55, 2004.
- [19] G. L. Warren, R. M. Maher, and E. J. Higbie, "Temporal patterns of plantar pressures and lower-leg muscle activity during walking: effect of speed," *Gait and Posture*, vol. 19, pp. 91–100, 2004.
- [20] C. J. Sneyers, R. Lysens, H. Feys, and R. Andries, "Influence of mala ligament of feet on the plantar pressure pattern in running," *Foot & Ankle*, vol. 4, no. 28, pp. 624–632, 1995.
- [21] C. Bertseh, H. Unger, W. Winkelmann, and D. Rosenbaum, "Evaluation of early walking patterns from plantar pressure distribution measurements," *Gait and Posture*, vol. 19, no. 3, pp. 235–242, 2004.
- [22] O. Hideshima, *External Ankle Supports Alter Kinematics and Kinetics during Drop-Jump Landing and Forward-Jump Landing Tasks*, North Dakota State University of Agriculture and Applied Science, 2014.

- [23] W. Niu, T. Feng, C. Jiang, and M. Zhang, "Peak vertical ground reaction force during two-leg landing: a systematic review and mathematical modeling," *BioMed Research International*, vol. 2014, Article ID 126860, 10 pages, 2014.
- [24] L. Lohmander, A. Östenberg, M. Englund, and H. Roos, "High prevalence of knee osteoarthritis, pain, and functional limitations in female soccer players twelve years after anterior cruciate ligament injury," *Arthritis and Rheumatism*, vol. 50, no. 10, pp. 3145–3152, 2004.
- [25] D. J. Haight, Z. F. Lerner, W. J. Board, and R. C. Browning, "A comparison of slow, uphill and fast, level walking on lower extremity biomechanics and tibiofemoral joint loading in obese and nonobese adults," *Journal of Orthopaedic Research*, vol. 32, no. 2, pp. 324–330, 2014.

## Research Article

# Effects of Pectus Excavatum on the Spine of Pectus Excavatum Patients with Scoliosis

WeiHong Zhong,<sup>1,2</sup> JinDuo Ye,<sup>1,2</sup> JingJing Feng,<sup>1,2</sup> LiYang Geng,<sup>1,2</sup> GuangPu Lu,<sup>1,2</sup> JiFu Liu,<sup>3</sup> and ChunQiu Zhang<sup>1,2</sup>

<sup>1</sup>Tianjin Key Laboratory of the Design and Intelligent Control of the Advanced Mechatronical System, Tianjin University of Technology, Binshuixi Road, No. 391, Tianjin 300384, China

<sup>2</sup>Tianjin Key Laboratory for Control Theory & Applications in Complicated Systems, Tianjin University of Technology, Binshuixi Road, No. 391, Tianjin 300384, China

<sup>3</sup>Military General Hospital of Beijing PLA, Beijing 100026, China

Correspondence should be addressed to WeiHong Zhong; zhong426@126.com

Received 24 February 2017; Revised 13 April 2017; Accepted 30 April 2017; Published 3 July 2017

Academic Editor: Ming Zhang

Copyright © 2017 WeiHong Zhong et al. This is an open access article distributed under the Creative Commons Attribution License, which permits unrestricted use, distribution, and reproduction in any medium, provided the original work is properly cited.

**Background.** There is high risk in the correction surgery of pectus excavatum with scoliosis because of the lack of the correction mechanism of pectus excavatum with scoliosis. This study performed a comprehensive analysis about the impact that pectus excavatum had on scoliosis and elaborated its biomechanical mechanism in pectus excavatum patients with scoliosis. **Methods.** 37 pectus excavatum patients were selected. According to age, Haller index of pectus excavatum, offset coefficient, vertical position, sternal torsion angle, and asymmetric index, 37 patients were, respectively, divided into 2 compared groups. The result was statistically calculated. **Results.** The scoliosis incidence and severity did not correlate with Haller index, offset coefficient, vertical position, sternal torsion angle, and asymmetric index of pectus excavatum, and there was no statistical significance between the two compared groups. **Conclusions.** The incidence and severity of scoliosis in PE patients with scoliosis have nothing to do with the geometric parameters of pectus excavatum but correlate with age. The scoliosis will aggravate with the increase of age. The heart may provide an asymmetric horizontal force to push the spines to the right. The mechanism of how the biomechanical factors exert influences on spines needs to be further investigated to keep the spine stable.

## 1. Background

Pectus excavatum (PE) is the most frequently observed congenital deformity of the chest which is characterized, in most cases, by a deep depression of the sternum in the anterior thoracic wall. There is a high percentage of scoliosis associated with PE [1, 2]. William Rainey Johnson reported that about more than 20% of PE patients had scoliosis [3]. In addition, surgical correction for PE has become more prevalent with the development of the minimally invasive Nuss procedure [4]. Due to the integrality of the anterior and posterior thorax, the Nuss procedure not only corrects concavity of the anterior region of the thorax through the placement of bars but also has dynamic effects on the spine in asymmetric

PE [5], which means PE correction may be accompanied by the risk of scoliosis generation or aggravation. We need to investigate the relationship between PE and scoliosis and to find how PE affects the spine in PE patients, especially in PE patients with scoliosis.

Up to now, no comprehensive analysis about the impact that PE has on scoliosis has been performed, although precious research has involved correlation among scoliosis, age, and severity of PE [6]. Being the accompanying symptom or the postoperative complications, the effecting factors of PE on scoliosis and the relationship between scoliosis and age and so on have not been studied in the past. This study aims to analyze the influences that all the geometric parameters of the congenital PE have on scoliosis and to

propose rational suggestions for studying out operation plans so as to offer essential help for surgeons to perform specific surgical procedures and it also tries to elaborate the biomechanical mechanisms of pectus excavatum.

## 2. Methods

**2.1. Patients.** The selection of patients was performed by referring to radiographic or computed tomographic images collected preoperatively. From patients of PE who underwent the Nuss procedure at the Military General Hospital of Beijing PLA from February 2009 to March 2014, a total of 37 patients (22 males and 15 females) with an asymmetry of the thorax and a mild to moderate deformity of the spine (with a Cobb angle  $\leq 30^\circ$ ) were selected, and we excluded patients having platy thorax and barrel chest. The patients were between the age of 4 and 44 in this study.

**2.2. Measurement.** In this study, spiral computerized tomography scan was employed and preoperative CT scans of 37 patients were collected and saved in Digital Image and Communication in Medicine (DICOM) format. Then, the preoperative CT images were inputted into the medical image 3D reconstruction software Mimics10.01 (Materialise, Belgium), in which all radiological measurements were conducted.

Cobb angle was defined as a coronal plane deformity on anteroposterior plain radiographs to describe scoliosis. As a general rule, a Cobb angle of  $10^\circ$  is the minimum angulation for scoliosis.

Haller index (HI) was created in 1987 by Drs. Haller, Kramer, and Lietman [6]. The index is the ratio of the transverse diameter and the anteroposterior diameter is

$$\text{Haller index} = \frac{T}{A} \times 100, \quad (1)$$

where  $T$  is the transverse diameter of the inside ribcage and  $A$  is the distance between the sternum and vertebrae (Figure 1). A normal Haller index is about 2.5. If the Haller index is greater than 3.25, the surgery is warranted [7]. The mean Haller index reported by Kelly et al. was  $5.15 \pm 2.32$  [8].

For the analysis and investigation of the degree and different types of asymmetric deformity of the chest, symmetry index (SI) and sternal rotation angle have been widely used [9, 10]. Symmetry index is defined as the following ratio:

$$\text{Symmetric index} = \frac{R}{L} \times 100. \quad (2)$$

The sternal torsion angle (STA) against the horizontal line was measured. The right-side depression of the chest wall, which indicates the counter clockwise twist of the sternum, is expressed as positive (Figure 1). Either the right- or left-side depression of PE, the sternal rotation angle that is less than  $5^\circ$ , greater than  $5^\circ$  but less than  $15^\circ$ , greater than  $15^\circ$  but less than  $25^\circ$ , and over  $25^\circ$  is regarded as symmetrical, mild, moderate and severe torsion, respectively [10].

In addition, to investigate the degree of asymmetric deformity of PE in the horizontal direction, offset coefficient (OC) was defined to describe the excursion degree of the

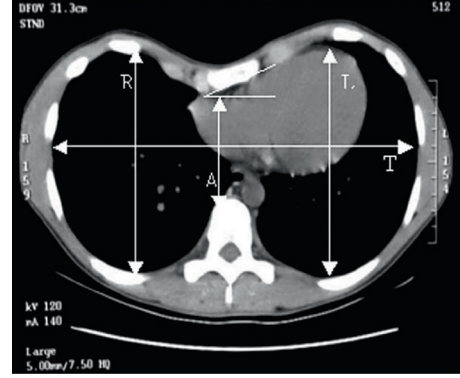


FIGURE 1: Demonstration of measurements made using Mimics on computer. The Haller index is calculated by  $T/A$  and asymmetry index by  $R/L \times 100$ . The sternal torsion angle is marked and represents moderate degree of torsion ( $+24.9^\circ$ ). All measurements were measured at maximum distances except for  $A$ , which was measured as the minimum distance between the anterior surface of the vertebral column and the deepest portion of the sternum.

center of PE apex (Figure 2). The offset coefficient is a hundred times the ratio of the distance  $A$  and distance  $B$ ; its mathematical relationship is shown as follows:

$$\text{Offset coefficient} = \frac{A}{B} \times 100, \quad (3)$$

where  $A$  is the distance between the left chest wall and the apex and  $B$  is the distance between the apex and the right chest wall. A normal offset coefficient is 1. If it is not equal to 1, meaning that PE is asymmetric and its apex offsets to the left or the right side. If it is more than 1, the PE apex is on the left chest; if less than 1, the PE apex is on the right chest. The greater the absolute value of the offset coefficient away from 1 is, the more severe the excursion of PE apex is.

**2.3. Groups.** 37 patients were divided into two age groups preoperatively—the child group ( $n = 15$ ) and the adult group ( $n = 22$ ). The ages were no more than 18 years old in the child group and older than 18 years old in the adult group.

According to the severity of PE, 37 patients were divided into two Haller index groups preoperatively—the mild group ( $n = 5$ ) and the severe group ( $n = 32$ ). The Haller indexes in the mild group were greater than 3.25 and less than 3.5, while the Haller indexes in the severe group were greater than or equal to 3.5.

37 patients were divided into 2 offset coefficient groups: the mild group ( $n = 7$ ), in which offset coefficient was less than or equal to 10; the sever group ( $n = 30$ ), in which offset coefficient was more than 10.

37 patients were divided into 2 sternal torsion angle groups: the mild group ( $n = 17$ ), in which the sternal torsion angle was less than  $25^\circ$ ; the sever group ( $n = 20$ ), in which the sternal torsion angle was equal to or more than  $25^\circ$ .

**2.4. Statistical Methods.** For statistical calculations, SPSS Version 20.0 for Windows (SPSS Inc., IBM Company, Chicago, IL) was used.

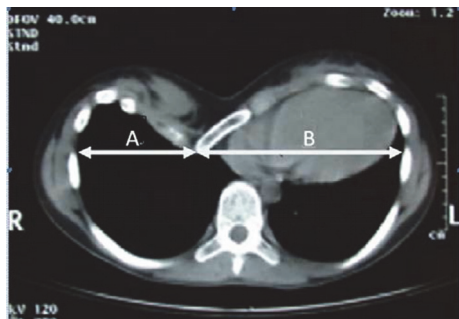


FIGURE 2: Demonstration of measurements using Mimics on computer. Offset coefficient calculated by  $A/B \times 100$  is shown in the figure. This CT of a 12-year-old patient exhibited 57 of the offset coefficient; PE apex is on the right chest.

2.5. *Ethical Committee.* This study has obtained approval by the school of mechanical engineering, Tianjin University of Technology and Military General Hospital of Beijing PLA. There is no conflict of interest to be declared.

### 3. Results and Discussion

3.1. *Scoliosis and Age.* The results of the scoliosis incidence in the age groups were shown in Table 1. 28 (75.68%) of the 37 patients had scoliosis with a Cobb angle greater than  $10^\circ$ . We found that 20 (71.42%) out of the 28 patients with a Cobb angle greater than  $10^\circ$  were from adults. The cases of scoliosis distributed in the adult group were with a percentage of 90.91%, and the incidence of scoliosis was 53.33% in children less than 18 years. The computed result ( $p < 0.05$ ) shows that there is a statistically significant difference between the two age groups, suggesting that age is correlated with scoliosis incidence.

Further statistics ( $p = 0.044$ ) indicated that there was also a statistically significant difference between the two age groups in the severity of scoliosis. The Cobb angles in the adult group were obviously higher than those in the child group (Figure 3).

In this study, the incidence of scoliosis in the adult group was 90.91% (Table 1), which is much higher than that in the child group (53.33%); the severity of scoliosis correlated with age. It is well known that the deformity of PE, including the depth and area of depression and degree of sternal twist causing asymmetry of the chest, progresses as the patients grow [10]. According to the biomechanical principle that deformity results from internal force, generation and change of horizontal internal force will result in the occurrence and change (including improvement or aggravation) of scoliosis. We speculate that the scoliosis deformity caused by internal force which the PE exerted on the thoracic cage progresses with age. The reason may be that as the patients grow older, their bones become more calcified, their costal cartilages become more brittle and more ossified, the internal horizontal force generated by PE pushes the heart more greatly, and the counterforce generated by the heart pushes the spine [6]; hence, the scoliosis becomes more severe.

TABLE 1: Age distribution of patients with a Cobb angle greater than  $10^\circ$ .

	Child group $\leq 18$ Y ( $n = 15$ )	Adult group $\geq 18$ Y ( $n = 22$ )	$p$
Scoliosis case (100%)	8 (53.33%)	20 (90.91%)	0.017 < 0.05

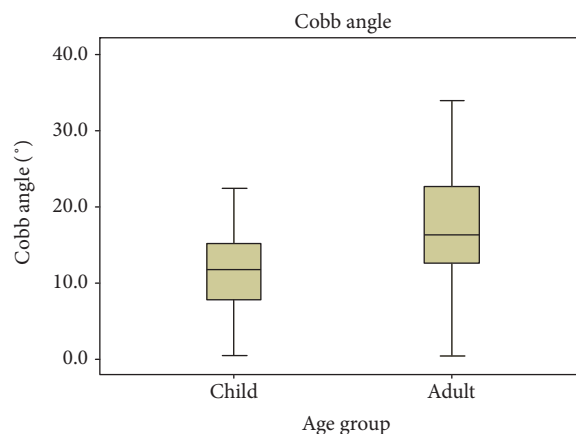


FIGURE 3: Cobb angles of the two age groups. Significant difference was found between the child and adult groups ( $p < 0.05$ ).

3.2. *Scoliosis and Haller Index.* With regard to the severity of the PE, 25 (89.29%) of the 28 scoliosis patients (Cobb angle  $> 10^\circ$ ) were from the severe HI group ( $HI > 3.5$ ), in which the incidence of scoliosis was 78.13%, while 3 scoliosis cases were from the mild HI group ( $3.25 < HI \leq 3.5$ ), in which the incidence of scoliosis was 60.00%. The computed result ( $p = 0.105$ ) shows that there is no statistic significant difference between the mild HI group and the severe HI group (Table 2).

Further statistics ( $p = 0.117$ ) indicated that there was also no statistically significant difference between the two Haller index groups in the severity of scoliosis.

In this study, the incidence and the severity of scoliosis have nothing to do with the Haller index of PE. In the view of mechanics principle, the severity of PE described in the form of Haller index has no impact on the internal force exerted on the thoracic cage, except on the depth of the concavity. It cannot break the balance between PE and the spine. So, it cannot change the incidence and the severity of scoliosis.

3.3. *Scoliosis and Offset Coefficient.* The results of the scoliosis incidence in offset coefficient groups were shown in Table 3. 23 (82.14%) of the 28 scoliosis cases were from the severe OC group ( $OC > 10$ ), in which the incidence of scoliosis was 76.67%, while 5 scoliosis cases were from the mild OC group ( $OC \leq 10$ ), in which the incidence of scoliosis was 66.67%. There is no statistic significant difference between the mild OC group and the severe OC group ( $p > 0.05$ , Table 3).

Further statistics ( $p = 0.813$ ) indicated that there was also no statistically significant difference between the two offset coefficient groups in the severity of scoliosis.

TABLE 2: Haller index distribution of patients with a Cobb angle greater than 10°.

	Mild group 3.2 < HI < 3.5 (n = 5)	Severe group HI ≥ 3.5 (n = 32)	p
Scoliosis case (100%)	3 (60%)	25 (78.13%)	0.105 > 0.05

TABLE 3: Offset coefficient distribution of patients with a Cobb angle greater than 10°.

	Mild OC group OC ≤ 10 (n = 7)	Severe OC group OC > 10 (n = 30)	p
Scoliosis case (100%)	5 (66.67%)	23 (76.67%)	1.000 > 0.05

TABLE 4: Vertical position distribution of pectus excavatum of patients with a Cobb angle greater than 10°.

	High group 1-6 (n = 18)	Low group 7-12 (n = 19)	p
Scoliosis case (100%)	16 (88.89%)	12 (63.16%)	1.000 > 0.05

Offset coefficient describes the excursion degree of PE apex in the horizontal direction, which represents the horizontal parameter of the PE position. Different offset coefficients contribute nothing to the generation and change of the horizontal internal force which is exerted to the spine. So, it can not have any effect on the incidence and severity of scoliosis.

3.4. *Scoliosis and Vertical Position of PE.* The cases of vertical position distribution of PE in the high group (n = 19) and the low group (n = 18) were close to equal (Table 4), and the scoliosis incidence in every group was 88.89% and 63.16%, respectively. The computed result indicated that the incidence and severity of scoliosis did not correlate with the vertical position of PE (p > 0.05), and there was no statistical significance between the high group and the low group in the incidence and severity of scoliosis (p > 0.05).

The results of the scoliosis direction in different vertical position of PE group were shown in Table 5. In 20 (54.05%) of 37 patients of PE, their scoliosis bent to the right, 8 (21.62%) patients bent to the left, and 9 (24.32%) patients had no scoliosis or their Cobb angles were no more than 10°. The computed result indicated that the direction of scoliosis correlated with the vertical position of PE (p = 0.024), and there was a statistical significance in the direction of scoliosis between the high and low groups (p < 0.05).

Vertical position distribution describes the parameter in the vertical direction of PE, and it does not change the horizontal internal force which can make the thoracic vertebra stable in the horizontal direction. So, it has nothing to do

TABLE 5: Vertical position distribution of patients with different scoliosis directions.

	High group 1-6 (n = 18)	Low group 7-12 (n = 19)	p
Scoliosis bent to the right (100%)	13 (72.22%)	7 (36.84%)	0.027 < 0.05
Scoliosis bent to the left (100%)	3 (16.67%)	5 (26.32%)	
No scoliosis	2 (11.11%)	7 (36.84%)	

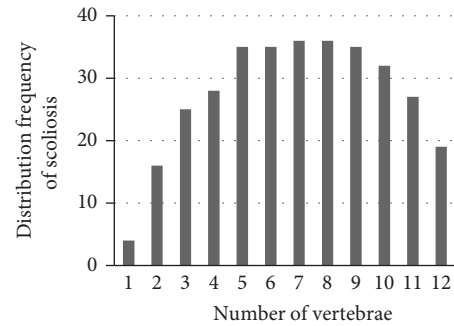


FIGURE 4: Distribution of the scoliosis vertical position in 37 patients in the form of thoracic vertebra number.

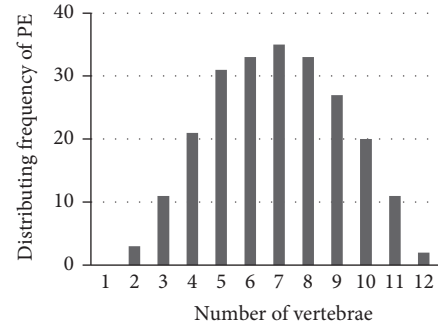


FIGURE 5: Distribution of the PE vertical position in 37 patients in the form of thoracic vertebra number.

with the incidence and the severity of scoliosis. But different vertical positions can affect the direction of scoliosis. We noticed that scoliosis is almost located at the same horizontal level with PE (Figures 4 and 5). Scoliosis in 37 patients mainly distributed from the 3rd to 11th thoracic vertebrae. 20 (71.43%) of the 28 PE with scoliosis patients bent to the right, and their PE position is mainly located in the scope of the 4th to 10th thoracic vertebrae where the heart was located. PE pushes the heart to the left, with the transformation of the ribs and costa cartilages; the internal counter force generated by the heart will push the thoracic vertebrae to the right, which means the heart may provide an asymmetric horizontal force to push the spines to the right in pectus excavatum patients with scoliosis. Thus, most of the scoliosis patients bent to the right, which verified that the heart

TABLE 6: Sternal torsion angle distribution of pectus excavatum of patients with a Cobb angle greater than 10°.

	Mild group STA < 25° (n = 17)	Severe group STA ≥ 25° (n = 20)	p
Scoliosis case (100%)	11 (64.71%)	17 (85.00%)	0.251 > 0.05

TABLE 7: Asymmetric index distribution of pectus excavatum of patients with a Cobb angle greater than 10°.

	Mild group 0.95 < SI < 1.05 (n = 22)	Severe group SI ≥ 1.05 or SI ≤ 0.95 (n = 15)	p
Scoliosis case (100%)	19 (86.36%)	9 (60.00%)	0.118 > 0.05

contributes to the internal force causing the spine bent to the right [6].

### 3.5. Scoliosis and Sternal Torsion Angle and Symmetric Index.

The results of the scoliosis incidence in two sternal torsion angle groups were shown in Table 6. We found that 20 (54.05%) of the 37 scoliosis cases were from the severe STA group (STA ≥ 25°), in which the incidence of scoliosis was 85.00%, while 17 (45.94%) scoliosis cases were from the mild STA group (STA < 25°), in which the incidence of scoliosis was 64.71%. There is no statistically significant difference between the mild STA group and the severe STA group ( $p > 0.05$ , Table 6).

Further statistics ( $p > 0.05$ ) indicated that there was also no statistically significant difference between the two STA groups in the severity of scoliosis.

The results of the scoliosis incidence in the two symmetric index groups were shown in Table 7. Only 9 (32.14%) of the 28 scoliosis cases were in the severe SI group (SI ≥ 1.05 or SI ≤ 0.95), in which the incidence of scoliosis was 60.00%, while 19 (67.86%) of the scoliosis cases were from the mild SI group (SI < 1.05), in which the incidence of scoliosis was 68.63%. There is no statistically significant difference between the SI mild group and the SI severe group ( $p > 0.05$ , Table 7).

Further statistics ( $p > 0.05$ ) indicated that there was also no statistically significant difference between the two symmetric index groups in the severity of scoliosis.

Sternal torsion angle and symmetric index describe the asymmetric degree of the chest, and they do not correlate with the incidence and severity of scoliosis because they cannot break the balance of the horizontal internal force between PE and scoliosis. Hence, they devote nothing to the generation and change of the horizontal internal force and have no effect on the incidence and severity of scoliosis.

## 4. Conclusions

The incidence and severity of scoliosis in PE patients with scoliosis correlate with age. The scoliosis will aggravate with the

increase of age, which suggests that once the scoliosis is diagnosed, treatment should be conducted as soon as possible.

The incidence and severity of scoliosis do not correlate with the Haller index, offset coefficient, vertical position of pectus excavatum, asymmetric index, and sternal torsion angle, which means that the severity of pectus excavatum and the horizontal and vertical positions of pectus excavatum have nothing to do with the geometric parameters of PE and do not have any effects on the incidence and severity of scoliosis. Namely, three-dimensional positional parameters and the symmetry of pectus excavatum in the human chest have no impact on scoliosis.

The heart may provide an asymmetric horizontal force to push the spines to the right, which means the mechanical factor may be the pathogenesis in pectus excavatum patients with scoliosis.

## Abbreviations

PE:	Pectus excavatum
CT:	Computed tomography
DICOM:	Digital Imaging and Communications in Medicine
HI:	Haller index
OC:	Offset coefficient
STA:	Sternal torsion angle
AI:	Asymmetric index.

## Conflicts of Interest

The authors declare that they have no competing interests.

## Authors' Contributions

WeiHong Zhong sorted the data and wrote the manuscript. JiFu Liu led and performed all the surgeries. Other authors collected and sorted the data. All authors read and approved the final manuscript.

## Acknowledgments

This study was supported by the National Nature Science Foundation of China (11372221, 11432016, and 11402172).

## References

- [1] D. Jaroszewski, D. Notrica, L. McMahon, D. E. Steidley, and C. Deschamps, "Current management of pectus excavatum: a review and update of therapy and treatment recommendations," *The Journal of the American Board of Family Medicine*, vol. 23, pp. 230–239, 2010.
- [2] A. K. Saxena, K. Schaarschmidt, J. Schlee, J. J. Morcate, and G. H. Willital, "Surgical correction of pectus excavatum: the Münster experience," *Langenbeck's Archives of Surgery*, vol. 384, pp. 187–193, 1999.
- [3] W. R. Johnson, D. Fedor, and S. Singhal, "Systematic review of surgical treatment techniques for adult and pediatric patients with pectus excavatum," *Journal of Cardiothoracic Surgery*, vol. 9, p. 25, 2014.

- [4] D. Nuss and M. Kuhn, "Our approach: minimally invasive surgical repair of pectus excavatum," *Contemporary Surgery*, vol. 63, pp. 444–451, 2007.
- [5] T. Nagasao, M. Noguchi, J. Miyamoto et al., "Dynamic effects of the Nuss procedure on the spine in asymmetric pectus excavatum," *The Journal of Thoracic and Cardiovascular Surgery*, vol. 140, no. 6, pp. 1294–1299, 2010.
- [6] Y. Wang, G. Chen, L. Xie et al., "Mechanical factors play an important role in pectus excavatum with thoracic scoliosis," *Journal of Cardiothoracic Surgery*, vol. 7, p. 118, 2012.
- [7] R. E. Kelly Jr., "Pectus excavatum: historical background, clinical picture, preoperative evaluation and criteria for operation," *Seminars in Pediatric Surgery*, vol. 17, pp. 181–193, 2008.
- [8] R. E. Kelly, M. J. Goretsky, and R. Obermeyer, "Twenty-one years of experience with minimally invasive repair of pectus excavatum by the Nuss procedure in 1215 patients," *Annals of Surgery*, vol. 252, no. 6, pp. 1072–1081, 2010.
- [9] M. J. Cartoski, D. Nuss, M. J. Goretsky et al., "Classification of the dysmorphology of pectus excavatum," *Journal of Pediatric Surgery*, vol. 41, pp. 1573–1581, 2006.
- [10] A. Yoshida, S. Uemura, M. Yamamoto, H. Nouse, H. Kuyama, and Y. Muta, "Correlation of asymmetric chest wall deformity and growth in patients with pectus excavatum," *Journal of Pediatric Surgery*, vol. 48, pp. 771–775, 2013.

## Research Article

# A Strain Feedback Compensation Method during Cell Tensile Experiments

**Rong Zhou, Yunshu Yang, Wenzhuo Zhang, and Yuanwen Zou**

*College of Materials Science and Engineering, Sichuan University, Chengdu 610065, China*

Correspondence should be addressed to Yuanwen Zou; [zyw@scu.edu.cn](mailto:zyw@scu.edu.cn)

Received 13 February 2017; Revised 30 March 2017; Accepted 23 April 2017; Published 18 June 2017

Academic Editor: Liping Wang

Copyright © 2017 Rong Zhou et al. This is an open access article distributed under the Creative Commons Attribution License, which permits unrestricted use, distribution, and reproduction in any medium, provided the original work is properly cited.

Cell tensile technique is an important and widely used tool in cell mechanical research. However, the strain control condition in traditional tensile experiments is not satisfied and would result in big errors. These strain errors will seriously impact the experimental accuracy and decrease the reliability and comparability of experimental results. In order to achieve the accurate strain control of the membrane during stretching, a strain feedback compensation method based on the digital image correlation is proposed in this paper. To evaluate the effect of the proposed compensation method, a series of stretching experiments in different strains ranging from 5% to 20% were performed. The results showed that our proposed method significantly decreased the errors of strain control. These results indicate that the strain feedback compensation method is very effective in controlling strain and can greatly improve the experimental accuracy.

## 1. Introduction

Biomechanical stimuli have been utilized to enhance the growth, strength, and functionality of engineered tissues [1, 2]. At the cellular level, mechanical stretching could vitally control over cell morphology, proliferation, lineage commitment, and differentiation [3, 4]. Cell tensile technique is a fundamental method to exert tension on cells. The cells adhered to the membrane would follow its deformation and thereby experience tensile strain. Obviously, the strain control of the membrane is of great importance. In traditional tensile experiments, operators calculate the moving distance of the clamps according to the initial clamping length of the membrane and the desired strain and then use it to control the motors. However, the actual strain condition of this method is not satisfied. Zhang et al. [5] proposed that the clamp-to-clamp strain was greater than the actual measured strain because the indicated displacement included the sliding of the specimen within clamps. Colombo et al. [6] analyzed the strain field of Flexcell system for different waveforms and frequencies and demonstrated that the measured strains of membranes showed notable differences between both the inputs and

the outputs of the Flexcell software. Riehl et al. [7] summarized many types of cell tensile devices and concluded that the strain conducted to the membrane is affected by numerous factors, including membrane properties, clamping method, and mode of loading. However, most of these devices, not only commercial devices but also lab-special devices tailored to experimental need, are short of direct strain monitor or feedback. Inaccurate strain control would decrease the repeatability and comparability of experimental results. To address this gap, a strain feedback compensation method is proposed in this paper for accurate strain control.

The strain feedback compensation method needs an accurate measurement to monitor strain. The commonly used strain measuring methods about membranes involve the marker tracking measurement, the resistance strain gauge measurement, and the finite element analysis. In the marker tracking measurement [6], several predefined markers on the specimen are used to track the position change and thereby compute the strain. The accuracy of this method completely depends on the distribution of markers. Therefore, it is often regarded as a rough measuring technique. The resistance strain gauge measurement [8] is a basic strain measurement,

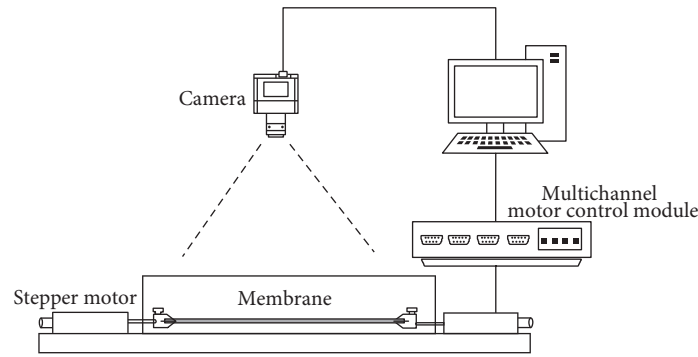


FIGURE 1: Experimental set-up.

but it is not suitable for the cell tensile experiments. On the one hand, the membrane is a kind of soft material so that the use of any contact-type sensor would affect its movement. On the other hand, this method is not able to measure the full-field strain distribution. The finite element analysis is commonly used in biomechanical researches. Many researchers [9–11] have used this method to compute the strain field of membranes. However, the finite element analysis is a theoretical calculation based on the models under ideal assumptions. It cannot be used to monitor actual strain during tensile experiments. Therefore, we need a highly accurate and contactless full-field strain measuring technique.

The digital image correlation (DIC) method is a widely used optical measuring technique [12]. Since it was first proposed [13, 14] in the 1980s, DIC has been extensively used in many fields [15–18]. Comparing to other strain measuring techniques, DIC has several advantages, such as fewer requirements in experimental environment, the absence of contact with specimen, and its high accuracy. In recent studies, many researchers focused on applying DIC to monitor the strain of biological tissues [19–24] and made great progress. Therefore, DIC is very suitable for monitoring the strain during the tensile experiments.

Thus, we proposed a strain feedback compensation method based on DIC to accurately control the strain of membranes during the tensile experiments. Five silicon rubber membranes with artificial speckle pattern were used as stretching specimens. Different strains ranging from 5% to 20% were conducted to the membranes. DIC was used for strain measurement during the whole process of strain feedback compensation at each strain level. The strain measured by DIC was then used as the parameter to compute the necessary compensation distance. Finally, we compared the strains measured before and after compensation with the target strains to evaluate the effect of our method.

## 2. Materials and Methods

**2.1. Experimental Set-Up.** The material of our membrane specimens is silica gel plate (DONGGUANSHI ZHISHENG RUBBER PRODUCTS Co. LTD), which is colorless and transparent. Therefore, the first step is to create the speckle pattern artificially. Lionello et al. [25] summarized several methods for creating speckle pattern on biological soft tissue. In this paper, the speckle pattern was made by spraying black

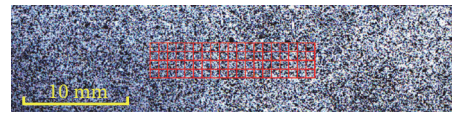


FIGURE 2: Selected region of interest (red rectangle).

and white quick-drying paints from an aerosol can. The white paint was first sprayed on the specimen to obtain a white background. Then, the black paint was sprayed on the specimen to obtain random black spots with a high contrast. In order to generate a fine mist of paints to ensure a uniform and random distribution of small paint dots, the distance between the nozzle and the specimen was maintained at more than 0.5 m [5]. Through these steps, the high-contrast speckle pattern suitable for DIC analysis was made. The size of the membrane specimens was 25 mm × 160 mm (thickness of 0.4 mm).

As depicted in Figure 1, the membrane was placed between two stainless steel clamps. During the experiments, an industrial camera (JHSM1400f, Shenzhen Jinghang Technology Co. Ltd.) was used for image capture. The images were recorded at the selected resolution of 2048 × 1536 pixels. Two stepper motors fixed on an optical platform were used to perform uniaxial stretching. A self-designed multichannel motor control module was used to control these stepper motors. A computer equipped with a 4-port RS-232 USB-to-serial converter (UPort 1450, MOXA) was programmed to provide the accurate synchrony of stepper motors via RS-232 serial ports and the image capture via USB. The acquired images were then processed with the DIC algorithm to calculate the strain field of the membrane.

**2.2. Digital Image Correlation.** DIC is an optical-numerical full-field measuring technique with subpixel accuracy. The method measures the displacement and strain field by tracking the same points (or pixels) between the two images recorded before and after deformation [12]. The image captured before and after stretching is called the reference image and deformed image, respectively. In general, the process of DIC involves three main steps. First, a region of interest (ROI) should be defined, which is further divided into evenly spaced virtual grids. As shown in Figure 2, the red rectangle shows the ROI and virtual grids. The intersection points of

the virtual grids are selected as the center point of each subset. The subset is the matching unit in the DIC algorithm. Next, the reference image and deformed image should be reconstructed by a certain kind of subpixel registration algorithm to further improve the accuracy of DIC. In this paper, the fourth-order keys interpolant (Keys 4) algorithm [26] is used as the subpixel registration algorithm because it has small bias error and negligible rotation error. Finally, a correlation criterion should be defined to evaluate the degree of similarity between the reference and deformed subsets. Pan [27] provided an overview of various correlation criteria used in DIC. In this paper, the zero-normalized sum of squared differences (ZNSSD) was used as the correlation criterion because of its insensitivity to offset and linear scale in illumination lighting. Through the matching process based on ZNSSD, every reference subset would find its target subset in the deformed image, and the displacement and strain field could be obtained.

**2.3. Strain Feedback Compensation Method.** In order to calculate the compensation distance during tensile experiments, the compensation equations of uniaxial tensile stretching are proposed in this paper:

$$\frac{D_t}{S_t} = \frac{D}{S_a}, \quad (1)$$

$$D_t = D + D_c, \quad (2)$$

$$D_c = \frac{D}{S_a} S_t - D, \quad (3)$$

where  $D_t$  is the necessary moving distance of the clamps to achieve the desired strain,  $D$  is the existing distance of the clamps,  $S_a$  is the actual strain measured by DIC,  $S_t$  is the desired target strain, and  $D_c$  is the necessary compensation distance. Equation (1) is based on the assumption that the stretching of the membrane remains in its mechanical linear region. Under the assumption, there is a linear relationship between the clamps' moving distance and the membrane's actual strain. Therefore, the ratio of  $D_t$  to  $S_t$  is equal to the ratio of  $D$  to  $S_a$ . Because the sliding between membrane and the clamps exists,  $D_t$  is not equal to  $D$ . As shown in (2),  $D_t$  is comprised of  $D$  and  $D_c$ . Substituting (2) into (1), the compensation equation (3) can be obtained, with which, the compensation distance  $D_c$  can be calculated.

The detailed process of the strain feedback compensation is shown in Figure 3. First, the image of membrane before stretching should be captured as the reference image. According to  $S_t$  and the initial clamping length of the membrane,  $D$  can be calculated and then used to control the stepper motors. This step is routine in traditional tensile experiments. After stretching, the image of stretched membrane should be captured as the deformed image. By inputting reference image and deformed image into the DIC program,  $S_a$  of the membrane can be calculated. Next,  $S_a$  should be compared with  $S_t$  to determine whether to perform the strain compensation. The judgment criterion is denoted by  $\delta$ , and the threshold is denoted by  $\delta_{th}$ . In practice,  $\delta$  can be set as an absolute error or relative error according to the

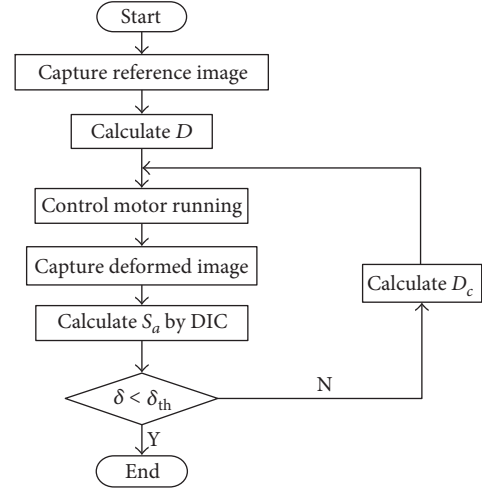


FIGURE 3: Flowchart of the strain feedback compensation process.

experimental requirements. In this paper,  $\delta$  represents the relative error between the actual strains and the target strains and  $\delta_{th}$  is set to be 0.5%. If  $\delta$  is greater than  $\delta_{th}$ , which means that the strain control does not satisfy the accuracy requirement, it is necessary to perform the strain compensation. According to (3), the compensation distance  $D_c$  can be calculated and then used to control the motors to complete compensation. Through the strain feedback compensation method, the strain can be accurately controlled.

### 3. Results and Discussion

In order to evaluate the effect of our proposed strain feedback compensation method, a series of tensile experiments were performed on five specimens at a large strain range from 5% to 20% in increments of 2.5%. The actual strains of all specimens at each strain level were measured by DIC. The strains measured before and after compensation were called the “before compensation” group and the “after compensation” group, respectively. The statistical analysis was performed using  $t$ -test ( $P < 0.01$ ) at each strain level. The results of all specimens are shown in Figures 4–6.

Figure 4 shows the strain field of 5# specimen calculated by DIC before and after compensation at the target strain of 10%. As shown in Figure 4, the strain distribution of both is generally uniform, indicating that the membrane is homogeneous. In addition, most strain values before compensation (see Figure 4(a)) concentrate on 9%, while those after compensation (see Figure 4(b)) concentrate on 10%, demonstrating that the strain compensation method affects the entire stretching region and makes the whole strain field closer to the target value.

All strain results measured before and after compensation are shown in Figure 5. The horizontal axis represents the target strains, and the vertical axis represents the actual strains measured by DIC. Different colors represent different specimens. The solid lines represent the “before compensation” group, and the dashed lines represent the “after compensation” group. In Figure 5, the actual strains of the “before compensation” group show a strong correlation

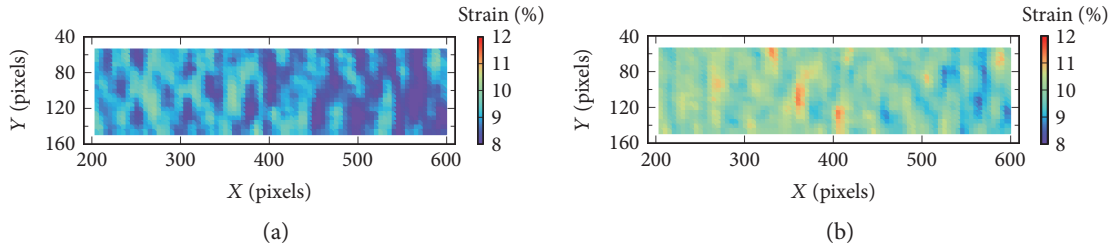


FIGURE 4: Strain field of 5# specimen calculated by DIC before (a) and after (b) compensation at the target strain of 10%.

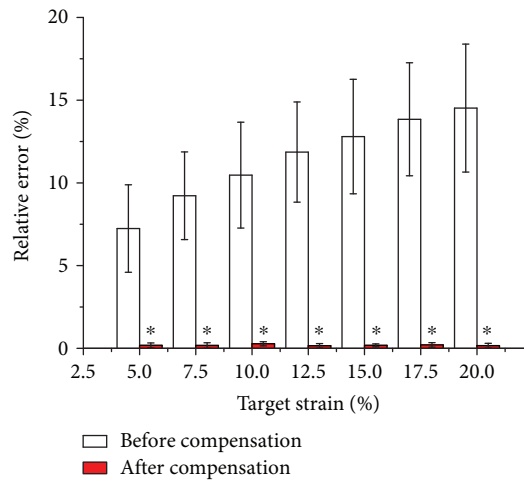
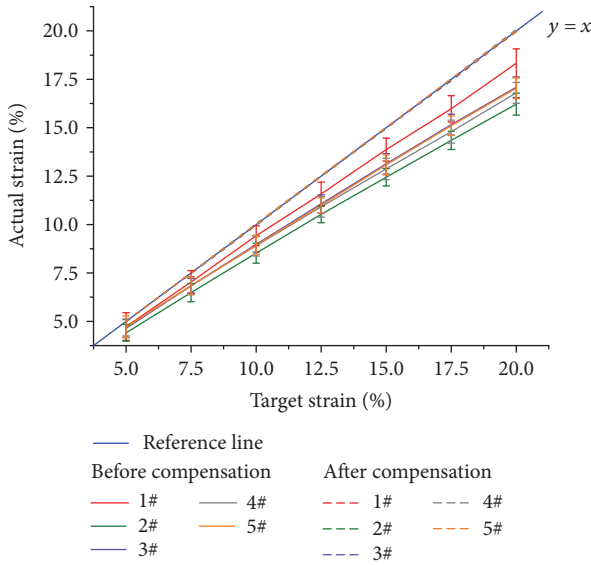


FIGURE 6: Relative error comparison at each strain level. Asterisk (\*) denotes statistically significant difference relative to the corresponding “before compensation” group at  $P < 0.01$ .

FIGURE 5: Strain control comparison. The solid lines represent the “before compensation” group, and the dashed lines represent the “after compensation” group. The error bars of the “after compensation” group are not shown.

( $r = 0.999$ ) with the target strains. This result demonstrates that all specimens remained in their mechanical linear region during the tensile experiments, satisfying the assumption of our strain feedback compensation method. The blue solid line is the reference line ( $y = x$ ), which represents an ideal situation of strain control that the actual strains equals to the target strains. As shown in Figure 5, the solid lines always stay below the reference line and all specimens show the same trend, which means that the errors before compensation mainly result from the systemic errors. Moreover, the dashed lines almost coincide with the reference line, which means that our strain compensation method is very effective.

The relative error comparisons at each strain level are shown in Figure 6. All the relative errors of the “after compensation” group are significantly lower than those of the “before compensation” group, showing statistically significant difference ( $P < 0.01$ ). The relative error of the “before compensation” group increases with the increment of target strains. It is also notable that no matter what the target strain is, the relative error after compensation is always below 0.5%, which demonstrates that the effect of our strain feedback compensation method is very significant.

As mentioned above, the errors before compensation mainly result from systemic errors. Before compensation, the actual strains all stay below the reference line in Figure 5. Yet, the moving distance of the clamps is accurately controlled. That is to say, the clamp-to-clamp strains are always greater than the actual measured strains, indicating that the sliding of clamps is a nonnegligible error source. In this study, the clamped regions of the specimens were marked before clamping and stretching, and the sliding phenomenon was observed. It is known that the sliding is strongly related to the friction force between objects in contact. To moderate the sliding effect and thus reduce the error, the friction force between the clamps and specimen should be increased. In tensile experiments, the friction force between the clamps and specimen is determined by the clamping force and the friction coefficient of the contact surface. In this study, the slopes of the five solid lines in Figure 5 are different, indicating that their sliding effects are different. However, the membrane properties and the clamps are the same among five experiments. The only differences among them are their clamping forces, operated manually, which cannot ensure the same. These results also demonstrate that the clamping force would affect the sliding effect. The clamping force cannot be too small or too large. Too small clamping force cannot ensure reliable clamping while too large force would damage

the membrane, a kind of soft material, leading to unexpected change of mechanical properties of the membrane. However, to the best of our knowledge, there are few studies on how to choose the clamping force in tensile experiments. Besides choosing an appropriate clamping force, increasing the friction coefficient is also a good way to increase the friction force. In previous studies, some approaches were used to strengthen the fixation between specimens and clamps. Gao and Desai [20] utilized the cyanoacrylate, a kind of super glue, to fix the specimen. To minimize the sliding effect of the specimen, Karimi et al. [22] used a pair of coarse sandpaper glued to the lower and upper grippers. King et al. [28] fabricated specific serrated friction grips for tensile tests. Although these methods reduce the sliding effect to some extent, the additional modification of clamps restricts their application.

The proposed method in this paper is independent of the clamps and mechanical stretching instruments. The actual measured strain during stretching is used as feedback to compensate the strain error resulting from sliding. The results in our experiments demonstrate that our method is able to realize accurate strain control using existing stretching instruments without additional modification of clamps. Although the clamping forces for the five specimens cannot stay the same in this study, with our compensation method, the actual strain of the specimens all reach to the expected accuracy at every strain level. In the future, more work can be done in analyzing the fixation and clamping force in cell tensile experiments. However, before the sliding problem is totally solved, the strain monitor and feedback is suggested in tensile experiments in order to ensure the reliability and repeatability of the experiments.

#### 4. Conclusions

In order to achieve accurate strain control, a strain feedback compensation method based on DIC is proposed in this paper. This method is independent of mechanical stretching instruments and can provide accurate strain feedback to help users monitor the strain condition. The compensation distance can be calculated by the proposed compensation equations. To evaluate the effect of our proposed method, a series of stretching experiments in different strains ranging from 5% to 20% were performed. The results showed that the proposed method can significantly decrease the strain errors and improve the experimental accuracy. Accurate strain control will allow researchers to design more complex and precise experiments and enhance the reliability and comparability of the test results.

#### Conflicts of Interest

The authors declare that there is no conflict of interests regarding the publication of this paper.

#### References

[1] H. M. Powell, K. L. Mcfarland, D. L. Butler, D. M. Supp, and S. T. Boyce, "Uniaxial strain regulates morphogenesis, gene

- expression, and tissue strength in engineered skin," *Tissue Engineering Part A*, vol. 16, no. 3, pp. 1083–1092, 2010.
- [2] Y. U. Lee, D. Hayman, E. A. Sprague, and H. C. Han, "Effects of axial stretch on cell proliferation and intimal thickness in arteries in organ culture," *Cellular and Molecular Bioengineering*, vol. 3, no. 3, pp. 286–295, 2010.
- [3] K. S. Kang, S. J. Lee, H. S. Lee, W. Moon, and D. W. Cho, "Effects of combined mechanical stimulation on the proliferation and differentiation of pre-osteoblasts," *Experimental & Molecular Medicine*, vol. 43, no. 6, pp. 367–373, 2011.
- [4] T. M. Maul, D. W. Chew, A. Nieponice, and D. A. Vorp, "Mechanical stimuli differentially control stem cell behavior: morphology, proliferation, and differentiation," *Biomechanics and Modeling in Mechanobiology*, vol. 10, no. 6, pp. 939–953, 2011.
- [5] D. Zhang, C. D. Eggleton, and D. D. Arola, "Evaluating the mechanical behavior of arterial tissue using digital image correlation," *Experimental Mechanics*, vol. 42, no. 4, pp. 409–416, 2002.
- [6] A. Colombo, P. A. Cahill, and C. Lally, "An analysis of the strain field in biaxial Flexcell membranes for different waveforms and frequencies," *Proceedings of the Institution of Mechanical Engineers Part H: Journal of Engineering in Medicine*, vol. 222, no. 8, pp. 1235–1245, 2008.
- [7] B. D. Riehl, J. H. Park, I. K. Kwon, and J. Y. Lim, "Mechanical stretching for tissue engineering: two-dimensional and three-dimensional constructs," *Tissue Engineering Part B Reviews*, vol. 18, no. 4, pp. 288–300, 2012.
- [8] H. Zhang, *The Study on the Biological Effects of Cyclic Substrate Strain on Human Pulmonary Epithelial Cells*, [Ph.D. Dissertation], College of Bioengineering, Chongqing University, P. R. China, 2002.
- [9] J. P. V. Geest, E. S. D. Martino, and D. A. Vorp, "An analysis of the complete strain field within Flexercell™ membranes," *Journal of Biomechanics*, vol. 37, no. 12, pp. 1923–1928, 2004.
- [10] W. G. Zhong, C. Xu, H. L. Mi, and F. Q. Zhang, "Stress analysis of silastic membrane in dynamic strain cell unit," *Journal of Medical Biomechanics*, vol. 22, no. 2, pp. 121–126, 2007.
- [11] X. L. Ma, S. Li, X. Fu et al., "Stress analysis and biocompatibility research on a cell carrier with silicone rubber membrane," *Journal of Medical Biomechanics*, vol. 26, no. 5, pp. 426–431, 2011.
- [12] B. Pan, K. Qian, H. Xie, and A. Asundi, "Two-dimensional digital image correlation for in-plane displacement and strain measurement: a review," *Measurement Science & Technology*, vol. 20, no. 6, p. 062001, 2009.
- [13] W. H. Peters and W. F. Ranson, "Digital imaging techniques in experimental stress analysis," *Optical Engineering*, vol. 21, no. 3, pp. 427–431, 1982.
- [14] T. C. Chu, W. F. Ranson, and M. A. Sutton, "Applications of digital image correlation techniques to experimental mechanics," *Experimental Mechanics*, vol. 25, no. 3, pp. 232–244, 1985.
- [15] F. Hild and S. Rous, "Digital image correlation: from displacement measurement to identification of elastic properties—a review," *Strain*, vol. 42, no. 2, pp. 69–80, 2006.
- [16] N. McCormick and J. Lord, "Digital image correlation," *Materials Today*, vol. 13, no. 12, pp. 52–54, 2010.
- [17] J. Huang, X. Pan, X. Peng et al., "High-efficiency cell-substrate displacement acquisition via digital image correlation method using basis functions," *Optics & Lasers in Engineering*, vol. 48, no. 11, pp. 1058–1066, 2010.

- [18] J. C. Passieux, F. Bugarin, C. David, J. N. Périé, and L. Robert, "Multiscale displacement field measurement using digital image correlation: application to the identification of elastic properties," *Experimental Mechanics*, vol. 55, no. 1, pp. 121–137, 2015.
- [19] D. Zhang and D. D. Arola, "Applications of digital image correlation to biological tissues," *Journal of Biomedical Optics*, vol. 9, no. 4, pp. 691–699, 2004.
- [20] Z. Gao and J. P. Desai, "Estimating zero-strain states of very soft tissue under gravity loading using digital image correlation," *Medical Image Analysis*, vol. 14, no. 2, pp. 126–137, 2010.
- [21] G. Okotie, S. Duenwaldkuehl, H. Kobayashi, M. J. Wu, and R. Vanderby, "Tendon strain measurements with dynamic ultrasound images: evaluation of digital image correlation," *Journal of Biomechanical Engineering*, vol. 134, no. 2, p. 024504, 2012.
- [22] A. Karimi, T. Sera, S. Kudo, and M. Navidbakhsh, "Experimental verification of the healthy and atherosclerotic coronary arteries incompressibility via digital image correlation," *Artery Research*, vol. 16, pp. 1–7, 2016.
- [23] E. Rizzuto, S. Carosio, M. Faraldi, S. Pisu, A. Musarò, and Z. D. Prete, "A DIC based technique to measure the contraction of a skeletal muscle engineered tissue," *Applied Bionics and Biomechanics*, vol. 2016, Article ID 7465095, 7 pages, 2016.
- [24] E. Rizzuto, S. Carosio, and Z. D. Prete, "Characterization of a digital image correlation system for dynamic strain measurements of small biological tissues," *Experimental Techniques*, vol. 40, no. 2, pp. 743–753, 2016.
- [25] G. Lionello, C. Sirieix, and M. Baleani, "An effective procedure to create a speckle pattern on biological soft tissue for digital image correlation measurements," *Journal of the Mechanical Behavior of Biomedical Materials*, vol. 39, pp. 1–8, 2014.
- [26] R. Keys, "Cubic convolution interpolation for digital image processing," *IEEE Transactions on Acoustics Speech & Signal Processing*, vol. 29, no. 6, pp. 1153–1160, 1981.
- [27] B. Pan, "Recent progress in digital image correlation," *Experimental Mechanics*, vol. 51, no. 7, pp. 1223–1235, 2011.
- [28] J. D. King, S. L. York, and M. M. Saunders, "Design, fabrication and characterization of a pure uniaxial microloading system for biologic testing," *Medical Engineering & Physics*, vol. 38, no. 4, pp. 411–416, 2016.

## Research Article

# Biomechanical Property of a Newly Designed Assembly Locking Compression Plate: Three-Dimensional Finite Element Analysis

Jiang-Jun Zhou,<sup>1</sup> Min Zhao,<sup>1</sup> Da Liu,<sup>2</sup> Hai-Ying Liu,<sup>3</sup> and Cheng-Fei Du<sup>3</sup>

<sup>1</sup>Department of Orthopedics, The 184th Hospital of PLA, Spinal Surgery Treatment Center of Nanjing Military Region, Yingtan, Jiangxi Province 335000, China

<sup>2</sup>Department of Orthopedics, General Hospital of Chengdu Command, Chengdu, Sichuan Province 610083, China

<sup>3</sup>Tianjin Key Laboratory for Advanced Mechatronic System Design and Intelligent Control, Tianjin University of Technology, Tianjin 300384, China

Correspondence should be addressed to Cheng-Fei Du; [ddccffb31@hotmail.com](mailto:ddccffb31@hotmail.com)

Received 24 February 2017; Accepted 3 May 2017; Published 18 June 2017

Academic Editor: Wenxin Niu

Copyright © 2017 Jiang-Jun Zhou et al. This is an open access article distributed under the Creative Commons Attribution License, which permits unrestricted use, distribution, and reproduction in any medium, provided the original work is properly cited.

In this study, we developed and validated a refined three-dimensional finite element model of middle femoral comminuted fracture to compare the biomechanical stability after two kinds of plate fixation: a newly designed assembly locking compression plate (NALCP) and a locking compression plate (LCP). CT data of a male volunteer was converted to middle femoral comminuted fracture finite element analysis model. The fracture was fixated by NALCP and LCP. Stress distributions were observed. Under slow walking load and torsion load, the stress distribution tendency of the two plates was roughly uniform. The anterolateral femur was the tension stress area, and the bone block shifted toward the anterolateral femur. Maximum stress was found on the lateral border of the number 5 countersink of the plate. Under a slow walking load, the NALCP maximum stress was  $2.160e+03$  MPa and the LCP was  $8.561e+02$  MPa. Under torsion load, the NALCP maximum stress was  $2.260e+03$  MPa and the LCP was  $6.813e+02$  MPa. Based on those results of finite element analysis, the NALCP can provide adequate mechanical stability for comminuted fractures, which would help fixate the bone block and promote bone healing.

## 1. Introduction

Less invasive stabilization systems and locking compression plates (LCP) have been widely used in clinical practice [1–3] and provide new options and challenges for modern fracture surgery. However, the plates and screws cannot completely solve all of the problems encountered. Fracture healing requires a relatively stable environment, accurate anatomical reduction, and reliable internal fixation—each of which can shorten the healing time [4]. A long distance between fracture fragments and the trunk indicates the probability of poor healing [5]. For severe comminuted fracture of the long bone shaft, conventional fixation methods using tensile screws or wires would result in poor stability and could destroy the periosteal blood supply. Park et al. [6] and Yang et al. [7] found that there was a higher failure rate in the treatment of nonisthmal femoral shaft nonunions with intramedullary nails. They

considered that the main reason of the failure was mechanical instability.

Our research group has developed a new design assembly locking compression plate (NALCP) under Chinese patent (Patent number ZL201220339335.2). This plate is made of Ti-6Al-4V and it has the same materials as the LCP. The main locking compression plate is equipped with runner plates on both sides that can move with the bone blocks and fix bone blocks using universal locking screws. A runner plate is placed on the main locking compression plate, thus making bone blocks integrate with the bone shaft and achieving better stability based on the screw-bone plate angular stability and plate-plate integrity. The aim of this study is to compare and analyze the mechanical properties of NALCP and LCP in the treatment of femoral shaft wedge comminuted fractures (AO classification type 32-C2.1) in the condition of slow walking loading. To accomplish it, the finite element analysis was used.

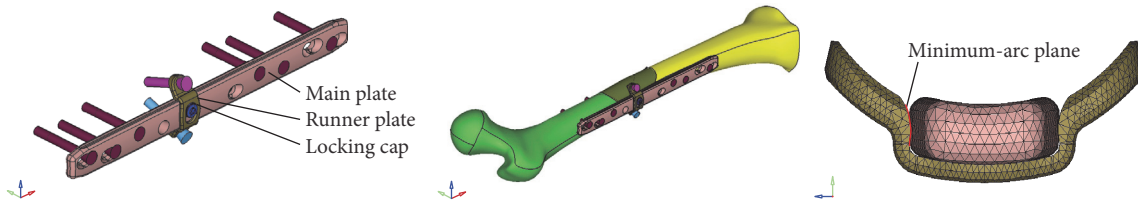


FIGURE 1: Runner plate integrates with the main plate through the locking female screws. Newly designed assembly locking compression plate (NALCP) fixated in long-bone comminuted fractures. Minimum-arc plane between the inner medial surface of the runner plate and the lateral surface of the main plate.

## 2. Materials and Methods

**2.1. Design of Runner Plate.** To achieve stability between the main plate and the runner plate, we connected the two plates using locking femoral screws. We also inserted universal locking screws through the runner plate to fix the bone block in a “crossover” manner (Figure 1). The inner medial surface of the runner plate was close to the lateral surface of the main plate, forming a minimum-arc plane. It can be disassembled from the main plate during surgery regardless of its shape (Figure 2).

### 2.2. Establishment of a Finite Element Model for Femoral Fixation

**2.2.1. Normal Femoral Geometrical Model.** A normal healthy volunteer (age 30 years, height 170 cm, weight 70 kg) underwent computed tomography (CT) scanning of the right lower extremity at a slice thickness of 0.625 mm. The scanned images were imported into medical image processing software Mimics 10.0 (Materialise Technologies, Leuven, Belgium) to segment the skeletal information of femur and then construct the geometry model of femoral in a reverse engineering software (Geomagic 9.0, Geomagic Inc. Morrisville, USA). Finally, the model of femur was converted into nonuniform rational B-spline (NURBS) surface as format of iges.

**2.2.2. Femoral Fixation Geometrical Model.** The geometrical model of wedge-fractured femoral was established in the finite element preprocessing software HyperMesh 11.0 (Altair Engineering Corp., Michigan, USA) and then was meshed on the same software platform. The bone fracture gap was set as 0.1 mm. The screw-plate fixation system model was developed by using SolidWorks CAD software (Dassault System SolidWorks Corp., Waltham, USA) (Figure 3). The NALCP main plate and runner plate were then assembled to match the bone shape, and bone blocks were fixed to the runner plate with two screws. For the LCP, bone blocks were fixed with an upwardly inclined screw on the main plate. The two fixation systems were introduced into HyperMesh software to simulate the assembly of fixation systems and femoral fracture models.

**2.2.3. Finite Element Model of Femoral Fixation.** The fixed femoral geometric entity models were meshed into finite element model in HyperMesh. The screw model was made up of hexahedrons, and the remaining models were formed as



FIGURE 2: Runner plate can be disassembled from the main plate regardless of its shape: red ellipse circle.

tetrahedrons. The overall size of the element was 3 mm [8, 9]. The greatest curvature in the model was treated with Variable Grid Density Biased Sampling technology, and the grid density within the model was coarsened [10, 11]. Some important locations, such as contacts and constraints, were artificially divided to improve calculation accuracy. Finally, two femoral fixation models were established. Their types and quantity of units are shown in Table 1.

### 2.3. Finite Element Analysis

**2.3.1. Material Allocation.** All models were simulated using homogeneous isotropic linear material. The elastic modulus of the plate was defined as  $1.10e+05$  MPa. The properties of the models' materials after meshing are shown in Table 1.

**2.3.2. Model Validation.** To confirm the reliability of the results of finite element analysis, we selected complete skeleton model before plate fixation. The load was given in accordance with Wang et al.'s study [12]. Strain of the node at the corresponding position was measured with eight strain gauges.

**2.3.3. Definitions of Contact, Constraint, Load, and Boundary Conditions.** For simulation of a slow walking load, the frictional contact is defined as contact between the main plate and the runner plate on the fracture surface. The fracture surface friction coefficient is 0.45, and the friction coefficient between the plates is 0.2. The femoral load in single legs during walking was simulated, and the load was given on the surface of the femoral head and the greater trochanter in a point-coupling manner to simulate the acetabular contact force and muscle abduction force. Six random degrees on the distal femur were constrained. The loading direction

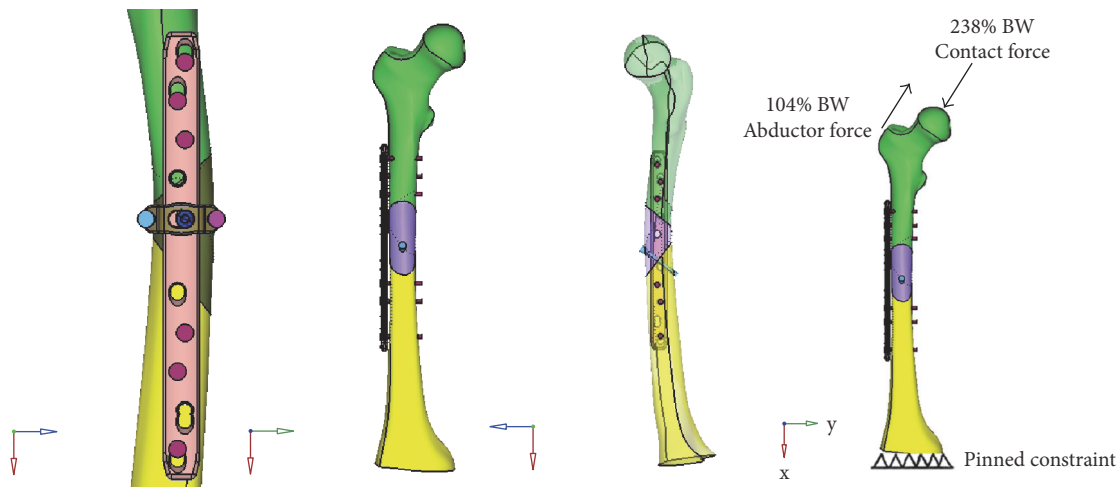


FIGURE 3: NALCP fixation, LCP fixation, and load imposed on the femur to simulate the slow walking state.

TABLE 1: Properties of the models' materials and the number of elements.

Model	Elastic modulus (MPa)	Poisson's ratio	Number of elements	Number of nodes
Cortical bone	$1.3e + 04$	0.3	85 583	19 682
Cancellous bone	$2.06e + 02$	0.3	13 426	58 381
NALCP	$1.10e + 05$	0.3	101 993	35 946
LCP	$1.10e + 05$	0.3	84 600	30 377

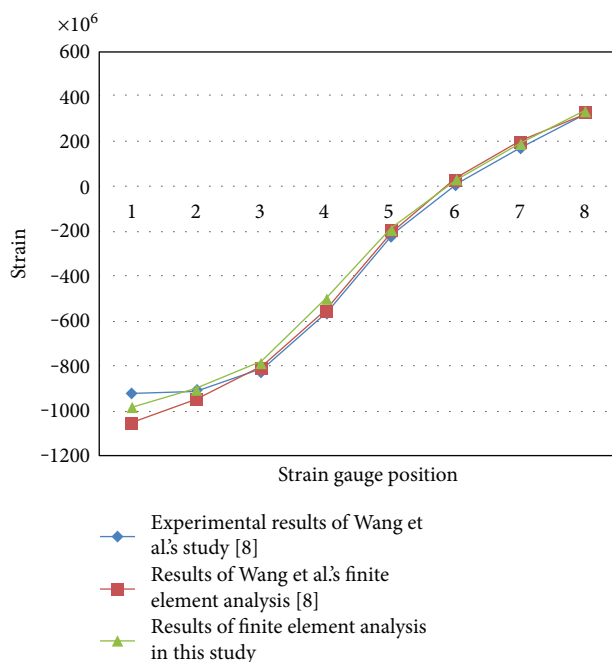


FIGURE 4: Experimental verification of complete skeleton finite element model. Results of our finite element analysis were consistent with Wang et al.'s results.

and size are shown in Figure 3 [13]. A static analysis step was defined in the HyperMesh software with the interface of a finite element solver (Abaqus6.11, Simula Corporation Pennsylvania, USA), and the interaction set, load, and boundary conditions were also added.

TABLE 2: Maximum stress of two fixed plate systems.

Fixation system	Main plate (MPa)	Runner plate (MPa)
NALCP	$1.557e+03$	$2.160e+03$
LCP	$8.561e+02$	—

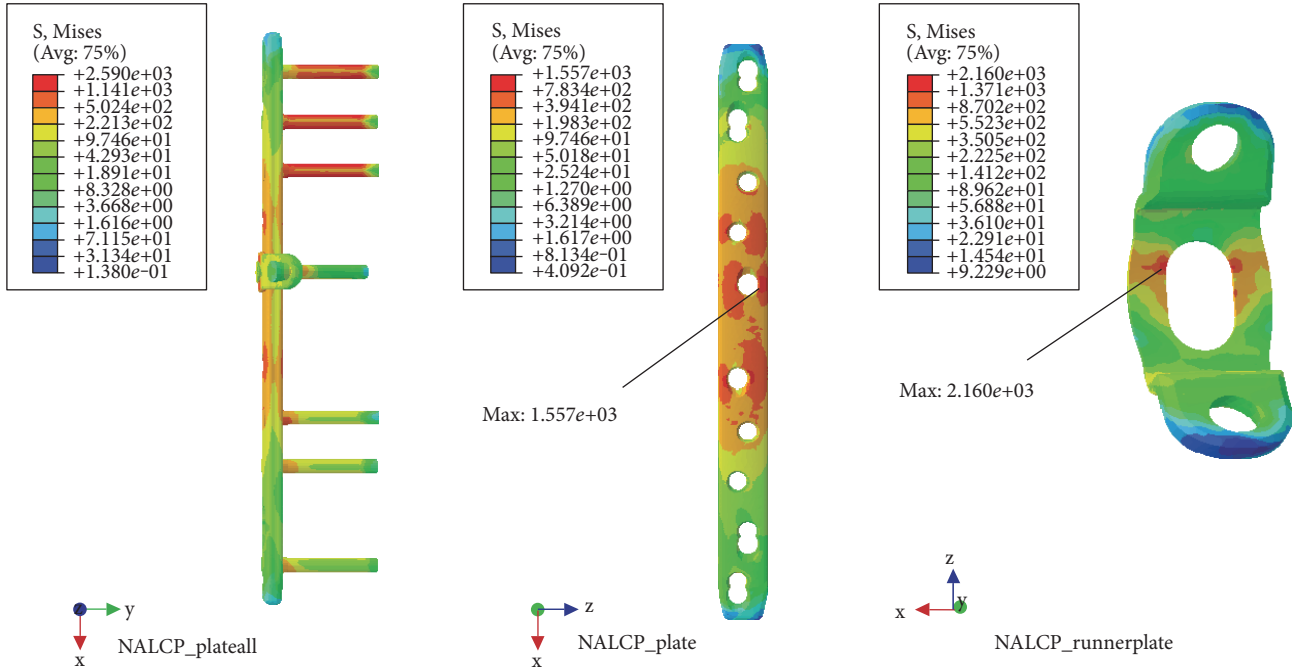


FIGURE 5: NALCP stress nephogram of the slow walking load.

**2.3.4. Finite Element Method.** Two fracture models with preset conditions were saved in .inp format and input into Abaqus for direct discrimination. The discriminating process takes 2 minutes, followed by postprocessing in Abaqus software.

**2.3.5. Outcome Measures.** The stress distributions of the plates and bone blocks were identified. The bone blocks were detected at the anterior, posterior, lateral, and medial borders of the contact plane at the distal and proximal fracture lines. The values were then averaged.

### 3. Results

**3.1. Results of Model Validation.** Results of finite element model validation of this study was consistent with mechanical test and finite element model results of Wang et al.'s study [12] (Figure 4). We concluded that the establishment of finite element model is credible.

The stress distribution tendencies of the two plates (NALCP and LCP) under two loading conditions were roughly uniform. No concentrated area of stress was found. The anterolateral femur was the area of greatest tension stress, and the bone block shifted toward the same area.

**3.2. Simulation of Slow Walking Load.** With the NALCP, maximum stress was situated at the lateral border of the number 5 countersink of the plate (between the runner plate and the main plate locking screw). Maximum stress on the runner plate was located between the locking screws and the runner plate contact area (Table 2, Figure 5). In the skeletal model, maximum stress was distributed at the countersink of the runner plate (Table 3, Figure 6). Under the condition of the slow walking load, the axial maximum stress was

TABLE 3: Stress distribution of the skeletal model.

Fixation system	Maximum stress	Axial maximum stress (MPa)	Tensional shear maximum stress (MPa)
NALCP	$3.696e+02$	$1.834e+00$	$3.488e+00$
LCP	$2.962e+02$	$5.858e+01$	$4.058e+00$

$1.834e+00$  MPa and tensional shear stress was  $3.488e+00$  MPa at the fracture plane.

The LCP maximum stress was also located in the lateral border of the number 5 countersink of the proximal plate (Table 2, Figure 7) and showed stress distribution similar to that with the NALCP. Maximum stress in the skeletal model was found in the bone block countersink (Table 3, Figure 8). Under the condition of the slow walking load, the axial maximum stress was  $5.858e+01$  MPa and tensional shear stress was  $4.058e+00$  MPa at the fracture plane.

**3.3. Torsional Load.** NALCP maximum stress was situated in the lateral border of the number 5 countersink of the proximal plate (between the runner plate and the main plate locking screw). Maximum stress on the runner plate was located between the area of contact of the locking screws and runner plate (Table 4, Figure 9). Maximum stress in the skeletal model was distributed at the countersink of the runner plate (Table 5, Figure 10). Under torsional loads, the axial maximum stress was  $1.923e+00$  MPa and tensional shear stress was  $3.604e+00$  MPa at the fracture plane.

The LCP maximum stress was also located in the lateral border of the number 5 countersink of the proximal plate (Table 4, Figure 11) and showed stress distribution similar

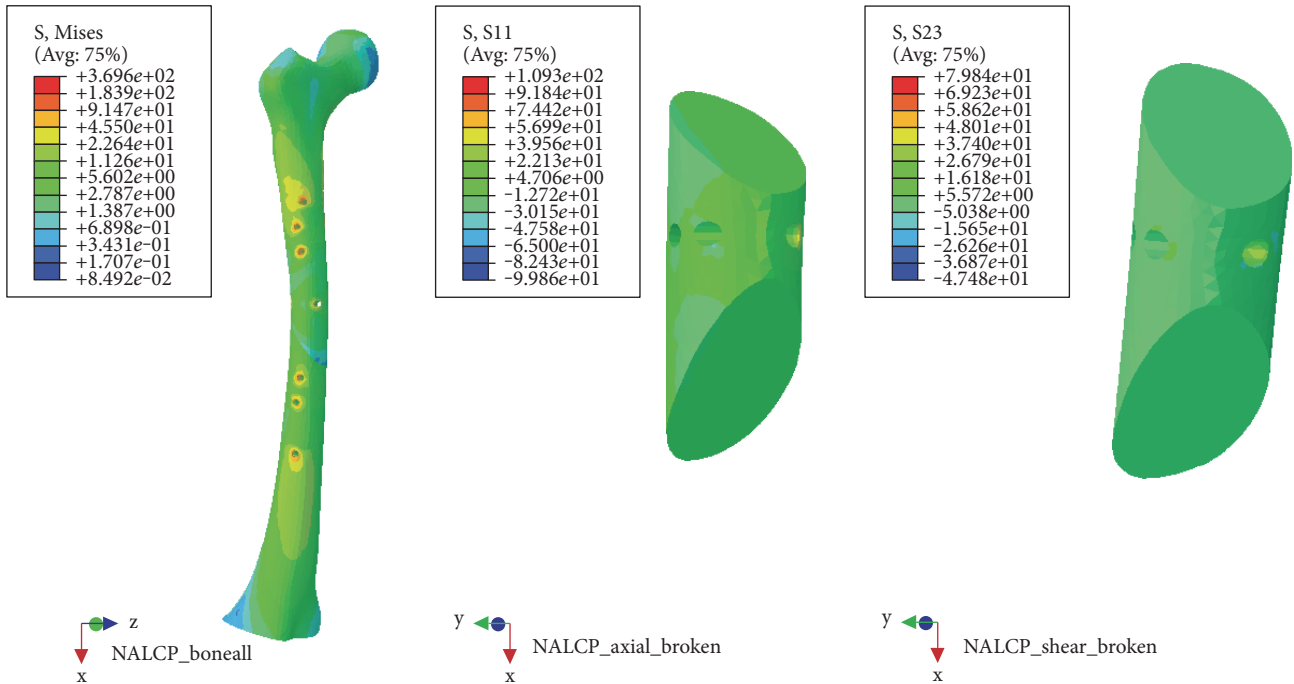


FIGURE 6: NALCP stress nephogram and bone block axial stress nephogram of the slow walking load.

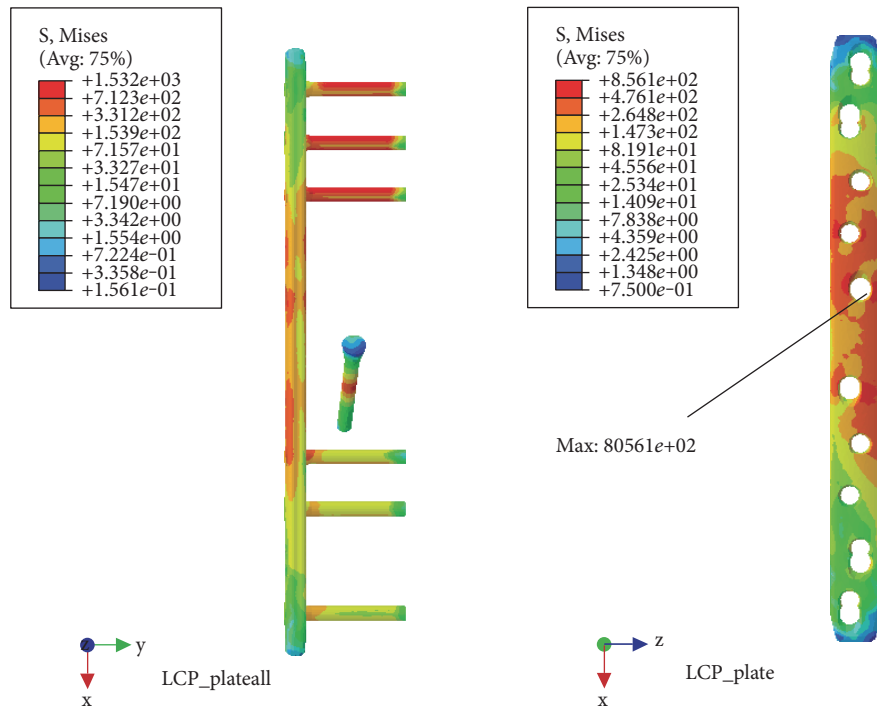


FIGURE 7: LCP stress nephogram of the slow walking load.

to that seen with NALCP. Maximum stress on the skeletal model was found in the number 1 countersink of the proximal model (Table 5, Figure 12). Under torsional load, the axial maximum stress was  $6.660e+01$  MPa and tensional shear stress was  $3.376e+01$  MPa at the fracture plane.

#### 4. Discussion

Modern high-energy trauma often leads to severely comminuted limb fractures. According to the AO classification, type B and C fractures are common. The currently used fixation

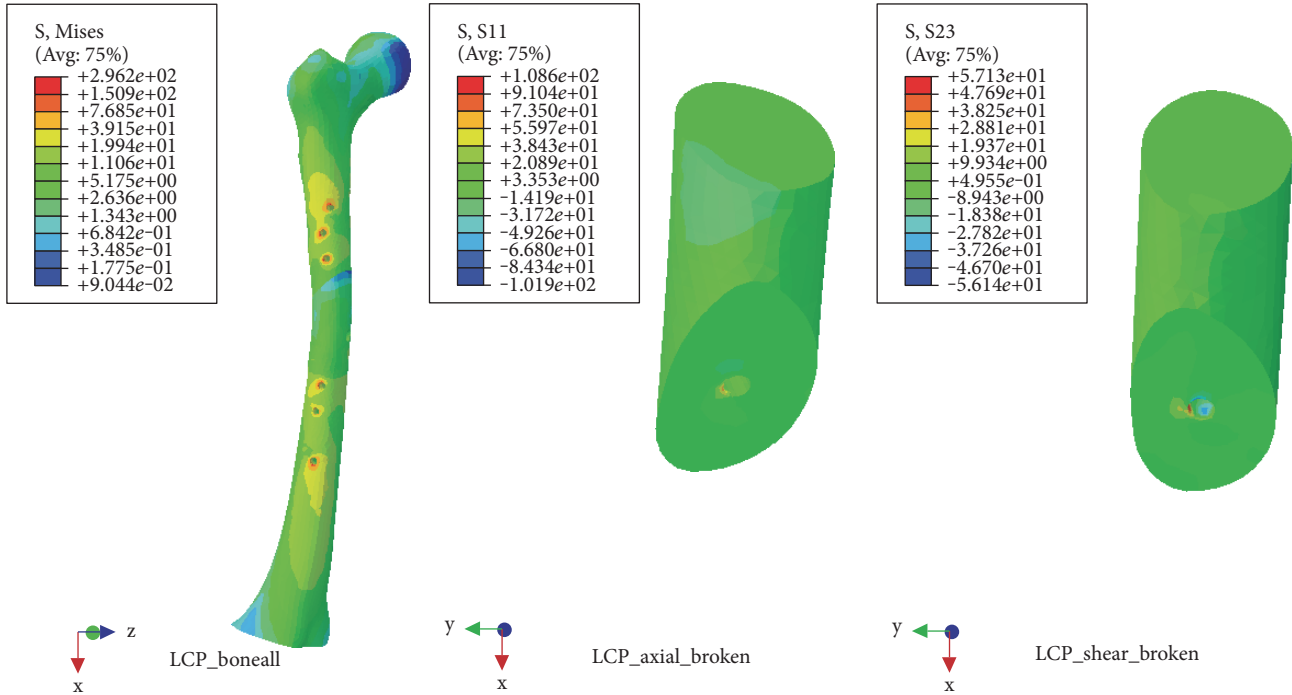


FIGURE 8: LCP stress nephogram and bone block axial stress nephogram of the slow walking load.

TABLE 4: Maximum stress of two fixation system plates.

Fixation system	Main plate (MPa)	Runner plate (MPa)
NALCP	1.565e+03	2.260e+03
LCP	6.813e+02	—

methods include plate-screw fixation and intramedullary nail fixation. LCP fixation requires at least four holes to reduce stress concentration and avoid plate breakage [14]. Although interlocking intramedullary nails in the treatment of comminuted fractures provide central fixation, high strength, good stability, and small stress concentration as detected by finite element analysis [15], they often induce bone nonunion and intramedullary nail rupture, especially during early weight-bearing activities [4]. With these two fixation methods, bone blocks are often fixed with a single tensile screw or a wire ring. However, fixation is poor and frequently leads to bone displacement.

Previous animal experiments [5] showed that the distance from free bone reflects the apparent impact on fracture healing. Under physiological conditions, when stress is greater than optimal, bone formation dominates in bone metabolism. In contrast, when stress is less than optimal, bone resorption dominates [16]. As for comminuted fractures, especially in weight-bearing bone, axial stress easily leads to a transversal shift of bone blocks [17]. Some authors [18] found that intraoperative unstable rotation and poor contact between bone blocks during treatment of femoral nonunion using intramedullary nails was alleviated after bone grafting and insertion of a steel plate to increase local stability.

Therefore, we designed an arc-shaped surface of the main plate and the runner plate. This innovation is conducive to convenient assembly and disassembly of the runner plate and does not affect the structure of the steel plate. This “micro-arc” design allows arbitrary use of a steel plate during surgery according to the bone blocks. It also increases the flexibility of its use. To enhance fixation, we adopted the use of the locking female screw to lock the runner plate and the main plate. Universal locking screws on both sides of the runner plate can achieve “crossover” triangular fixation of bone blocks. Hence, bone blocks were integrated with the fracture shaft through the runner plate and main plate, achieving strong fixation depending on the screw-plate angular stability.

Finite element analysis has been applied extensively in orthopedic biomechanical analyses and for testing new materials [19–22]. Previous studies focused only on stress distribution of the steel plate and skeleton, leaving stress distribution on the contact surface of the fracture unclear [23, 24]. Also, if only stable fixation was performed after fracture surgery without axial stress, bone callus would grow slowly. Sufficient axial pressure and tension force stimulation and may accelerate the formation of callus at the fracture area [24, 25]. Therefore, under a slow walking load, axial stress of the bone block’s contact surface in the finite element analysis can directly reflect postoperative stress stimulation in bone blocks. It is also an indicator of stability of the bone fracture stump after new internal fixation.

A normal healthy volunteer underwent computed tomography (CT) scanning, and the scanned images were imported into several medical image processing software to establish a finite element model. By experimental verification, the results of our finite element analysis were consistent

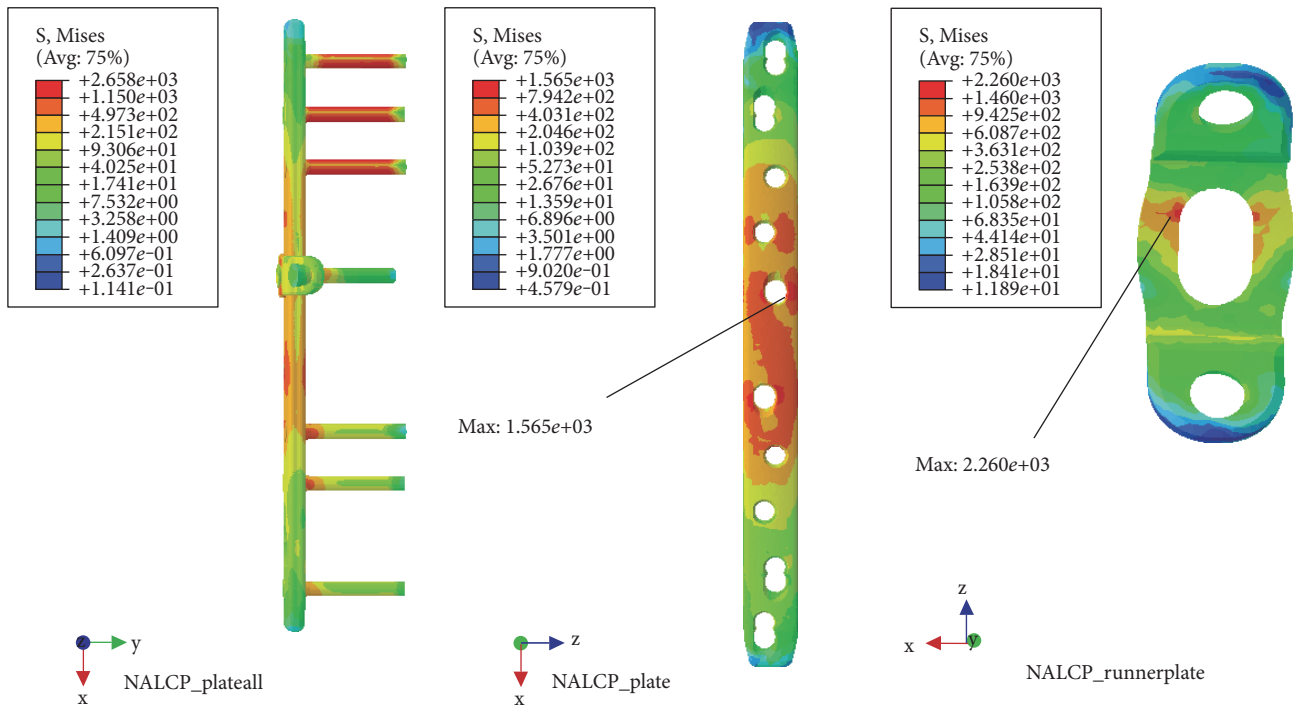


FIGURE 9: NALCP stress nephogram of the torsional load.

TABLE 5: Stress distribution of the skeletal model.

Fixation system	Maximum stress (MPa)	Axial maximum stress (MPa)	Tensional shear maximum stress (MPa)
NALCP	4.393e+02	1.923e+00	3.604e+00
LCP	3.387e+02	6.660e+01	3.376e+01

with Wang et al.'s results [12]. Finite element analysis of stress distribution nephogram showed that the stress distribution for the NALCP and LCP systems were similar under slow walking loads. Also, the distance from the bone fracture line to the main plate screws was the high-stress area with both systems, showing uniform stress distribution. Both NALCP and LCP maximum stress was located at the lateral edge of the number 5 countersink of the proximal plate. The maximum stress of the LCP-combined screw fixation was significantly lower than that of the NALCP. The LCP maximum stress was about 54.98% that of NALCP maximum stress. LCP axial stress was 31.94 times that of NALCP axial stress, and the tension shear stress was 1.16 times that of NALCP shear stress. Under torsional loads, NALCP and LCP showed similar stress distributions, and the maximum stress was concentrated at the lateral edge of the number 5 countersink of the proximal plate. The LCP plate maximum stress was 43.53% that of the NALCP plate, the axial stress was 34.63 times that of NALCP axial stress, and the tension shear stress was 9.37 times that of NALCP shear stress. In summary, the axial stress and tension shear stress in the NALCP skeletal model were significantly lower than those in the LCP

model. Thus, NALCP enhances the stability of bone blocks under stimulation of a slow walking load and a torsional load [17], improving the fixation effect, preventing lateral displacement of the bone block, and promoting bone healing.

Stoffel et al. [3] investigated the distance of the screw to the fracture site in finite element analysis using the LCP. Their results demonstrated that the maximum stress of the plate occurred at the innermost screw hole. When bone fracture gap was 1 mm during simulating simple fracture, with increasing the distance of the screw to the fracture site, equivalent stress of the plate and the innermost screw was reduced. However, when the bone fracture gap was 6 mm during simulating comminuted fracture, the result was the opposite. Dong et al. [26] also found that for simple femoral shaft fracture, maximum stress on the locking plate and screw gradually decreased with outward movement of the innermost screw. For comminuted fracture, the fracture site could not produce effective contact for stress transfer, so the further deformation of the locking plate could not be prevented. Thus, maximum stress on the locking plate and screw increased. Lee et al. [24] confirmed that for comminuted fracture, locking screws as close as practicable to the fracture site resulted in a high stability of the fixation, and stress concentration did not obviously increase. In our result, the maximum stress of NALCP and LCP are all near the fracture site and are consistent with Lee et al.'s [27] and Xiong et al.'s [28] results. When NALCP obtained an effective stability, the stress on the main plate was less compared with the LCP.

In this study, longitudinal force loaded on the femoral head reached 238% of body weight [12], simulating slow walking, which is much higher than the load value used

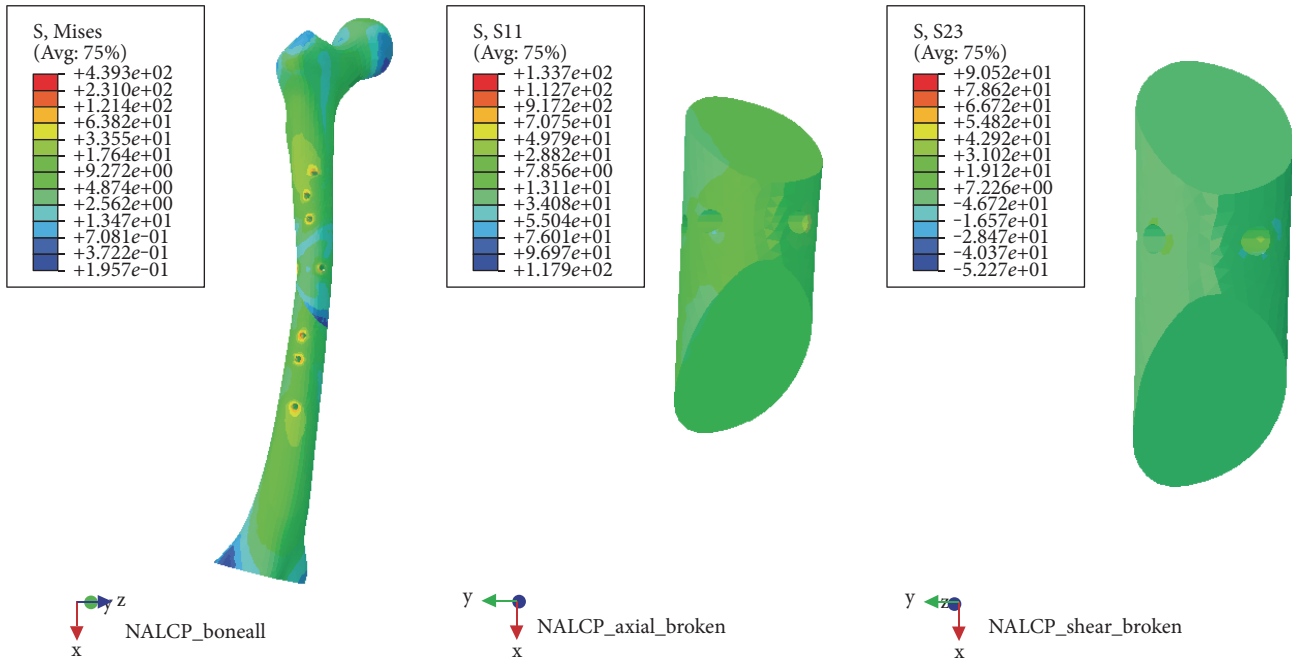


FIGURE 10: NALCP stress and axial stress nephograms of the torsional load.

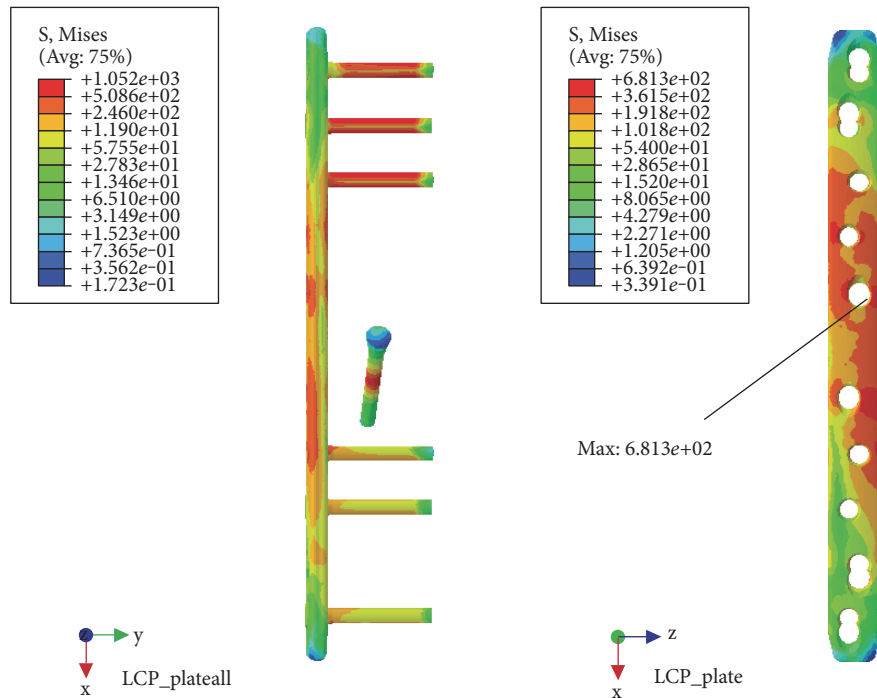


FIGURE 11: LCP stress nephogram of the torsional load.

previously [14, 23, 29]. The results showed that the stress of the NALCP and LCP plates exceeded 600 MPa, the yield strength of titanium alloy. Therefore, the patients could not engage in early full weight-bearing walk. The contact area between the locking screw and the runner plate was the

high-stress area. Maximum stress under each of the two loads was higher than maximum stress of the main plate, which is the stress concentration point throughout the fixation system. The potential focus of future studies will be how to reduce stress concentration on the runner plate.

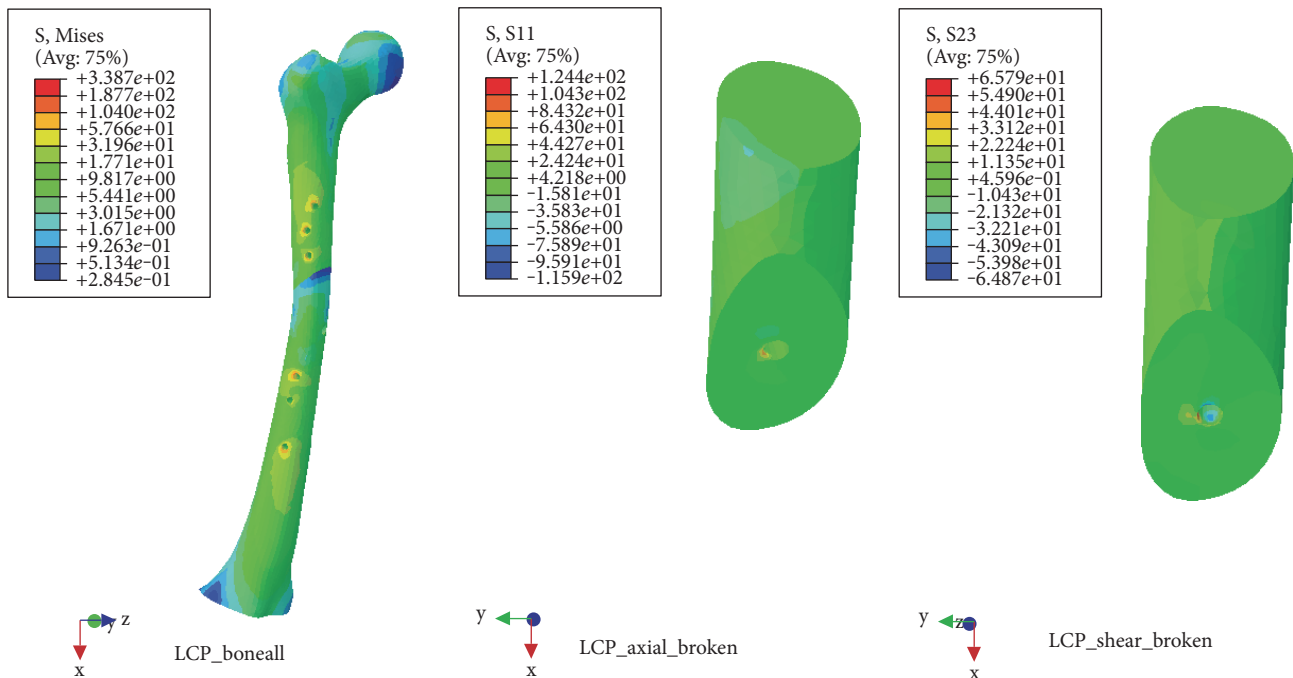


FIGURE 12: LCP stress and axial stress nephograms of the torsional load.

## 5. Conclusion

Based on results of finite element analysis, NALCP can provide a strong mechanical stability for comminuted fractures. NALCP is more convenient to fix bone fragments and to promote bone healing compared with the conventional LCP. Nevertheless, because of the lack of biomechanical experiment of solid specimens, our results deserve further investigations.

## Conflicts of Interest

The authors declare that there is no conflict of interest regarding the publication of this paper.

## Authors' Contributions

Jiang-Jun Zhou and Min Zhao are co-first authors and they contributed equally to this work.

## Acknowledgments

The project was supported by the National Natural Science Foundation of China (NSFC, 11602172, 11432016, and 11402172), the 2013 Major Scientific Research Projects of Logistics Department of PLA (BNJ13J003), the Nanjing Military Medical Technology Innovation Project (12MA049), and the Science Support Programs of Jiangxi Province (20132BBG70092).

## References

- [1] M. Schütz, M. Müller, M. Käab, and N. Haas, "Less invasive stabilization system (liss) in the treatment of distal femoral fractures," *Acta Chirurgiae Orthopaedicae et Traumatologiae Cechoslovaca*, vol. 70, no. 2, pp. 74–82, 2003.
- [2] M. Florin, M. Arzdorf, B. Linke, and J. A. Auer, "Assessment of stiffness and strength of 4 different implants available for equine fracture treatment: a study on a 20° oblique long-bone fracture model using a bone substitute," *Veterinary Surgery*, vol. 34, no. 3, pp. 231–238, 2005.
- [3] K. Stoffel, U. Dieter, G. Stachowiak, A. Gächter, and M. S. Kuster, "Biomechanical testing of the LCP—how can stability in locked internal fixators be controlled?" *Injury*, vol. 34, Supplement 2, pp. B11–B19, 2003.
- [4] M. Nassiri, B. Macdonald, and J. M. O'Byrne, "Computational modelling of long bone fractures fixed with locking plates - how can the risk of implant failure be reduced?" *Journal of Orthopaedics*, vol. 10, no. 1, pp. 29–37, 2013.
- [5] Y.p. Liu, J. J. Jiang, T. Sun et al., "The experimental study of the influence of the fracture fragment displaced distance on fracture healing," *Chinese Journal of Traumatology*, vol. 26, no. 10, pp. 923–929, 2010.
- [6] J. Park, S. G. Kim, H. K. Yoon, and K. H. Yang, "The treatment of nonisthmal femoral shaft nonunions with im nail exchange versus augmentation plating," *Journal of Orthopaedic Trauma*, vol. 24, no. 3, pp. 89–94, 2010.
- [7] K. H. Yang, J. R. Kim, and J. Park, "Nonisthmal femoral shaft nonunion as a risk factor for exchange nailing failure," *Journal of Trauma and Acute Care Surgery*, vol. 72, no. 2, pp. E60–E64, 2012.
- [8] M. Bessho, I. Ohnishi, J. Matsuyama, T. Matsumoto, and K. Imai, "Prediction of strength and strain of the proximal femur by a CT-based finite element method," *Journal of Biomechanics*, vol. 40, no. 8, pp. 1745–1753, 2007.
- [9] J. E. Koivumäki, J. Thevenot, P. Pulkkinen, V. Kuhn, and T. M. Link, "Ct-based finite element models can be used to estimate

- experimentally measured failure loads in the proximal femur,” *Bone*, vol. 50, no. 4, pp. 824–829, 2012.
- [10] M. Ni, W. X. Niu, D. W. C. Wong, W. Zeng, J. Mei, and M. Zhang, “Finite element analysis of locking plate and two types of intramedullary nails for treating mid-shaft clavicle fractures,” *Injury*, vol. 47, no. 8, pp. 1618–1623, 2016.
- [11] M. Ni, D. W. C. Wong, J. Mei, W. X. Niu, and M. Zhang, “Bio-mechanical comparison of locking plate and crossing metallic and absorbable screws fixations for intra-articular calcaneal fractures,” *Science China Life Sciences*, vol. 59, no. 9, pp. 958–964, 2016.
- [12] G. D. Wang, H. B. Jiang, Y. M. Zhang, X. W. Zhao, and T. Pan, “Three-dimensional finite element analysis on intramedullary controlled dynamic nailing for femoral shaft fracture,” *Chinese Journal of Tissue Engineering Research*, vol. 18, no. 40, pp. 6524–6530, 2014.
- [13] I. A. Radcliffe and M. Taylor, “Investigation into the affect of cementing techniques on load transfer in the resurfaced femoral head: a multi-femur finite element analysis,” *Clinical Biomechanics*, vol. 22, no. 4, pp. 422–430, 2007.
- [14] T. Niikura, Y. L. Sang, Y. Sakai, K. Nishida, and R. Kuroda, “Causative factors of fracture nonunion: the proportions of mechanical, biological, patient-dependent, and patient-independent factors,” *Journal of Orthopaedic Science*, vol. 19, no. 1, pp. 120–124, 2014.
- [15] S. Q. Mu, Z. Yuan, L. Zhang et al., “A biomechanical evaluation of intramedullary expansive locking nail in treatment of femoral fractures,” *Chinese Journal of Orthopaedic Trauma*, vol. 11, no. 9, pp. 845–849, 2009.
- [16] S. M. Perren, “The biomechanics and biology of internal fixation using plates and nails,” *Orthopedics*, vol. 12, no. 12, pp. 21–34, 1989.
- [17] M. Steiner, L. Claes, A. Ignatius, U. Simon, and T. Wehner, “Disadvantages of interfragmentary shear on fracture healing—mechanical insights through numerical simulation,” *Journal of Orthopaedic Research*, vol. 32, no. 7, pp. 865–872, 2014.
- [18] J. Z. Zhang, Z. Liu, T. S. Sun et al., “Augmentative plate fixation to treat femoral atrophic nonunions subsequent to intramedullary nailing,” *Chinese Journal of Traumatology*, vol. 27, no. 5, pp. 451–455, 2011.
- [19] W. R. Taylor, E. Roland, H. Ploeg, D. Hertig, and R. Klabunde, “Determination of orthotropic bone elastic constants using FEA and modal analysis,” *Journal of Biomechanics*, vol. 35, no. 6, pp. 767–773, 2002.
- [20] J. J. Zhou, Z. Min, Y. B. Yan, W. Lei, R. D. Lv, and Z. Y. Zhu, “Finite element analysis of a bone healing model: 1-year follow-up after internal fixation surgery for femoral fracture,” *Pakistan Journal of Medical Sciences*, vol. 30, no. 2, pp. 343–347, 2014.
- [21] J. J. Zhou, Y. Rui, M. Zhao et al., “Personalized finite element modeling analysis of femur bone healing after intramedullary nailing,” *Journal of Mechanics in Medicine and Biology*, vol. 16, no. 5, article 1650061, 2016.
- [22] M. Cimerman and A. Kristan, “Preoperative planning in pelvic and acetabular surgery: the value of advanced computerised planning modules,” *Injury*, vol. 38, no. 4, pp. 442–449, 2007.
- [23] C. L. Du, X. L. Ma, J. X. Ma et al., “Influence of anteversion angles on stress distributions of the proximal femur after femoral neck fracture fixations: a finite element analysis,” *Journal of Medical Biomechanics*, vol. 27, no. 6, pp. 603–607, 2012.
- [24] L. Claes, P. Augat, S. Schorlemmer, C. Konrads, A. Ignatius, and C. Ehrnthaller, “Temporary distraction and compression of a diaphyseal osteotomy accelerates bone healing,” *Journal of Orthopaedic Research*, vol. 26, no. 6, pp. 772–777, 2008.
- [25] U. Sigurdson, O. Reikeras, and S. E. Utvag, “The influence of compression on the healing of experimental tibial fractures,” *Injury*, vol. 42, no. 10, pp. 1152–1156, 2011.
- [26] W. Dong, B. Lu, X. M. Shi, X. X. Xu, X. L. Xu, and Z. L. Wang, “The finite element analysis in the treatment of femur shaft fracture by LCP,” *Journal of Practical Orthopaedics*, vol. 20, no. 9, pp. 818–820, 2014.
- [27] C. H. Lee, K. S. Shih, C. C. Hsu, and T. Cho, “Simulation-based particle swarm optimization and mechanical validation of screw position and number for the fixation stability of a femoral locking compression plate,” *Medical Engineering & Physics*, vol. 36, no. 1, pp. 57–64, 2014.
- [28] Y. Xiong, Q. Li, B. Liu, F. Zhao, D. Wang, and Z. Zhang, “Finite element analysis of bridge combined fixation system and the locking plate-screw system on the application for femoral fractures,” *Chinese Journal of Tissue Engineering Research*, vol. 16, no. 30, pp. 5516–5519, 2012.
- [29] G. X. Yuan, L. Wang, W. B. Zhang, Y. H. Shen, and B. Chen, “The finite element analysis of intramedullary and extramedullary fixation in osteoporotic patients with intertrochanter fracture of femur,” *Chinese Journal of Orthopaedic Trauma*, vol. 14, no. 10, pp. 876–882, 2012.

## Research Article

# Endogenous Production of n-3 Polyunsaturated Fatty Acids Promotes Fracture Healing in Mice

Yuhui Chen,<sup>1</sup> He Cao,<sup>1</sup> Dawei Sun,<sup>2</sup> Changxin Lin,<sup>1</sup> Liang Wang,<sup>1</sup> Minjun Huang,<sup>1</sup> Huaji Jiang,<sup>1</sup> Zhongmin Zhang,<sup>1</sup> Dadi Jin,<sup>1</sup> Baiyu Zhang,<sup>3</sup> and Xiaochun Bai<sup>1</sup>

<sup>1</sup>Department of Orthopedic, The Third Affiliated Hospital of Southern Medical University, Guangzhou 510665, China

<sup>2</sup>Department of Orthopedics & Microsurgery, Guangdong Second Provincial General Hospital, Guangzhou 510317, China

<sup>3</sup>Department of Rehabilitation Medicine, Sun Yat-Sen Memorial Hospital, Sun Yat-Sen University, Guangzhou 510120, China

Correspondence should be addressed to Dadi Jin; nyorthop@163.com, Baiyu Zhang; baiyuzsu@aliyun.com, and Xiaochun Bai; baixc15@smu.edu.cn

Received 28 January 2017; Revised 16 March 2017; Accepted 10 April 2017; Published 14 June 2017

Academic Editor: Wenxin Niu

Copyright © 2017 Yuhui Chen et al. This is an open access article distributed under the Creative Commons Attribution License, which permits unrestricted use, distribution, and reproduction in any medium, provided the original work is properly cited.

Bone fracture is a global healthcare issue for high rates of delayed healing and nonunions. Although n-3 polyunsaturated fatty acid (PUFA) is considered as a beneficial factor for bone metabolism, only few studies till date focused on the effects of n-3 PUFAs on fracture healing. In this study, we investigated the effect of endogenous n-3 PUFAs on fracture healing by measuring femur fracture repair in both *fat-1* transgenic mice and WT mice. Proximal femoral fracture model was established in *fat-1* transgenic mice and WT mice, respectively, and then the fracture was analyzed by using X-ray, micro-computed tomography (micro-CT), and histological assessment at 7, 14, 21, 28, and 35 days after fixation. The results showed that compared with WT mice, *fat-1* mice exhibited acceleration in fracture healing through radiographic and histological analysis (18–21 days versus 21–28 days postfracture). Meanwhile, X-ray and micro-CT analysis that showed better remodeling callus formation were in the *fat-1* group compared to WT group. Furthermore, histological analysis revealed that endogenous n-3 PUFAs promoted local endochondral ossification and accelerated the remodeling of calcified calluses after fracture. In conclusion, the present study indicated that endogenously produced n-3 PUFAs promote fracture healing process and accelerate bone remodeling in mice, and supplementation of n-3 PUFAs was positively associated with fracture healing.

## 1. Introduction

Fracture is delineated as a major healthcare problem worldwide within the rapid aging population. The rate of fracture union was about 20%, which still remains as a severe clinical issue even with the improvements of internal fixations in orthopedic management over the past decades [1]. Several researchers have concentrated on diet management for fracture healing, which includes intake of vitamin D and calcium for their modulatory roles in skeletal metabolism [2]. Although vitamin D and calcium deficiency results in high risk of fractures and delay in skeletal development, intake of either vitamin D or calcium accelerates fracture healing due to limited absorption into the digestive tract and in turn balancing the whole body metabolism. Recently, the modulation of fatty acids (FAs) in bone-remodeling

process has been reported [3]. For instance, arachidonic acid (AA), a polyunsaturated omega-6 fatty acid, acts as a precursor for the synthesis of lipid signaling molecules such as prostaglandins (PGs) and leukotrienes (LTs). This plays a negative role in fracture healing and AA inhibition, which resulted in the enhancement of fracture healing [4, 5]. According to a clinical study, total fat and animal fat rich in saturated fatty acids might increase the risk of hip fractures in elders [6]. Nevertheless, other FAs like eicosapentaenoic acid (EPA) (20:5; n-3) and docosahexaenoic acid (DHA) (22:6; n-3) were reported to reduce the risk of fractures [7].

Recently, remarkable benefits of n-3 PUFAs on bone metabolism have been reported widely. Bonnet and Ferrari have demonstrated that long-term supplementation of n-3 PUFAs promoted the strength of diaphyseal bone in mice [8]. Consistent with the past investigation [3], our recent

study also showed that endogenously produced n-3 PUFAs attenuated the bone loss of ovariectomized mice through bone marrow adipogenesis inhibition [9]. In addition, serum levels of n-3 PUFAs were positively correlated with the bone mineralization in both mice and human, and the fracture risk was increased by intake of saturated FAs while reduced by intake of n-3 PUFAs [3, 6, 10–12].

Although potential benefits of n-3 PUFAs on bone metabolism are promising, no study has yet evaluated the role of n-3 PUFAs on fracture healing or management of diet postfracture. Moreover, *fat-1* transgenic mice can convert n-6 to n-3 PUFAs endogenously; this transgenic mice provide an opportunity to distinguish the regulatory role of n-3 PUFAs [13]. Therefore, the purpose of this present study is to investigate the efficacy of endogenously produced n-3 PUFAs on fracture healing in mice femoral fracture model.

## 2. Materials and Methods

**2.1. Animals and Diet.** All animal experiments were carried out with the approval of Southern Medical University Animal Care and Use Committee in accordance with the ethical treatment of animal guidelines. All surgeries were performed under chloral hydrate and xylazine anesthesia, and all efforts were made to minimize animal suffering. Briefly, *fat-1* transgenic mice were mated with C57BL/6 wild-type mice to obtain *fat-1* positive C57BL/6 mice (*fat-1*) and *fat-1* negative C57BL/6 mice (WT). The genotypes of mice were identified by the presence of *fat-1* gene. Mice were housed under specific pathogen-free (SPF) conditions with day and night cycles of 12h each. The temperature and humidity was maintained at  $25 \pm 3^\circ\text{C}$  and  $65 \pm 5\%$ , respectively, and fed diets containing 10% corn oil. After 12 weeks postnatal, sixty mice were selected and were randomly divided into the following two groups: WT ( $n = 30$ ) and *fat-1* ( $n = 30$ ), 6 mice were randomly selected and harvested at each time point.

**2.2. Surgical Procedure.** Mice were anesthetized by intraperitoneal injection of xylazine (25 mg/kg body weight) and ketamine (75 mg/kg body weight); then a 4 mm medial incision was performed on the right knee, and the patella was dislocated under sterile condition. After a hole (0.45 mm in diameter) was drilled into the intracondylar notch by using a 26-gauge needle, a guide wire (0.2 mm in diameter) was inserted into the femoral intramedullary canal through the needle. The needle was removed, and the guide wire was retained to stabilize the impending fracture. Then, a standardized proximal fracture was manifested on right femur by using a 3-point bending devices. Subsequently, for establishing a simulation model of internal fixation in clinic, a nail (0.45 mm in diameter) was implanted through the guide wire. Finally, the patella was repositioned, and the incision was closed in the 2 layers; the guide wire was removed and extended beyond the needle cut.

**2.3. Sample Harvest.** Mice were anesthetized via intraperitoneal injection with pentobarbital sodium phosphate-buffered saline (PBS) solution of 30 mg/kg body weight and were sacrificed for harvesting right femur samples at weeks

1, 2, 3, 4, and 5 after fracture establishment. The right femurs were then stored at  $4^\circ\text{C}$  for further analysis.

**2.4. X-Ray Radiography.** Radiographs were measured by digital radiographic system (Kodak, DirectView DR 3500, Rochester, NY). The right femurs of each group were analyzed at weeks 1, 2, 3, 4, and 5 postfracture, respectively. Fracture healing was evaluated with callus maturity by using Goldberg classification (stage 1: nonunion, stage 2: possible union, and stage 3: complete union) [14]. Mean radiological score of 5 weeks was calculated for both groups.

**2.5. Micro-Computed Tomography (Micro-CT).** Micro-CT scan was used for measuring with ZKKS-MCT-III micro-CT system (Guangzhou Zhongke Kaisheng Medical Technology Company Ltd., Guangzhou, China). Each sample was placed and then secured with foam board to avoid shifting during scan.

**2.6. Histological Analysis.** At 1, 2, 3, 4, and 5 weeks postfracture, right femurs were collected and were decalcified by 19% EDTA solution for about 2–4 weeks and then were dehydrated through successive grades of ethanol, rinsed with xylene, and embedded in paraffin. Sections of  $4\ \mu\text{m}$  were prepared sagittally at the fracture site. The sections were stained by Safranin O/Fast Green staining (SO/FG) and were observed under a light microscope (Olympus BX51, Japan).

**2.7. Statistical Analysis.** Data were expressed as mean  $\pm$  SD, and Student's *t*-test was performed to analyze statistical significance. Representative experiments were presented in the Results section and figures of this study. Statistical significance was achieved when  $p < 0.05$ .

## 3. Results

**3.1. X-Ray Analysis.** The results revealed that in the same diet conditions, no significant difference was presented in the body weight of mice in the two groups ( $p > 0.05$ , data not shown). The fracture healing of each group was assessed by X-ray analysis at 1, 2, 3, 4, and 5 weeks postsurgery (Figure 1). X-ray radiographs (Figure 1) demonstrated that the fracture line was observed in the WT group at 4 weeks postfracture, but was barely detectable in *fat-1* group at the same time. In addition, results showed that callus formation in *fat-1* group reached peak at 2 weeks postfracture, which was earlier than that in WT group (3 weeks postfracture). Calcified calluses and bone unions were observed in WT mice at 3 and 4 weeks postfracture, respectively, but was accelerated in *fat-1* mice (2 and 3 weeks postfracture). Moreover, remodeling of calcified callus was initiated at 3 weeks postfracture in *fat-1* group when compared to WT group (5 weeks postfracture).

Simultaneously, for a better measurement of fracture healing, Goldberg classification was used to reveal the callus maturity in the two groups at 5 weeks postfracture [14]. Results showed that the score of *fat-1* group ( $n = 6$  for each time point) was significantly higher than that of WT group (Figure 2). Taken together, these data suggested remarkable acceleration of fracture healing in *fat-1* mice and the

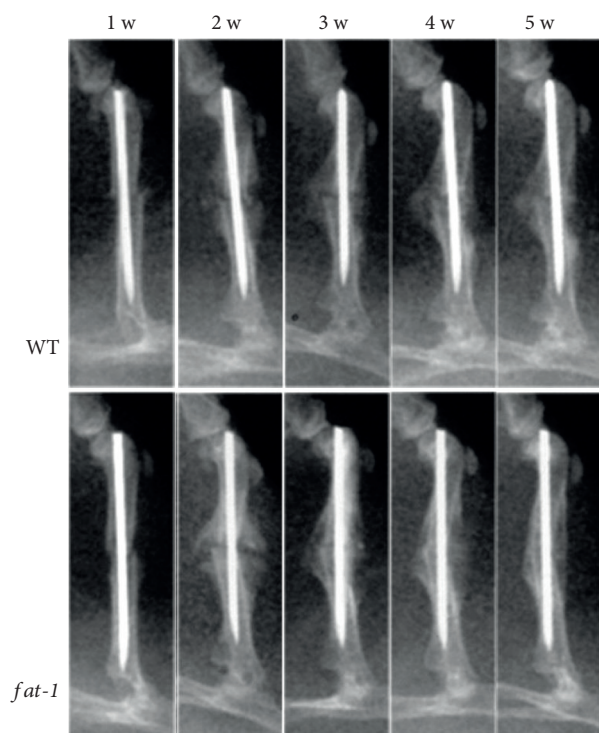


FIGURE 1: X-ray images of WT and *fat-1* mice at 1, 2, 3, 4, and 5 weeks postfracture.

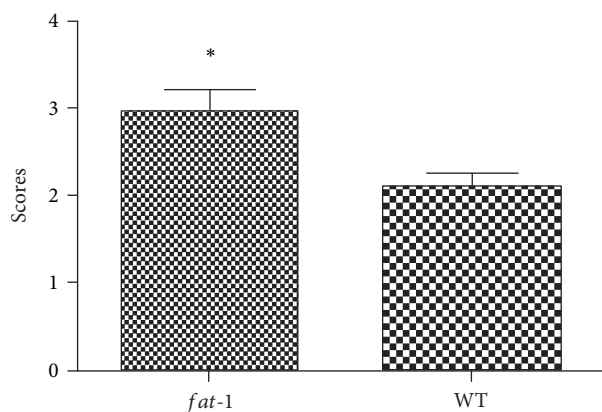


FIGURE 2: The Goldberg scores of two groups at 5 weeks postfracture. \*  $p < 0.05$ .

endogenously produced n-3 PUFAs promoted the fracture healing process of mice.

**3.2. Micro-CT Measurement.** To measure the mineralization of fracture 3D reconstruction of the fractured femur was performed at 5 weeks postfracture, respectively. Though all the fracture healing process has been completed at this time point, the cortical remodeling and cortical bone mass in the fracture area of *fat-1* group presented a significant enhancement compared to those of WT group (Figure 3). These results suggested that in addition to the acceleration of

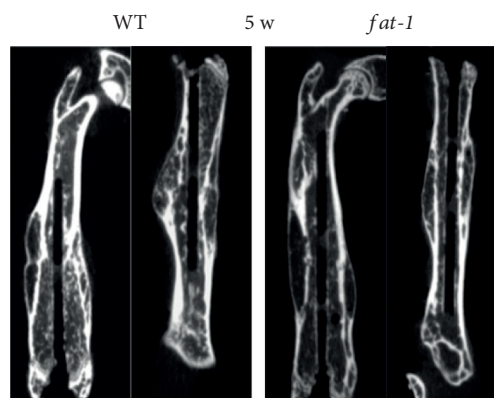


FIGURE 3: Bone remodeling of WT and *fat-1* mice at 5 weeks postfracture.

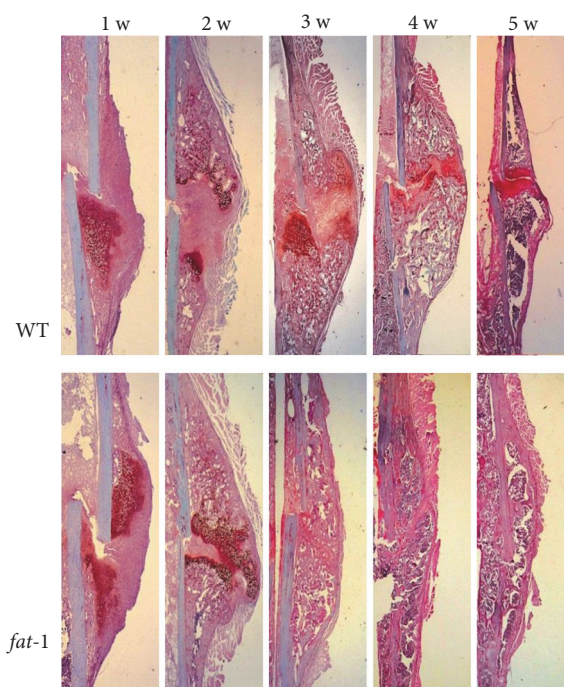


FIGURE 4: Histological measurement of WT and *fat-1* mice at 1, 2, 3, 4, and 5 weeks postfracture.

bony regeneration, the endogenously produced n-3 PUFAs enhanced the strength of new bone as well.

**3.3. Histological Analysis.** To evaluate the formal healing process postfracture of each group, SO/FG stain of each group was performed at 1, 2, 3, 4, and 5 weeks after fracture (Figure 4). The fracture healing process of mice undergoing callus formation, endochondral ossification, and remodeling was described previously [15]. In our observations, mature woven bone and continuous callus formation were presented in the fracture area of *fat-1* group at about 3 weeks postfracture, but early formation of these in WT mice (5 weeks) suggested a promotion of endochondral ossification during the fracture healing process of *fat-1* mice. In addition, clear remodeling was observed in fracture area of *fat-1* mice at

3 weeks postfracture, while remodeling was initiated in WT mice at 4 weeks postfracture. Therefore, our results showed that *fat-1* mice exhibited acceleration in callus formation, endochondral ossification, and remodeling process compared to WT group.

#### 4. Discussion

Recently, the positive roles of n-3 PUFAs in bone remodeling and antiosteoporosis have been demonstrated [3, 16]. Simultaneously, the reduction of n-6/n-3 PUFA ratio in the serum level was positively correlated with mammalian bone mineral density (BMD) and mechanical loading as well [17]. Although former studies have already provided new insights into the effects of n-3 PUFAs on bone metabolism, only few studies focused on the effects of n-3 PUFAs on fracture repair. Therefore, in this present study, we utilized the transgenic *fat-1* mice to determine if the endogenously produced n-3 PUFAs could accelerate fracture healing. To our knowledge, this study is the first study to reveal the effect of endogenous n-3 PUFAs on fracture healing by establishing a transgenic animal model.

Omega-3 polyunsaturated fatty acids are a group of essential fatty acids which cannot be synthesized in sufficient amounts in the body, therefore, they can be supplemented through human diet [18]. The potential health benefits of these have been demonstrated in the past decades, which reduced the risk of coronary heart disease and fracture, and other potential benefits in the prevention and treatment of autoinflammatory disorders, and insulin resistance [19]. The *fat-1* mice are accomplished by transgenic technique and can endogenously converse n-6 PUFAs to n-3 PUFAs, thus were compared to WT mice. The serum ratio of n-6/n-3 PUFAs was significantly lower in *fat-1* transgenic mice compared with control that had sufficient n-6 PUFA intake [13]. In the present study, to eliminate the potential interference factors from diets, *fat-1* mice were chosen to investigate the efficacy of n-3 PUFAs on fracture repair.

Similarly, our results showed a remarkable acceleration of healing time in *fat-1* mice compared to WT mice both radiologically as well as histologically [8]. Meanwhile, the terminal BMD and remodeling in the fracture area of *fat-1* mice enhancement suggested that endogenous n-3 PUFAs can promote fracture healing and optimized the final mineralization of fracture in mice.

Although the present study provided advanced evidence to indicate the positive role of n-3 PUFAs in fracture repair and bone metabolism, the clear mechanism of n-3 PUFAs in modulating the bone repair was absent in our results; this point was the major limitation of our investigation. Therefore, in our future works, the potential signaling that is correlated with skeletal and FA metabolism should be clearly distinguished.

Some studies suggested that AA, a classic n-6 PUFA, has been reported to inhibit endochondral ossification and bone mineralization through activating inflammatory factors like PGE-2 and LTs [20, 21]. In addition, diet supplementation of AA promoted bone formation and reduced the postmenopausal bone loss [22]. Moreover, serum phospholipid levels

of n-3 PUFAs were positively associated with BMD in healthy populations and high serum levels of n-3 PUFAs reduced the risk of osteoporosis in postmenopausal women [23, 24]. Bone-remodeling process was considered to be the vital factor in the maintenance of adult bone mass [25, 26], and consistent with these investigations, our study results demonstrated acceleration of bone remodeling and callus calcification in *fat-1* mice postfracture.

Nevertheless, numerous evidences have proved the vital role of inflammation in fracture healing, and the knockdown of inflammatory factors in mice resulted in the delay of bone repair [27]. Moreover, the local stromal cell recruitment and angiogenesis in the fracture area suppressed the inflammation and then reduced osteogenesis, which lead to the retardation of fracture healing [28]. Therefore, the positive role of n-3 PUFAs in skeletal metabolism is a complex issue and need to be studied deeply. However, most of the investigators believed in the hypothesis that n-6 PUFAs convert to n-3 PUFAs endogenously or intake of n-3 PUFAs may promote bone repair by inhibiting inflammation. Although the mechanism still needed further research, n-3 PUFAs has been shown to reduce the formation of PGE-2 and promotes bone formation through enhancing the expression of insulin-like growth factors, which are powerful growth stimulators for bone remodeling [29, 30]. Meanwhile, muscle-derived n-3 PUFAs have also been shown to increase the digestive calcium absorption and decrease the release of inflammatory cytokines of osteoclasts [29].

In the present study, endogenous conversion of n-6 to n-3 PUFAs promotes terminal differentiation of endochondral ossification and accelerates remodeling of calcified callus in fracture healing of *fat-1* mice. With multiple beneficial effects of n-3 PUFAs in cardio-protection and insulin resistance reduction [16], intake of these has potential application in fracture healing. Our study provides compelling evidence to support the dietary supplementation of n-3 PUFAs in fractures. Meanwhile, a lower n-6/n-3 PUFA ratio should be considered as an impact factor in the diet management of patient with bone fracture.

#### 5. Conclusion

We investigated the effect of endogenous n-3 PUFAs on fracture healing by measuring femur fracture repair in both *fat-1* transgenic mice and WT mice in this study. Our results showed that compared with WT mice, *fat-1* mice exhibited accelerations in healing the fracture. Meanwhile, better endochondral ossification and remodeling callus were presented in *fat-1* mice postfracture. In conclusion, the present study indicated that endogenously produced n-3 PUFAs promoted fracture healing process and accelerated bone remodeling, which suggested that supplementation of n-3 PUFAs may play a positive role in fracture healing.

#### Conflicts of Interest

All authors declared that they have no conflicts of interest to this work.

## Authors' Contributions

Yuhui Chen, He Cao, and Dawei Sun contributed equally to this manuscript.

## Acknowledgments

This research was supported by grants from the National Natural Sciences Foundation of China (30973036, 30870955, 91029727), Program for New Century Excellent Talents in University (NCET-08-0646), and The State Key Development Program for Basic Research of China (2009CB 918904).

## References

- [1] P. Hernigou and J. Pariat, "History of internal fixation (part 1): early developments with wires and plates before world war II," *International Orthopaedics*, pp. 1–11, 2016.
- [2] B. R. Childs, B. A. Andres, and H. A. Vallier, "Economic benefit of calcium and vitamin D supplementation: Does it outweigh the cost of nonunions?" *Journal of Orthopaedic Trauma*, vol. 30, no. 8, pp. e285–e288, 2016.
- [3] J. Banu, A. Bhattacharya, M. Rahman, J. X. Kang, and G. Fernandes, "Endogenously produced n-3 fatty acids protect against ovariectomy induced bone loss in fat-1 transgenic mice," *Journal of Bone and Mineral Metabolism*, vol. 28, no. 6, pp. 617–626, 2010.
- [4] J. J. Wixted, P. J. Fanning, T. Gaur et al., "Enhanced fracture repair by leukotriene antagonism is characterized by increased chondrocyte proliferation and early bone formation: a novel role of the cysteinyl LT-1 receptor," *Journal of Cellular Physiology*, vol. 221, no. 1, pp. 31–39, 2009.
- [5] J. A. Cottrell and J. P. O'Connor, "Pharmacological inhibition of 5-lipoxygenase accelerates and enhances fracture-healing," *The Journal of Bone and Joint Surgery. American Volume*, vol. 91, no. 11, pp. 2653–2665, 2009.
- [6] F. F. Zeng, H. L. Xie, F. Fan et al., "Association of dietary fat intake with the risk of hip fractures in an elderly Chinese population: a matched case-control study," *Geriatrics & Gerontology International*, vol. 15, no. 10, pp. 1171–1178, 2015.
- [7] M. C. Kruger, M. Coetzee, M. Haag, and H. Weiler, "Long-chain polyunsaturated fatty acids: Selected mechanisms of action on bone," *Progress in Lipid Research*, vol. 49, no. 4, pp. 438–449, 2010.
- [8] N. Bonnet and S. L. Ferrari, "Effects of long-term supplementation with omega-3 fatty acids on longitudinal changes in bone mass and microstructure in mice," *The Journal of Nutritional Biochemistry*, vol. 22, no. 7, pp. 665–672, 2011.
- [9] T. Y. Chen, Z. M. Zhang, X. C. Zheng et al., "Endogenous n-3 polyunsaturated fatty acids (PUFAs) mitigate ovariectomy-induced bone loss by attenuating bone marrow adipogenesis in FAT1 transgenic mice," *Drug Design, Development and Therapy*, vol. 7, pp. 545–552, 2013.
- [10] M. J. Toscano, F. Booth, L. J. Wilkins et al., "The effects of long (C20/22) and short (C18) chain omega-3 fatty acids on keel bone fractures, bone biomechanics, behavior, and egg production in free-range laying hens," *Poultry Science*, vol. 94, no. 5, pp. 823–835, 2015.
- [11] T. B. Harris, X. Song, I. Reinders et al., "Plasma phospholipid fatty acids and fish-oil consumption in relation to osteoporotic fracture risk in older adults: the age, gene/environment susceptibility study," *The American Journal of Clinical Nutrition*, vol. 101, no. 5, pp. 947–955, 2015.
- [12] F. Wauquier, L. Leotoing, C. Philippe, M. Spilmont, V. Coxam, and Y. Wittrant, "Pros and cons of fatty acids in bone biology," *Progress in Lipid Research*, vol. 58, pp. 121–145, 2015.
- [13] J. X. Kang, "Fat-1 transgenic mice: a new model for omega-3 research," *Prostaglandins, Leukotrienes, and Essential Fatty Acids*, vol. 77, no. 5, pp. 263–267, 2007.
- [14] M. Goldberg, A. Powell, J. W. Shaffer, J. Zika, G. D. Bos, and K. G. Heiple, "Bone grafting: role of histocompatibility in transplantation. [J]," *Journal of Orthopaedic Research Official Publication of the Orthopaedic Research Society*, vol. 3, no. 4, pp. 389–404, 1985.
- [15] H. Drissi and D. N. Paglia, "Surgical procedures and experimental outcomes of closed fractures in rodent models," *Methods in Molecular Biology*, vol. 1226, pp. 193–211, 2015.
- [16] M. M. Rahman, A. Bhattacharya, J. Banu, J. X. Kang, and G. Fernandes, "Endogenous n-3 fatty acids protect ovariectomy induced bone loss by attenuating osteoclastogenesis," *Journal of Cellular and Molecular Medicine*, vol. 13, no. 8B, pp. 1833–1844, 2009.
- [17] R. C. Poulsen, P. J. Moughan, and M. C. Kruger, "Long-chain polyunsaturated fatty acids and the regulation of bone metabolism," *Experimental Biology and Medicine (Maywood, N.J.)*, vol. 232, no. 10, pp. 1275–1288, 2007.
- [18] N. Kajarabille, J. Diaz-Castro, S. Hijano, M. Lopez-Frias, I. Lopez-Aliaga, and J. J. Ochoa, "A new insight to bone turnover: role of omega-3 polyunsaturated fatty acids," *Scientific World Journal*, vol. 2013, Article ID 589641, 16 pages, 2013.
- [19] R. Feng, M. Wang, C. Yan et al., "Endogenous n-3 fatty acids alleviate carbon-tetrachloride-induced acute liver injury in fat-1 transgenic mice," *Oxidative Medicine and Cellular Longevity*, vol. 2016, Article ID 7962948, 12 pages, 2016.
- [20] C. A. Clark, T. F. Li, K. O. Kim et al., "Prostaglandin E2 inhibits BMP signaling and delays chondrocyte maturation," *Journal of Orthopaedic Research*, vol. 27, no. 6, pp. 785–792, 2009.
- [21] X. Zhang, N. Ziran, J. J. Goater et al., "Primary murine limb bud mesenchymal cells in long-term culture complete chondrocyte differentiation: TGF-beta delays hypertrophy and PGE2 inhibits terminal differentiation," *Bone*, vol. 34, no. 5, pp. 809–817, 2004.
- [22] B. A. Watkins, Y. Li, H. E. Lippman, S. Reinwald, and M. F. Seifert, "A test of Ockham's razor: Implications of conjugated linoleic acid in bone biology," *The American Journal of Clinical Nutrition*, vol. 79, no. 6, pp. 1175S–1185S, 2004.
- [23] B. Tartibian, B. Hajizadeh Maleki, J. Kanaley, and K. Sadeghi, "Long-term aerobic exercise and omega-3 supplementation modulate osteoporosis through inflammatory mechanisms in post-menopausal women: a randomized, repeated measures study," *Nutrition & Metabolism (London)*, vol. 8, no. 1, p. 71, 2011.
- [24] C. Cervellati, G. Bonaccorsi, E. Cremonini et al., "Bone mass density selectively correlates with serum markers of oxidative damage in post-menopausal women," *Clinical Chemistry and Laboratory Medicine*, vol. 51, no. 2, pp. 333–338, 2013.
- [25] K. A. Hruska, T. Sugatani, O. Agapova, and Y. Fang, "The chronic kidney disease-mineral bone disorder (CKD-MBD): Advances in pathophysiology," *Bone*, 2017.
- [26] Y. M. Chen, S. C. Ho, and S. S. Lam, "Higher sea fish intake is associated with greater bone mass and lower osteoporosis risk

- in postmenopausal Chinese women,” *Osteoporosis International*, vol. 21, no. 6, pp. 939–946, 2010.
- [27] C. Schlundt, T. El Khassawna, A. Serra et al., “Macrophages in bone fracture healing: their essential role in endochondral ossification,” *Bone*, 2015.
- [28] D. O. Zubov, “Immunoregulatory role of mesenchymal stem cells in bone reparation processes,” *Fiziologicheskii Zhurnal*, vol. 54, no. 4, pp. 30–36, 2008.
- [29] M. N. Weitzmann and R. Pacifici, “Estrogen deficiency and bone loss: an inflammatory tale,” *The Journal of Clinical Investigation*, vol. 116, no. 5, pp. 1186–1194, 2006.
- [30] F. Bastami, P. Nazeman, H. Moslemi, M. Rezai Rad, K. Sharifi, and A. Khojasteh, “Induced pluripotent stem cells as a new getaway for bone tissue engineering: a systematic review,” *Cell Proliferation*, vol. 50, no. 2, p. e12321, 2017.

## Research Article

# The Effect of Lumbar Disc Herniation on Spine Loading Characteristics during Trunk Flexion and Two Types of Picking Up Activities

Shengzheng Kuai,<sup>1,2</sup> Weiqiang Liu,<sup>1,2</sup> Run Ji,<sup>3</sup> and Wenyu Zhou<sup>4</sup>

<sup>1</sup>Department of Mechanical Engineering, Tsinghua University, Beijing, China

<sup>2</sup>Biomechanics and Biotechnology Lab, Research Institute of Tsinghua University in Shenzhen, Shenzhen, China

<sup>3</sup>National Research Center for Rehabilitation Technical Aids, Beijing, China

<sup>4</sup>Department of Orthopedics, Shenzhen Second People's Hospital, Shenzhen, China

Correspondence should be addressed to Wenyu Zhou; [zhouwenyu\\_spn@163.com](mailto:zhouwenyu_spn@163.com)

Received 22 February 2017; Revised 16 April 2017; Accepted 26 April 2017; Published 11 June 2017

Academic Editor: Wenxin Niu

Copyright © 2017 Shengzheng Kuai et al. This is an open access article distributed under the Creative Commons Attribution License, which permits unrestricted use, distribution, and reproduction in any medium, provided the original work is properly cited.

The main purpose of this study was to investigate the compensatory response of the muscle activities of seventeen major muscle groups in the spinal region, intradiscal forces of the five lumbar motion segment units (MSUs), and facet forces acting on the ten lumbar facet joints in patients with lumbar disc herniation (LDH). Twenty-six healthy adults and seven LDH patients performed trunk flexion, ipsilateral picking up, and contralateral picking up in sequence. Eight optical markers were placed on the landmarks of the pelvis and spinal process. The coordinates of these markers were captured to drive a musculoskeletal model to calculate the muscle activities, intradiscal forces, and facet forces. The muscle activities of the majority of the seventeen major muscle groups were found increases in LDH patients. In addition, the LDH patients displayed larger compressive forces and anteroposterior forces on all the five lumbar MSUs and more lumbar facet inventions on most facet joints. These findings suggest that the LDH patients demonstrate compensatory increases in the most trunk muscle activities and all spinal loads. These negative compensatory responses increase the risk of the aggravation of disc herniation. Therefore, treatment should intervene as earlier as possible for the severe LDH patients.

## 1. Introduction

Low back pain (LBP) is a major health problem that has an enormous effect on many people especially on those who are sitting for prolonged periods. The patients with LBP usually alter their motion patterns to compensate for limited functional motion through different strategies [1]. This alternation may cause local or global musculoskeletal overload which is believed to play a causative role in exacerbating the back disorders or pain [2, 3].

Trunk flexion is a major component of many activities of daily living (ADLs) and is also a routine examination program in the clinical evaluation of LBP [4]. Picking up an

object from the floor is also common, but harder, functional activity and may reveal more compensatory strategies in LBP patients. Studies about the two activities have mainly focused on the kinematic analysis including the ranges of motion (ROM) in the lumbar, pelvis, and hip [1, 5–7] and the rhythm between lumbar and hip [8, 9] or between lumbar and pelvis [10–12].

Relevant kinetic studies during the trunk flexion and picking up activities have been limited to the people without back pain [13–15]. Two studies [16, 17] on healthy people have found that the spinal loads and muscle activities would be altered when they were required to change their lumbar rhythm subjectively. Patients with LBP

usually adjust their lumbar rhythm due to pain, which may increase the spinal loads and muscle forces and therefore place their trunk system in higher risks of back disorders, tissue injuries, and fatigue.

However, most LBP patients' kinetic studies related to the loads acting on the lumbar region have mainly focused on the different kinds of lifting [18–21] and sit-to-stand [22, 23]. It has been found that LBP patients demonstrate greater compressive forces and shear forces acting on the lumbar region during lifting. Nonetheless, to the authors' knowledge, none of previous reports from the literature have explored the effect of LBP on compressive force and shear force of every lumbar motion segment unit (MSU) during ADLs such as trunk flexion and picking up.

Apart from the intradiscal forces, the muscle forces and activities are also affected by LBP in previous studies. Yahia et al. [24] have found that LBP patients display the deficit of trunk muscles, especially in the extensors when carrying out the isokinetic evaluation. Dubois et al. [25–27] have also reported that LBP would induce increases in lumbar erector spinae (ES) activities during functional tasks.

Facet joint (FJ) is a part of the three-column structure of the vertebrae and plays an important role in load transmission and maintenance of the stability of the spinal motion. In previous kinetic studies during ADLs, the FJ was usually not taken into consideration. However, the facet orientation in the lumbar region has been found irregular alteration in lumbar disc herniation patients [28]. Also, the facet forces have been found amplification under excessive physiological loads that could be induced by LBP [29].

LBP includes a variety of subtypes. The kinematic difference has been found among different subgroups of LBP patients during different ADLs [12, 30, 31]. Likewise, the muscle activation patterns have also been found to be heterogeneity among LBP individuals [32].

Thus, the purpose of this study was to investigate the impact of LBP caused by lumbar disc herniation (LDH) on intradiscal forces and facet forces at five lumbar MSUs and the activities of the eight back main muscle groups and nine front main muscle groups in the spinal region during trunk flexion, ipsilateral picking up, and contralateral picking up. We explored three hypotheses: (1) there were more back muscle activities and less front muscle activities in LDH patients; (2) in the lumbar pathological region, the compressive forces decreased while the antero-posterior shear forces increased in patients with LDH; and (3) there were more interventions of facet joint in the LDH group.

## 2. Method

**2.1. Subject.** Twenty-six healthy adults (mean age  $23.6 \pm 1.92$  years, mean height  $169.9 \pm 5.9$  cm, mean weight  $63.5 \pm 8.4$  kg) and seven LDH patients (mean age  $28.7 \pm 4.5$  years, mean height  $170.1 \pm 3.4$  cm, mean weight  $67.4 \pm 5.3$  kg) participated in this study. The inclusive criteria of the healthy group were

(a) no visible motor dysfunction, (b) no any kinds of surgery within recent one year, (c) no any back pain, and (d) no intense exercise 24 hours before trial. The enroll criteria of LDH patients were that (a) the patients were diagnosed with lumbar disc herniation in the course of discopathy in lumbar spine. The diagnosis was made by at least two specialist orthopedic surgeons and confirmed by X-ray imaging and MRI. (b) The disc herniation was diagnosed to occur at the lower lumbar level by MRI. (c) The patients had the ability to conduct level walking and stair climbing. In the examination, the patients were required to attempt to walk and climb stairs. They were deemed to maintain the movement ability if they could perform at least 20 gait cycles. In this study, the disc herniation was found to happen at L4L5 level in three-seventh cases, at L5S1 level in another three-seventh cases, and at both L4L5 and L5S1 levels in one-seventh cases. This study was approved by the Department of Orthopedics of Shenzhen Second People's Hospital in China. All the participants were given informed consent before trial.

**2.2. Protocol.** The subjects lay in the prone position on a bed, and one surgeon helped to locate the landmarks of the spinous processes of the third and seventh thoracic vertebra (T3, T7), of the first, third, and fifth lumbar vertebra (L1, L3, L5), left and right posterior superior iliac spine (LPSIS, RPSIS), and the iliac crest (IC). Then eight 3D active optical markers were placed on these landmarks (Figure 1(a)). The Optotrak Certus motion analysis system (Northern Digital Inc., Ontario, Canada) was applied to capture the motion of these optical markers at the sample rate of 100 Hz.

Before trials, one surgeon demonstrated the activities of trunk flexion, ipsilateral picking up, and contralateral picking up (Figure 1(b)) and then guided them to practice the three activities several times until they felt they could perform every activity naturally. Every trial was repeated three times for data collection.

**2.3. Testing Procedure.** Before the trial, the participants maintained a neutral upright standing position for at least five seconds to collect the data of baseline. Then, they flexed forward to their maximum voluntary rotation and subsequently returned to their initial position. During the process, the subjects were asked to keep their knee extended. After finishing the task of trunk flexion, the subjects were allowed to take a no more than ten-minute rest. Next, the subjects picked up a small adhesive tape two hundred millimeters in front of their right foot using their right hand. During this ipsilateral picking up activity and subsequent contralateral picking up activity, the subjects were encouraged to give priority to flex their trunk. Likewise, the subjects would have a rest. Afterward, they picked up the object in front of their left foot using their right hand. During the two types of picking up, the subjects were not encouraged to flex their knees except that some subjects could not finish the task without knee flexion.

**2.4. Musculoskeletal Model and Simulation.** A generic FacetJointModel model in the Anybody managed model

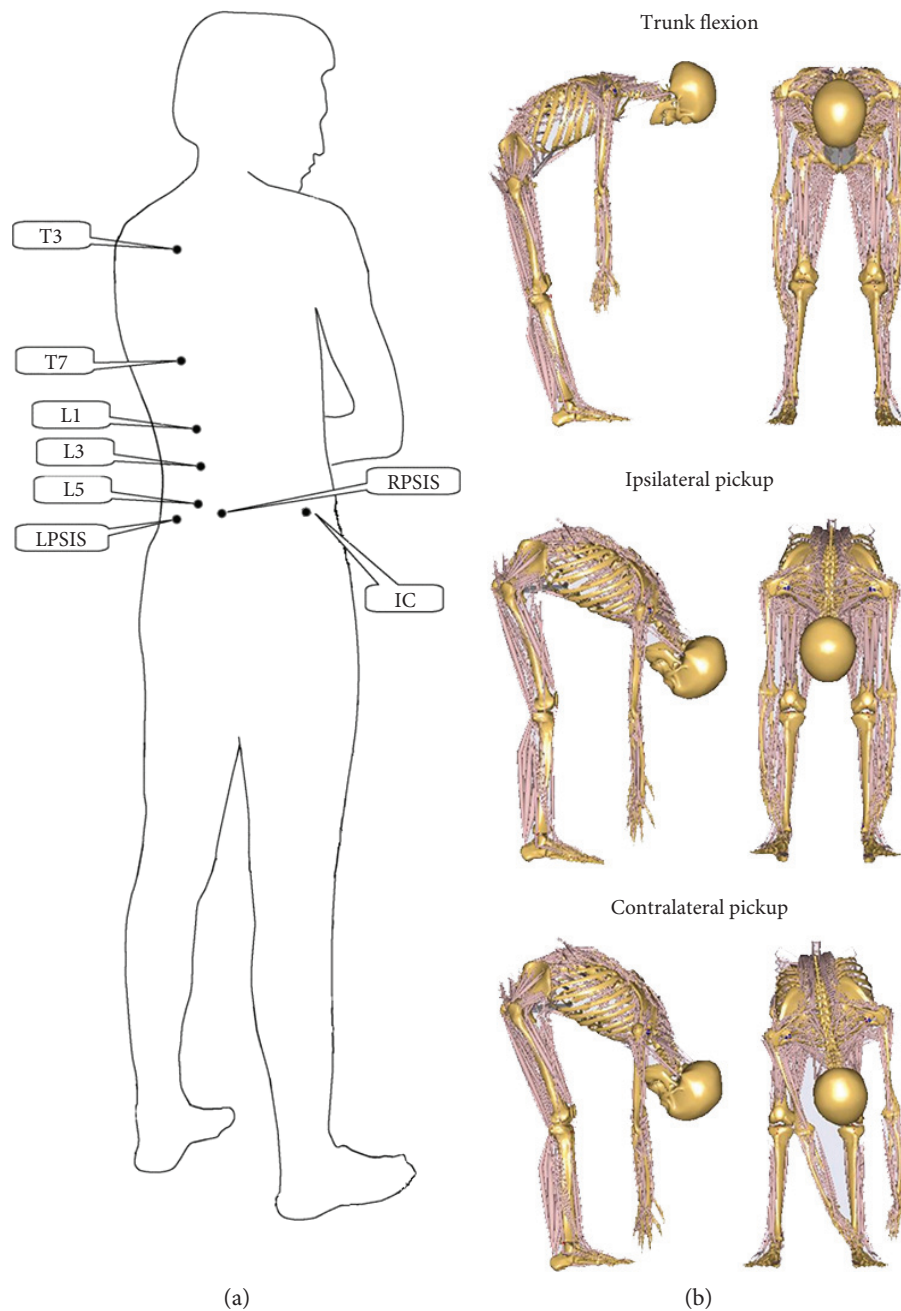


FIGURE 1: (a) Schematic of the marker placement. (b) Schematic of the test procedure.

repository (AMMR, version 1.6) of Anybody modeling system (Anybody modeling system version 6.0.6, Aalborg, Denmark) was applied to calculate the muscle activities, intradiscal forces, and facet forces. This inverse dynamic analysis software and the model were selected since it could quickly predict the forces in a redundant system. In addition, this model has been validated in terms of the minimum-maximum optimization algorithm [33] which was used to solve the recruitment problem. A detailed description of the model has been previously reported and developed by de Zee et al. [33, 34]. In brief, the spinal region consisted of the cervical, thoracic, and

lumbar spines. The cervical and thoracic segments were modeled as a single lumped segment. The lumbar spine included five rigid bodies. These segments were connected with an intervertebral joint which was modeled as a spherical joint. The location of each joint was based on the work by Pearcy and Bogduk [35].

The muscles in the model were divided into several functional fascicles. The following muscle fascicles were involved in this spine model: 5 transversus, 3 spinalis, 1 rectus abdominis (RA), 58 erector spinae (ES), 38 lumbar multifidus, 24 thoracic multifidus, 12 oblique externus, 12 oblique internus, 22 psoas major, 10 quadratus lumborum, and 18

semispinalis. All the muscles fascicles were solved as force component in the redundant model system and could only exert tensile force [33, 36, 37].

The model also included ten facet joints in the lumbar region. The location of each facet joint was modeled as a node in the center of the facet contact side on each vertebra, and the orientation of each facet joint was based on the work by Masharawi et al. [38]. The facet force was determined by the distance between the superior and inferior articular facet points of the adjacent vertebra. The contact force solved by this model has been validated based on previous studies [39].

In the Anybody system, the model was driven by the default coefficient of spinerhythm. To investigate the abnormal kinetic characteristics in LDH patients, the model was developed and driven by the captured markers placed on the landmarks of the selected segments. In this study, the motions of L2, L3, and L4 were determined by attributing different weights to the captured markers (Table 1). The other two lumbar segments (L1, L5) were driven using the default ratio of coefficient of spinethytm between L1L2Jnt and L2L3Jnt and between L4L5Jnt and L5S1Jnt, respectively. The pelvic segment was driven by the three markers on the landmarks of the pelvis, and the motion of thoracic segment was determined by the two markers on the thoracic landmarks.

**2.5. Data Analysis.** The excursion angle of the thoracic segment with respect to the baseline was recorded. The analyzed period defined the onset as the moment when the excursion firstly reached the three degrees and the termination as the moment when the excursion firstly raised at the ninety degrees or maximum excursion angle in the condition that the subjects could not flex their trunk over ninety degrees. The maximum muscle activities of the seventeen main muscle groups and the intradiscal forces were analyzed with respect to every excursion angle and normalized to 0–90 degrees with ninety-one points. In addition, the intradiscal forces were also normalized to the weight of every subject.

In the model, the facet force was zero when there was no contact between the superior and inferior articular facet points of the adjacent vertebra. In this study, less than 10N force was regarded as no contact and more than 50N force was considered as a strong contact. The facet force between the two threshold values was deemed to be weak contact. Thus, in the present study, the facet intervention includes two levels, namely, the small level that expresses the weak contact and the large level that expresses the strong contact. The durations of small level and large level in the whole period were counted, respectively. Independent group *t*-tests were applied to analyze the difference between healthy subjects and LDH patients on the durations of facet contact in two levels. Data analysis were performed using a custom-made program implemented in MATLAB (The MathWorks, Inc.).

### 3. Results

**3.1. The Activities of the Main Front and Back Muscle Groups in the Spinal Region.** During the trunk flexion movement,

TABLE 1: The weight of markers in trunk section for lumbar vertebrae and thoracic segment.

	Marker T3	Marker T7	Marker L1	Marker L3	Marker L5
Thx	1/2	1/2	0	0	0
L2	0	0	1/2	1/2	0
L3	0	0	1/6	2/3	1/6
L4	0	0	0	1/2	1/2

Thx: the lumped thoracic segment; L1: the first lumbar vertebra; L2: the second lumbar vertebra; L3: the third lumbar vertebra; L4: the fourth lumbar vertebra; L5: the fifth lumbar vertebra; T3: the third thoracic vertebra; T7: the seventh thoracic vertebra.

there was a slight tendency towards larger maximum muscle activities of the four back muscle groups (Figure 2) and IO, EO, PM, and QL (Figure 3) in the end range of flexion. Moreover, the RA was consistently in a larger muscle activity comparing with that in the controls. During the ipsilateral picking up movement, the patients demonstrated more muscle activities of the four back muscle groups (Figure 2) and PM, QL, right EO, and left IO of the front muscle groups (Figure 3) with the increasing flexion angle. Similar to that of trunk flexion, patients demonstrated higher muscle activity of RA in the middle and end ranges of ipsilateral picking up movement. During the contralateral picking up movement, the maximum muscle activities of the four back muscle groups in LDH patients were found larger than those in the controls in the middle and end ranges of this movement.

**3.2. The Intradiscal Forces in the Spinal Region.** The compressive forces and shear forces of all the five lumbar MSUs are shown in Figures 4 and 5, respectively. During the trunk flexion movement, LDH patients demonstrated larger compressive forces on all the five lumbar intervertebral discs (LIDs) with the increase in the flexion angle. During both ipsilateral picking up and contralateral picking up movements, there were significant increases in all the five LIDs in the middle range of the picking up movement in LDH patients. As the flexion angle increasing, the LDH patients demonstrated larger shear forces on all the five LIDs during all the three movements.

**3.3. The Interventions of Facet Joints in the Spinal Region.** Figure 6 presents the durations of facet intervention on both sides of the five MSUs during the analyzed period. During the trunk flexion movement, LDH patients displayed significantly longer durations of facet intervention on the left facet of L2L3 at a small level, and on the left facets of L4L5 and L5S1 at a large level. During the ipsilateral picking up movement, there were significant increases in the durations of facet intervention on the right facet of L2L3 at a small level and left facets of L2L3, L5S1, the right facet of L5S1 at a large level in LDH patients. In addition, the left facets of L1L2, L2L3, L4L5, and L5S1 and the right facets of L2L3 and L4L5 were found to prolong the durations of facet intervention at a large level significantly during contralateral picking up movement in LDH patients.

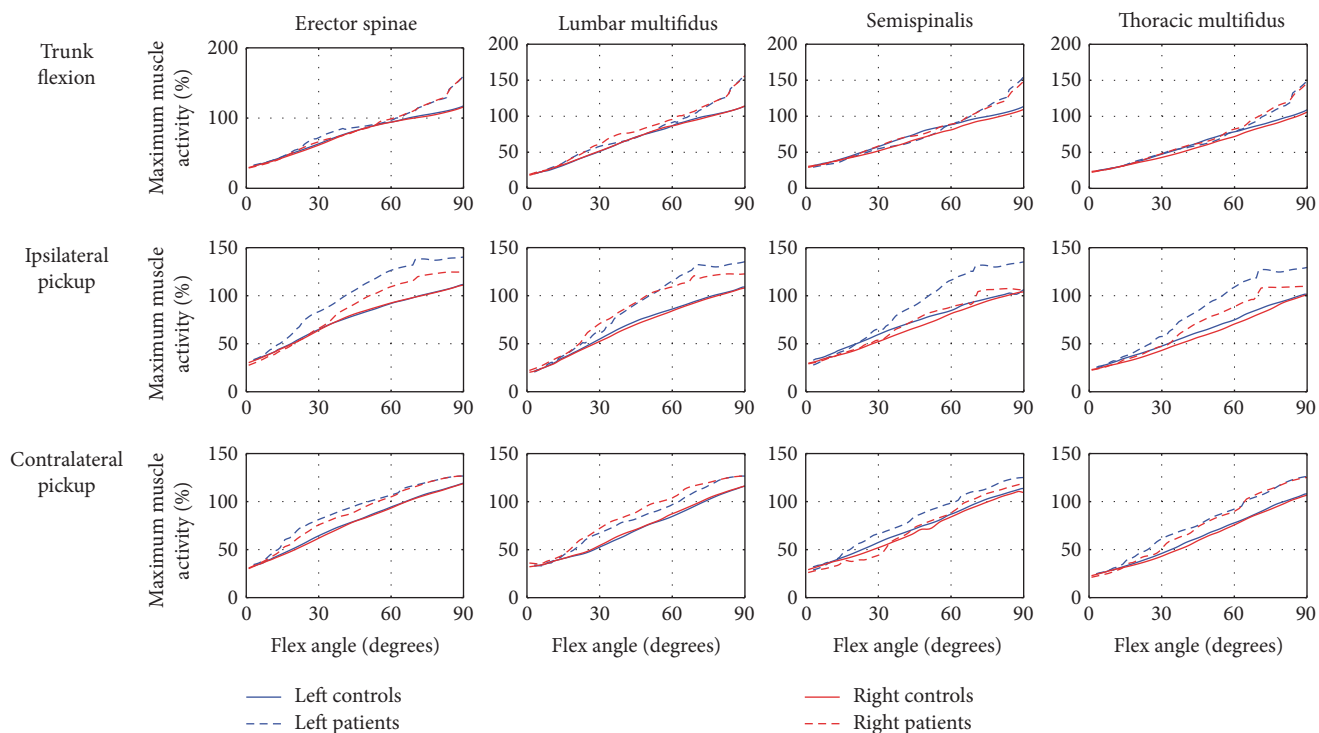


FIGURE 2: The comparison of the maximum muscle activities of the back main muscle groups in the spinal region between controls and LDH patients. The red and blue solid line—maximum muscle activity in controls; the red and blue dash-dotted line—maximum muscle activity in LDH patients.

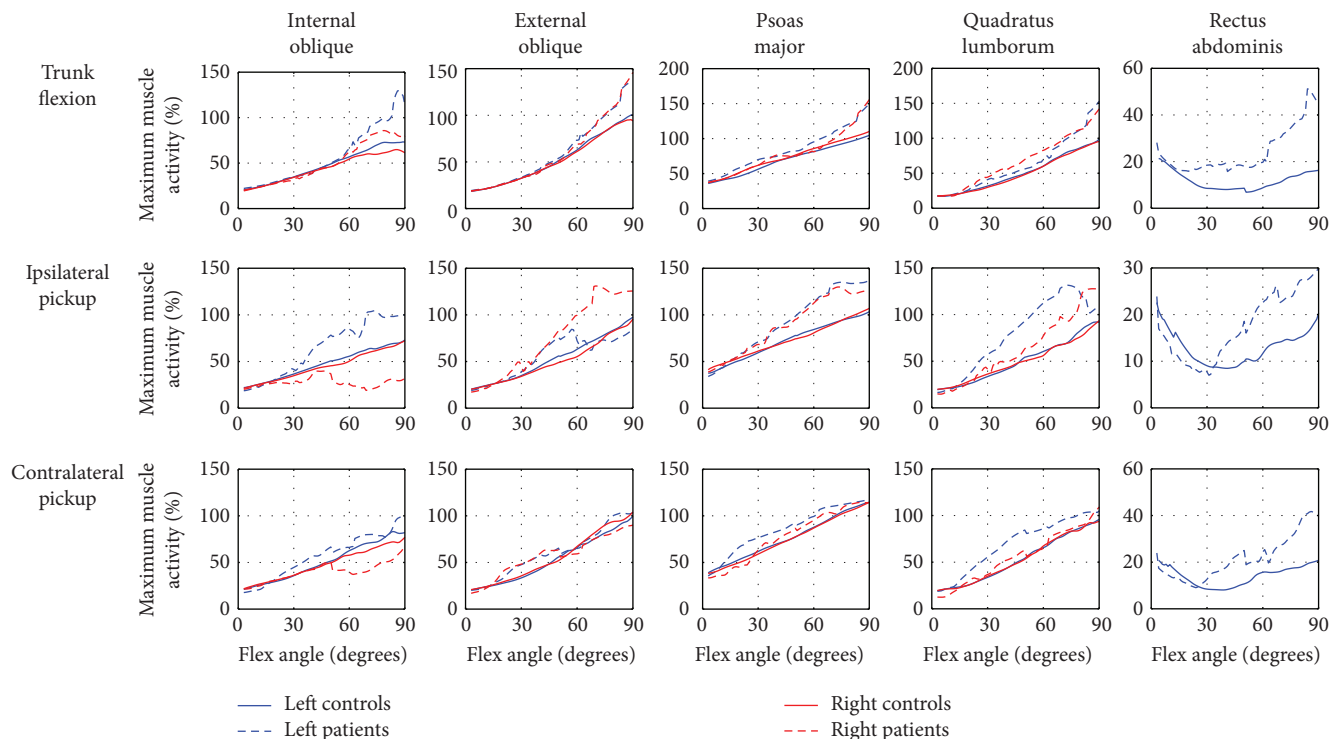


FIGURE 3: The comparison of the maximum muscle activities of the front main muscle groups in the spinal region between controls and LDH patients. The red and blue solid line—maximum muscle activity in controls; the red and blue dash-dotted line—maximum muscle activity in LDH patients.

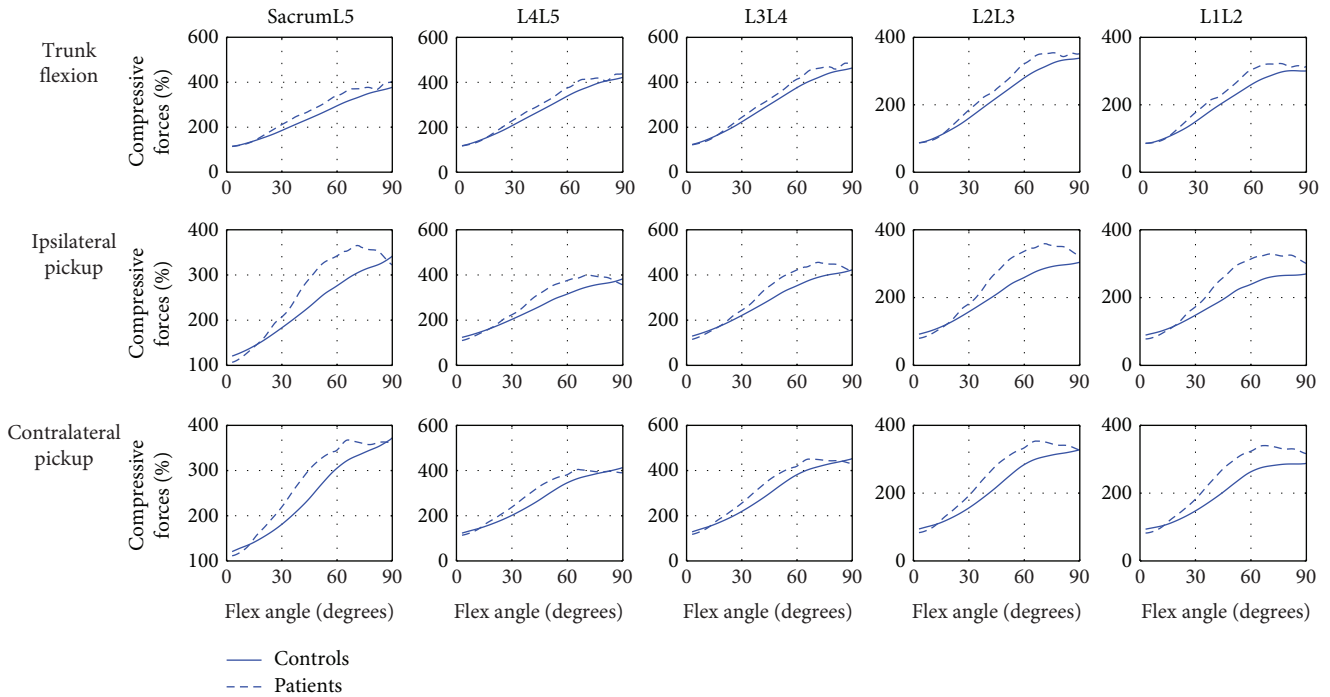


FIGURE 4: The comparison of the compressive forces in five lumbar discs between controls and LDH patients. The blue solid line—maximum muscle activity in controls; the blue dash-dotted line—maximum muscle activity in LDH patients.

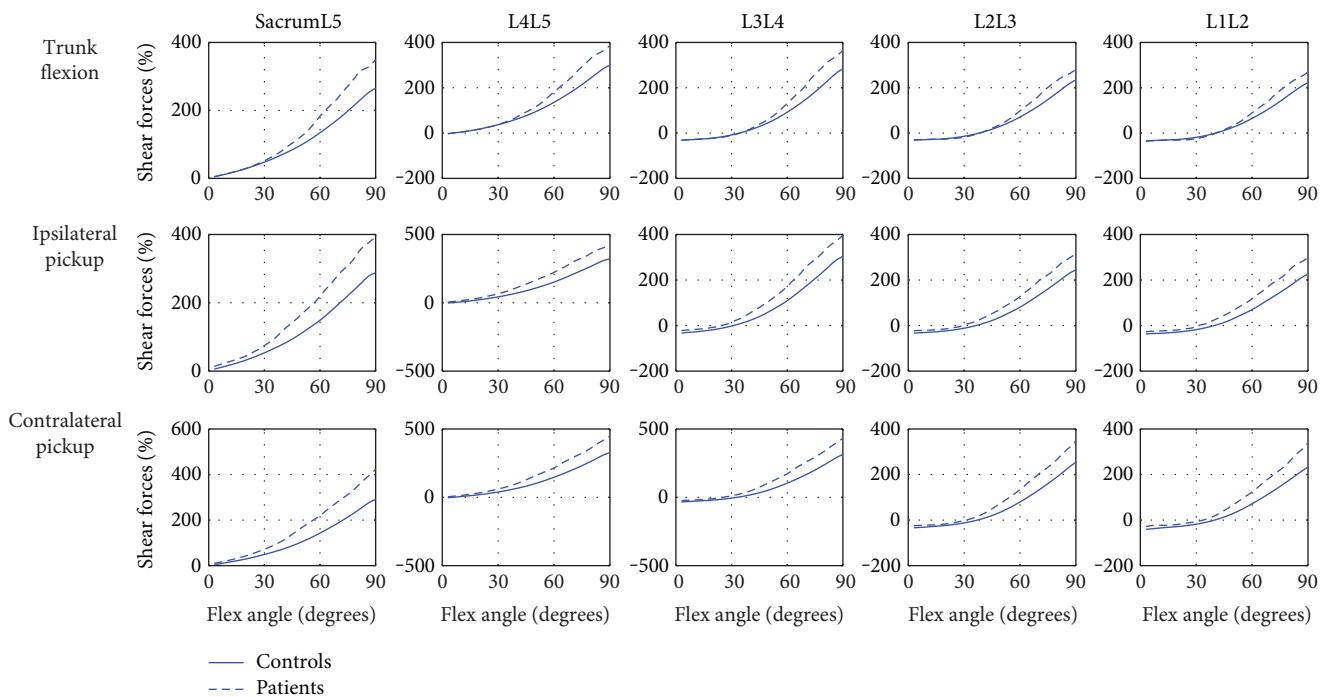


FIGURE 5: The comparison of the anteroposterior shear forces in five lumbar discs between controls and LDH patients. The blue solid line—maximum muscle activities in controls; the blue dash-dotted line—maximum muscle activities in LDH patients.

#### 4. Discussion

This study aims to explore how LDH affect the maximum muscle activities of the seventeen main muscle groups in the spinal

region and structural loads acting on every lumbar MSU during trunk flexion and two types of picking up activities.

The maximum muscle activities of all the eight back main muscle groups manifested an increasing tendency at the

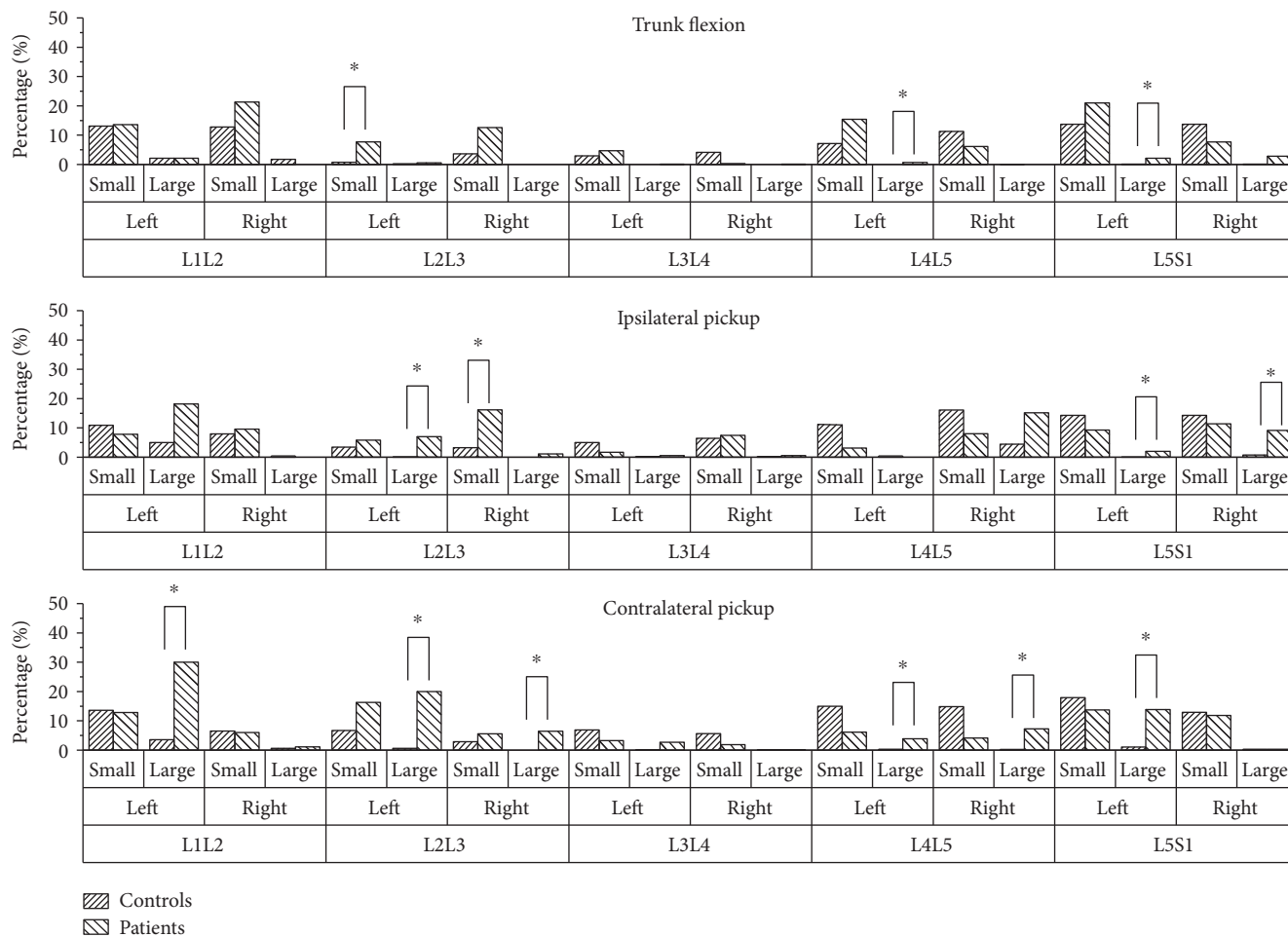


FIGURE 6: The durations and levels of the facet intervention during the analyzed period. Large represents the sum of duration when the facet forces are more than 50 N; small represents the sum of the duration when the facet forces are between 10 N and 50 N. \* indicates the significant difference between controls and patients.

middle and end ranges of two picking up activities in patients with LDH, supporting the first half of the first hypothesis. However, the maximum muscle activities of all the nine front main muscle groups were not found a reduction in LDH patients which was not consistent with the last part of the first hypothesis. The patients displayed greater compressive forces and anteroposterior shear forces during the three ADLs, which supported the first half of the second hypothesis and disproved the last half part of the second hypothesis. The more facet inventions were found in patients with LDH during the three ADLs, approving the third hypothesis.

In this study, the muscle activation patterns in LDH patients were not all in consistent with the expectations. In agreement with the previous literature [25–27], LDH patients increased the muscle activities of the back main muscle groups, which may be ascribable to muscle spasm [40] or an attempt to improve spinal stability and protect damaged passive tissue or structure [41–43]. However, the increased muscle activities in the back region did not relieve the muscle activities in the front region in the present study, which was probably because the only increased back muscle activities were not sufficient to compensate for the reduced passive spine stability. Unfortunately, both the increase in the back

muscle activities and front muscle activities would lead to a negative consequence because the causative and adaptive relationship between the abnormal muscle activities and lumbar disc herniation development may actually be circular: a higher level of muscle activities predisposes to pain development, following which the muscle activities further increase to alleviate the pain, and the cycle perpetuates.

Compressive forces and shear forces are the two most direct factors that affect the disc herniation [44]. In the third hypothesis, LDH patients should decrease compressive force to reduce the risk of aggravating the disc herniation and increase shear forces as compensation. However, the hypothesis was not validated in this study. The finding showed that both compressive forces and shear forces were greater in LDH patients than in healthy subjects, which was in accordance with prior reports [18, 21, 32]. The larger compressive forces and shear forces were related to excessive muscle coactivity [45], and the increased muscle activities were also found in this study. Moreover, the increase in the intradiscal forces would impose damage to the annulus fibrosus and further induce disc herniation [46].

The facet joint (FJ) is an important structure in lumbar spine and plays a significant role in providing stability to

the spinal system. During trunk flexion, small intervention played a predominant role in providing spinal loads. Moreover, five of the ten facet joints were found longer durations of small intervention while only one found shorter duration of small intervention in LDH patients. During ipsilateral picking up and contralateral picking up, the ten FJs mainly demonstrated intervention at a large level. In LDH patients, the durations of large intervention were found significant increases ( $P < 0.05$ ) in three of the ten FJs during ipsilateral picking up and six of the ten FJs during contralateral picking up. Noteworthy was that none of the ten FJs was found a reduction in durations of large intervention. These findings might be due to the restriction in the direction of extension and rotation by FJ [47] and the increased rotation movement from trunk flexion to contralateral picking up activity. The increased FJ intervention in LDH patients might also be a compensatory manifestation of the deficit of soft tissue' stability.

To sum up, it has been suggested that LDH patients displayed more muscle activities, larger intradiscal forces, and more facet interventions during trunk flexion and two types of picking up. These changes might be a compensatory response to relieve pain and improve spinal stability. However, these responses further burdened the trunk musculature, passive soft tissue, and spinal structure during functional tasks. These findings revealed the compensatory mechanism in LDH patients and the necessity of receiving treatments for these patients in terms of spinal loading system.

Some limitations of this study should be noted. First, the sample of patients was relatively small, which might limit the statistical power of the result. Second, only L1, L3, and L5 were placed on optical markers so L1 and L5 could not be driven by captured markers directly. The intersegmental motion difference between L1 and L2 and between L4 and L5 was omitted, which might reduce the difference between two groups in muscle force. Third, the definition of no contact and strong contact of the facet joint was a little arbitrary.

## 5. Conclusions

The present study has shown that LDH patients displayed more muscle activities in the majority of the seventeen main muscle groups in the spinal region, greater compressive forces and anteroposterior shear forces acting on the five lumbar motion segment units, and more facet interventions in the majority of the ten lumbar facet joints. The compensatory response of kinetics in LDH patients played a rather negative role in maintaining the spinal stability and further led to the development of disc herniation. Therefore, patients with severe lumbar disc herniation should receive treatment intervention as early as possible in terms of the compensatory response of muscle activity and spinal load. Moreover, the method in the study will be useful for clinician to assess the biomechanical improvement after different treatments and may also be used towards the development of more effective personalized rehabilitation strategies.

## Conflicts of Interest

The authors declare that there is no conflict of interests regarding the publication of this paper.

## Acknowledgments

The authors thank Shenzhen Second People's Hospital and Research Institute of Tsinghua University in China. They provided the equipment and helped to collect the experimental data. The authors also thank all the participants. This research was funded by the Economy, Trade and Information Commission of Shenzhen Municipality (Grant no. SMJKPT20140417010001), the Innovation Commission of Science and Technology of Shenzhen Municipality (Grant no. JCYJ20151030160526024), and the Guangdong Provincial Department of Science and Technology (Grant no. 2014A020212655).

## References

- [1] G. L. K. Shum, J. Crosbie, and R. Y. W. Lee, "Movement coordination of the lumbar spine and hip during a picking up activity in low back pain subjects," *European Spine Journal*, vol. 16, no. 6, pp. 749–758, 2007.
- [2] M. S. Thiese, K. T. Hegmann, E. M. Wood et al., "Prevalence of low back pain by anatomic location and intensity in an occupational population," *BMC Musculoskeletal Disorders*, vol. 15, no. 1, p. 283, 2014.
- [3] L. Manchikanti, "Epidemiology of low back pain," *Pain Physician*, vol. 3, no. 2, pp. 167–192, 2000.
- [4] W. S. Marras, K. E. Lewis, S. A. Ferguson, and M. Parnianpour, "Impairment magnification during dynamic trunk motions," *Spine*, vol. 25, no. 5, pp. 587–595, 2000.
- [5] D. G. Cobian, N. S. Daehn, P. A. Anderson, and B. C. Heiderscheit, "Active cervical and lumbar range of motion during performance of activities of daily living in healthy young adults," *Spine*, vol. 38, no. 20, pp. 1754–1763, 2013.
- [6] L. R. Van Dillen, S. P. Gombatto, D. R. Collins, J. R. Engsborg, and S. A. Sahrman, "Symmetry of timing of hip and lumbopelvic rotation motion in 2 different subgroups of people with low back pain," *Archives of Physical Medicine and Rehabilitation*, vol. 88, no. 3, pp. 351–360, 2007.
- [7] J. E. Bible, D. Biswas, C. P. Miller, P. G. Whang, and J. N. Grauer, "Normal functional range of motion of the lumbar spine during 15 activities of daily living," *Journal of Spinal Disorders & Techniques*, vol. 23, no. 2, pp. 106–112, 2010.
- [8] M. A. Esola, M. C. PW, G. K. Fitzgerald, and S. Siegler, "Analysis of lumbar spine and hip motion during forward bending in subjects with and without a history of low back pain," *Spine*, vol. 21, no. 1, pp. 71–78, 1996.
- [9] P. W. McClure, M. Esola, R. Schreier, and S. Siegler, "Kinematic analysis of lumbar and hip motion while rising from a forward, flexed position in patients with and without a history of low back pain," *Spine*, vol. 22, no. 5, pp. 552–558, 1997.
- [10] R. F. Jandre and A. R. Macedo, "Influence of hamstring tightness in pelvic, lumbar and trunk range of motion in low back pain and asymptomatic volunteers during forward bending," *Asian Spine Journal*, vol. 9, no. 4, pp. 535–540, 2015.
- [11] K. Hasebe, K. Sairyo, Y. Hada et al., "Spino-pelvic-rhythm with forward trunk bending in normal subjects without low back

- pain," *European Journal of Orthopaedic Surgery and Traumatology*, vol. 24, Supplement 1, pp. S193–S199, 2014.
- [12] M. H. Kim, C. H. Yi, O. Y. Kwon et al., "Comparison of lumbopelvic rhythm and flexion-relaxation response between 2 different low back pain subtypes," *Spine*, vol. 38, no. 15, pp. 1260–1267, 2013.
- [13] I. Takahashi, S. I. Kikuchi, K. Sato, and N. Sato, "Mechanical load of the lumbar spine during forward bending motion of the trunk - a biomechanical study," *Spine*, vol. 31, no. 1, pp. 18–23, 2006.
- [14] W. S. Marras, M. J. Jorgensen, and K. G. Davis, "Effect of foot movement and an elastic lumbar back support on spinal loading during free-dynamic symmetric and asymmetric lifting exertions," *Ergonomics*, vol. 43, no. 5, pp. 653–668, 2000.
- [15] A. Tafazzol, N. Arjmand, A. Shirazi-Adl, and M. Parnianpour, "Lumbopelvic rhythm during forward and backward sagittal trunk rotations: combined in vivo measurement with inertial tracking device and biomechanical modeling," *Clinical Biomechanics*, vol. 29, no. 1, pp. 7–13, 2014.
- [16] N. Arjmand and A. Shirazi-Adl, "Biomechanics of changes in lumbar posture in static lifting," *Spine*, vol. 30, no. 23, pp. 2637–2648, 2005.
- [17] R. Arshad, T. Zander, M. Dreischarf, and H. Schmidt, "Influence of lumbar spine rhythms and intra-abdominal pressure on spinal loads and trunk muscle forces during upper body inclination," *Medical Engineering & Physics*, vol. 38, no. 4, pp. 333–338, 2016.
- [18] W. S. Marras, S. A. Ferguson, D. Burr, K. G. Davis, and P. Gupta, "Functional impairment as a predictor of spine loading," *Spine*, vol. 30, no. 7, pp. 729–737, 2005.
- [19] W. E. Hoogendoorn, P. M. Bongers, H. C. de Vet et al., "Flexion and rotation of the trunk and lifting at work are risk factors for low back pain - results of a prospective cohort study," *Spine*, vol. 25, no. 23, pp. 3087–3092, 2000.
- [20] J. S. Han, V. K. Goel, J. Y. Ahn et al., "Loads in the spinal structures during lifting: development of a three-dimensional comprehensive biomechanical model," *European Spine Journal*, vol. 4, no. 3, pp. 153–168, 1995.
- [21] W. S. Marras, K. G. Davis, S. A. Ferguson, B. R. Lucas, and P. Gupta, "Spine loading characteristics of patients with low back pain compared with asymptomatic individuals," *Spine*, vol. 26, no. 23, pp. 2566–2574, 2001.
- [22] G. L. K. Shum, J. Crosbie, and R. Y. W. Lee, "Effect of low back pain on the kinematics and joint coordination of the lumbar spine and hip during sit-to-stand and stand-to-sit," *Spine*, vol. 30, no. 17, pp. 1998–2004, 2005.
- [23] G. L. K. Shum, J. Crosbie, and R. Y. W. Lee, "Three-dimensional kinetics of the lumbar spine and hips in low back pain patients during sit-to-stand and stand-to-sit," *Spine*, vol. 32, no. 7, pp. E211–E219, 2007.
- [24] A. Yahia, S. Jribi, S. Ghroubi, M. Elleuch, S. Baklouti, and M. H. Elleuch, "Evaluation of the posture and muscular strength of the trunk and inferior members of patients with chronic lumbar pain," *Joint, Bone, Spine*, vol. 78, no. 3, pp. 291–297, 2011.
- [25] J. D. Dubois, M. Piché, V. Cantin, and M. Descarreaux, "Effect of experimental low back pain on neuromuscular control of the trunk in healthy volunteers and patients with chronic low back pain," *Journal of Electromyography and Kinesiology*, vol. 21, no. 5, pp. 774–781, 2011.
- [26] M. E. Geisser, A. J. Haig, A. S. Wallbom, and E. A. Wiggert, "Pain-related fear, lumbar flexion, and dynamic EMG among persons with chronic musculoskeletal low back pain," *Clinical Journal of Pain*, vol. 20, no. 2, pp. 61–69, 2004.
- [27] R. D'Hooge, P. Hodges, H. Tsao, L. Hall, D. MacDonald, and L. Danneels, "Altered trunk muscle coordination during rapid trunk flexion in people in remission of recurrent low back pain," *Journal of Electromyography and Kinesiology*, vol. 23, no. 1, pp. 173–181, 2013.
- [28] H. G. Wang, Z. F. Zhang, and Y. Zhou, "Irregular alteration of facet orientation in lumbar segments: possible role in pathology of lumbar disc herniation in adolescents," *World Neurosurgery*, vol. 86, pp. 321–327, 2016.
- [29] C. F. Du, N. Yang, J. C. Guo, Y. P. Huang, and C. Zhang, "Biomechanical response of lumbar facet joints under follower preload: a finite element study," *BMC Musculoskeletal Disorders*, vol. 17, no. 1, p. 13, 2016.
- [30] W. Dankaerts, P. O'Sullivan, A. Burnett, L. Straker, P. Davey, and R. Gupta, "Discriminating healthy controls and two clinical subgroups of nonspecific chronic low back pain patients using trunk muscle activation and lumbosacral kinematics of postures and movements: a statistical classification model," *Spine*, vol. 34, no. 15, pp. 1610–1618, 2009.
- [31] S. P. Gombatto, D. R. Collins, S. A. Sahrman, J. R. Engsborg, and L. R. Van Dillen, "Patterns of lumbar region movement during trunk lateral bending in 2 subgroups of people with low back pain," *Physical Therapy*, vol. 87, no. 4, pp. 441–454, 2007.
- [32] D. M. Ikeda and S. M. McGill, "Can altering motions, postures, and loads provide immediate low back pain relief: a study of 4 cases investigating spine load, posture, and stability," *Spine*, vol. 37, no. 23, pp. E1469–E1475, 2012.
- [33] M. de Zee, L. Hansen, C. Wong, J. Rasmussen, and E. B. Simonsen, "A generic detailed rigid-body lumbar spine model," *Journal of Biomechanics*, vol. 40, no. 6, pp. 1219–1227, 2007.
- [34] M. de Zee, P. Mikkelsen, C. Wong, E. B. Simonsen, and J. Rasmussen, "The influence of the center of rotation position on facet joint loading and end plate loading investigated with musculoskeletal simulation," in *Proceedings, XXIIInd Congress of the International Society of Biomechanics*, Cape Town, South Africa, 5–9 July 2009.
- [35] M. J. Pearcy and N. Bogduk, "Instantaneous axes of rotation of the lumbar intervertebral joints," *Spine*, vol. 13, no. 9, pp. 1033–1041, 1988.
- [36] M. Christophy, N. A. Senan, J. C. Lotz, and O. M. O'Reilly, "A musculoskeletal model for the lumbar spine," *Biomechanics and Modeling in Mechanobiology*, vol. 11, no. 1–2, pp. 19–34, 2012.
- [37] K.-S. Han, T. Zander, W. R. Taylor, and A. Rohlmann, "An enhanced and validated generic thoraco-lumbar spine model for prediction of muscle forces," *Medical Engineering & Physics*, vol. 34, no. 6, pp. 709–716, 2012.
- [38] Y. Masharawi, B. Rothschild, G. Dar et al., "Facet orientation in the thoracolumbar spine - three-dimensional anatomic and biomechanical analysis," *Spine*, vol. 29, no. 16, pp. 1755–1763, 2004.
- [39] H. Schmidt, F. Heuer, L. Claes, and H. J. Wilke, "The relation between the instantaneous center of rotation and facet joint forces - a finite element analysis," *Clinical Biomechanics*, vol. 23, no. 3, pp. 270–278, 2008.
- [40] P. J. Watson, C. K. Booker, C. J. Main, and A. C. Chen, "Surface electromyography in the identification of chronic low

- back pain patients: the development of the flexion relaxation ratio,” *Clinical Biomechanics (Bristol, Avon)*, vol. 12, no. 3, pp. 165–171, 1997.
- [41] K. P. Granata and K. F. Orishimo, “Response of trunk muscle coactivation to changes in spinal stability,” *Journal of Biomechanics*, vol. 34, no. 9, pp. 1117–1123, 2001.
- [42] J. H. van Dieen, L. P. Selen, and J. Cholewicki, “Trunk muscle activation in low-back pain patients, an analysis of the literature,” *Journal of Electromyography and Kinesiology*, vol. 13, no. 4, pp. 333–351, 2003.
- [43] T. Ritvanen, N. Zaproudina, M. Nissen, V. Leinonen, and O. Hänninen, “Dynamic surface electromyographic responses in chronic low back pain treated by traditional bone setting and conventional physical therapy,” *Journal of Manipulative and Physiological Therapeutics*, vol. 30, no. 1, pp. 31–37, 2007.
- [44] N. Inoue and A. A. E. Orias, “Biomechanics of intervertebral disk degeneration,” *Orthopedic Clinics of North America*, vol. 42, no. 4, pp. 487–499, 2011.
- [45] S. A. Ferguson, W. S. Marras, D. L. Burr, K. G. Davis, and P. Gupta, “Differences in motor recruitment and resulting kinematics between low back pain patients and asymptomatic participants during lifting exertions,” *Clinical Biomechanics*, vol. 19, no. 10, pp. 992–999, 2004.
- [46] M. Noguchi, C. E. Gooyers, T. Karakolis, K. Noguchi, and J. P. Callaghan, “Is intervertebral disc pressure linked to herniation?: an in-vitro study using a porcine model,” *Journal of Biomechanics*, vol. 49, no. 9, pp. 1824–1830, 2016.
- [47] A. Shiraziadl and G. Drouin, “Load-bearing role of facets in a lumbar segment under sagittal plane loadings,” *Journal of Biomechanics*, vol. 20, no. 6, pp. 601–613, 1987.

## Research Article

# A Numerical Investigation into the Effects of Overweight and Obesity on Total Knee Arthroplasty

Changjiang Wang,<sup>1,2</sup> Yuan Guo,<sup>1</sup> Junfen Shi,<sup>3</sup> and Weiyi Chen<sup>1</sup>

<sup>1</sup>*Institute of Applied Mechanics and Biomedical Engineering, Taiyuan University of Technology, Taiyuan, Shanxi 030024, China*

<sup>2</sup>*School of Engineering and Informatics, University of Sussex, Brighton BN1 9QJ, UK*

<sup>3</sup>*Bioengineering Science Research Group, University of Southampton, Southampton SO17 1BJ, UK*

Correspondence should be addressed to Yuan Guo; [guoyuantyut1980@163.com](mailto:guoyuantyut1980@163.com)

Received 23 February 2017; Accepted 12 April 2017; Published 29 May 2017

Academic Editor: Jie Yao

Copyright © 2017 Changjiang Wang et al. This is an open access article distributed under the Creative Commons Attribution License, which permits unrestricted use, distribution, and reproduction in any medium, provided the original work is properly cited.

Overweight and obesity increase risks of knee osteoarthritis, which is a major cause of disability. Severe knee osteoarthritis can be treated by knee arthroplasty. Total knee arthroplasty has been used in overweight and obese patients; however, clinical reports showed that the outcome of this group of patients was not good as normal-weight patients. Two computer models were created in this paper to simulate the effect of excess loads on the distal femoral bone and contact pressures in total knee arthroplasty during a gait cycle. The numerical results showed increased stress in periprosthetic distal femoral bones and higher contact pressure on tibial polyethylene insert during the stance phase. Based on the computer simulation results and published research work, cementless total knee arthroplasty with thicker tibial polyethylene insert may be a better option for overweight patients.

## 1. Introduction

Obesity has reached epidemic proportions globally, with more than 1.9 billion adults were overweight in 2014 according to World Health Organization and at least 600 million of them are clinically obese. Overweight is a body mass index (BMI) greater than or equal to  $25 \text{ kg/m}^2$ , obesity is a BMI greater than or equal to  $30 \text{ kg/m}^2$ , and morbid obesity is a BMI greater than or equal to  $40 \text{ kg/m}^2$ . Obesity significantly increases the risk of developing numerous medical conditions including osteoarthritis, which is the commonest cause of severe disability among older people in the UK and North America [1]. Longitudinal data have shown that obesity is a powerful risk factor for the development of knee osteoarthritis; for every 5 kg increase in weight, the risk increases by 30% [2]. Leung et al. [3] studied the association between body mass index and risk of total knee replacement; they concluded that BMI is one of the most important predictors of risk of knee osteoarthritis and the risk of total knee replacement.

Osteoarthritis of the knee can be treated either conservatively or surgically. Currently, the main surgical intervention is knee replacement, and whilst highly effective for most patients, all joint replacements will fail in time requiring revision [1]. Studies to date report conflicting results related to the impact of obesity on total knee arthroplasty (TKA) outcomes. A number of studies reported that obesity negatively impacts on outcomes following TKA, specifically significantly increasing the need for revision surgery [4], increasing cost of rehabilitation [5], and reducing the survivorship of the prosthesis [6] and focal osteolysis [7]. Conversely, other studies reported that outcomes between obese and nonobese patients following TKA are comparable, specifically in terms of rate of complications and knee function [8] and general and disease-specific measures of health and function [9]. Foran et al. [10] reported that the change of Knee Society Score (KSS) which assesses knee pain and function in obese patients after total knee replacement is about 20% less than that of nonobese patients. Deakin et al. [11] in 2017 reported that when compared to obese and nonobese patients,

morbidity obese patients undergoing TKA had a four points lower Oxford knee score.

A common public misconception is that osteoarthritis leads to obesity and that the surgical treatment (joint replacement) of this disabling joint disease leads to patient weight loss. Booth [12] reported that only 18% of obese patients lose weight after joint replacement. Recent study by Schwartzmann et al. [13] from postoperative analysis showed that patients undergoing TKA only reduce the BMI slightly,  $0.08 \text{ kg/m}^2$ . Therefore, it is important to study the effect of excess weight on the total knee replacement after the operation.

Gait analysis on obese individuals has identified kinematic adaptations including slower velocity, shorter step length, increased double support time, decreased knee range of motion, and larger ground reaction forces in the obese compared to lean individuals [14]. Spyropoulos et al. [15] compared the movement of the hip, knee, and ankle in obese and normal-weight men while the subjects walked over level ground at their preferred speed. Obese adults were found to adopt a slower walking velocity than nonobese subjects during testing. DeVita and Hortobagyi [16] tested the effects of obesity on lower extremity joint kinetics and energetics during walking by analysing the motion of obese healthy adults and lean adults. They found obese participants used altered gait biomechanics and had less knee torque and power at their self-selected walking speed and equal knee torque and power while walking at the same speed as lean individuals.

Physiological loads giving rise to implant-bone relative micromovements of the order of 100 or 200  $\mu\text{m}$  may inhibit bone in-growth, resulting in the formation of a fibrous tissue layer around the prosthesis and eventually promoting loosening of the implant [17]. Taylor and Tanner [18] proposed that migration of implant is due to the progressive failure of the supporting cancellous bone. The degree of implant migration is dependent on the initial mechanical environment and can be determined using patient-specific finite element analysis [19].

Au et al. [20] developed a three-dimensional finite element model to study bone and interface stresses for four different tibial prosthesis designs. All implant models demonstrated a reduction of cancellous bone stress plus high compression beneath the central fixation posts. Shi et al. [21] developed a finite element model and studied the contact pressure on two types of total knee replacement; they identified the effects of malalignment and different loadings on the outcome of total knee replacement.

Walker et al. [22] measured the quantitative changes in bone mineral density (BMD) in the distal femur after cemented total knee arthroplasty in osteoarthritis knee joints. An average decrease in bone density of 17.1% was measured adjacent to the prosthesis at the 12-month follow-up examination. Bone loss was most rapid during the first 3 months after TKA. Spittlehouse et al. [23] reported the greatest BMD decrease of 16% in the distal anterior femur over the first 6-month postoperative period in 16 patients with uncemented knee prostheses.

The exercise rehabilitation regimen adopted immediately after a TKA is a very important factor because of the known

relationship between osseointegration and implant micromotion. Booth [12] suggested that modified postoperative regimens were needed for obese patients, but there was a lack of research indicating the modification required in the exercise regimen. Bizzini et al. [24] reported, using a random sample, that supplementing an exercise rehabilitation regimen with an adapted agility and perturbation training programme can allow patients to regain better functions in the activities of daily living within the first 3 postoperative months. However, there is still a scarcity of research relating to obese and morbidly obese patients.

The most common reasons for TKR revisions are polyethylene wear and aseptic loosening. The generation of polyethylene wear particles and the resulting osteolysis is a cause of long-term loosening of TKR joint. Because of the change of stress status postoperatively, bone remodelling after TKA is also an important factor causing malalignment and loosening. Therefore, the effect of overweight and obesity on the TKA needs to be studied; in the paper, TKA components were modelled within a lower limb during a gait cycle, and the effect of excess weight on the stresses in the distal femoral periprosthetic bone were investigated. The changes of contact pressures on tibial polyethylene insert due to excess weight were also simulated.

## 2. Methods

*2.1. Computer Models.* Two computer dynamic models were created using MSC/ADAMS and used to study the effect of overweight on the distal femur and implants. Computer model one (CM1) shown in Figure 1 was used to investigate the influence of body weight on stress distribution in the distal femoral bone during a gait cycle. The geometrical models of the lower limb in this computer simulation model were obtained from the University of Brussels website [25]. The TKR implant used in the simulation is based on PFC Sigma system implant. The lower limb bone models in STL format were imported into MSC/ADAMS. The CM1 consists of anatomically correct bone models of the femur, tibia, fibula, and patella. The ligaments were added in anatomically correct location, and the knee prosthesis were inserted to ensure satisfactory alignment. Zero degree posterior slope of tibial tray was created to assemble the implant. The computer model two (CM2) shown in Figure 2 was used to study implant contact pressures related to wear testing and investigate the influence of overweight on the contact pressure in the tibial bearing component. The CM2 has six degrees of freedom, three translations, and three rotations of the knee joint. The femoral component was allowed to move vertically in the inferior-superior direction to rotate about a frontal axis to simulate valgus and varus rotation and to rotate about a transverse axis to simulate flexion and extension. The tibial components were allowed to translate in the anterior-posterior (AP) and medial-lateral (ML) directions and rotate about a fixed vertical axis located in the middle of the tibial condyles to simulate internal-external (IE) rotation. In CM2, the total AP translation restraint spring stiffness is 30 N/mm. The coefficient of friction between the femoral component and tibial bearing component is 0.04.

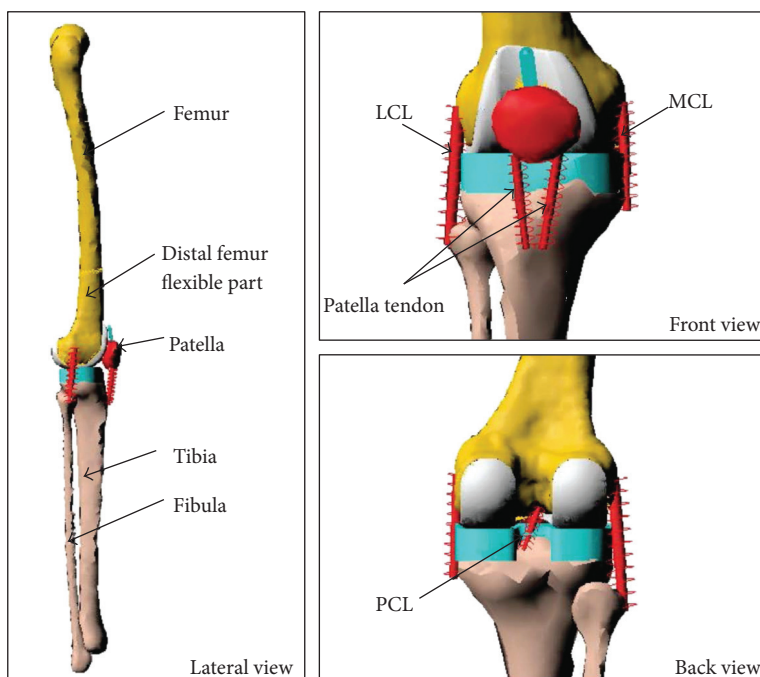


FIGURE 1: Finite element model of a total knee arthroplasty in a lower limb.

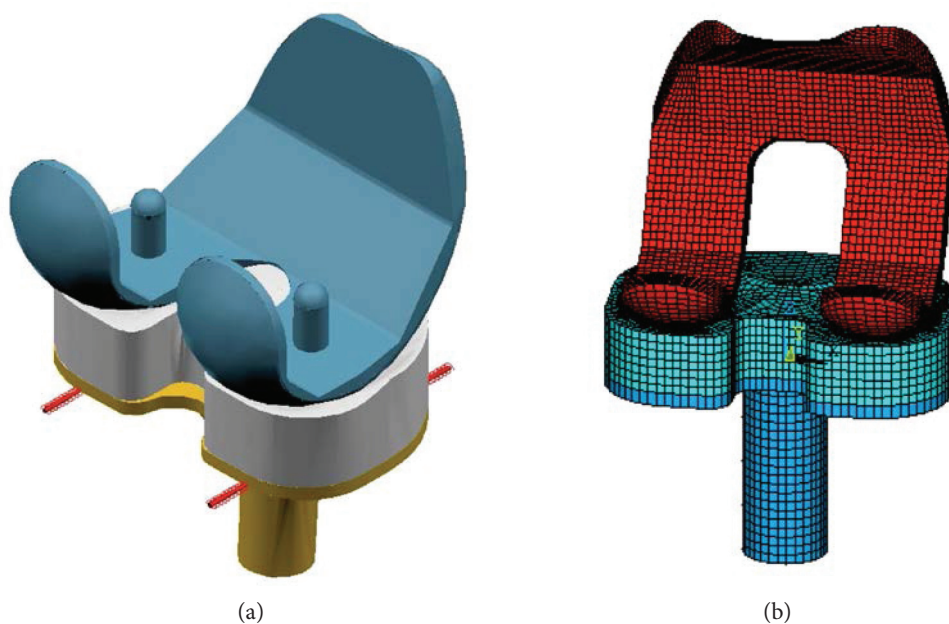


FIGURE 2: Finite element models of total knee arthroplasty components: (a) TKA computer model and (b) finite element mesh of the model.

**2.2. Loadings and Material Properties.** The first loading case is shown in Figure 3 and referred as normal weight loading; hip vertical and quadriceps load during a gait cycle were applied on CM1. The load data was adopted from published work [26–28]. A quadriceps force balances the vertical load through the patella ligament. The loading cases of 1.5 and 2 times normal weight were simulated by applying 1.5 and 2 times vertical load and quadriceps load, respectively. Stress distributions in the distal femur under different body weights can be obtained and compared. Boundary conditions on

CM1 were applied to reproduce the Purdue knee simulator environments [27]. The Purdue simulator applies a vertical load and a flexion angle at a simulated hip and controls the horizontal AP and ML ankle translation. Rotation of the ankle in all directions is allowed in the computer model. The inputs to this computer model include vertical axial load on hip, quadriceps force, tibio-femoral AP translation, and AP and ML ankle translation. Loads and material properties used in this computer model are the same as those used in the published paper [21].

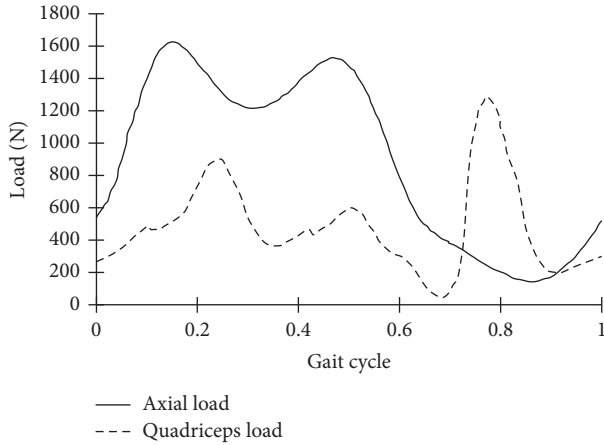


FIGURE 3: Hip axial (vertical) and quadriceps load during a gait cycle.

With CM2, a gait cycle was simulated; the time histories for the axial force, internal and external torque, AP force, and flexion and extension angles are adopted from ISO 14243-1 [29]. The ISO is about test loading and displacement parameters for wear-testing machines for wear of total knee-joint prostheses. The IE rotation restraint was 0.6 Nm per degree according to ISO 14243-1. A 1.5 times vertical load was applied on the CM2 to simulate overweight.

The nonlinear material property of polyethylene is used as the same as in the paper of Taylor and Barrett [30]. As reported in the papers [31, 32], that polyethylene insert thickness is a very important factor in the design of total knee replacement, the thickness affects the wear of polyethylene; therefore, three thickness of tibial polyethylene insert 6.8 mm, 9.6 mm, and 12.3 mm were also compared for normal and overweight gait loads in this paper. The material properties in the two models are listed in Table 1.

### 3. Results and Discussion

Compared with Halloran's research work [27], the maximum posterior translation of tibial components obtained in this paper was 5.89 mm that is higher than the 5 mm in Halloran's research. The maximum internal rotation of the tibial tray obtained in this paper was 3.9° that is lower than the 4.6° in Halloran's research. The difference may be due to different implant geometries that were used; however, the results are comparable.

**3.1. Influence of Body Weight on Stress Distribution in Distal Femur.** Using the computer model CM1 shown in Figure 1, which simulated the hip and quadriceps forces, the stress distributions in the distal femoral bone were simulated for normal weight and 1.5 and 2 times normal weight, respectively. To show the effect of overweight clearly on the stresses in the distal femur during a gait cycle, stresses in different zones were compared; these zones are labelled and shown in Figure 4.

The von Mises stress at different zones for normal weight and 1.5 and 2 times the normal weight is plotted and shown in Figure 5. The increase of stress levels in all zones in

TABLE 1: Material properties.

Material	Elastic modulus (MPa)	Poisson's ratio
Cortical bone	17,962	0.3
Metaphyseal cortical bone	7500	0.3
Cancellous bone 1	1091	0.3
Cancellous bone 2	400	0.3
Cancellous bone 3	100	0.3
Bone cement (PMMA)	2100	0.4
Cobalt-chrome alloy	193,000	0.29
Titanium alloy	110,000	0.33

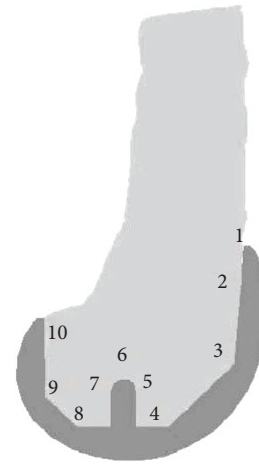
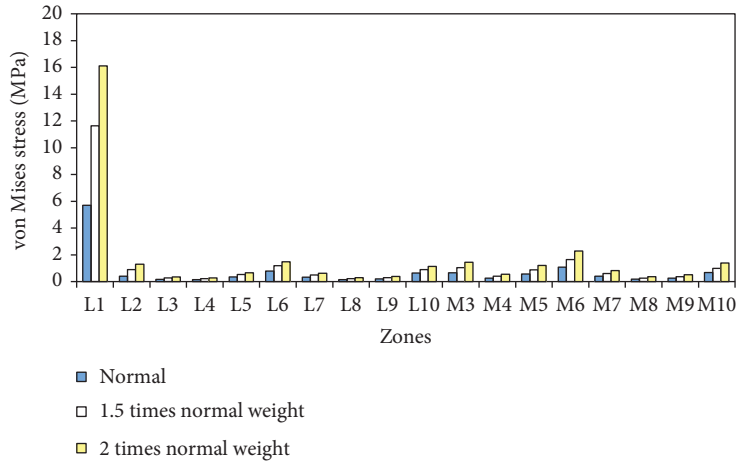


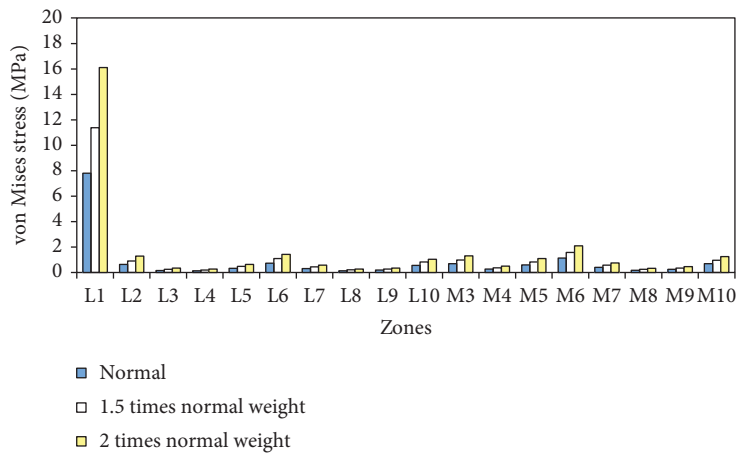
FIGURE 4: Distal femoral zones defined adjacent to the prosthesis.

conditions of overweight can be seen in Figure 5. Stresses at 15% and 50% of the gait cycle increased approximately in proportion to weight because the vertical force was the major force component during the stance phase period. However, the increase of stresses in the bone at 70% of the gait cycle was not proportional to the body weight. It can therefore be concluded that the increase of stress for overweight patients is directly related to the vertical load on the knee joint during walking. It was noticed that the stress values in zone 1 is much higher than other zones in Figure 5; this is because the zone 1 is cortical bone and other zones are cancellous bone. The increase rate of stresses in zone 1 at 15% of gait cycle is higher than the increase rate of load. In this computer simulation of TKA during a walking gait cycle, the increase of stress in conditions of overweight may result in the failure of bone-implant interface.

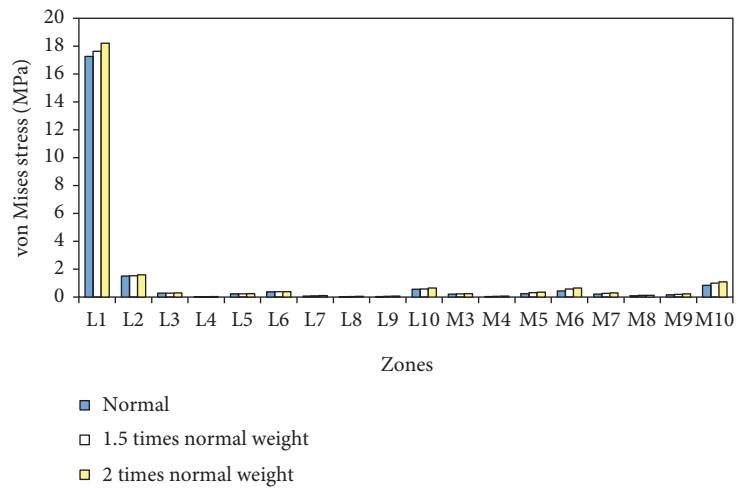
The increased weight leads to higher forces at the interface between bone and TKA components, which increases the chance of component aseptic loosening. Bagsby et al. [33] studied TKA in morbidly obese patients; after comparing the outcomes of cemented and cementless TKA, they concluded that cementless TKA may be a good option for morbidly obese patients, because a long-term biologic interface may better tolerate the excess loads generated at the



(a)



(b)



(c)

FIGURE 5: Comparison of stress distribution in distal femur after TKR with different body weight at (a) 15% of gait cycle, (b) 50% of gait cycle, and (c) 70% of gait cycle (L is for lateral condyle and M for medial condyle).

bone-metal interface. The analysis in this paper did show the increased stress values in bones next to the TKA components and agrees with the findings by Bagsby et al. [33].

3.2. *Effect of Body Weight on Tibio-Femoral Contact Pressure and Tibial Polyethylene Thickness in Mitigating the Effect.* The second computer model CM2 shown in Figure 3

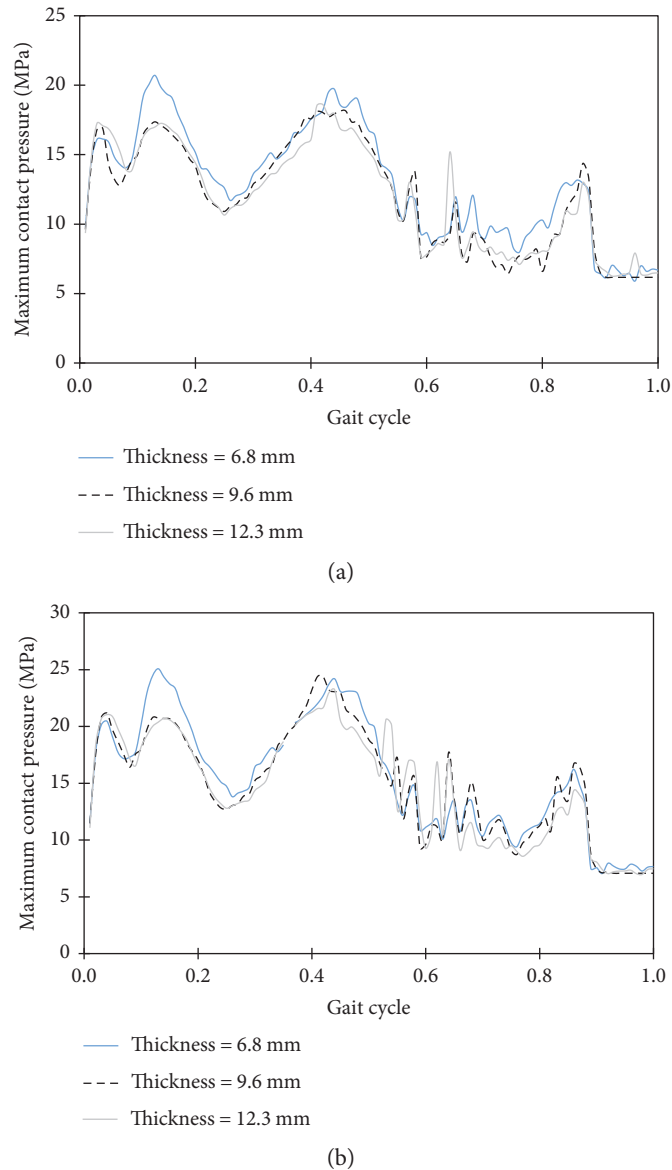


FIGURE 6: Comparison of maximum contact pressures on tibial polyethylene inserts under the load of (a) normal weight and (b) 1.5 times the normal weight.

simulates the TKR wear test environments as specified in the ISO standard. Therefore, this model is used to show the effect of overweight on the contact pressures in TKR. To investigate the influence of body weight on contact pressure in knee components, normal weight and overweight were simulated with the FE model CM2. An increased vertical load of 1.5 times the normal load was applied to simulate overweight. Taylor and Barrett [30] found that the thickness of tibial polyethylene insert affects the contact pressure on the polyethylene; the contact pressure decreased when the thickness of polyethylene increased. Therefore, three thickness of polyethylene were modelled to show how the thickness of the tibial insert could mitigate the effect of overweight. Figure 6 shows the maximum contact pressure in the TKR with different thickness of polyethylene inserts under normal weight and overweight loads; contact pressure is shown as the function of a gait cycle. On the tibial polyethylene inserts,

contact pressures in the 9.6 and 12.3 mm thickness design were lower than the 6.8 mm design under the normal weight and overweight loads. It can be seen that the maximum contact pressures are 25 MPa and 20.7 MPa on the 6.8 mm-thick tibial polyethylene insert, and these values were decreased to 20 MPa and 17 MPa on the 9.6 mm-thickness under 1.5 times and normal weight load, respectively. Therefore, the increased tibial polyethylene thickness could mitigate the adverse effect of increased weight in obese patients. The maximum contact pressure on the 12.3 mm thickness tibial polyethylene insert is nearly the same as in the 9.6 mm thickness; this means that an optimal thickness of tibial polyethylene insert could be determined for obese patients.

Liza et al. [34] studied the wear of a retrieval of a 10-year tibial polyethylene insert. As they mentioned, there were several damage modes to the polyethylene. Delamination

and pitting which are related to fatigue wear were the most common feature of damage on tibial polyethylene inserts; the increased contact pressure will cause more wear. From the simulated results in this paper, it can be seen that contact pressures on the polyethylene insert were increased due to excess weight; however, the increased thickness of polyethylene decreased the contact pressure. When a thicker tibial polyethylene insert is designed in TKR, thinner tibial metal tray could be used to minimise bone cutting in the tibia. Recent research work on the effect of tibial metal tray thickness on tibial bone remodelling by Martin et al. [35] showed that there was a significant increase in the medial tibial bone loss in the metal tibial tray of 4 mm-thick than in the 2.7 mm-thick tibial tray. Therefore, thick tibial polyethylene inserts and thin metal tibial tray could be used in TKR for overweight and obese patients. Gait analysis [14] on obese individuals showed that they have shorter step length and larger ground reaction forces compared to lean individuals. The shorter step length requires more steps for obese patients to cover the same travel distance than normal people. The increased number of cycles and higher contact pressure are not good for the wear of polyethylene; therefore, more research on the TKR for obese patients should be carried out. Although this research were able to show the effect of overweight on TKR, it has limitations because the gait cycle of obese individuals was assumed to be similar to the normal people but with increased hip and quadriceps forces. To improve the finite element modelling of obese patients with TKR, gait measurement of this group should be conducted and patient-specific model should be created in future analyses.

The rehabilitation exercise after TKR is important in patient recovery and gain knee function. The computer models created in this research can be used to facilitate the simulation of the impact of obesity during postoperative exercise rehabilitation regimens following TKA, specifically it will identify if any particular exercise exacerbates stress/loading around the TKA components.

#### 4. Conclusion

From the analysis of the total knee arthroplasty using the computer models, the stresses in the distal femoral bone were found to increase with body weight. Stresses at 15% and 50% of the gait cycle increased approximately in proportion to weight. The maximum stress in femoral bone was increased from 7.8 to 16 MPa when the body weight was doubled at 50% of the gait cycle. The higher stress indicates that the risk of femoral component migration will increase with the excess body weight. From the simulation of total knee components with increased load, the maximum contact pressures on the tibial polyethylene inserts were increased; this can lead to more wear in the tibial polyethylene inserts. Based on the simulation results in this paper and other researchers' findings, cementless total knee arthroplasty with thick tibial polyethylene insert and thin metal tibial tray may be a better option for overweight patients.

#### Conflicts of Interest

The authors declare that there are no competing interests regarding the publication of this paper.

#### Acknowledgments

The authors would like to thank the financial support by the National Natural Science Foundation of China (no. 11472185). The authors thanked all the participants in this study.

#### References

- [1] R. Jester, "Osteoarthritis and total joint replacements," in *Orthopaedic and Trauma Nursing (2nd edition)*, Kneale and Davis, Eds., Churchill Livingstone, Edinburgh, 2005.
- [2] A. Jones and M. Doherty, "Intraarticular corticosteroids are effective in osteoarthritis but there are no clinical predictors of response," *Annals of the Rheumatic Diseases*, vol. 55, no. 11, pp. 829–832, 1996.
- [3] Y.-Y. Leung, J. C. Allen, M. Noviani et al., "Association between body mass index and risk of total knee replacement, the Singapore Chinese health study," *Osteoarthritis and Cartilage*, vol. 23, no. 1, pp. 41–47, 2015.
- [4] J. R. H. Foran, M. A. Mont, A. D. Rajadhyaksha, L. C. Jones, G. Etienne, and D. S. Hungerford, "Total knee arthroplasty in obese patients: a comparison with a matched control group," *The Journal of Arthroplasty*, vol. 19, no. 7, pp. 817–824, 2004.
- [5] H. K. Vincent, K. R. Vincent, L. W. Lee, and A. P. Alfano, "Effect of obesity on inpatient rehabilitation outcomes following total knee arthroplasty," *Clinical Rehabilitation*, vol. 21, no. 2, pp. 182–190, 2007.
- [6] K. R. Berend, A. V. Lombardi, T. H. Mallory, J. B. Adams, and K. L. Groseth, "Early failure of minimally invasive unicompartamental knee arthroplasty is associated with obesity," *Clinical Orthopaedics and Related Research*, vol. 440, pp. 60–66, 2005.
- [7] D. D. Spicer, D. L. Pomeroy, W. E. Badenhause et al., "Body mass index as a predictor of outcome in total knee replacement," *International Orthopaedics*, vol. 25, no. 4, pp. 246–249, 2001.
- [8] A. K. Amin, J. T. Patton, R. E. Cook, and I. J. Brenkel, "Does obesity influence the clinical outcome at five years following total knee replacement for osteoarthritis," *The Journal of Bone and Joint Surgery*, vol. 88, no. 3, pp. 335–340, 2006.
- [9] R. G. Deshmukh, J. H. Hayes, and I. M. Pinder, "Does body weight influence outcome after total knee arthroplasty? A 1-year analysis," *The Journal of Arthroplasty*, vol. 17, no. 3, pp. 315–319, 2002.
- [10] J. R. H. Foran, M. A. Mont, G. Etienne, L. C. Jones, and D. S. Hungerford, "The outcome of total knee arthroplasty in obese patients," *The Journal of Bone and Joint Surgery*, vol. 86A, no. 8, pp. 1609–1615, 2004.
- [11] A. H. Deakin, A. Iyayi-Igbinovia, and G. J. Love, "A comparison of outcomes in morbidly obese, obese and non-obese patients undergoing primary total knee and total hip arthroplasty," *The Surgeon, Journal of the Royal Colleges of Surgeons of Edinburgh and Ireland*, pp. 1–6, 2016, Article in Press.

- [12] R. E. Booth, "Total knee arthroplasty in the obese patient: tips and quips," *The Journal of Arthroplasty*, vol. 17, no. 4, Supplement 1, pp. 69–70, 2002.
- [13] C. R. Schwartsmann, A. M. Borges, G. L. S. Freitas, E. Z. Migon, G. K. Oliveira, and M. W. Rodrigues, "Do patients lose weight after total knee replacement?" *Revista Brasileira de Ortopedia*, vol. 52, no. 2, pp. 159–163, 2017.
- [14] B. McGraw and B. A. McClenaghan, "Gait and postural stability in obese and nonobese prepubertal boys," *Archives of Orthopaedic and Trauma Surgery*, vol. 81, no. 4, pp. 484–489, 2000.
- [15] P. Spyropoulos, J. C. Pisciotto, K. N. Pavlou, M. A. Cairns, and S. R. Simon, "Biomechanical gait analysis in obese men," *Archives of Physical Medicine and Rehabilitation*, vol. 72, no. 13, pp. 1065–1070, 1991.
- [16] P. Devita and T. Hortobagyi, "Obesity is not associated with increased knee joint torque and power during level walking," *Journal of Biomechanics*, vol. 36, no. 9, pp. 1355–1362, 2003.
- [17] M. Viceconti, R. Muccini, M. Bernakiewicz, M. Baleani, and L. Cristofolini, "Large-sliding contact elements accurately predict levels of bone-implant micromotion relevant to osseointegration," *Journal of Biomechanics*, vol. 33, no. 12, pp. 1611–1618, 2000.
- [18] M. Taylor and K. E. Tanner, "Fatigue failure of cancellous bone: a possible cause of implant migration and loosening," *Journal of Bone and Joint Surgery (British)*, vol. 79, no. 2, pp. 181–182, 1997.
- [19] A. Perillo-Marcone, L. Ryd, K. Johnsson, and M. Taylor, "A combined RSA and FE study of the implanted proximal tibia: correlation of the post-operative mechanical environment with implant migration," *Journal of Biomechanics*, vol. 37, no. 8, pp. 1205–1213, 2004.
- [20] A. G. Au, A. B. Liggins, V. J. Raso, and A. Amirfazli, "A parametric analysis of fixation post shape in tibial knee prostheses," *Medical Engineering & Physics*, vol. 27, no. 2, pp. 123–134, 2005.
- [21] J. F. Shi, C. J. Wang, T. Laoui, W. Hart, and R. Hall, "A dynamic model of simulating stress distribution in the distal femur after total knee replacement," *Proceedings of the Institution of Mechanical Engineers-Part H: Journal of Engineering in Medicine*, vol. 221, no. 8, pp. 903–912, 2007.
- [22] P. S. Walker, G. W. Blunn, and J. Perry, "Methodology for long-term wear testing of total knee replacements," *Clinical Orthopaedics and Related Research*, vol. 372, pp. 290–301, 2000.
- [23] A. J. Spittlehouse, C. J. Getty, and R. Eastell, "Measurement of bone mineral density by dual-energy x-ray absorptiometry around an uncemented knee prosthesis," *The Journal of Arthroplasty*, vol. 14, no. 8, pp. 957–963, 1999.
- [24] M. Bizzini, I. Croci-Maspoli, S. Buechele, N. Maffioletti, and U. Munzinger, "Agility and perturbation training for patients after total knee arthroplasty. A case-control study, 15th international congress of the world confederation for physical therapy, Vancouver, Canada, 2-6 June 2007," *Physiotherapy*, vol. 93, no. S1, p. S61, 2007.
- [25] University of Brussels, *Virtual Animation of the Kinematics of the Human for Industrial, Educational and Research Purposes*, VAKHUM Public Dataset, [http://www.ulb.ac.be/project/vakhum/public\\_dataset/public-data.htm](http://www.ulb.ac.be/project/vakhum/public_dataset/public-data.htm).
- [26] G. Bergmann, G. Deuretzbacher, M. O. Heller et al., "Hip contact forces and gait patterns from routine activities," *Journal of Biomechanics*, vol. 34, no. 7, pp. 859–871, 2001.
- [27] J. P. Halloran, A. J. Petrella, and P. J. Rullkoetter, "Explicit finite element modeling of total knee replacement mechanics," *Journal of Biomechanics*, vol. 38, no. 2, pp. 323–331, 2005.
- [28] D. A. Winter, *Biomechanics and Motor Control of Human Movement*, John Wiley & Sons, New York, 1990.
- [29] ISO 14243-1, *Implants for Surgery—Wear of Total Knee-Joint Prostheses. Part 1: Loading and Displacement Parameters for Wear-Testing Machines with Load Control and Corresponding Environmental Conditions for Test*, International Organisation for Standardization, Switzerland, 2009.
- [30] M. Taylor and D. S. Barrett, "Explicit finite element simulation of eccentric loading in total knee replacement," *Clinical Orthopaedic Related Research*, vol. 414, pp. 162–171, 2003.
- [31] J. F. Shi, C. J. Wang, F. Berryman, and W. Hart, "The effect of polyethylene thickness in fixed- and mobile-bearing total knee replacement," *Proceedings of the Institution of Mechanical Engineers-Part H: Journal of Engineering in Medicine*, vol. 222, no. 5, pp. 657–667, 2007.
- [32] P. Massin, "How does total knee replacement technique influence polyethylene wear," *Orthopaedic & Traumatology: Surgery and Research*, vol. 103, no. 1S, p. S21, 2017.
- [33] D. T. Bagnall, K. Issa, L. S. Smith et al., "Cemented vs cementless total knee arthroplasty in morbidly obese patients," *The Journal of Arthroplasty*, vol. 31, no. 8, pp. 1727–1731, 2016.
- [34] S. Liza, A. S. M. A. Haseeb, A. A. Abbas, and H. H. Masjuki, "Failure analysis of retrieved UHMWPE tibial insert in total knee replacement," *Engineering Failure Analysis*, vol. 18, no. 6, pp. 1415–1423, 2011.
- [35] J. R. Martin, C. D. Watts, D. L. Levy, T. M. Miner, B. D. Springer, and R. H. Kim, "Tibial tray thickness significantly increases medial tibial bone resorption in cobalt-chromium total knee arthroplasty implants," *The Journal of Arthroplasty*, vol. 32, no. 1, pp. 79–82, 2017.

## Research Article

# Numerical Investigation on the Biomechanical Performance of Laparoscopic-Assisted Plate Used for Fixing Pelvic Anterior Ring Fracture

Yiqian He,<sup>1</sup> Yongtao Lu,<sup>1</sup> Baosheng Yin,<sup>2</sup> and Li Yu<sup>2</sup>

<sup>1</sup>State Key Lab of Structural Analysis for Industrial Equipment, Department of Engineering Mechanics, International Research Center for Computational Mechanics, Dalian University of Technology, Dalian 116024, China

<sup>2</sup>Department of Orthopaedics, First Affiliated Hospital of Dalian Medical University, Dalian, Liaoning 116044, China

Correspondence should be addressed to Li Yu; dl\_yuli@163.com

Received 12 January 2017; Revised 17 March 2017; Accepted 27 March 2017; Published 23 May 2017

Academic Editor: Liping Wang

Copyright © 2017 Yiqian He et al. This is an open access article distributed under the Creative Commons Attribution License, which permits unrestricted use, distribution, and reproduction in any medium, provided the original work is properly cited.

Because of the minimal soft tissue injury, the laparoscopic-assisted internal fixation is a promising technique in fixing the pelvic anterior ring fracture. The aim of this study was to investigate the biomechanical performance of the laparoscopic-assisted plate by the finite element method. Four kinds of implants were investigated, that is, the laparoscopic-assisted plate (LAP), the percutaneous anterior pelvic bridge (PAPB), the transramus intraosseous screw (TIS), and the open reduction (OR). The stability of the implants was investigated under three loading cases, showing that when the LAP was used, the stress at the fracture site was smaller than that at other parts, while for other implants, the high stress was always around the fracture site. In conclusion, the LAP demonstrated a good biomechanical performance in fixing the pelvic anterior ring fracture and is a promising technique in clinical applications.

## 1. Introduction

The pelvis is a bony structure complex, consisting of several segments that form a solid ring, which protects the organs (vascular structures, genital, urinary, and gastrointestinal) that it contains [1, 2]. The disruption of the pelvic ring often resulted from high-energy traumas, accounting for 3%-4% of all fractures, and has a high mortality of 19% [1, 2]. Pelvic anterior ring fixation methods, such as the formal open plating, external fixation, and transramus intraosseous screw fixation, are currently widely used in clinics [2]. Recently, a laparoscopic-assisted minimally invasive technique was developed for fixing pelvic ring fractures [3, 4]. This technique has many advantages, such as minimal soft tissue dissection, diminished blood loss, and reduced postoperative

pain. Clinically, the authors' group has successfully completed one case using the laparoscopic-assisted plate (LAP) in treating a 35-year-old patient who had anterior pelvic ring fractures on both sides. The X-ray image after the operation is shown in Figure 1.

When the pelvic ring was fixed, a stable effect was expected by the surgeons. Therefore, the biomechanical stability is a key parameter for evaluating the performance of the implant. Generally, experimental testing and finite element analysis (FEA) are two widely used approaches to investigate the stability of the implants, but there are very limited investigations on the implants used in fixing pelvic anterior ring fractures. On the experimental side, Acklin et al.'s study is the only work which performed a mechanical testing on the plates and screws used in anterior pelvic ring

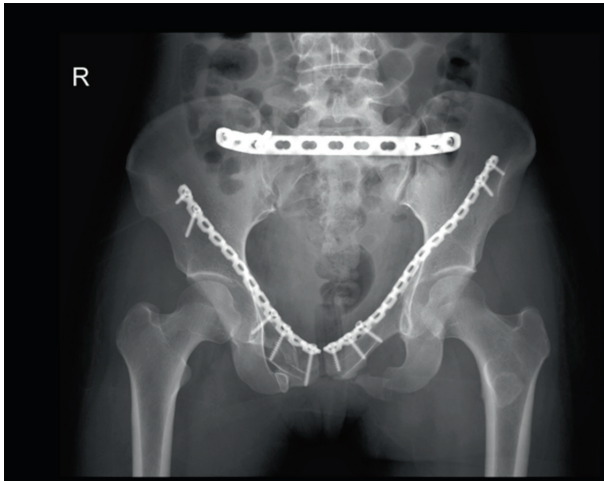


FIGURE 1: The X-ray image of the pelvis with the laparoscopic-assisted plate.

fractures, and it was found that the plates were superior to the screws [5]. On the FE side, although FEA is proved to be an effective tool for choosing the best surgical method [6, 7], there is no previous numerical work on the investigation of the biomechanical stability of the implants used in fixing the pelvic anterior ring fractures.

Giving the fact that the laparoscopic-assisted plate (LAP) is a new technique in fixing the pelvic anterior ring fracture and there is no investigation on the stability of the LAP, the aim of this study was to evaluate the biomechanical stability of the LAP and compare its stability with three other implant fixations, that is, the laparoscopic-assisted plate open reduction, percutaneous anterior pelvic bridge, and transramus intraosseous screw.

## 2. Material and Method

**2.1. Clinical CT Scan.** The CT scan of a 25-year-old healthy male was performed with a 64-Slice LightSpeed1 CT Scanner (Phillips, Netherlands). The CT data was obtained with an image interval of 1.0 mm and an image resolution of  $0.69 \times 0.69 \text{ mm}^2$ .

**2.2. Finite Element Model of the Pelvis.** The CT images were segmented through a semiautomatic process based on the pixel density using the image processing software Mimics (version 16, Software and Services for Biomedical Engineering, Materialise HQ, Belgium). The 3D geometry model was created and smoothed using the reverse engineering software Geomagic Studio (version 12, Raindrop Geomagic, NC, USA), and a bone fracture at the anterior ring of the pelvis was generated (Figure 2). The FE mesh was generated in the FE preprocessing software Hypermesh (version 13.0, Altair Engineering, Troy, MI, USA), and the FE mesh was imported to the FE analysis software Abaqus v.6.12 (version 6.12, Dassault Systemes Simulia Corp., Providence, RI, USA) for the calculations. The cortical bone of the pelvis was assumed to have a homogeneous thickness of

1.6 mm [8]. The FE model of the pelvis contains 349164 linear triangle elements (Type S3 in Abaqus). The ligaments in the pelvis were built by using spring elements in Abaqus (Figure 2). The connections between the synchondrosis pubis and bilateral pubis, as well as the sacrum-iliac (SI) joint facet, were fully constrained for simplification.

### 2.3. Finite Element Models of the Implants

**2.3.1. Laparoscopic-Assisted Plate (LAP).** As shown in Figure 2(a), a plate was fixed clinging to the medial ilium plate from iliac fossa to symphysis. Totally, five screws were fixed: two were placed at the locations with a distance of 10 mm to the fracture end, two were placed at the iliac crest with the distances of 25 mm and 15 mm to the fracture end, respectively, and the last screw was fixed at the pubic tubercle. The length, width, and height of the LAP were  $167 \text{ mm} \times 10 \text{ mm} \times 3 \text{ mm}$ , respectively.

**2.3.2. Percutaneous Anterior Pelvic Bridge (PAPB).** Four screws were used to fix the percutaneous steel plate between the anterior superior iliac spine and the pubic tubercle as shown in Figure 2(b). The length, width, and height of PAPB are  $160 \text{ mm} \times 10 \text{ mm} \times 3 \text{ mm}$ , respectively.

**2.3.3. Transramus Intraosseous Screw (TIS).** A transramus intraosseous screw was inserted into the pubic branch as shown in Figure 3. The length and diameter of the screw were 64 mm and 6.5 mm, respectively, and the diameter of the screw cap was 8 mm.

**2.3.4. Open Reduction (OR).** The fixation method was the same with the case for the laparoscopic-assisted minimally invasive plate as shown in Figure 2(a), but the inguinal ligament was cut off.

In building the finite element model for all the implants in this paper, quadratic tetrahedral elements are used with the element type C3D10 in Abaqus.

**2.4. Boundary Conditions.** In the generated FE models, the acetabulums were fully fixed and three loading cases were considered as described below (Figure 4):

- (1) Vertical force (VF): A vertical force of 500 N was applied on the surface of the sacrum (Figure 4) [8].
- (2) Open book-like force (OBLF): Two outward horizontal forces of 250 N were applied at both ends of the anterior superior iliac spine (Figure 4).
- (3) Close book-like force (CBLF): Two inward horizontal forces of 250 N were applied at both ends of the anterior superior iliac spine (Figure 4).

Because the interest of this study was on the deformation occurred at the fracture site, the values of displacements at the fracture site are calculated to characterize the stability of the pelvis with different implants. Eight points at the fracture end were selected, and the average resultant displacement of these points was calculated (Figure 5). First,

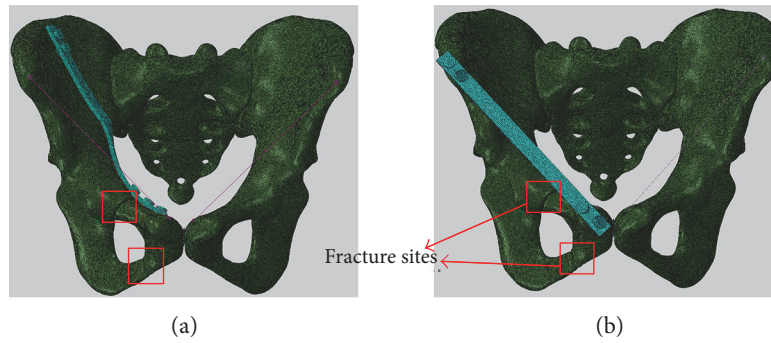


FIGURE 2: The finite element pelvic model with an anterior ring fracture fixed by a laparoscopic-assisted plate (LAP) (a) and a percutaneous anterior pelvic bridge (PAPB) (b).

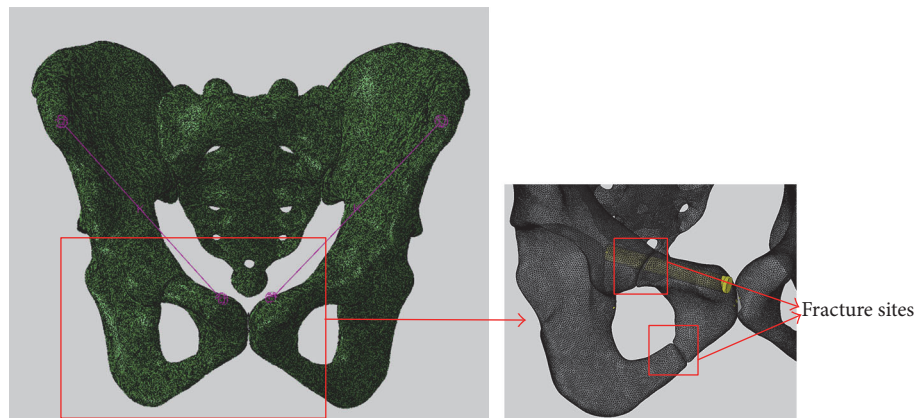


FIGURE 3: An FE model of the pelvis with a transramus intraosseous screw.

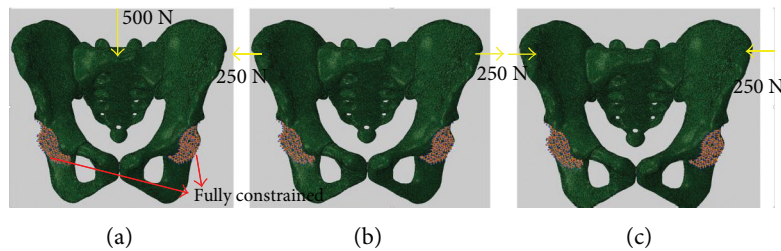


FIGURE 4: Boundary conditions applied on the pelvis, vertical force loading (a), open book-like force loading (b), and close book-like force loading (c).

the resultant displacement at each point was using the following formula:

$$u_T = \sqrt{u_x^2 + u_y^2 + u_z^2}, \quad (1)$$

where  $u_x$ ,  $u_y$ , and  $u_z$  are the displacements along the  $x$ -,  $y$ -, and  $z$ -axes, respectively.

Then, the average resultant displacement was calculated as the average of the eight resultant displacements.

**2.5. Material Parameters.** Young's modulus and Poisson's ratio of the cortical bones were set as  $E_c = 43530$  MPa and  $\nu_c = 0.2$  [8]. The stiffness of the inguinal ligament was  $k_l = 250$  N/mm [9]. Young's modulus and Poisson's ratio of

all implants are titanium alloy with  $E_I = 118.6$  GPa and  $\nu_c = 0.33$  [10].

### 3. Results

**3.1. The Average Displacement at the Fracture Site.** Under the three loading cases, the average displacement at the fracture site is the smallest when the LAP was implanted followed by the TIS and PAPB. Under the vertical force, the average displacements at the fracture site are shown in Table 1. The average displacements of the LAP, PAPB, TIS, and OR are 0.0089 mm, 0.023 mm, 0.019 mm, and 0.0094 mm, respectively. Under the open book-like force load, the average displacements with fixation methods of

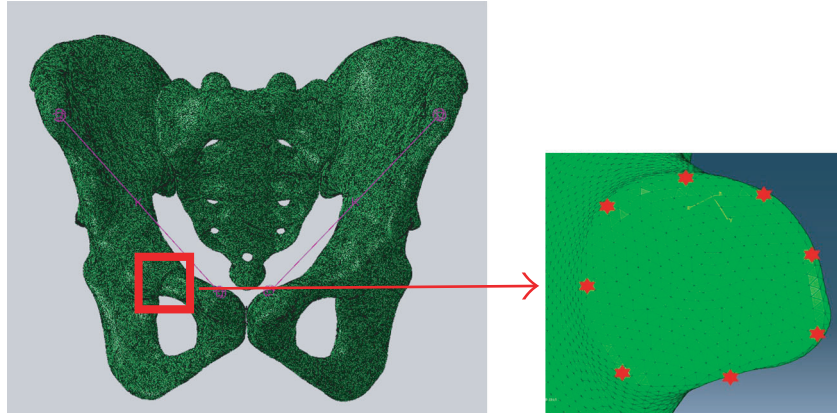


FIGURE 5: The points selected for investigation at the fracture surface.

TABLE 1: Node resultant displacements and the average value (mm) at the fracture site under different loading cases.

	N 1	N 2	N 3	N 4	N 5	N 6	N 7	N 8	Average
Under the loading of vertical force									
LAP	0.01	0.011	0.0092	0.0072	0.0086	0.007	0.0064	0.012	0.0089
PAPB	0.027	0.022	0.019	0.02	0.027	0.025	0.023	0.026	0.0230
TIS	0.025	0.0099	0.023	0.012	0.017	0.026	0.016	0.027	0.019
OR	0.011	0.012	0.0095	0.0074	0.009	0.0072	0.0066	0.013	0.0094
Under the loading of open book-like force									
LAP	0.031	0.036	0.033	0.029	0.026	0.025	0.026	0.036	0.030
PAPB	0.23	0.25	0.22	0.22	0.24	0.27	0.27	0.26	0.250
TIS	0.059	0.028	0.052	0.033	0.041	0.062	0.042	0.065	0.048
OR	0.031	0.037	0.033	0.027	0.024	0.023	0.023	0.037	0.029
Under the loading of close book-like force									
LAP	0.031	0.036	0.033	0.029	0.026	0.025	0.026	0.036	0.030
PAPB	0.23	0.25	0.22	0.22	0.24	0.27	0.27	0.26	0.250
TIS	0.058	0.028	0.052	0.033	0.041	0.062	0.042	0.065	0.048
OR	0.029	0.037	0.032	0.026	0.022	0.021	0.022	0.0365	0.028

the LAP, PAPB, TIS, and OR are 0.030 mm, 0.25 mm, 0.048 mm, and 0.029 mm, respectively (Table 1). Under the close book-like force loading, the average displacements are the same as the results with loading OBLF. The reason is that symmetric loading is applied, and only the scalar quantity of displacements is calculated without considering its direction.

**3.2. The Distribution of von Mises Stresses at the Fracture Sites.** In this part, only the LAP and the TIS are selected for comparing the stress distribution, as the PAPB produces worse stability as shown in the comparison of displacements at the fracture site, and the results of the displacement of the OR are similar with those of the LAP. The maximum stresses produced on the LAP are not always lower than those produced on the TIS. Under the vertical force, the maximum von Mises stresses are 34.885 MPa and 41.298 MPa for the LAP and TIS, respectively (Figure 6). Under the open book-like force load, the maximum von Mises stresses are

156.699 MPa and 98.834 MPa for the LAP and TIS, respectively (Figure 6). Under the close book-like force loading, the von Mises stresses in the implants are the same as the case with loading OBLF.

The LAP improved the stress distribution. At the fracture site, the stress produced on the LAP is much lower than that produced on the TIS. On the other hand, for the LAP, the high stress occurred in the center location of the plate and not at the fracture site, while for the TIS, the high stress always occurred at the fracture site. Therefore, the LAP is superior to the TIS for fixing the pelvic anterior ring fracture.

## 4. Discussion

The pelvic anterior ring fracture is a serious public problem that is always involving pubic symphysis, usually causing the failure of the pelvis and the fracture at the pelvic posterior ring. Surgical treatment with internal fixations is widely used in the treatment of the pelvic anterior ring fracture. The

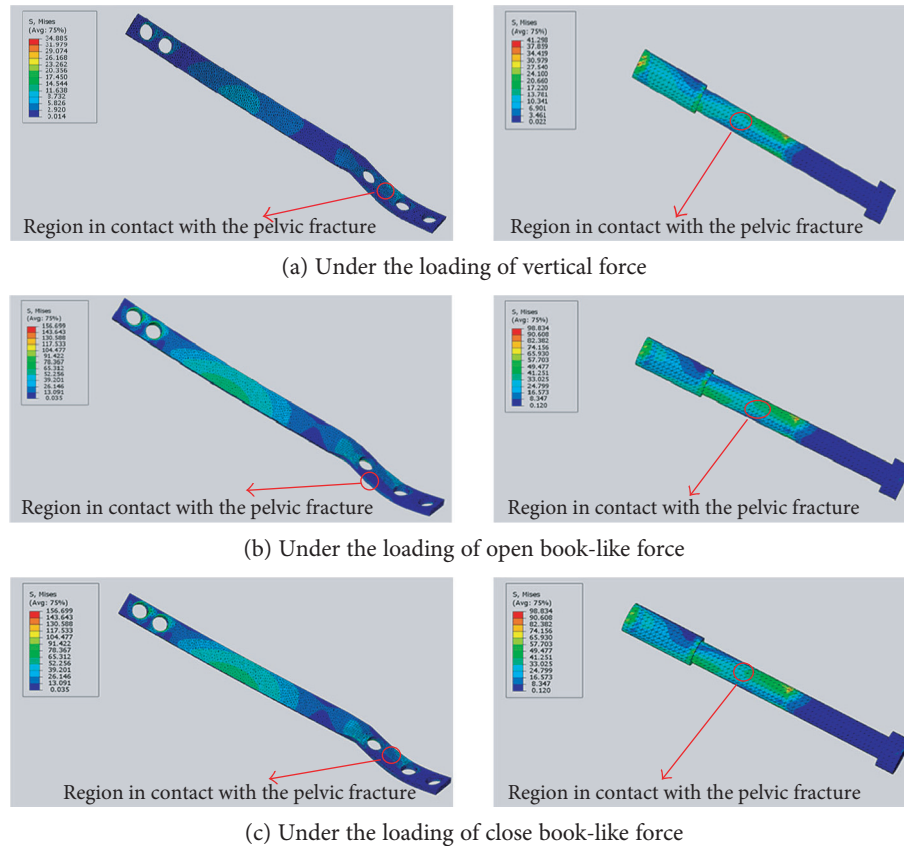


FIGURE 6: The distributions of von Mises stresses on the laparoscopic-assisted plate (left) and transramus intraosseous screw (right) under different loadings

traditional open reduction method usually uses ilioinguinal operative approach, which can sufficiently expose surgical field including the quadrilateral surface of the upper and lower surface of the pubic branch. Because the anatomic relationship is complicated in this region, the intraoperative injury involving important vessels and nerves could occur, including iliac external vascular injury, iliac external vascular thrombosis, femoral nerve injury, femoral lateral skin nerve injury, inguinal hernia, lymph leakage, and infection [11].

Hirvensalo et al. firstly introduced the “Stoppa” approach for complex hernia repair in the treatment of a pelvic fracture in 1993 [12]. By cutting rectus abdominis muscle at the vertical center of the inferior belly, the pelvic structure was sufficiently exposed so that the operative field was much clearer [13, 14]. Although the “Stoppa” approach is superior to the ilioinguinal approach, some complications could still happen, including peritoneal perforation, vascular nerve injury, deep vein thrombosis, pulmonary embolism, inguinal hernia, incision infection, and traumatic arthritis [15]. Hence, the application of this approach is very limited because of possible trauma and complications.

Cole et al. used the percutaneous anterior pelvic bridge to deal with the fracture of the pelvic anterior ring in 2012 [15, 16]. The operation made incision over the iliac crest and the pubic bone, inserting a plate from a subcutaneous channel upon the inguinal ligament, and then screws were fixed on the iliac crest and the tuberculum pubicum. The

characteristics of this technique were that the plate was located upon the subcutaneous inguinal ligament like a “bridge” over the anatomical structures including lateral femoral cutaneous nerve, ilioinguinal nerve, iliohypogastric nerve, and femoral artery, femoral vein, and femoral nerve. In this method, the fracture reduction was not necessary, so only a simple operation with a short time was required, and bleeding was less [16]. From the biomechanical stability point of view, the FEA results presented in this paper showed that this operation method performed worse than the implants with the TIS and LAP under the three kinds of external loadings. In addition, there are inevitable complications because of the involvement of skin impact, pain, and subcutaneous placement.

With the development of imaging technology, some minimally invasive internal fixation techniques have been proposed. Among these methods, the transramus intraosseous screw method has advantages of small surgical trauma, less bleeding, and good posture adaptability [11]. The results of FE analysis show that there is relatively significant stress concentration under vertical stress and open book stress, which could increase the risk of breaking the screw. Hence, this technique may be clinically suitable for the close book anterior ring pelvic fracture, while not suitable for pubic branch stenosis or deformity cases. Furthermore, this method is demanding for navigation system, and there are still some other risks including a screw into

the hip joint, screw deformation and breakage, nerve and blood vessel injury.

Zobrist et al. firstly reported two laparoscopic-assisted plate (LAP) cases in fixing the anterior pelvic ring fracture in 2002 [3]. Compared with other internal fixation methods, the LAP method has many advantages in fixing the pelvic anterior ring fracture. First, it builds pneumoperitoneum in the peritoneal clearance instead of cutting off the rectus abdominis, and thus the entire superior ramus of the pubis, pubic symphysis, and external iliac vessels can be clearly exposed. Second, under the view of endoscopy, part of the iliopectineal fascia is cut off to connect the iliac wing plate and the inner pelvic clearance, and a plate is inserted clinging to the surface of the bone, avoiding cutting off the rectus abdominis. Therefore, the LAP method can effectively prevent the cutaneous nerve injury and incisional hernia. The fracture reduction and internal fixation can be completed under a direct vision.

The FE results in this paper showed that the LAP has superior stability compared to the PAPB and TIS methods. Therefore, the LAP method is very promising in the treatment of the pelvic anterior ring fracture. However, it should be noted that the clinical experience of laparoscopic learning curve is long, and a good anatomical basis and open surgery experience are needed; the operation time in the initial stage is also long. Compared with the open reduction, the complications of the minimally invasive plate are significantly less, and the stability of the fixation is similar.

Due to the complexity of the human pelvis, some simplifications were made in the FE models and thus some limitations should be noted in this study. First, the cortical thickness was assumed to be constant with a value of 1.6 mm in the FE models. Considering that the aim of this study was to compare the biomechanical stability of different implants in the same pelvis, the implication made in the FE model was reasonable. Second, bilateral inguinal ligaments were simulated according to the simplification in this paper, and the connections between the synchondrosis pubis and bilateral pubis, as well as the sacrum-iliac (SI) joint facet were fully constrained in Abaqus. Considering that the forces were mainly transferred through the cortex and implant and the deformation was small (in linear elastic region), the simplification on the ligament modeling is reasonable. Last but not least, the positions of the fixed screws on the LAP or PAPB plate could make some influences on the results. The influence of screw positions will be investigated in the further work.

## 5. Conclusion

The biomechanical stabilities of four kinds of internal fixation methods for the anterior pelvic ring fracture were numerically investigated by the finite element method. The results showed that the laparoscopic-assisted plate (LAP) performed the best in the treatment of the pelvic anterior ring fracture, followed by the transramus intraosseous screw (TIS), while the percutaneous anterior pelvic bridge (PAPB) was the worst. Obviously, considering the good performance of the LAP method in biomechanical

stability and other advantages of this method in clinical operations, it can be expected that the LAP method will have a good application prospect for treating the pelvic anterior ring fracture.

## Conflicts of Interest

The authors have no conflicts to declare.

## Acknowledgments

This work was funded by the Liaoning Province Science & Technology Project (2013225002), National Natural Science Foundation of China (11572077), and the Chinese Fundamental Research Funds for the Central Universities (DUT15RC(3)130).

## References

- [1] P. Grubor, S. Milicevic, M. Biscevic, and R. Tanjga, "Selection of treatment method for pelvic ring fractures," *Medical Archives*, vol. 65, no. 5, pp. 278–282, 2011.
- [2] G. Falzarano, A. Medici, S. Carta et al., "The orthopedic damage control in pelvic ring fractures: when and why—a multicenter experience of 10 years' treatment," *Journal of Acute Disease*, vol. 3, no. 3, pp. 201–206, 2014.
- [3] R. Zobrist, P. Messmer, L. S. Levin, and P. Regazzoni, "Endoscopic-assisted, minimally invasive anterior pelvic ring stabilization: a new technique and case report," *Journal of Orthopaedic Trauma*, vol. 16, no. 7, pp. 515–519, 2002.
- [4] P. A. Cole, E. A. Dyskin, and J. A. Gilbertson, "Minimally-invasive fixation for anterior pelvic ring disruptions," *Injury: International Journal of the Care of the Injured*, vol. 46, Supplement 3, pp. S27–S34, 2015.
- [5] Y. P. Acklin, I. Zderic, J. Buschbaum et al., "Biomechanical comparison of plate and screw fixation in anterior pelvic ring fractures with low bone mineral density," *Injury: International Journal of the Care of the Injured*, vol. 47, no. 7, pp. 1456–1460, 2016.
- [6] M. Ni, D. W. C. Wong, J. Mei, W. X. Niu, and M. Zhang, "Biomechanical comparison of locking plate and crossing metallic and absorbable screws fixations for intra-articular calcaneal fractures," *Science China Life Sciences*, vol. 59, no. 9, pp. 958–964, 2016.
- [7] M. Ni, W. Niu, D. W. C. Wong, W. Zeng, and J. MeiM. Zhang, "Finite element analysis of locking plate and two types of intramedullary nails for treating mid-shaft clavicle fractures," *Injury*, vol. 47, no. 8, pp. 1618–1623, 2016.
- [8] J. Xiao, Q. S. Yin, M. C. Zhang et al., "Three-dimensional finite element analysis of pelvis under vertical loading," *Journal of Clinical Rehabilitative Tissue Engineering Research*, vol. 12, no. 39, pp. 7615–7619, 2008.
- [9] Y. C. Gao, Z. Guo, and J. Fu, "Three-dimensional finite element analysis of the pelvis in sitting stance," *Journal of Clinical Rehabilitative Tissue Engineering Research*, vol. 15, no. 22, pp. 3997–4001, 2011.
- [10] Z. Zhongjun, F. He, and H. Ma, "The test analysis of titanium Young's modulus and Poisson's ratio," *Engineering & Test*, vol. 47, no. 4, pp. 32–33, 2007.
- [11] J. Zhang, K. Wu, W. Zhang, W. Wu, and S. Hou, "Percutaneous fixation of pelvic fracture by acutrak full thread headless

- hollow compression screw,” *Chinese Journal of Reparative and Reconstructive Surgery*, vol. 26, no. 1, pp. 91–96, 2012.
- [12] E. Hirvensalo, J. Lindahl, and O. Böstman, “A new approach to the internal fixation of unstable pelvic fractures,” *Clinical Orthopaedics and Related Research*, vol. 297, no. 297, pp. 28–32, 1993.
- [13] Q. L. Zhu, Y. L. Lou, G. R. Xu, L. J. Rong, M. H. Yan, and G. Z. Yang, “Reduction and fixation of fracture of pubic rami by inserting construction plate through the punctiform-incision approach,” *China Journal of Orthopaedics and Traumatology*, vol. 21, no. 5, pp. 337–339, 2008.
- [14] P. A. Cole, E. M. Gauger, J. Anavian, T. V. Ly, R. A. Morgan, and A. A. Heddings, “Anterior pelvic external fixator versus subcutaneous internal fixator in the treatment of anterior ring pelvic fractures,” *Journal of Orthopaedic Trauma*, vol. 26, no. 5, pp. 269–277, 2012.
- [15] C. Moazzam, A. A. Heddings, P. Moodie, and P. A. Cole, “Anterior pelvic subcutaneous internal fixator application: an anatomic study,” *Journal of Orthopaedic Trauma*, vol. 26, no. 5, pp. 263–268, 2012.
- [16] T. G. Hiesterman, B. W. Hill, and P. A. Cole, “Surgical technique: a percutaneous method of subcutaneous fixation for the anterior pelvic ring: the pelvic bridge,” *Clinical Orthopaedics and Related Research*, vol. 470, no. 8, pp. 2116–2123, 2012.

## Research Article

# How Arch Support Insoles Help Persons with Flatfoot on Uphill and Downhill Walking

Yu-Ping Huang,<sup>1,2</sup> Kwantae Kim,<sup>1</sup> Chen-Yi Song,<sup>3</sup> Yat-Hon Chen,<sup>4</sup> and Hsien-Te Peng<sup>5</sup>

<sup>1</sup>Graduate Institute of Sport Coaching Science, Chinese Culture University, Taipei, Taiwan

<sup>2</sup>School of Sports Science, Nantong University, Jiangsu, China

<sup>3</sup>Department of Health Promotion and Gerontological Care, Taipei College of Maritime Technology, Taipei, Taiwan

<sup>4</sup>Global Action Inc., Taipei, Taiwan

<sup>5</sup>Department of Physical Education, Chinese Culture University, Taipei, Taiwan

Correspondence should be addressed to Hsien-Te Peng; [sid125peng@yahoo.com.tw](mailto:sid125peng@yahoo.com.tw)

Received 22 December 2016; Revised 4 March 2017; Accepted 15 March 2017; Published 9 April 2017

Academic Editor: Wenxin Niu

Copyright © 2017 Yu-Ping Huang et al. This is an open access article distributed under the Creative Commons Attribution License, which permits unrestricted use, distribution, and reproduction in any medium, provided the original work is properly cited.

The main purpose of this study was to investigate the effect of arch support insoles on uphill and downhill walking of persons with flatfoot. Sixteen healthy college students with flatfoot were recruited in this study. Their heart rate, peak oxygen uptake ( $\text{VO}_2$ ), and median frequency (MDF) of surface electromyogram were recorded and analyzed. Nonparametric Wilcoxon signed-rank test was used for statistical analysis. The main results were as follows: (a) peak  $\text{VO}_2$  significantly decreased with arch support insoles compared with flat insoles during uphill and downhill walking (arch support insole versus flat insole: uphill walking,  $20.7 \pm 3.6$  versus  $31.6 \pm 5.5$ ; downhill walking,  $10.9 \pm 2.3$  versus  $16.9 \pm 4.2$ ); (b) arch support insoles could reduce the fatigue of the rectus femoris muscle during downhill walking (MDF slope of arch support insole:  $0.03 \pm 1.17$ , flat insole:  $-6.56 \pm 23.07$ ); (c) insole hardness would increase not only the physical sensory input but also the fatigue of lower-limb muscles particularly for the rectus femoris muscle (MDF slope of arch support insole:  $-1.90 \pm 1.60$ , flat insole:  $-0.83 \pm 1.10$ ) in persons with flatfoot during uphill walking. The research results show that arch support insoles could effectively be applied to persons with flatfoot to aid them during uphill and downhill walking.

## 1. Introduction

Uphill and downhill walking exercise is considered a healthy recreational activity. Walking exercise is a popular activity worldwide. "Walking for Health" is the largest organization in England advocating for healthy walking. It consists of 70,000 walkers and encourages more than 63,000 people to engage in regular walking activity. This institution offers more than 3000 short-distance walks per week and provides a solution to the problem of sedentary behavior [1]. Hanson and Jones [2] showed that the benefits of walking exercise include reduction in systolic blood pressure, body mass index, and total cholesterol, among others. Previous studies have proved that walking exercise is beneficial for reducing blood pressure, reducing fasting glucose levels, and increasing  $\text{VO}_{2\text{max}}$  [3]. Moreover, Werner et al. [4] indicated that uphill walking with an inclination of 2%

to 8% (equal to  $1.2^\circ$ – $4.6^\circ$ ) and constant velocity of each gait on an inclined treadmill can improve the symmetry of the human body. Nowadays, to relieve pressure at the workplace among urban workers, more and more people engage in walking exercise; however, persons with foot issues such as flatfoot are limited in their enjoyment of walking.

Persons with flatfoot have a foot arch support disability in which the midfoot collapses in the medial longitudinal side [5]. The midfoot functions as a shock absorber in the plantar portion, while it allows the foot arch to maintain appropriate elasticity in order to reduce the impact of the ground reaction force (GRF). Constant impact on the plantar aspect by the GRF increases the occurrence of injuries such as heel pain, pelvic malalignment, and plantar fasciitis [6]. Previous studies have identified that functional disorders in the foot could cause lower back, hip, knee, and ankle joint injuries [7, 8]. Persons with flat feet might develop hallux valgus, plantar

fasciitis, metatarsal pain, knee and back pain, and other problems without proper treatment [9]. Therefore, persons with flatfoot may not be able to sustain their body weight during prolonged uphill and downhill walking.

In prolonged walking, the arch support is important for mitigating plantar pressure and maintaining dynamic stability [10–13]. Previous studies reported that elderly persons with foot pain or leg symptoms who wore arch support insoles at a minimum duration of 4 h/day for 8 weeks showed improvement in standing balance and prevention of falls [10]. Saadah et al. [13] reported the effect of medial arch support in 16 hospital security guards during standing and walking before and after work and suggested that use of insole support to reduce the foot pressure and muscle work can strengthen the medial arch. Jafarnezhadgero et al. [14] indicated that walking with arch support insoles could reduce the impact of the vertical GRF by 6.9% while increasing the propulsion force by 7% and that the reduction in load rate through the arch support insoles could reduce the risk of lower-extremity injuries and damage caused by the GRF during walking.

Providing a solution, such as the use of arch support insoles, to facilitate participation in prolonged walking exercises and prevent lower-limb injuries is important in persons with flatfoot. Specifically, wearing arch support insoles might return flat feet to the condition of a normal arch. In order to examine the fatigue for people with flatfoot, the current study referred to previous researches which considered the heart rate [15], oxygen consumption [15, 16], and electromyography (EMG) [15, 16] as physical working capacity (PWC) of the fatigue thresholds. The purpose of this study was to investigate the effect of arch support insoles on the heart rate (HR), peak oxygen uptake ( $\text{VO}_2$ ), and median frequency (MDF) of lower-limb muscles during uphill and downhill walking in persons with flatfoot. We hypothesized that the use of arch support insoles would lower the HR, peak  $\text{VO}_2$ , and MDF of lower-limb muscles.

## 2. Materials and Methods

**2.1. Participants.** The participants were 16 healthy college students (age:  $18.3 \pm 0.7$  years, height:  $167.5 \pm 6.4$  cm, weight:  $65.1 \pm 14.4$  kg, body mass index:  $23.2 \pm 4.7$ , widest foot width:  $8.5 \pm 0.7$  cm, and narrowest foot width:  $6.1 \pm 1.1$  cm) with flatfoot (defined as an arch index (AI) of  $72\% \pm 10\%$ ) [17, 18]. All participants provided written informed consent. This study was approved by the Institutional Review Board of Antai Medical Care Corporation, Antai Tian-Sheng Memorial Hospital (TSMH, approval number 16-107-B1). The inclusion criteria required the absence of lower-limb injuries and of previous surgery in the lower limbs within the span of a year.

**2.2. Experimental Protocol.** Each participant's footprint was recorded with a footprint device (Footdisc Inc., Taipei, Taiwan) during 1 day of the experiment. Then, AI was calculated by using the narrowest foot width divided by the widest foot width from the footprint [17].

Another day was scheduled for the performance of the formal experiment. The participants were instructed to perform 15 min uphill and 15 min downhill walking randomly in standardized footwear (Maximizer16; Mizuno Taiwan Corporation, Taipei, Taiwan) with either a pair of arch support foot insoles (Footdisc) or a pair of flat insoles (Maximizer16, Mizuno Taiwan Corporation). The uphill and downhill walking was a simulated walking on a  $\pm 9^\circ$  [19, 20] inclined treadmill (XG-1812X; New Noble Sport Equipment Co. Ltd., Ningbo, China) with a speed of 0.75 m/s (2.7 km/h) [19, 20]. The hardness of the forefoot, midfoot, and heel of the insoles was measured with a hardness tester (Teclock GS-709N Type A; Teclock Co., Tokyo, Japan).

An HR monitor (H7; Polar Electro Inc., Kempele, Finland) was used to record the HR, and a portable spirometer (Metamax 3B; Cortex, Leipzig, Germany) was used to measure the peak  $\text{VO}_2$ . Electromyogram (EMG) data were collected by using a Delsys system (Trigno wireless; Delsys Inc., Boston, MA, USA) with a 1000 Hz sampling rate.

The surface EMG (sEMG) sensors were adhered in parallel to the muscle belly of the subject's leg following the direction of muscle fibers. Before adhering the sensors on the muscles, the subjects stood tiptoe to mark the position of the gastrocnemius (GAS), did dorsiflexion to mark the position of the tibialis anterior (TA), did knee flexion to mark the position of the biceps femoris (BF), and did knee extension to mark the position of the rectus femoris (RF) with a black pen [21]. Then, the researchers shaved the participants' skin, removed hair impurities utilizing sandpaper, and cleaned with alcohol cotton sheet in order to gain better EMG signal. Additionally, we fixed the sensors on the leg using breathable tape to ensure the best conductivity and reduce the noise interference.

**2.3. Data Processing.** For dynamic contractions, MDF has been confirmed as a reliable indicator of muscle fatigue [22–24]. EMG spectrum will show lower signal expansion after muscle fatigue [23], and MDF will shift to the left of EMG spectral, that is, the MDF will decrease, which indicates the phenomenon of muscle fatigue [25, 26].

The raw data of EMG signals were converted into an MDF-time graph by using EMGWorks Analysis software (Delsys Inc., Boston, MA, USA) with a 0.125 s window length and 0.0124 s overlap. Then, the MDF-time graph was processed by using curve fit calculation (Figure 1). The slope of the curve was calculated to present the decrease/increase of MDF during uphill and downhill walking. The formula of the MDF slope was  $(Y_2 - Y_1)/(X_2 - X_1)$  (where  $Y_1$  = first MDF value of the curve,  $Y_2$  = smallest or last MDF value of the curve,  $X_1$  = time of  $Y_1$ , and  $X_2$  = time of  $Y_2$ ).

**2.4. Statistics.** SPSS 18.0 (SPSS Science Inc., Chicago, IL, USA) for Windows was used for statistical calculations. Nonparametric Wilcoxon signed-rank test was used to compare the differences between arch support insole and flat insole in terms of HR, peak  $\text{VO}_2$ , and slope of MDF

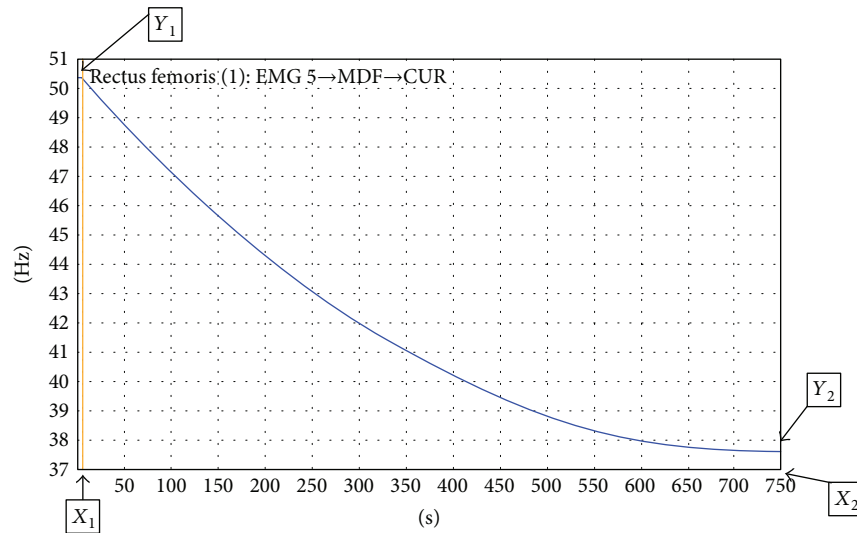


FIGURE 1: Graph after curve fitting.



(a)



(b)

FIGURE 2: Flat insoles (a) and arch support insoles (b).

during uphill and downhill walking. The level of significance was set at  $p < 0.05$ .

### 3. Results

**3.1. Hardness of Insoles.** The hardness of the forefoot, midsole, and heel areas was measured by using Teclock GS-709N Type A (Teclock Co.) for the two experimental conditions. The flat insole showed 35, 20, and 35 pointers, whereas the arch support insole showed 20, 60, and 20 pointers, respectively (Figure 2) (Table 1). In other words, the material of the arch support insole was harder than that of the flat insole in the midfoot region.

**3.2. Peak Oxygen Uptake.** Table 2 shows the outcomes of parameters during uphill and downhill walking. The peak  $VO_2$  showed significant differences between arch support insole and flat insole during both uphill and downhill walking (both  $p < 0.001$ ). The peak  $VO_2$  with arch support insole during both uphill and downhill walking was significantly smaller than that with flat insole based on positive ranks.

**3.3. Median Frequency.** The MDF slope of RF showed significant differences between arch support insole and flat

TABLE 1: Hardness of insoles.

Areas	Arch support insole (pointer)	Flat insole (pointer)
Forefoot	20	35
Midfoot	60	20
Heel	20	35

insole during uphill and downhill walking. During uphill walking, the MDF slope of RF with arch support insole ( $-1.90 \pm 1.60$  Hz/min) was significantly smaller than that with flat insole ( $-0.83 \pm 1.10$  Hz/min) (Table 2) based on positive ranks ( $p = 0.036$ ). During downhill walking, the MDF slope of RF with flat insole ( $-6.56 \pm 23.07$  Hz/min) was significantly smaller than that with arch support insole ( $0.03 \pm 1.17$  Hz/min) based on negative ranks ( $p = 0.023$ ). No difference was found in the HR and MDF slope of TA, BF, and GAS.

### 4. Discussion

The primary findings of the present study indicated that the peak  $VO_2$  significantly decreased during both uphill and

TABLE 2: Parameter outcomes during uphill and downhill walking.

	Uphill walking		Downhill walking	
	Arch support insole	Flat insole	Arch support insole	Flat insole
Heart rate (bpm)	141.4 ± 16.0	140.9 ± 14.4	103.6 ± 11.9	105.1 ± 12.6
Peak VO <sub>2</sub> * (mL min <sup>-1</sup> kg <sup>-1</sup> )	20.7 ± 3.6 <sup>a*</sup>	31.6 ± 5.5 <sup>a*</sup>	10.9 ± 2.3 <sup>a*</sup>	16.9 ± 4.2 <sup>a*</sup>
MDF slope of muscles				
Rectus femoris* (Hz/min)	-1.90 ± 1.60 <sup>a*</sup>	-0.83 ± 1.10 <sup>a*</sup>	0.03 ± 1.17 <sup>b*</sup>	-6.56 ± 23.07 <sup>b*</sup>
Tibialis anterior (Hz/min)	-1.12 ± 1.67	-1.12 ± 1.03	-1.43 ± 1.84	-1.79 ± 2.08
Biceps femoris (Hz/min)	-1.23 ± 1.73	-1.21 ± 0.99	-0.79 ± 1.57	-1.54 ± 0.93
Gastrocnemius (Hz/min)	-1.38 ± 1.63	-1.03 ± 1.25	-1.34 ± 2.25	-2.01 ± 1.72

\*Significant difference was found between arch support insole and flat insole,  $p < 0.05$ . <sup>a</sup>Based on positive ranks. <sup>b</sup>Based on negative ranks. *Note.* A negative value of the MDF slope means a decrease of MDF.

downhill walking and that the decrease of the MDF of RF was significantly small only during downhill walking with arch support insole.

Wearing arch support insole could be beneficial for persons with flatfoot because their peak VO<sub>2</sub>, which represents the highest value of oxygen uptake in the span of 15 min uphill and 15 min downhill walking, decreased. Hreljac [27] indicated that an increase in exercise intensity, such as from walking to running, would lead to energy expenditure by the plantarflexor and dorsiflexor muscles. Haykowsky et al. [28] indicated that a high intensity of exercise would result in a significant increase of peak VO<sub>2</sub> compared with moderate-intensity exercise. In other words, peak VO<sub>2</sub> could be considered the intensity index of body loading. In the aspect of physiology, arch support insoles could reduce the loading of the human body. Therefore, persons with flatfoot who wear arch support insoles may be able to easily engage in the recreational exercise of uphill and downhill walking. We suggest that the arch support insole might effectively reduce the exercise loading due to the impact of uphill and downhill walking.

During downhill walking, RF showed more fatigue with flat insole than that with arch support insole. In previous researches, an effective EMG characteristic analysis for detection of muscle fatigue was based on the MDF, which would be smaller as the muscle fatigue increases [29, 30]. The MDF shift resulted from the change of the conduction velocity [31] and the change in intramuscular pH [32]. In the current study, when participants wore the arch support insole, a significantly lower decrease of MDF was observed only in RF muscle during downhill walking. However, a contrary outcome was found during uphill walking. It could be conjectured to be because of the different contraction types of RF during uphill and downhill walking. The contraction of the RF in uphill walking was considered to be concentric, whereas that in downhill walking was considered eccentric. In general, eccentric contraction was induced by a higher ground impact force compared with that in concentric contraction. Previous researchers indicated that activation of fast-twitch muscle fibers may be associated with a higher risk of injuries in eccentric contraction [33]. The arch support insole for persons with flatfoot could reduce RF fatigue, especially during downhill walking.

During uphill walking, RF showed more fatigue with arch support insole than that with flat insole. This outcome was in contrast to our hypothesis that the arch support insole should cause less muscle fatigue compared with the flat insole during uphill walking because the center of pressure is evenly redistributed on both feet owing to the arch support. Iglesias et al. [34] stated that increasing the insole hardness would increase the physical sensory input. Perry et al. [35] measured different midsole hardness conditions during walking along an 8 m walkway. They found that the range of the center of mass of the whole body increased (soft: 0.14 m, hard: 0.16 m) when the midsole hardness increased. A harder material of insole provides more strength for supporting the leg, which leads to more GRF and increases the range of the center of mass during walking. Yick et al. [36] also indicated that harder insoles would increase muscle activities. In other words, wearing arch support insoles not only could increase the leg support against GRF but also would cause more fatigue of the extremity muscles during uphill walking.

There are two limitations of this study. First, the 15 min uphill and downhill walking exercises were finished within 1 day. Gollhofer et al. [37] indicated that the movement in the conversion between concentric and eccentric contractions during exercise could reduce muscle fatigue; however, the conversion could cause damage to the muscles. The issue may happen to decrease the muscle fatigue during the slope walking in the current study. Second, a flexible flatfoot has an arch support on nonweight bearing but lost the arch support on weight bearing. A rigid flatfoot has loss of the longitudinal arch height [38]. The semirigid flatfoot means not much arch with and without pressure. They all have a common phenomenon which is no arch support on weight bearing. Therefore, in the current study, we recorded the footprint when participants were standing (weight bearing). Uphill and downhill walking are associated with the weight bearing (body weight). Therefore, we did not focus on those impacts of differences in the flexible flatfoot, rigid flatfoot, and semirigid flatfoot.

## 5. Conclusion

Wearing arch support insoles can be beneficial for uphill and downhill walking exercises in persons with flatfoot because

the results of this study showed that oxygen uptake was effectively decreased during uphill and downhill walking, and there was less RF muscle fatigue during downhill walking.

## Conflicts of Interest

The authors declare that there is no conflict of interest regarding the publication of this paper.

## Authors' Contributions

The study was designed by Hsien-Te Peng and Yu-Ping Huang. Participant collection was supervised by Kwantae Kim and Yu-Ping Huang. Laboratory tests were performed by Kwantae Kim, Hsien-Te Peng, and Yu-Ping Huang. Data were collected and analyzed by Kwantae Kim and Hsien-Te Peng. Data interpretation and manuscript preparation were undertaken by Hsien-Te Peng, Yu-Ping Huang, Chen-Yi Song, and Yu-Ping Huang. All authors have read and approved the final version of the manuscript and agree with the order of presentation of the authors.

## References

- [1] J. South, "Health promotion by communities and in communities: current issues for research and practice," *Scandinavian Journal of Public Health*, vol. 42, Supplement 15, pp. 82–87, 2014.
- [2] S. Hanson and A. Jones, "Is there evidence that walking groups have health benefits? A systematic review and meta-analysis," *British Journal of Sports Medicine*, vol. 49, no. 11, pp. 710–715, 2015.
- [3] A. E. Tjønnå, I. M. Leinan, A. T. Bartnes et al., "Low- and high-volume of intensive endurance training significantly improves maximal oxygen uptake after 10-weeks of training in healthy men," *PloS One*, vol. 8, no. 5, pp. 1–7, 2013.
- [4] C. Werner, A. R. Lindquist, A. Bardeleben, and S. Hesse, "The influence of treadmill inclination on the gait of ambulatory hemiparetic subjects," *Neurorehabilitation and Neural Repair*, vol. 21, no. 1, pp. 76–80, 2007.
- [5] M. Kido, K. Ikoma, K. Imai et al., "Load response of the medial longitudinal arch in patients with flatfoot deformity: in vivo 3D study," *Clinical Biomechanics (Bristol, Avon)*, vol. 28, no. 5, pp. 568–573, 2013.
- [6] J. Y. Jung, J. H. Kim, J. K. Choi, Y. Won, and J. J. Kim, "Association analysis of flat foot and high-arch foot using data mining," in *Proceedings of the 12th International Conference on Applied Computer and Applied Computational Science*, Kuala Lumpur, Malaysia, 2013.
- [7] P. Harradine, L. Bevan, and N. Carter, "An overview of podiatric biomechanics theory and its relation to selected gait dysfunction," *Physiotherapy*, vol. 92, no. 2, pp. 122–127, 2006.
- [8] A. R. Bird and C. B. Payne, "Foot function and low back pain," *Foot (Edinburgh, Scotland)*, vol. 9, no. 4, pp. 175–180, 1999.
- [9] C. R. Lee, M. K. Kim, and M. S. Cho, "The relationship between balance and foot pressure in fatigue of the plantar intrinsic foot muscles of adults with flexible flatfoot," *Journal of Physical Therapy Science*, vol. 24, no. 8, pp. 699–701, 2012.
- [10] T. H. Chen, L. W. Chou, M. W. Tsai, M. J. Lo, and M. J. Kao, "Effectiveness of a heel cup with an arch support insole on the standing balance of the elderly," *Clinical Interventions in Aging*, vol. 9, pp. 351–356, 2014.
- [11] F. Madehkhaksar and A. Egges, "Effect of dual task type on gait and dynamic stability during stair negotiation at different inclinations," *Gait & Posture*, vol. 43, pp. 114–119, 2016.
- [12] X. Qu, "Impacts of different types of insoles on postural stability in older adults," *Applied Ergonomics*, vol. 46, Part A, pp. 38–43, 2015.
- [13] H. Saadah, D. Furqonita, and A. Tulaar, "The effect of medial arch support over the plantar pressure and triceps surae muscle strength after prolonged standing," *Medical Journal of Indonesia*, vol. 24, no. 3, pp. 146–149, 2015.
- [14] A. Jafarnezhadgero, N. Farahpour, and M. Damavandi, "The acute effects of the application of arch support insole on ground reaction forces during walking," *Journal of Research in Rehabilitation Sciences*, vol. 11, no. 3, pp. 145–159, 2005.
- [15] C. L. Camic, T. J. Housh, G. O. Johnson et al., "An EMG frequency-based test for estimating the neuromuscular fatigue threshold during cycle ergometry," *European Journal of Applied Physiology*, vol. 108, no. 2, pp. 337–345, 2010.
- [16] K. C. Cochrane, T. J. Housh, H. C. Bergstrom et al., "Perceptual and physiological fatigue thresholds during cycle ergometry," *Journal of Exercise Physiologyonline*, vol. 17, no. 5, pp. 95–107, 2014, ISSN 1097-9751.
- [17] F. Forriol and J. Pascual, "Footprint analysis between three and seventeen years of age," *Foot & Ankle International*, vol. 11, no. 2, pp. 101–104, 1990.
- [18] D. L. Riddiford-Harland, J. R. Steele, and L. H. Storlien, "Does obesity influence foot structure in prepubescent children?" *International Journal of Obesity*, vol. 24, no. 5, pp. 541–544, 2000.
- [19] J. R. Franz and R. Kram, "The effects of grade and speed on leg muscle activations during walking," *Gait & Posture*, vol. 35, no. 1, pp. 143–147, 2012.
- [20] D. J. Haight, Z. F. Lerner, W. J. Board, and R. C. Browning, "A comparison of slow, uphill and fast, level walking on lower extremity biomechanics and tibiofemoral joint loading in obese and nonobese adults," *Journal of Orthopaedic Research*, vol. 32, no. 2, pp. 324–330, 2014.
- [21] J. R. Cram, G. S. Kasman, and J. Holtz, *Introduction to Surface Electromyography*, Aspen Publishers, Gaithersburg, Maryland, 1998.
- [22] M. R. Al-Mulla, F. Sepulveda, and M. Colley, "A review of non-invasive techniques to detect and predict localised muscle fatigue," *Sensors*, vol. 11, no. 4, pp. 3545–3594, 2011.
- [23] D. R. Rogers and D. T. MacIsaac, "A comparison of EMG-based muscle fatigue assessments during dynamic contractions," *Journal of Electromyography and Kinesiology*, vol. 23, no. 5, pp. 1004–1011, 2013.
- [24] M. Cifrek, S. Tonković, and V. Medved, "Measurement and analysis of surface myoelectric signals during fatigued cyclic dynamic contractions," *Measurement*, vol. 27, no. 2, pp. 85–92, 2000.
- [25] D. Farina, M. Fosci, and R. Merletti, "Motor unit recruitment strategies investigated by surface EMG variables," *Journal of Applied Physiology*, vol. 92, no. 1, pp. 235–247, 2002.
- [26] M. Cifrek, V. Medved, S. Tonković, and S. Ostojić, "Surface EMG based muscle fatigue evaluation in biomechanics," *Clinical Biomechanics*, vol. 24, no. 4, pp. 327–340, 2009.

- [27] A. Hreljac, "Preferred and energetically optimal gait transition speeds in human locomotion," *Medicine and Science in Sports and Exercise*, vol. 25, no. 10, pp. 1158–1162, 1993.
- [28] M. J. Haykowsky, M. P. Timmons, C. Kruger, M. McNeely, D. A. Taylor, and A. M. Clark, "Meta-analysis of aerobic interval training on exercise capacity and systolic function in patients with heart failure and reduced ejection fractions," *The American Journal of Cardiology*, vol. 111, no. 10, pp. 1466–1469, 2013.
- [29] S. Thongpanja, A. Phinyomark, P. Phukpattaranont, and C. Limsakul, "Mean and median frequency of EMG signal to determine muscle force based on time-dependent power spectrum," *Elektron Elektrotech*, vol. 19, no. 3, pp. 51–56, 2013.
- [30] G. T. Allison and T. Fujiwara, "The relationship between EMG median frequency and low frequency band amplitude changes at different levels of muscle capacity," *Clinical Biomechanics*, vol. 17, no. 6, pp. 464–469, 2002.
- [31] M. Solomonow, C. Baten, J. O. S. Smit et al., "Electromyogram power spectra frequencies associated with motor unit recruitment strategies," *Journal of Applied Physiology*, vol. 68, no. 3, pp. 1177–1185, 1990.
- [32] B. Gerdle, S. Karlsson, A. G. Crenshaw, J. Elert, and J. Fridén, "The influences of muscle fibre proportions and areas upon EMG during maximal dynamic knee extensions," *European Journal of Applied Physiology*, vol. 81, no. 1, pp. 2–10, 2000.
- [33] M. P. Mchugh, T. F. Tyler, S. C. Greenberg, and G. W. Gleim, "Differences in activation patterns between eccentric and concentric quadriceps contractions," *Journal of Sports Sciences*, vol. 20, no. 2, pp. 83–91, 2002.
- [34] M. E. Losa Iglesias, R. Becerro de Bengoa Vallejo, and D. Palacios Peña, "Impact of soft and hard insole density on postural stability in older adults," *Geriatric Nursing*, vol. 33, no. 4, pp. 264–271, 2012.
- [35] S. D. Perry, A. Radtke, and C. R. Goodwin, "Influence of footwear midsole material hardness on dynamic balance control during unexpected gait termination," *Gait & Posture*, vol. 25, no. 1, pp. 94–98, 2007.
- [36] K. L. Yick, L. T. Tse, W. T. Lo, S. P. Ng, and J. Yip, "Effects of indoor slippers on plantar pressure and lower limb EMG activity in older women," *Applied Ergonomics*, vol. 56, pp. 153–159, 2016.
- [37] A. Gollhofer, P. V. Komi, M. Miyashita, and O. Aura, "Fatigue during stretch-shortening cycle exercises: changes in mechanical performance of human skeletal muscle," *International Journal of Sports Medicine*, vol. 8, no. 2, pp. 71–78, 1987.
- [38] C. Napolitano, S. Walsh, L. Mahoney, and J. McCrea, "Risk factors that may adversely modify the natural history of the pediatric pronated foot," *Clinics in Podiatric Medicine and Surgery*, vol. 17, no. 3, pp. 397–417, 2000.

## Research Article

# Effect of Graded Facetectomy on Lumbar Biomechanics

Zhi-li Zeng,<sup>1</sup> Rui Zhu,<sup>1,2</sup> Yang-chun Wu,<sup>1</sup> Wei Zuo,<sup>1</sup> Yan Yu,<sup>1</sup>  
Jian-jie Wang,<sup>1</sup> and Li-ming Cheng<sup>1</sup>

<sup>1</sup>Spine Division of Orthopaedic Department, Tongji Hospital, Tongji University School of Medicine, 389 Xincun Road, Shanghai 200065, China

<sup>2</sup>Department of Histology and Embryology, Tongji University School of Medicine, 1239 Siping Road, Shanghai 200092, China

Correspondence should be addressed to Rui Zhu; zhurui08@hotmail.com

Received 21 November 2016; Revised 8 January 2017; Accepted 23 January 2017; Published 19 February 2017

Academic Editor: Jie Yao

Copyright © 2017 Zhi-li Zeng et al. This is an open access article distributed under the Creative Commons Attribution License, which permits unrestricted use, distribution, and reproduction in any medium, provided the original work is properly cited.

Facetectomy is an important intervention for spinal stenosis but may lead to spinal instability. Biomechanical knowledge for facetectomy can be beneficial when deciding whether fusion is necessary. Therefore, the aim of this study was to investigate the biomechanical effect of different grades of facetectomy. A three-dimensional nonlinear finite element model of L3–L5 was constructed. The mobility of the model and the intradiscal pressure (IDP) of L4–L5 for standing were inside the data from the literature. The effect of graded facetectomy on intervertebral rotation, IDP, facet joint forces, and maximum von Mises equivalent stresses in the annuli was analyzed under flexion, extension, left/right lateral bending, and left/right axial rotation. Compared with the intact model, under extension, unilateral facetectomy increased the range of intervertebral rotation (IVR) by 11.7% and IDP by 10.7%, while the bilateral facetectomy increased IVR by 40.7% and IDP by 23.6%. Under axial rotation, the unilateral facetectomy and the bilateral facetectomy increased the IVR by 101.3% and 354.3%, respectively, when turned to the right and by 1.1% and 265.3%, respectively, when turned to the left. The results conclude that, after unilateral and bilateral facetectomy, care must be taken when placing the spine into extension and axial rotation posture from the biomechanical point of view.

## 1. Introduction

Lumbar stenosis is one of the leading sources of lower back pain worldwide. It is defined as a narrowing of the lumbar spinal canal [1] due to degeneration of the spinal canal and neural foramen. An estimated 73 million people will be over the age of 65 of which 30% are projected to have symptomatic lumbar spinal stenosis in the US by the year 2030 [1]. Surgery is typically required for patients with lumbar stenosis over the age of 65 years [2]. Although nonoperative treatments with accompanying lifestyle modifications and disc microsurgery are becoming more and more popular, the gold standard treatment for lumbar stenosis is still open surgery [2]. The most common surgery for decompression is facetectomy and laminectomy, with the choice of unilateral or bilateral intervention depending on the degree of stenosis. An unfortunate but unavoidable downside to removing anatomical structures of the spine is an altered load-bearing and

motion environment. Greater spinal instability and larger deformation may occur. Knowing the level of instability under physiological loading can help the surgeon to decide whether additional spinal fusion is necessary.

Several groups have reported on the biomechanical behavior of the spine after resecting dorsal lumbar regions using in vitro experimental studies. In 1990, Abumi et al. [3] showed that removing supraspinous/interspinous ligaments did not affect the range of motion but that total facetectomy made the spine unstable. Okawa et al. [4] applied cyclic compressive and bending loads to a cadaveric spinal unit simulating partial facetectomy with intact spinous processes and ligaments. The results showed that facetectomy did not have a significant effect on flexion, but there was a significant effect on compression and extension. Similarly, Zhou et al. [5] performed in vitro unilateral graded facetectomy on 5 cadavers and failed to find any significant negative effects to the range of flexion and extension. However, if the range of graded

facetectomy exceeded 50%, spinal stability under lateral bending and axial rotation was greatly impacted. Saying that, the use of cadaveric experiments presents several limitations. The number of the cadaveric specimens is limited and the individual differences in anatomy are not reproducible across multiple experiments. Also, most specimens are from elderly individuals with variations in bone quality [6].

Finite element (FE) analysis is an important method for biomechanical investigations. Material properties can be varied and geometries can be generated and manipulated as desired according to different aims of studies. A number of FE studies around facetectomy have been reported in the literature. In 2003, Zander et al. [7] used a validated FE model to study both facetectomy and laminectomy, recording parameters such as motion, intradiscal pressures (IDP), stress, and facet joint forces. However, only standing and forward bending were investigated. Lee and Teo [8] investigated different spinal motions after laminectomy using a L2-L3 lumbar FE model. The results showed that total laminectomy increased motion and annulus stress, except when under lateral bending. Chen et al. [9] found that posterolateral fusion with hemilaminectomy may relax the stress concentrations on the intervertebral disc above the fusion mass when placed in flexion. Kiapour et al. [10] evaluated the biomechanical mechanism of Dynesys dynamic stabilization which was a semirigid pedicle screw fixation system for graded facetectomy. More recently, Erbulut [11] created an asymmetric FE model of the lumbar spine and subjected it to graded facet injuries in order to study the effect on the range of motion. Total left unilateral medial facetectomy, total bilateral facetectomy, 50% unilateral medial facetectomy, and 75% unilateral medial facetectomy were modeled. However, only the medial section of the segment was involved and only motion parameters were calculated. Involving more parameters, such as pressure and stress, under a range of spinal postures would help to create a more comprehensive biomechanical understanding of the environment in the spine after graded facetectomy.

Therefore, the aim of this study is to construct an FE model of a spinal segment and investigate the biomechanical effect of graded facetectomy on intervertebral rotation (IVR), intradiscal pressure, facet joint forces, and maximum von Mises equivalent stresses for flexion, extension, left/right lateral bending, and left/right axial rotation.

## 2. Materials and Methods

**2.1. Finite Element Model of L3–L5.** A nonlinear finite element model of L3–L5 was constructed from CT image data obtained from a 25-year-old Chinese male without any history of spinal disease. The CT images saved as Digital Imaging and Communications in Medicine format were imported into Simpleware Software (Simpleware Ltd.). After segmentation, feature extraction, smoothing, and mesh processes, the elements and nodes were imported to an FE software for remesh. The vertebrae were meshed using tetrahedral elements, and the intervertebral discs were meshed using hexahedral elements in the ABAQUS software. The FE model consisted of 32,850 nodes and 96,970

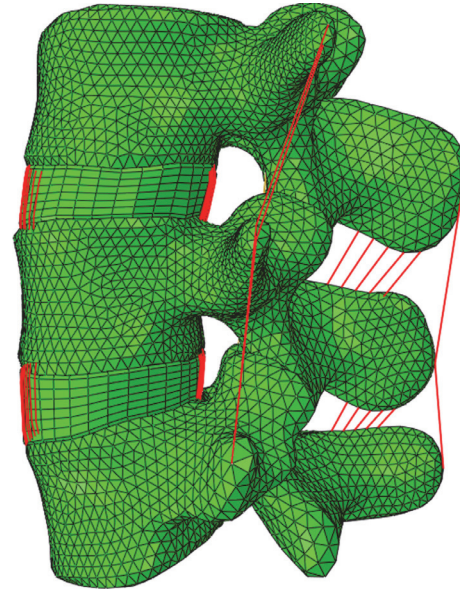


FIGURE 1: Finite element model of L3–L5.

elements. Each vertebra consisted of a cortical shell, a cancellous core, and a posterior bony structure. The 0.5 mm thick cortical shell [12] and the posterior bony structure were modeled as isotropic elastic materials, while the cancellous core was modeled as transverse isotropic. The cartilaginous endplates were 0.8 mm thick [13]. Each intervertebral disc was composed of an incompressible nucleus pulposus and surrounding annulus fibrosus. Rebar elements of two times seven layers were used to represent the fiber and the fiber stiffness decreased from the outside towards the centre [14]. The vertebrae and intervertebral discs were tied together. There was a gap of 0.5 mm [15] between the curved facet joints, and a thin cartilaginous layer of 0.25 mm was created for each facet articular surface. All seven ligaments of the lumbar spine were integrated according to their anatomical positions and were represented by tension-only spring elements with nonlinear material properties [16]. The FE model of L3–L5 is shown in Figure 1, and the material properties are shown in Table 1.

**2.2. Validation.** To validate the model, a moment of 7.5 Nm was applied to the top surface of L3 in the direction of flexion, extension, right lateral bending, and right axial rotation. The inferior endplate of L5 was rigidly fixed. The IVR of L4–L5, the region of concern in this study, was calculated and compared with in vitro data [17]. In addition, the IVR of L3–L5 was compared with in vitro data from whole lumbar specimens [18]. As a whole lumbar spine has five vertebrae and four spinal motion units, a direct comparison is unsuitable. Therefore, a ratio for IVR between L3–L5 and L1–L5 was adopted according to data from Percy et al. [19, 20]. This ratio was calculated for flexion-extension, lateral bending, and axial rotation, and the IVR of L3–L5 was justified according to this ratio. A subsequent 500 N axial compressive follower load was also applied and the IDP was estimated and compared with in vivo data [28].

TABLE 1: Material properties used for the different tissues in the finite element model.

Component	Elastic modulus (MPa)	Poisson ratio	References
Cortical bone	10,000	0.30	[16]
Cancellous bone (transverse isotropic)	200/140 (axial/radial)	0.45/0.315	[21]
Posterior bony structures	3,500	0.25	[14]
Ligaments	Nonlinear		[16]
Cartilage of endplate	Hyperelastic, neo-Hookean, $C_{10} = 0.3448$ , $D_1 = 0.3$		
Nucleus pulposus	Incompressible		[16]
Ground substance of annulus fibrosis	Hyperelastic, neo-Hookean, $C_{10} = 0.3448$ , $D_1 = 0.3$		[22]
Fibers of annulus fibrosis	Stiffness decreased from the outer to the centre		[14]
Facet joint	Soft contact		[15]

TABLE 2: Loads used to simulate flexion, extension, lateral bending, and axial rotation.

	Flexion	Extension	Lateral bending	Axial rotation
Rohlmann et al. [23, 24]	1175 N + 7.5 Nm	500 N + 7.5 Nm	—	—
Dreischarf et al. [25, 26]	—	—	700 N + 7.8 Nm	720 N + 5.5 Nm

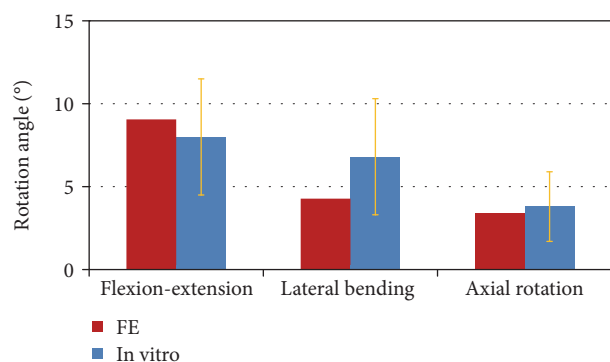


FIGURE 2: Comparison of the calculated intervertebral rotations of L4-L5 in the finite element (FE) model against experimental data [17] under a moment of 7.5 Nm for different loading cases.

**2.3. Graded Facetectomy Model.** Starting from the intact model, different graded facetectomies were simulated by modifying the facet joint of L4-L5 with the facet capsular ligament: 50% unilateral facetectomy, total left unilateral facetectomy, and total bilateral facetectomy. Regarding 50% unilateral facetectomy, different portions could be removed, depending on the surgical approaches. Therefore, to study sensitivity, four different 50% unilateral facetectomies were simulated by removing the upper, lower, outer, and medial portions of the left facet joint of L4-L5, respectively.

**2.4. Boundary and Loading Conditions.** The inferior endplate of L5 was rigidly fixed as a boundary condition. Flexion, extension, right lateral bending, left lateral bending, right axial rotation, and left axial rotation of the upper body were investigated. All loads (Table 2) were chosen according to Rohlmann et al. [23, 24] and Dreischarf et al. [25, 26]. The

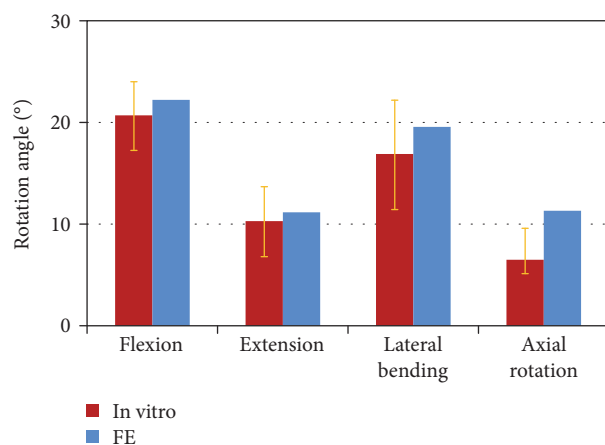


FIGURE 3: Comparison of the rotations in the finite element (FE) model and measured (Rohlmann et al. [18]) rotations in the lumbar spine under a moment of 7.5 Nm for different loading cases.

finite element program ABAQUS, version 6.13 (Dassault Systèmes, Versailles, France) was used for the simulations.

### 3. Results

**3.1. Validation.** The calculated IVR of the L4-L5 motion segment was within the range of in vitro experimental data [17] (Figure 2). Regarding the overall rotation, the estimated IVR was compared with in vitro data (Figure 3). The mobility of the model in flexion-extension and lateral bending was inside the range measured for seven lumbar specimens [18]. The mobility of the model in axial rotation was slightly outside, but the mobility for a single motion segment was still within the range of other published data [27]. Regarding the axial compressive load, the estimated IDP of L4-L5 in a standing position was 0.44 MPa. This is comparable to in vivo

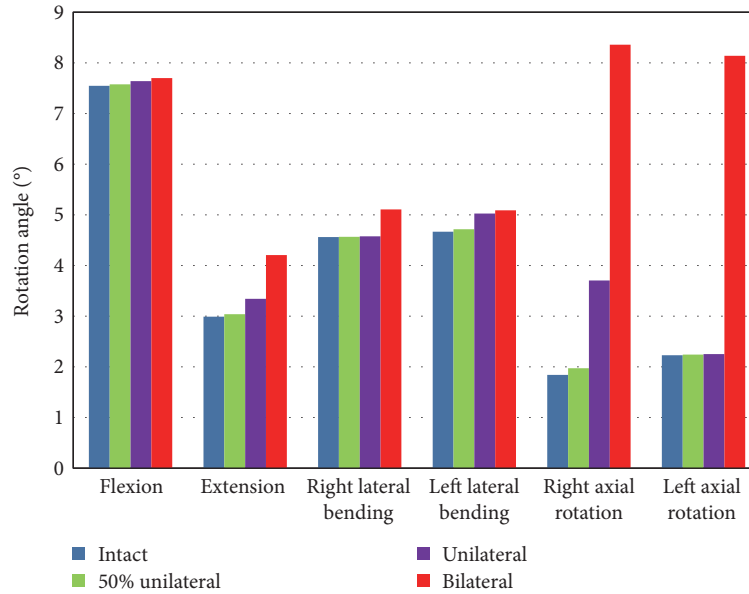


FIGURE 4: The values of rotation angles in each motion plane for the intact model and graded facetectomy models.

measurements by Wilke et al. [28], who recorded 0.50 MPa for spinal loading.

**3.2. Intervertebral Rotation.** The rotation angles in each motion plane for the intact model and graded facetectomy models are summarized in Figure 4. The values presented for the 50% unilateral facetectomy were the mean values calculated for the four different 50% unilateral facetectomies simulated. In flexion, graded facetectomy had only a minor effect. In extension, unilateral facetectomy increased IVR by 11.7% and bilateral facetectomy increased IVR by 40.7%. For right lateral bending, unilateral facetectomy and bilateral facetectomy increased the IVR by 0.3% and 11.9%, respectively, while for left lateral bending, this was 7.7% and 9.0%, respectively. In general, facetectomy had a large effect on the axial rotation. The 50% unilateral facetectomy, unilateral facetectomy, and the bilateral facetectomy increased the right axial rotation of the L4-L5 motion segment by 7.2%, 101.3%, and 354.3%, respectively, and by 0.6%, 1.1%, and 265.3%, respectively, for left axial rotation. For all loading types, the 50% facetectomy only increased the IVR by a maximum of 7.2%, which occurred under right axial rotation.

In most times, different types of partial resection resulted in similar IVR with a difference of less than 2%. Only for right axial rotation, removing the lower and outer portion of the left L4-5 facet joint increased the IVR by 6.4% (0.12°) and 19.2% (0.35°), respectively.

**3.3. Intradiscal Pressure and Facet Joint Force.** In most cases, facetectomy had only a minor influence on the IDP. In extension, the unilateral facetectomy and the bilateral facetectomy increased the IDP by 10.7% and 23.6%, respectively, and for left axial rotation, the bilateral facetectomy increased the IDP by 9.6%. The extension movement also produced the greatest facet joint force on the contralateral facet joint. For this loading case, the 50% unilateral facetectomy increased the contralateral facet joint force by

25% on average and the total unilateral facetectomy increased the force by 108.1%.

**3.4. Maximum von Mises Equivalent Stresses in the Annuli.** The four 50% unilateral facetectomy procedures only resulted in slightly different results for maximum von Mises stress in the annuli in comparison to the intact model. Unilateral facetectomy increased the maximum von Mises stress in the annuli by 13.1% in extension and 23.5% in right axial rotation. Bilateral facetectomy increased the maximum von Mises stress in the annuli by 32.3% in extension and 59.3% in axial rotation.

## 4. Discussion

An FE model of L3-L5 was constructed in this study, and the mobility of the model and the IDP were calculated for validation study. The effect of graded facetectomy on intervertebral rotations, intradiscal pressure, facet joint forces, and maximum von Mises equivalent stresses in the annuli was analyzed for all six loading conditions.

Regarding validation for the overall rotation, the calculated overall IVR of L3-L5 was justified. For example, the calculated axial rotation of L3-L5 was 6.54° in our FE model under a 7.5 Nm moment. According to Pearcy et al., the ratio between the rotation of L3-L5 and L1-L5 is 60% [19, 20]. The estimated axial rotation of L1-L5 in our model was 10.9° (6.54°/60%). Figure 3 showed the comparison between the justified IVR of L1-L5 and in vitro data [18]. All calculated data for the IDP, the IVR of L4-L5, and the overall IVR were inside the range of in vivo/in vitro data, respectively. Therefore, the load and mobility of the FE model were in the physiological range.

For the four 50% unilateral facetectomies simulated, there were no significant differences in results after resecting different portions of the vertebra compared with the intact model. Fusion or dynamic stabilization may not be necessary.

Similarly, Zhou et al. [5] also concluded that lumbar stability was not significantly affected if graded facetectomy was performed to remove less than 50% of bone, which is the same as our finding. In right axial rotation, removing the lower and outer portions of the left L4-5 facet joint increased the IVR by 6.4% and 19.2%, respectively. Although the absolute values were only 0.12° and 0.35°, retaining these portions of the bone may be beneficial. Choi et al. [29] also suggested that the resection should not involve the articular surface as preserving a larger articular surface is important for maintaining spinal stability.

This study demonstrated that total unilateral and bilateral facetectomy had little impact on the IVR in flexion and lateral bending, which is similar to in vitro results reported by Quint et al. [30]. These two facetectomy procedures also had a minor influence on the IDP and facet joint forces in flexion and lateral bending. For extension, total unilateral and bilateral facetectomy increased the IVR by 11.7% and 40.7%. After total unilateral facetectomy, the contralateral facet joint force increased by 108.1% in extension. This was the largest increase in contralateral facet joint force among all loading cases. At the same time, the increased IDP and the maximum von Mises stresses in the annuli in this model indicated a greater load through the intervertebral disc of L4-L5. This would inevitably lead to a greater risk of intervertebral disc degeneration and arthritis of the facet joints. Therefore, extension postures need to be achieved with care after total unilateral/bilateral facetectomy.

The facetectomy had a significant effect on IVR in axial rotation. Notably, after bilateral facetectomy, the IVR for right and left axial rotation increased by 354.3% and 265.3%. This is comparable to results from the literature [11]. Besides spinal instability, greater IDP of L4-L5 intervertebral disc and stress in the annuli will result in rupture of the annulus fibrosus. These remind us that axial rotation is another position needed to be treated carefully from the biomechanical point of view. Meanwhile, due to the change of stability, fusion or dynamic stabilization would be needed to reconstruct the lumbar stability from the biomechanical results. In this study, only the biomechanical aspects were regarded, but clinical experiences are inevitable as well; a cooperation of surgeons and bioengineers could induce the individual optimum for specific patients.

The majority of previous publications on spinal biomechanics constructed models based on the anatomy of European or American subjects [7, 10, 11]. However, differences in anatomy have been demonstrated between European or American people and Asian people, especially for the orientation of the facet joint. Grogan et al. [31] reported a mean facet joint angle of the lumbar spine from American subjects to be 37°. Yang and Wang reported this to be 47° for the lumbar spine of Chinese [32], while the value for Thais measured by Pichaisak et al. was 46° [33]. Given the vast and ever-growing Asian population, a concise FE analysis of graded facetectomy may be of great benefit across an array of disciplines and professions for Asians.

Some limitations of this study should be noted. In the case of spine, only a few parameters such as intervertebral

rotation and intradiscal pressure were measurable and thus suitable for validation. Therefore, facet joint forces and the maximum von Mises equivalent stresses in the annuli were presented only by relative ratios. The model used for simulation was from an asymptomatic volunteer. The effects of different pathological factors on the stability of spine after graded facetectomy need to be investigated in further study. In addition, the effects of muscle forces and bone mineral density on facetectomy need further study as well. Although several simplifications were made, the reported results are reliable because the same parameters were chosen for all loading cases. The results in the present study should be viewed as a comparative analysis between graded facetectomy models and an intact model for all six spinal loading conditions.

## 5. Conclusions

The results conclude that, after unilateral and bilateral facetectomy, care must be taken when placing the spine into extension and axial rotation posture from the biomechanical point of view.

## Competing Interests

The authors declare that there is no conflict of interest regarding the publication of this paper.

## Acknowledgments

This work was supported by the National Natural Science Foundation of China (Grant no. 81572138 and Grant no. 31300779) and the Shanghai Municipal Commission of Health and Family Planning (Project 20144Y0245).

## References

- [1] C. Ammendolia, P. Cote, Y. R. Rampersaud et al., "The boot camp program for lumbar spinal stenosis: a protocol for a randomized controlled trial," *Chiropractic & Manual Therapies*, vol. 24, no. 1, p. 25, 2016.
- [2] S. J. Atlas, R. B. Keller, D. Robson, R. A. Deyo, and D. E. Singer, "Surgical and nonsurgical management of lumbar spinal stenosis: four-year outcomes from The Maine Lumbar Spine Study," *Spine (Phila Pa 1976)*, vol. 25, no. 5, pp. 556–562, 2000.
- [3] K. Abumi, M. M. Panjabi, K. M. Kramer, J. Duranceau, T. Oxland, and J. J. Crisco, "Biomechanical evaluation of lumbar spinal stability after graded facetectomies," *Spine (Phila Pa 1976)*, vol. 15, no. 11, pp. 1142–1147, 1990.
- [4] A. Okawa, K. Shinomiya, K. Takakuda, and O. Nakai, "A cadaveric study on the stability of lumbar segment after partial laminotomy and facetectomy with intact posterior ligaments," *Journal of Spinal Disorders*, vol. 9, no. 6, pp. 518–526, 1996.
- [5] Y. Zhou, G. Luo, T. W. Chu et al., "The biomechanical change of lumbar unilateral graded facetectomy and strategies of its microsurgical reconstruction: report of 23 cases," *Zhonghua Yi Xue Za Zhi*, vol. 87, no. 19, pp. 1334–1338, 2007.
- [6] H. Li and Z. Wang, "Intervertebral disc biomechanical analysis using the finite element modeling based on medical images," *Computerized Medical Imaging and Graphics*, vol. 30, no. 6-7, pp. 363–370, 2006.

- [7] T. Zander, A. Rohlmann, C. Klockner, and G. Bergmann, "Influence of graded facetectomy and laminectomy on spinal biomechanics," *European Spine Journal*, vol. 12, no. 4, pp. 427–434, 2003.
- [8] K. K. Lee and E. C. Teo, "Effects of laminectomy and facetectomy on the stability of the lumbar motion segment," *Medical Engineering & Physics*, vol. 26, no. 3, pp. 183–192, 2004.
- [9] C. S. Chen, C. K. Feng, C. K. Cheng, M. J. Tzeng, C. L. Liu, and W. J. Chen, "Biomechanical analysis of the disc adjacent to posterolateral fusion with laminectomy in lumbar spine," *Journal of Spinal Disorders & Techniques*, vol. 18, no. 1, pp. 58–65, 2005.
- [10] A. Kiapour, D. Ambati, R. W. Hoy, and V. K. Goel, "Effect of graded facetectomy on biomechanics of Dynesys dynamic stabilization system," *Spine (Phila Pa 1976)*, vol. 37, no. 10, pp. E581–E589, 2012.
- [11] D. U. Erbulut, "Biomechanical effect of graded facetectomy on asymmetrical finite element model of the lumbar spine," *Turkish Neurosurgery*, vol. 24, no. 6, pp. 923–928, 2014.
- [12] W. T. Edwards, Y. Zheng, L. A. Ferrara, and H. A. Yuan, "Structural features and thickness of the vertebral cortex in the thoracolumbar spine," *Spine (Phila Pa 1976)*, vol. 26, no. 2, pp. 218–225, 2001.
- [13] U. M. Ayturk and C. M. Puttlitz, "Parametric convergence sensitivity and validation of a finite element model of the human lumbar spine," *Computer Methods in Biomechanics and Biomedical Engineering*, vol. 14, no. 8, pp. 695–705, 2011.
- [14] A. Shirazi-Adl, A. M. Ahmed, and S. C. Shrivastava, "Mechanical response of a lumbar motion segment in axial torque alone and combined with compression," *Spine (Phila Pa 1976)*, vol. 11, no. 9, pp. 914–927, 1986.
- [15] V. K. Goel, Y. E. Kim, T. H. Lim, and J. N. Weinstein, "An analytical investigation of the mechanics of spinal instrumentation," *Spine (Phila Pa 1976)*, vol. 13, no. 9, pp. 1003–1011, 1988.
- [16] A. Rohlmann, T. Zander, H. Schmidt, H. J. Wilke, and G. Bergmann, "Analysis of the influence of disc degeneration on the mechanical behaviour of a lumbar motion segment using the finite element method," *Journal of Biomechanics*, vol. 39, no. 13, pp. 2484–2490, 2006.
- [17] B. Ilharreborde, M. N. Shaw, L. J. Berglund, K. D. Zhao, R. E. Gay, and K. N. An, "Biomechanical evaluation of posterior lumbar dynamic stabilization: an in vitro comparison between universal clamp and Wallis systems," *European Spine Journal*, vol. 20, no. 2, pp. 289–296, 2011.
- [18] A. Rohlmann, S. Neller, L. Claes, G. Bergmann, and H. J. Wilke, "Influence of a follower load on intradiscal pressure and intersegmental rotation of the lumbar spine," *Spine*, vol. 26, no. 24, pp. E557–E561, 2001.
- [19] M. J. Pearcy and S. B. Tibrewal, "Axial rotation and lateral bending in the normal lumbar spine measured by three-dimensional radiography," *Spine (Phila Pa 1976)*, vol. 9, no. 6, pp. 582–587, 1984.
- [20] M. Pearcy, I. Portek, and J. Shepherd, "Three-dimensional x-ray analysis of normal movement in the lumbar spine," *Spine (Phila Pa 1976)*, vol. 9, no. 3, pp. 294–297, 1984.
- [21] K. Ueno and Y. K. Liu, "A three-dimensional nonlinear finite element model of lumbar intervertebral joint in torsion," *Journal of Biomechanical Engineering*, vol. 109, no. 3, pp. 200–209, 1987.
- [22] R. Eberlein, G. Holzapfel, and C. A. Schulze-Bauer, "An anisotropic model for annulus tissue and enhanced finite element analyses of intact lumbar disc bodies," *Computer Methods in Biomechanics and Biomedical Engineering*, vol. 4, no. 3, pp. 209–229, 2000.
- [23] A. Rohlmann, T. Zander, M. Rao, and G. Bergmann, "Applying a follower load delivers realistic results for simulating standing," *Journal of Biomechanics*, vol. 42, no. 10, pp. 1520–1526, 2009.
- [24] A. Rohlmann, T. Zander, M. Rao, and G. Bergmann, "Realistic loading conditions for upper body bending," *Journal of Biomechanics*, vol. 42, no. 7, pp. 884–890, 2009.
- [25] M. Dreischarf, A. Rohlmann, G. Bergmann, and T. Zander, "Optimised loads for the simulation of axial rotation in the lumbar spine," *Journal of Biomechanics*, vol. 44, no. 12, pp. 2323–2327, 2011.
- [26] M. Dreischarf, A. Rohlmann, G. Bergmann, and T. Zander, "Optimised in vitro applicable loads for the simulation of lateral bending in the lumbar spine," *Medical Engineering & Physics*, vol. 34, no. 6, pp. 777–780, 2012.
- [27] F. Heuer, H. Schmidt, Z. Klezl, L. Claes, and H. J. Wilke, "Stepwise reduction of functional spinal structures increase range of motion and change lordosis angle," *Journal of Biomechanics*, vol. 40, no. 2, pp. 271–280, 2007.
- [28] H. Wilke, P. Neef, B. Hinz, H. Seidel, and L. Claes, "Intradiscal pressure together with anthropometric data—a data set for the validation of models," *Clinical Biomechanics (Bristol, Avon)*, vol. 16, Suppl 1, pp. S111–S126, 2001.
- [29] G. Choi, S. H. Lee, P. Lokhande et al., "Percutaneous endoscopic approach for highly migrated intracanal disc herniations by foraminoplastic technique using rigid working channel endoscope," *Spine (Phila Pa 1976)*, vol. 33, no. 15, pp. E508–E515, 2008.
- [30] U. Quint, H. J. Wilke, F. Loer, and L. E. Claes, "Functional sequelae of surgical decompression of the lumbar spine—a biomechanical study in vitro," *Zeitschrift für Orthopädie und Ihre Grenzgebiete*, vol. 136, no. 4, pp. 350–357, 1998.
- [31] J. Grogan, B. H. Nowicki, T. A. Schmidt, and V. M. Haughton, "Lumbar facet joint tropism does not accelerate degeneration of the facet joints," *American Journal of Neuroradiology*, vol. 18, no. 7, pp. 1325–1329, 1997.
- [32] X. Yang and J. Wang, "The affections of the orientations and the severity of degeneration of facet joints to the degenerative lumbar spondylolisthesis," *Chinese Journal of Spine and Spinal Cord*, vol. 19, no. 1, pp. 52–55, 2009.
- [33] W. Pichaisak, C. Chotiyarnwong, and P. Chotiyarnwong, "Facet joint orientation and tropism in lumbar degenerative disc disease and spondylolisthesis," *Journal of the Medical Association of Thailand*, vol. 98, no. 4, pp. 373–379, 2015.